Semiconductors, Vol. 35, No. 6, 2001, pp. 613–614. Translated from Fizika i Tekhnika Poluprovodnikov, Vol. 35, No. 6, 2001, pp. 641–642.

II International Conference on Amorphous and Microcrystalline Semiconductors

The II International Conference on Amorphous and Microcrystalline Semiconductors took place in St. Petersburg from July 3 to July 5, 2000. The conference was organized by the Russian Academy of Sciences and represented by the Ioffe Physicotechnical Institute. The Organizing Committee Chairman was E.I. Terukov, and the members were K.D. Tséndin, O.I. Kon'kov, and I.N. Trapeznikova.

There were 168 papers presented at the conference. Scientists from France, Germany, South Korea, Great Britain, Cuba, Latvia, and all the countries belonging to the Commonwealth of Independent States attended the conference.

The so-called Kolomiets lecture was delivered by É.A. Lebedev and had the title "Transport of Charge Carriers in Unordered Materials"; É.A. Lebedev is a follower and colleague of the late Professor B.T. Kolomiets, is the discoverer of the switching effect in vitreous chalcogenide semiconductors, and is the developer of the transit-time method for studying the charge-carrier transport in unordered semiconductors. During the plenary session, lectures were given by leading scientists in the field of unordered semiconductors, i.e., by A.M. Andriesh (Moldova), S.A. Dembovskiĭ, Yu.S. Tver'yanovich, K.D. Tséndin, A.L. Talis, E.I. Terukov, V.V. Sobolev, A.I. Popov (all from Russia), Ya. Teteris (Latvia), and Jean-Paul Kleider (France); in these lectures, the latest achievements in the physics of vitreous chalcogenide semiconductors and amorphous materials were reviewed.

Five lines can be distinguished in the scope of the conference:

(1) amorphous hydrogenated silicon and its alloys,

(2) amorphous and diamond-like carbon,

(3) microcrystalline and nanocrystalline semiconductors,

(4) vitreous chalcogenide semiconductors, and

(5) technological applications.

In the papers devoted to amorphous silicon, much consideration was given to various methods for obtaining the films and to the interrelation between these methods and the states of impurities and defects; these states affect physical properties such as electrical conductivity, luminescence, and optical absorption. Attention of participants of the conference was drawn to the papers by O.A. Golikova, V.G. Golubev, M.S. Bresler, V.Kh. Kudoyarova, S.P. Vikhrov, A.G. Kazanskiĭ, and V.P. Afanas'ev. Particular interest was attracted to the communications delivered by M.S. Bresler, which were devoted to the observation and study of the effect of stimulated radiation in the films of hydrogenated amorphous silicon doped with erbium, and to that delivered by V.G. Golubev, which was concerned with enhancement of the photoluminescence intensity in the vicinity of 1.54 μm in the *a*-Si:(H, Er) films installed in a planar Fabry–Perot microcavity. The participants of the conference gave much attention to the problems in the technology of fabrication (and to studies) of nanostructured and microcrystalline silicon samples; this attention is caused by the suppression of the Staebler–Wronski effect in such samples, which is of interest in relation to practical applications.

In the papers devoted to amorphous and diamond-like carbon, various methods (chemical, ion-plasma, and electron-beam treatments) for the structural modification of the material were considered; metastable states arising as a result of such modification were discussed. Particular interest was expressed in the effect of the field emission of electrons in carbon films obtained by different methods; attention was also drawn to the issues related to special features of morphology of such films, their optical properties, microhardness, wettability, and liquid adhesion. An approach advanced in the papers delivered by A.L. Talis, M.I. Samoĭlovich, and M.I. Mironov is of much interest; this approach makes it possible to describe the noncrystalline diamond-like structures in terms of generalized crystallography.

The third line in the scope of the conference was widely represented by the papers devoted to nanocrystalline, microcrystalline, and porous silicon as well as by the papers concerned with fullerene-containing materials. The papers presented by Jean-Paul Kleider, O.A. Golikova, and V.P. Afanas'ev contained interesting information about the so-called polymorphous (nanostructured) silicon films, whose structure and properties differ from those of the films of hydrogenated amorphous silicon and which are actively studied at present. We should highlight an interesting paper presented by A.B. Pevtsov and devoted to the production and characterization of three-dimensional arrays of GaN and InN nanoclusters in the opal matrix, which is topical in relation to the possibility of forming the semiconducting nanostructures and photonic crystals in such materials. The papers presented by V.V. Popov, V.V. Sobolev, É.A. Lebedev, and V.A. Yukhimchuk were devoted to studies of the structural and optical

1063-7826/01/3506-0613$21.00

properties and electron spin resonance in nanostructured and porous materials.

Among the papers devoted to chalcogenide and other vitreous semiconductors, particular attention was paid to those concerned with specific features of electron energy spectrum in these materials and to changes in this spectrum as a result of varying the growth methods and of doping. Great interest was expressed in the papers presented by V.Ya. Kogaĭ (ultrafast dissolution of metals in chalcogenide vitreous semiconductors), O.Yu. Prikhod'ko (effects of the methods for thermal evaporation and high-frequency cosputtering on the electron spectrum of amorphous S–Se films), and the papers presented by A.A. Babaev and devoted to the effect of low impurity concentrations on photoluminescence and charge-carrier drift in the arsenic sulfide samples. The application-oriented studies of vitreous chalcogenide semiconductors included such topics as the writing of data (K.D. Tséndin), photoluminescence in vitreous chalcogenide semiconductors doped with the rare-earth elements (A.S. Tver'yanovich), the development of photoresists based on thin films of vitreous chalcogenide semiconductors (V.I. Vlasov), and the design of an acoustooptical modulator for the diode-laser emission (L.A. Kulakova).

The papers concerned with prospects of the technical applications of vitreous chalcogenide semiconductors were widely presented at the conference. In addition to the aforementioned applications based on vitreous chalcogenide semiconductors, we may mention the photoluminescent and electroluminescent structures based on various materials, thin-film solar cells, and the development of thermally stable polymers that are based on polyimides and feature efficient photoluminescence. It is remarkable that there were papers in which not only the prospects of using amorphous materials in practical medicine to develop new devices and materials having unique physicochemical and biochemical properties were proven but the operating prototypes were also demonstrated.

Numerous topical issues were discussed in three poster sessions.

In the closing roundtable discussion, it was noted that the conference was timely and topical and that the papers presented were of high scientific quality. In the discussion held at the closure of the conference, it was persistently wished that the next conference be convened in two years.

The abstracts of the papers presented at the conference were published. The organizing committee recommended the most interesting papers be published in this issue of "Fizika i Tekhnika Poluprovodnikov" ("Semiconductors").

The convening of the conference was made possible by the support of the Russian Foundation for Basic Research (project no. 00-02-26038). The Ioffe Physicotechnical Institute of the Russian Academy of Sciences contributed appreciably to the conference organization. The role of the St. Petersburg State Technical University should be acknowledged for providing the conference site (in the House of Scientists at Lesnoĭ).

Evgeniĭ Terukov,
Organizing Committee
Chairman

Semiconductors, Vol. 35, No. 6, 2001, pp. 615–620. Translated from Fizika i Tekhnika Poluprovodnikov, Vol. 35, No. 6, 2001, pp. 643–648.

II INTERNATIONAL CONFERENCE ON AMORPHOUS AND MICROCRYSTALLINE SEMICONDUCTORS

The Relation between Recombination at Interface States and the Anomalously Small Exponent of the Current–Illuminance Characteristic in Microcrystalline Silicon

K. V. Koughia and E. I. Terukov*

Ioffe Physicotechnical Institute, Russian Academy of Sciences, Politekhnicheskaya ul. 26, St. Petersburg, 194021 Russia

** e-mail: eug.terukov@pop.ioffe.rssi.ru*

Submitted November 9, 2000; accepted for publication November 15, 2000

Abstract—The recombination of nonequilibrium charge carriers in *p*-Si doped lightly with boron was analyzed; the samples were obtained by high-frequency decomposition of silane diluted heavily with hydrogen under conditions of a high high-frequency power. The columnar formations composed of microcrystallites are typical of the structure of such a material. It was established that, in a limited temperature range, the dominant recombination mechanism may be related to recombination at intercolumnar boundaries in combination with tunneling and partial thermal activation. Such recombination leads to an anomalously small exponent in the current–illuminance characteristic $\gamma = 0.3$. The suggested model makes it possible to calculate the temperature dependences of γ for various levels of doping of the material and predicts a decrease in the efficiency of doping and an increase in the defect concentration in the material with an increasing concentration of introduced boron. The recombination mechanism changes at elevated temperatures; as a result, the recombination at the boundaries governed by the Shockley–Read statistics becomes prevalent. Tunneling-related recombination within the columns is dominant at low temperatures. Both mechanisms lead to an increase in γ to conventional values ($\gamma \approx 0.7$). © *2001 MAIK "Nauka/Interperiodica".*

1. INTRODUCTION

In the group of silicon materials including those with an amorphous, nanocrystalline, microcrystalline, or polycrystalline structure, the amorphous and polycrystalline materials are indubitable leaders in the number of publications devoted to recombination of nonequilibrium charge carriers. It is generally accepted that recombination in amorphous silicon is controlled by localized states in the mobility gap; these states act as the centers of the capture and recombination of nonequilibrium charge carriers, whereas recombination at the crystal boundaries is predominant in polycrystalline silicon. Compared to the above materials, the number of publications devoted to nanocrystalline and microcrystalline materials is much less, which is apparently related to the complexity of studying these materials and, as a consequence, to difficulties in interpreting the data obtained.

In fact, a realistic model of recombination in an unordered and inhomogeneous semiconductor should take into account three recombination processes: inside the "main" and "incorporated" materials and also at the corresponding interfaces. All three recombination processes are competitive, and each of them can play a determining role under given experimental conditions. Identification of the main and incorporated materials can be extremely diverse. Thus, for nanocrystalline silicon, the role of the main material is played by the amorphous matrix, whereas crystalline inclusions act as an incorporated material. The situation is more complicated for microcrystalline silicon. It is known that this material features an extremely inhomogeneous structure, in which the microcrystallites are combined into columnar formations linked to each other by an amorphous "connecting fabric" [1]. For such a structure, the microcrystallites combined in columnar formations may represent the main material, whereas the amorphous connecting binders may constitute the incorporated material.

An intriguing property of microcrystalline silicon is the observed (in a limited temperature range) anomalously flat current–illuminance characteristic with an exponent that may be as small as 0.15 [2–4]. Such a small exponent of the current–illuminance characteristic was observed previously in heavily doped and compensated germanium at sufficiently low temperatures, in that case this effect was related to the spatial separation of recombining nonequilibrium charge carriers owing to fluctuations of the conduction- and valence-band edges [5]. In this paper, we show that the current–illuminance characteristic with an exponent smaller than 0.5 in microcrystalline silicon may be related to the recombination of nonequilibrium electrons and holes at the charged boundaries of columnar formations that ensure the spatial separation of charge carriers.

1063-7826/01/3506-0615$21.00

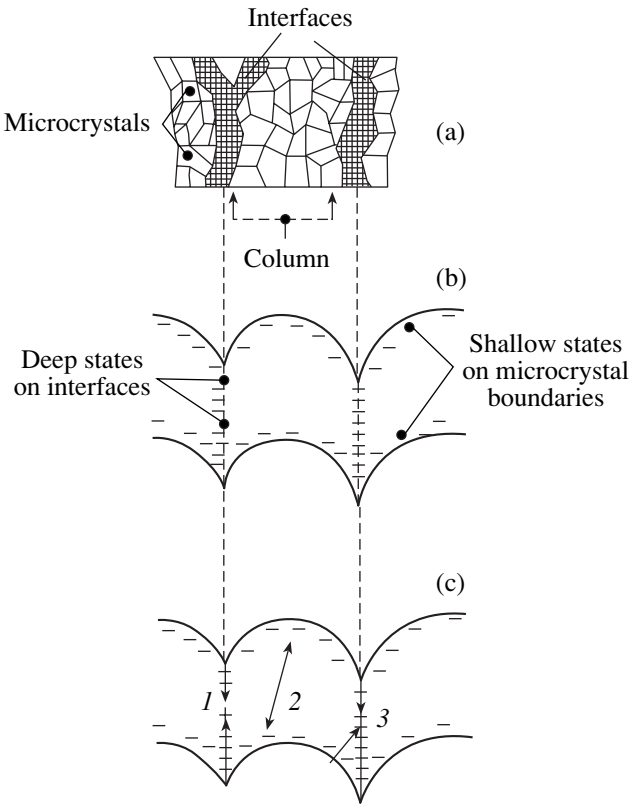

Fig. 1. (a) Schematic representation of the structure of microcrystalline silicon. (b) Energy-band diagram of lightly doped microcrystalline *p*-Si. (c) Possible mechanisms for recombination of nonequilibrium charge carriers: (*1*) the Shockley–Read recombination at intercolumnar boundaries, (*2*) tunneling recombination within the columns, and (*3*) tunneling recombination at intercolumnar boundaries.

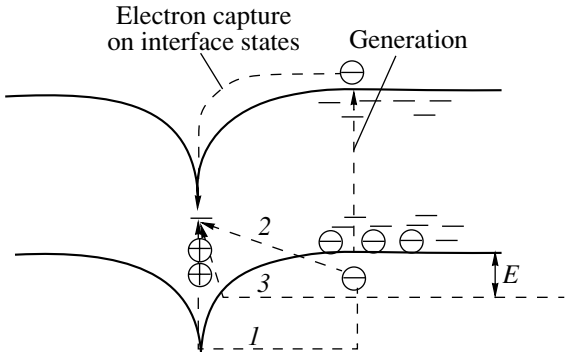

Fig. 2. Possible mechanisms of recombination at the intercolumnar boundary. *E* denotes the energy for which tunneling occurs: (*1*), (*2*), and (*3*) correspond to the thermally activated process, tunneling transition, and combined process, respectively.

2. RESULTS AND DISCUSSION

Microcrystalline silicon, whose properties are discussed in this paper, was obtained by high-frequency (HF) decomposition of silane-containing mixtures under conditions of high HF power and a high degree of dilution of SiH_4 with hydrogen [4]. It is characteristic of such a material that its conductivity is *n*-type due to light doping with oxygen during the film deposition [6] and that its structure is inhomogeneous; in this structure (shown schematically in Fig. 1a), the microcrystallites 10–30 nm in size are combined into much larger (100–300 nm) columnar formations with clearly pronounced interfaces [1, 4]. Light doping with boron makes it possible to obtain samples with nearly intrinsic conductivity. The presumed energy-band diagram of the material that is doped lightly with boron and has a columnar structure is shown in Fig. 1b. The band bending at the intercolumnar boundaries is related to the accumulation of holes at the deep states as a result of doping with boron.

In Fig. 1c, we illustrate the most probable mechanisms for the recombination of nonequilibrium charge carriers. In order to calculate the characteristics of the Shockley–Read recombination at the column boundaries, we may use the well-developed models for unordered materials; however, these models always yield an exponent larger than 0.5 for the current–illuminance characteristic [7, 8]. It should be noted that we disregard the probability of the Shockley–Read recombination in the bulk of the columns, because the estimations show that recombination at the boundaries is prevalent for all reasonable values of the parameters. An interesting hypothetical mechanism of the decrease in the exponent of the current–illuminance characteristic in unordered material was suggested previously [9] and was related to the smoothing of fluctuations in the potential due to the accumulation of nonequilibrium charge carriers and variation in the current-flow level. Seemingly, a similar situation could arise in the material we studied owing to an illumination-induced modulation of the charge trapped at the interface states. However, our calculations show that this possibility may only be realized (if at all) in a fairly narrow range of the material parameters and that the exponent of the current–illuminance characteristic cannot be smaller than 0.5 at high and low temperatures. This contradicts the experimental data. Therefore, we believe that another type of recombination is prevalent in the material we studied.

Tunneling-related recombination may be dominant in the bulk of an unordered semiconductor at fairly low temperatures. This recombination is also well studied in a wide temperature range, and it is known that this type of recombination yields the exponent of the current–illuminance characteristic in the range from 0.6 to 1, i.e., much larger than that observed experimentally [10, 11]. We now consider the tunneling recombination at the intercolumnar interfaces.

A scheme of this recombination process is illustrated in Fig. 2. Apparently, the recombination proceeds in two stages. In the first stage, electrons are captured by the interface states. This is a fast process, because the column boundaries are charged positively

and attract the nonequilibrium electrons. Most probably, the net rate is governed by the second (comparatively slow) process of penetration of nonequilibrium holes to the interface states. This penetration may occur both by thermally overcoming the barrier and by tunneling or recombination processes (lines *1*, *2*, and *3* in Fig. 2, respectively).

We now estimate the recombination rate as a function of the energy E, for which tunneling of a hole to the interface occurs; we have

$$R(E) = N_i \sigma_p v_p p_0 \exp\left(-\frac{E}{kT}\right)\exp\left[-\frac{r(E)}{a}\right], \quad (1)$$

where N_i is the concentration of the recombination centers at the interface, σ_p is the cross section of the nonequilibrium-hole capture, v_p is the thermal velocity of holes, p_0 is the nonequilibrium-hole concentration at the mobility edge of the valence band (E_v), $r(E)$ is the tunneling distance, and a is a constant that specifies the penetration of the charge-carrier wave function into the potential barrier.

We assumed that the probability of tunneling is proportional to $\exp[-r(E)/a]$, which is a typical assumption for localized charge carriers. The best approximation for delocalized charge carriers is given by [12]

$$D \propto \exp\left\{-\frac{1}{\hbar}\int_{L/2}^{0}\sqrt{2\mu[E(r)-E]}\,dr\right\}. \quad (2)$$

Both approximations yield a tunneling probability that decreases exponentially with distance. However, we believe that the localized-carrier approximation is more realistic because the sizes of microcrystallites forming the columns are very small; as a result, the wave function of nonequilibrium charge carriers is profoundly perturbed and differs substantially from that of quasifree charge carriers.

The dependence $r(E)$ can be calculated from the barrier shape [13]; i.e.,

$$E(r) = \frac{e^2 N_a}{4\varepsilon\varepsilon_0}\left(\frac{p_s^2}{2N_a^2} - \frac{2p_s}{N_a}r + r^2\right), \quad (3)$$

where p_s is the surface density of holes trapped at the intercolumnar boundary and N_a is the acceptor concentration.

An analysis of (1) and (2) shows that there is a well-pronounced maximum in the recombination rate; this maximum corresponds to the tunneling distance equal to

$$r_{\max} = \frac{p_s}{N_a} - \frac{2\varepsilon\varepsilon_0 kT}{ae^2 N_a}. \quad (4)$$

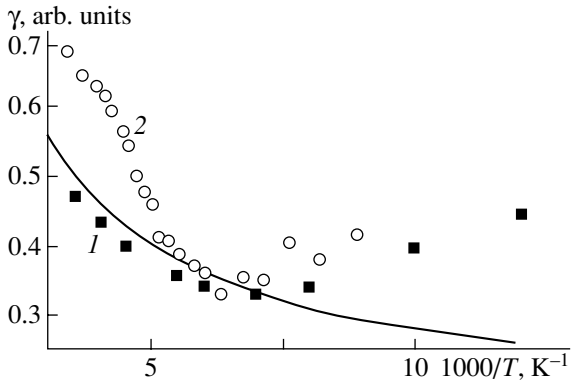

Fig. 3. Comparison of the calculated dependence of the exponent in the current–illuminance characteristic on reciprocal temperature (solid line) with experimental data (*1*) [2] and (*2*) [3]. Parameters used in the calculation are listed in the table.

As a result, a characteristic recombination time related to $r_{\max}$ exists for each boundary with the surface-state density of p_s; thus, we have

$$\tau(p_s) = \tau_0 \exp\left(-\frac{4\varepsilon\varepsilon_0 kT}{a^2 e^2 N_a}\right)\exp\left(\frac{2p_s}{aN_a}\right), \quad (5)$$

where τ_0 is the preexponentioal factor related to the charge-carrier thermal velocity, the capture cross sections, etc.

In terms of such a model, the boundaries with low p_s feature short recombination times, whereas those with high p_s have long recombination times. As a consequence, the boundary states with low p_s are predominantly unoccupied, whereas those with high p_s are mainly occupied. Obviously, p_s is a random quantity that fluctuates from one boundary to another. If $g(p_s)$ is a distribution function for the quantity p_s, the total concentration of nonequilibrium charge carriers can be calculated by integrating over all the interfaces as

$$p = N_s\int_0^\infty g(p_s) f(G, p_s)\,dp_s, \quad (6)$$

The model parameters used in calculations whose results are shown in Fig. 3

Acceptor concentration	$N_a = 1.1 \times 10^{18}$ cm^{-3}
Interface concentration	$N_s = 6 \times 10^{15}$ cm^{-3}
Variance of distribution of the surface-state density at the interfaces	$p_{sm} = 1 \times 10^{12}$ cm^{-2}
Localization radius of the wave function	a = 12 Å
The time preexponentional factor	$\tau_0 = 10^{-12}$ s

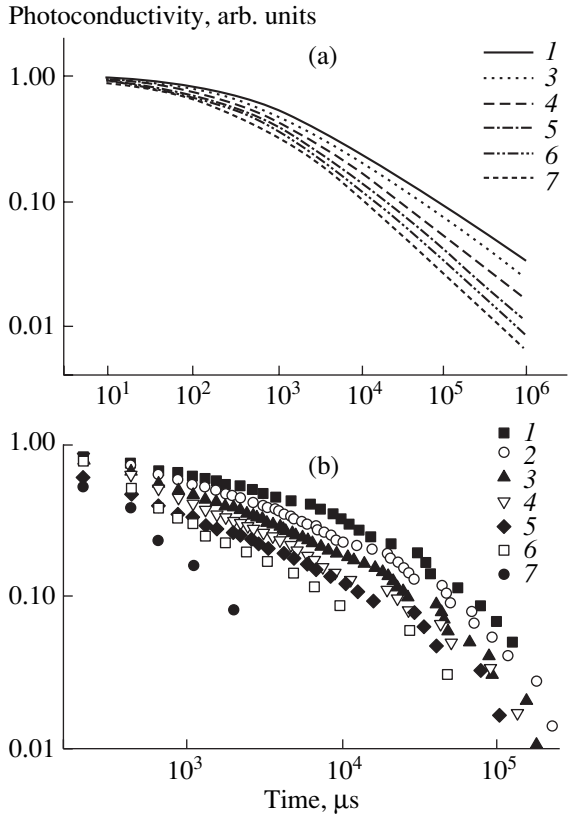

Fig. 4. Decay of photoconductivity after the illumination was switched off. (a) The results of calculations and (b) experimental data [4]. T = (*1*) 194, (*2*) 232, (*3*) 261, (*4*) 297, (*5*) 327, (*6*) 351, and (*7*) 373 K.

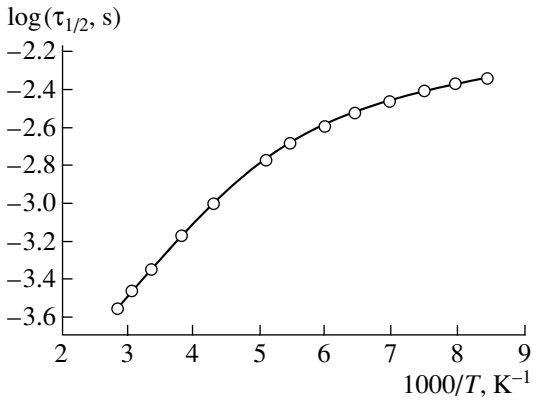

Fig. 5. Calculated temperature dependence of the half-decay time $\tau_{1/2}$ of photoconductivity after illumination was switched off.

where $f(G, p_s)$ is the occupancy function for the boundary states; this function can be determined by equating the generation and recombination rates per boundary; thus, we have

$$f(G, p_s) = \frac{1}{1 + N_s/G\tau(p_s)}, \tag{7}$$

where N_s is the total concentration of boundaries and G is the generation rate for the electron–hole pairs.

Let us now discuss the possible form of the distribution function $g(p_s)$. The following assumptions are valid for this distribution. First, the actual form of the distribution $g(p_s)$ for low p_s is not very important because the corresponding boundaries do not contribute to the concentration of nonequilibrium charge carriers. Second, it is reasonable to assume that the fraction of the boundaries with high p_s is relatively small; consequently, for high p_s, $g(p_s)$ is a descending function, and, most probably, this descent is fairly steep. It is found that the model is not very sensitive to a specific distribution shape. Thus, we performed the calculations for exponential

$$g(p_s) \propto \exp(-\lambda p_s) \tag{8}$$

and Gaussian

$$g(p_s) \propto \exp\left(-\frac{p_s^2}{p_{sm}^2}\right) \tag{9}$$

distributions. Both functions yield qualitatively similar results, and a current–illuminance characteristic with an exponent less than 0.5 is actually obtained. However, distribution (9) describes the temperature dependences of the exponent in the current–illuminance characteristic and of the photoconductivity kinetics slightly better; therefore, the results presented below were obtained using distribution (9).

It is pertinent to mention immediately a plausible interpretation of the quantity p_{sm}, which appears in the distribution function. Since this quantity specifies the variance of the distribution of the surface density of states at the interfaces, it may be used to assess the degree of disorder in the material.

Substituting (5), (7), and (9) into (6), we can numerically calculate the dependences of the nonequilibrium-carrier concentration on the generation rate and temperature. The results of such a calculation (represented as the $\gamma(1/T)$ dependence) are shown in Fig. 3. Experimental data reported previously [2, 3] are also shown for the sake of comparison. In the table, we list the model parameters that yield the closest agreement with experimental data. We may state that all the values are quite reasonable.

We should specially discuss a discrepancy between the model and experiment at high and low temperatures. To this end, we should return to Fig. 1c, in which the competition between three recombination mechanisms is illustrated. It seems quite obvious that the Shockley–Read recombination (*1*) is bound to be prevalent at high temperatures and yields $\gamma \approx 0.7$, in complete agreement with experimental data. At very low temperatures, pure tunneling mechanism (*2*) is apparently predominant, which also results in an appreciable increase in the exponent γ [10, 11]. Therefore, the agreement between the suggested model and the exper-

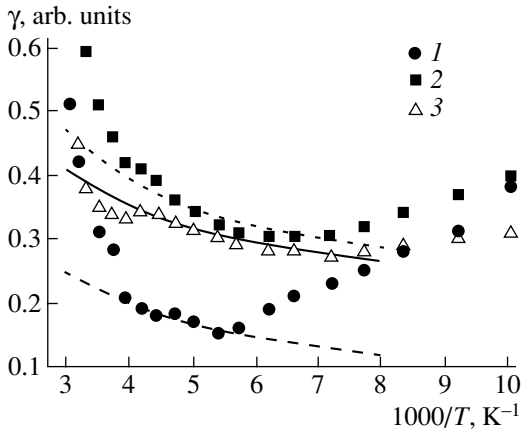

Fig. 6. Comparison of calculated (lines) and experimental (*1, 2, 3*) temperature dependences of the exponent γ of the current–illuminance characteristic in the samples with different concentrations of boron impurity. Content of diborane in the gaseous mixture was $C_{B_2H_6}$ = (*1*) 2, (*2*) 5, and (*3*) 10 ppm.

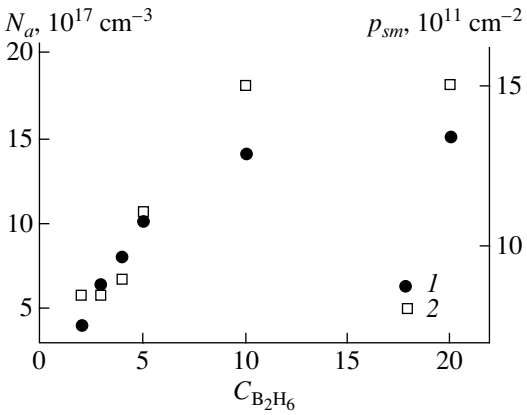

Fig. 7. Dependences of (*1*) the ionized-acceptor concentration N_a and (*2*) a degree of disorder in the material p_{sm} on the concentration of doping impurity (boron).

iment may exist only in a narrow temperature range, in which mechanism (*3*) is predominant.

The model makes it possible to calculate not only the steady-state characteristics of photoconductivity but also the time dependences of photoconductivity after the illumination has been switched off. In fact, following the cessation of excitation, the interfaces free themselves of charge carriers via recombination; this process develops in time t with recombination times inherent in the interfaces. Therefore, by analogy with Eq. (6), we may assume that

$$p(t) = N_s\int_0^\infty g(p_s)\,f(G, p_s)e^{-t/\tau(p_s)}dp_s. \qquad (13)$$

The results of calculations based on the above parameters are shown in Fig. 4a and are to be compared with experimental data in Fig. 4b [4]. In Fig. 5, we show the calculated temperature dependence of the photoconductivity half-decay time $\tau_{1/2}$. We may note that there is reasonable agreement between theory and experiment; this agreement may be apparently further improved if we take into account recombination mechanisms (*1*) and (*2*) illustrated in Fig. 1c.

Temperature dependences of the exponent in the current–illuminance characteristic are affected profoundly by the degree of doping of the material. Figure 6 shows the results of calculations; experimental data reported recently [4] are also shown for the sake of comparison. In Fig. 7, we show the dependence of the parameters that are used in calculations and ensure the best fit to experimental data on the fraction of diborane $C_{B_2H_6}$ in the initial gaseous mixture. The results obtained can be treated in the following manner. For low diborane content, the doping efficiency (associated with the concentration of ionized acceptors N_a) is directly proportional to $C_{B_2H_6}$, whereas the disorder degree (associated with p_{sm}) is almost independent of the introduced-impurity concentration. As $C_{B_2H_6}$ increases, the doping efficiency decreases owing apparently to an increase in the number of defects and in the degree of disorder of the material. The dependence levels off for the highest doping level; i.e., all the introduced impurity atoms become electrically inactive owing to an increase in the concentration of compensating defects. This treatment is in excellent agreement with the published experimental data for both microcrystalline and amorphous silicon [4, 14].

3. CONCLUSION

Microcrystalline silicon has a highly inhomogeneous structure, in which the microcrystallites are combined into columnar formations separated by interfaces that play a determining role in the recombination of nonequilibrium charge carriers. When boron is introduced, the intercolumnar boundaries accumulate positive charge and become less accessible to nonequilibrium holes. At fairly low temperatures, the penetration of holes to the interface is controlled by subbarrier tunneling, which gives rise to a large spread in recombination lifetimes and, as a consequence, to the exponent of a current–illuminance characteristic smaller than 0.5; as a result, an extended tail in the photoconductivity decay after the cessation of excitation is observed. This mechanism of recombination is found to be very sensitive to the spread in the properties of interfaces and in the concentration of ionized acceptors. Furthermore, this mechanism is effective in a comparatively narrow temperature range; i.e., the Shockley–Read recombination is predominant at high temperatures, whereas the

tunneling recombination within the columns is prevalent at low temperatures.

REFERENCES

1. M. Luysberg, P. Hapke, R. Carius, and F. Finger, Philos. Mag. A **75**, 31 (1997).
2. Z. H. Zhou, S. D. Baranovsky, S. Yamasaki, and K. Ikuta, Fiz. Tekh. Poluprovodn. (St. Petersburg) **32**, 905 (1998) [Semiconductors **32**, 807 (1998)].
3. A. G. Kazanskiĭ, H. Mell, E. I. Terukov, and P. A. Forsh, Fiz. Tekh. Poluprovodn. (St. Petersburg) **34**, 373 (2000) [Semiconductors **34**, 367 (2000)].
4. D. Ruff, *Elecktrischer Transport in Mikrokristallinen Silicium. Thesis* (Philipps–Universitat Marburg, Marburg–Lahn, 1999).
5. R. Rentzsch and I. S. Shlimak, Phys. Status Solidi A **43**, 231 (1977).
6. P. Torres, J. Meier, R. Flückkiger, *et al.*, Appl. Phys. Lett. **69**, 1373 (1996).
7. W. Shockley and W. T. Read, Phys. Rev. **87**, 835 (1952).
8. G. W. Taylor and J. G. Simmons, J. Non-Cryst. Solids **8–10**, 940 (1972).
9. A. Ya. Shik, Zh. Éksp. Teor. Fiz. **68**, 1859 (1975) [Sov. Phys. JETP **41**, 932 (1975)].
10. B. I. Shklovsky, E. I. Levin, H. Frizsche, and S. D. Baranovskii, in *Advances in Disordered Semiconductors*, Vol. 3: *Transport, Correlation and Structural Defects*, Ed. by H. Fritzsche (World Scientific, Singapore, 1990), p. 161.
11. C. V. Koughia and I. S. Shlimak, in *Advances in Disordered Semiconductors*, Vol. 3: *Transport, Correlation and Structural Defects*, Ed. by H. Fritzsche (World Scientific, Singapore, 1990), p. 213.
12. A. S. Davydov, *Quantum Mechanics* (Nauka, Moscow, 1973; Pergamon, Oxford, 1976).
13. K. M. Doshchanov, Fiz. Tekh. Poluprovodn. (St. Petersburg) **30**, 558 (1996) [Semiconductors **30**, 305 (1996)].
14. W. E. Spear and P. G. LeComber, in *The Physics of Hydrogenated Amorphous Silicon* (Springer-Verlag, Berlin, 1984), Vol. 1.

Translated by A. Spitsyn

Semiconductors, Vol. 35, No. 6, 2001, pp. 621–626. Translated from Fizika i Tekhnika Poluprovodnikov, Vol. 35, No. 6, 2001, pp. 649–654.

II INTERNATIONAL CONFERENCE ON AMORPHOUS AND MICROCRYSTALLINE SEMICONDUCTORS

Effect of Erbium on Electronic Traps in PECVD-grown *a*-Si:H(Er)/*c*-Si Structures

V. S. Lysenko*, I. P. Tyagulskiĭ*, I. N. Osiyuk*, A. N. Nazarov*, Ya. N. Vovk*, Yu. V. Gomenyuk*, E. I. Terukov, and O. I. Kon'kov****

** Institute of Semiconductor Physics, National Academy of Sciences of Ukraine, pr. Nauki 45, Kiev, 03028 Ukraine*

*** Ioffe Physicotechnical Institute, Russian Academy of Sciences, Politekhnicheskaya ul. 26, St. Petersburg, 194021 Russia*

Submitted November 9, 2000; accepted for publication November 15, 2000

Abstract—Electrical properties and characteristics of defects in the upper part of the band in Er-doped *a*-Si:H grown by plasma-enhanced chemical vapor deposition were studied for the first time. © *2001 MAIK "Nauka/Interperiodica".*

1. INTRODUCTION

The observation of efficient room-temperature photoluminescence (PL) from Er ions in amorphous hydrogenated silicon *a*-Si:H(Er) produced by magnetron sputtering [1] stimulated studies of Er luminescence in *a*-Si:H(Er) fabricated by various technologies. For example, the first observation of Er luminescence in *a*-Si:H(Er) produced by plasma-enhanced chemical vapor deposition (PECVD), known to be the basic method for fabrication of device-quality amorphous silicon for solar cells, was reported in [2]. According to [3], the electroluminescence is excited owing to the Auger process, in which electrons from the *a*-Si:H conduction band are captured by silicon dangling bonds (*D*-centers), with energy transferred to the *f*-shell of Er ions. The introduction of erbium into an amorphous *a*-Si:H matrix induces, along with the dangling bonds, local distortions of hydrogen–silicon and silicon–silicon bonds. As is known, sets of shallow traps are formed near the edges of the allowed bands in the latter case. Until now, the character of Er-induced electrically active centers in amorphous hydrogenated Si (their activation energy and energy distribution) remained unclarified; however, these data may be helpful in deriving both the physical model and the technology of the Er-based electroluminescent structures (suppression of nonradiative recombination, etc.).

In this communication, we report new data on the electrical properties and characteristics of levels in the upper part of the forbidden band for *a*-Si:H(Er) produced by PECVD with $Er(TMHD)_3$ metalorganic powder as the Er source.

2. SAMPLES AND EXPERIMENTAL METHODS

The samples were grown in a conventional installation for the PECVD of *a*-Si:H from a 25% SiH_4 + 75% Ar gas mixture. Powdered $Er(TMHD)_3$ heated in a special thermal evaporator to temperatures of 140, 165, or 190°C served as an Er source. For details of *a*-Si:H(Er) layer fabrication, see [4]. Single-crystal KÉF-4.5 or KÉF-40 (*n*-Si:P, ρ = 4.5 or 40 Ω cm) substrates were used. Films were deposited at substrate temperature T_s = 220°C. The thickness of the films under study was 0.6 μm at a deposition time of 60 min. The concentration profiles for the introduced Er and H, and for the accompanying C and O impurities, were determined by SIMS. The Er concentration was 3×10^{20} and 1×10^{21} cm^{-3} in films obtained at evaporator temperatures of 140 and 190°C, respectively, and the oxygen concentration was 5×10^{21} cm^{-3} for both modes. The Al contact was deposited by thermal evaporation onto the *a*-Si:H(Er) surface. The contact to the back side of the single-crystal substrate (*c*-Si) was deposited using a Ga–Zn eutectic alloy.

The energy spectrum of electrically active centers in the *a*-Si:H(Er)/*c*-Si heterostructures obtained was studied by thermally stimulated current spectroscopy in a wide temperature range from 7 to 350 K. In the interval 7–170 K (further designated as the "low-temperature" (LT) range), a liquid-helium cryogenic installation was used, and at 80–350 K (henceforth, "high-temperature" (HT) range), an installation with liquid nitrogen was used. Computerized thermal controllers of the cryogenic setups allowed either a linear mode of sample heating at a constant rate of 0.1–0.3 K/s, or "fractional" (stepwise) heating [5].

Different schemes were used to measure the thermally stimulated currents in the LT and HT temperature intervals. For LT studies, an *a*-Si:H(Er)/*c*-Si heterostructure was short-circuited at room temperature and cooled in the dark to 7–10 K (filling temperature, T_{fill}). Then a reverse bias V_{fill} (filling voltage) was applied across the structure, and the structure was illuminated by a low-intensity incandescent lamp for 1 min. Once the illumination terminated, the structure was heated at

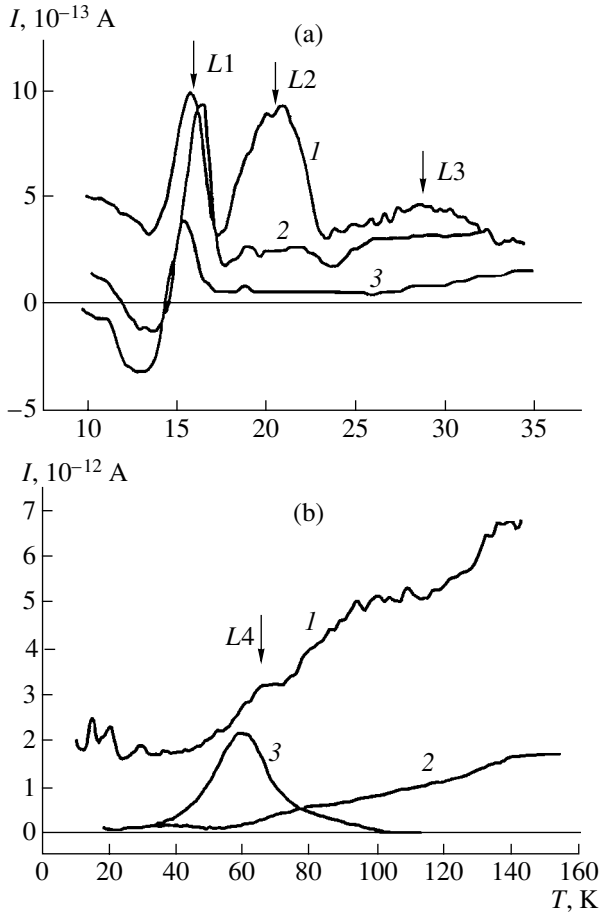

Fig. 1. Low-temperature spectra of thermally stimulated current in *a*-Si:H(Er)/*c*-Si samples fabricated at varied temperatures of the Er source, °C: (*1*) 190 and (*2*) 140; (*3*) undoped film. Filling under illumination at 7 K. (a) Initial portion of the spectrum (10–35 K). For convenience, curve *1* is shifted downwards by 1.5×10^{-13} A; (b) whole spectrum.

a constant rate, and a thermally stimulated current was recorded.

For studies at liquid nitrogen and higher temperatures, the filling voltage was applied across the structure at various filling temperatures in the HT range (from 100 to 320 K), and the structure was cooled down to the liquid nitrogen temperature under bias. Then the filling bias was cut off, the structure was short-circuited with an electrometer, and a thermally stimulated current was recorded during heating. In several experiments, the centers were filled at 77 K by illuminating a reverse-biased structure.

3. RESULTS AND DISCUSSION

Figure 1 shows a typical thermally stimulated current spectra taken in the LT range for *a*-Si:H(Er)/*c*-Si heterostructures. As can be seen, the introduction of Er significantly modifies the spectrum at temperatures over 17 K; i.e., two Er-related peaks (*L*2 and *L*3) appear at 21 and 30 K, respectively. With the Er concentration raised from 3×10^{20} to 1×10^{21} cm^{-3}, the amplitude of the *L*2 peak increases by nearly an order of magnitude, and a relatively broad peak *L*3 appears.

With increasing Er concentration, the thermally stimulated current grows significantly over the entire temperature range (Fig. 1b, curves *1*, *2*). At high Er concentrations, a well-resolved structure of peaks appears in the temperature range 80–160 K (Fig. 1b, curve *1*).

Figure 2 presents an HT-range (80–350 K) spectrum of thermally stimulated current in the structure with the highest Er concentration. This figure also demonstrates the effect of the filling voltage on the thermally stimulated current spectrum, which made it possible to determine the peak temperatures for separate peaks forming the current. It is significant that the application of a bias to the structure at liquid nitrogen temperature did not give rise to thermally activated processes, which indicates that the deep levels are localized inside the *a*-Si:H layer. Measurements of the thermally stimulated current at varied filling temperatures and also filling under illumination at 80 K served as complementary methods to determine the number of current peaks and the temperatures of their maxima. A qualitative analysis of these results led to the conclusion that the thermally stimulated current spectra observed originate from electron traps lying in the upper part of the band gap, with the exception of the *P*1 peak (Fig. 2), which has a polarization nature.

The activation energies of the electron traps were determined using the initial rise analysis [6], the temperature positions of current peaks [7], and the fractional glow technique [8]. The "shoulders" in the temperature dependence of the effective activation energies shown in Fig. 3 reveal a quasi-discrete system of levels related to electrically active defects [8]. The activation energies of traps, determined by various methods, are listed in the table.

Among the traps existing in the upper part of the band gap of *a*-Si:H(Er)/*c*-Si heterostructures in the temperature range 7–350 K, three groups of dominant centers can be distinguished.

First, there are shallow centers forming a clearly defined peak of the thermally stimulated current with peak temperature T_{max} = 15–16 K. No pronounced dependence on the Er content in the film was found (the same peak is observed in the undoped *a*-Si:H layer (Fig. 1, curve *3*), but its intensity in *a*-Si:H(Er) layers is somewhat higher). This peak is observed for undoped layers deposited on both KÉF-4.5 or KÉF-40 substrates. Thus, it is not related to shallow impurities, thermal donors, or substrate defects. The activation energy evaluated from the peak temperature is 34 meV. An analysis of the peak shape by the method described in [11] demonstrated that the peak half-width *L*1 is always less than that predicted by theory for the nar-

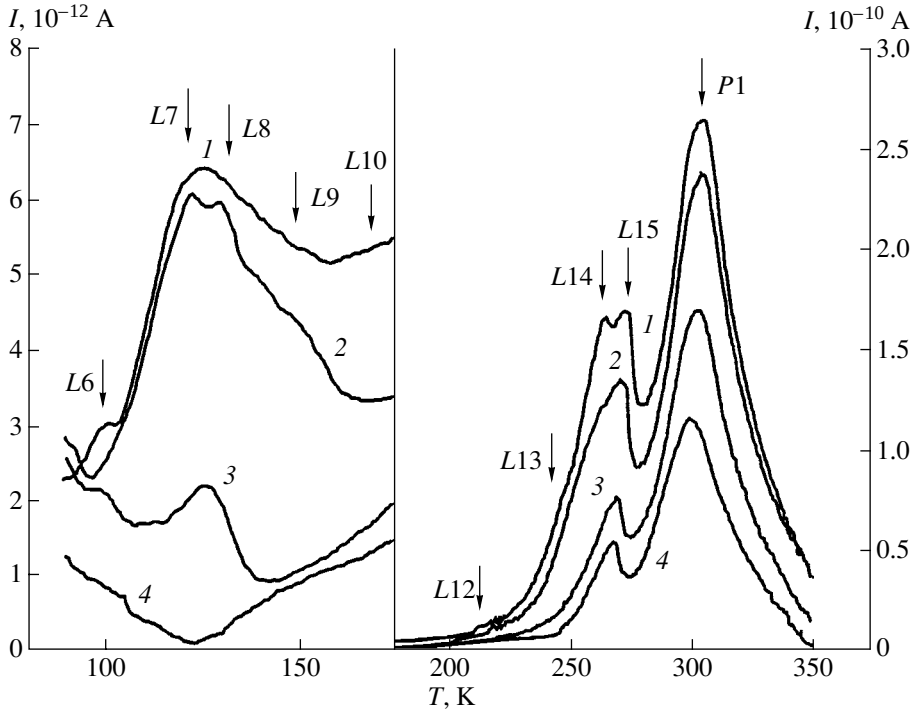

Fig. 2. Thermally stimulated current in *a*-Si:H(Er)/*c*-Si structure (Er source temperature 190°C). Levels filled at 320 K at filling voltages V_{fill}: (*1*) 8, (*2*) 6, (*3*) 4, and (*4*) 2 V.

rowest peak of a purely thermally activated nature (monoenergetic level located in the *c*-Si surface layer, with low retrapping). It should be noted that similar peaks of thermally stimulated current, observed in SiO_2/Si [12] and *a*-SiC/*c*-Si [13] systems, were attributed to traps localized in thin (0.4–2.5 nm) interfacial layers between SiO_2 (or *a*-SiC) and crystalline Si, separated from the *c*-Si substrate by a potential barrier. As the structure is heated, the traps are depleted via activated tunneling involving phonons localized on defects at the interface (a thermally stimulated current appears) [14]. The correlation between the activation energy of traps and the energies of local surface phonons of varied nature is most evident for SiO_2/Si structures [14]. In our opinion, similar considerations can also be applied to the *a*-Si:H(Er)/*c*-Si system. As mentioned in [1], the material under study has a complex structure, with both C–H bonds and O–H groups in the Er atom environment, and its Raman spectra reflect the enhancement of compositional and structural disorder through incorporation of (Er, O, and C) impurities into the matrix of amorphous hydrogenated silicon. The phase inhomogeneity of the *a*-Si:H(Er)/*c*-Si structures is also demonstrated by SIMS data (Fig. 4) confirmed by optical studies [4]. In our opinion, the *L*1 peak is associated with a trap localized at the *a*-Si:H(Er)/*c*-Si interface, and the discharge of this trap on heating occurs by the mechanism proposed in [14]. The increase in the peak amplitude upon introduction of erbium may be due to enhanced mechanical stresses at the interface, induced by the impurities appearing at the interface during growth. Peak *L*4 can also be attributed to the first group of peaks, not associated directly with the presence of erbium. The maximum amplitude of this peak is observed in undoped samples, and is seen as a shoulder in doped structures (Fig. 1b). It is necessary to note that this peak is not observed in the low-temperature (20–100 K) spectra of thermally stimulated conductivity in

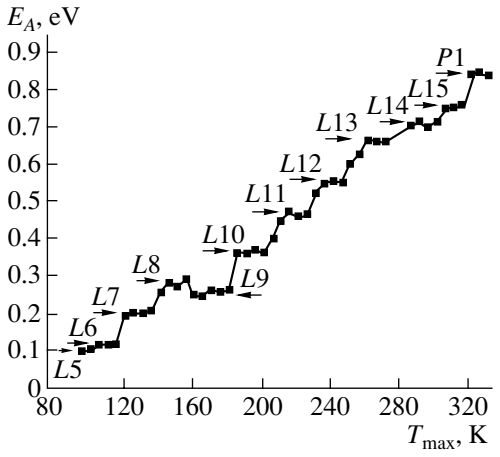

Fig. 3. Temperature dependence of the effective activation energy E_A obtained by fractional glow technique from the thermally stimulated current spectra presented in Fig. 2 for *a*-Si:H(Er)/*c*-Si structures (Er source temperature 190°C).

bulk *a*-Si:H [15], and a detailed study of *a*-Si:H/*c*-Si heterointerfaces is necessary to reveal its nature.

To the second group we attribute the levels responsible for thermally stimulated peaks *L*2 and *L*3 (Fig. 1a) with activation energies of 43 and 62 meV, whose amplitudes grow with increasing erbium concentration. Presumably, the levels observed in *a*-Si:H(Er)/*c*-Si have the same nature as the shallow donors in single-crystal Si with ion-implanted Er, detected both in Hall measurements (activation energy of 70 meV) [16], and by deep level transient spectroscopy (DLTS) [10]. In our opinion, the erbium-containing complex, forming a monoenergetic donor with activation energy of 70 meV [16] during ion implantation, is identical to the center with an activation energy of 62 meV. The lower activation energy may be due both to the conditions of shallow donor formation in the amorphous matrix and to the markedly nonequilibrium nature of the thermal-activation analysis used in the present study (influence of strong electric field and effects similar to the Poole–Frenkel effect). Indeed, the donor nature of two shallow electron states have been revealed in [10] by analyzing the manifestations of the Poole–Frenkel effect by DLTS. The deeper state had an activation energy of 60 meV (see the table), and the energy of an additional, shallower level *E*(*S*) could not be determined [10]. It is not unlikely that a similar shallow donor (or a donor band in the density-of-states tail) in the *a*-Si:H(Er) layer is responsible for the peak of the current with an activation energy of 43 meV. The doping capacity of erbium-related centers is also confirmed by changes in the background dark conductivity of the structures under study (Fig. 5). With increasing erbium concentration, the conductivity grows dramatically, and its temperature dependence is modified.

To the third group of erbium-induced centers, we attribute the levels manifesting themselves in the temperature range 90–280 K. The comparison of the observed transformation of these centers upon Er and O coimplantation and annealing with the DLTS data [9, 10] for deep levels created by Er implantation in *c*-Si (pure epitaxial or single-crystal with varied content of residual oxygen) suggests that at least the observed levels *L*7–*L*13 are related to Er complexes or to Er located in unstable configurations. The formation of a stable Er–O complex with activation energy $E_c - 0.15$ eV was found in [10]; this complex is responsible for the efficient excitation of Er via the recombination of electron–hole pairs bound at this level [17]. In [10], the enhancement of the Er electroluminescence was attrib-

Activation energies of the thermally stimulated current peaks in *a*-Si:H(Er)/*c*-Si structures

Experiment		Published data				Supposed nature of levels
Type of trap	Peak temperature T_{max}, K	Activation energy, eV				
		J.T. Randall *et al.* [7]	R.A. Cresswell *et al.* [8]	S. Limbertino *et al.* [9]	J.L. Benton *et al.* [10]	
*L*1	15.8	0.034				Traps at the *a*-Si:H(Er)/*c*-Si interface
*L*2	20.9	0.043			*E*(*S*)	Donor levels
					0.09	
*L*3	29.2	0.062			0.06	
*L*4	60	0.12				Unrelated to erbium
*L*5	90	0.18	0.10			Er–O complexes
*L*6	100	0.20	0.11			
				0.15 (*E*5)	0.14	
*L*7	120	0.25	0.20	0.20 (*E*4)	0.18	
*L*8	128	0.27	0.28	0.26 (*E*3)	0.27	
*L*9	138	0.28	0.24			
*L*10	147	0.30	0.34	0.36 (*E*2)	0.31	
					0.32	
*L*11	176		0.46		0.48	
*L*12	225		0.55	0.51 (*E*1)		
*L*13	240		0.60			
*L*14	260		0.65			*D* center?
*L*15	274		0.76			
*P*1	304		0.84			Polarization of an Er complex

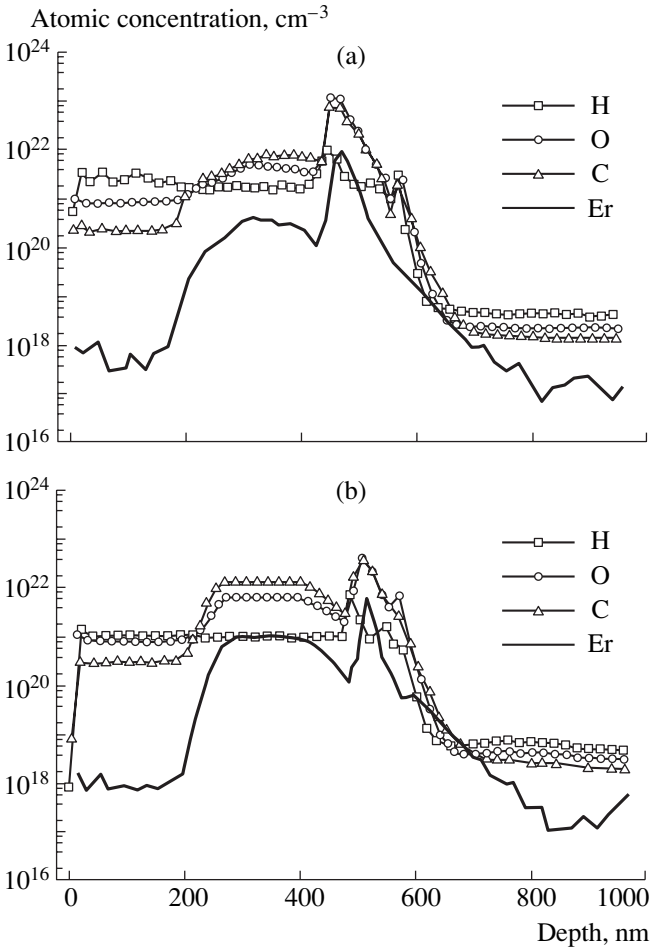

Fig. 4. Distribution of components across the film thickness, measured by SIMS. Films grown in the course of 60 min with doping at Er source temperature T_{Er}: (a) 140 and (b) 195°C.

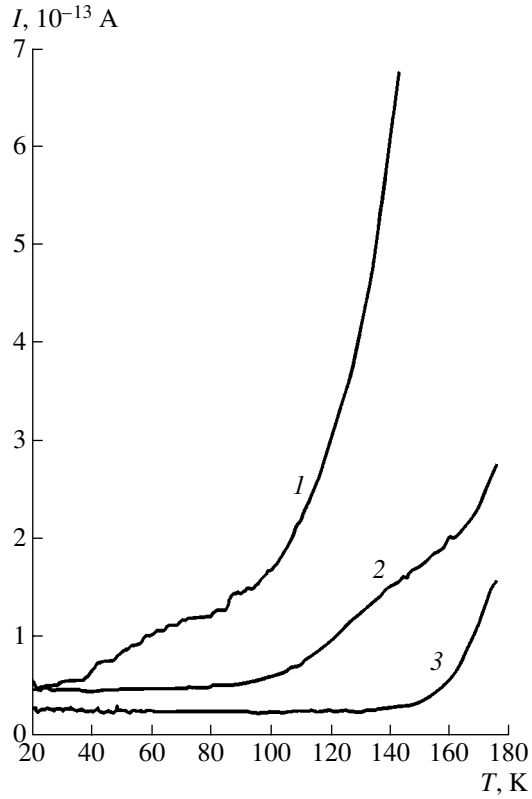

Fig. 5. Temperature dependence of the reverse dark current in *a*-Si:H(Er)/*c*-Si structures obtained at Er source temperature T_{Er} = (*1*) 190, (*2*) 165, and (*3*) 140°C.

uted to the level at 0.16 eV. The authors of [16] suggest that the observed transformation of the E_c – 0.117 eV donor state to a deeper donor state with energy E_c – 0.145 eV on raising the postimplantation annealing temperature is favorable for the excitation of Er-containing complexes. Thus, the presence of deep levels with energies of 0.117, 0.145, 0.15, and 0.16 eV in Er-doped single-crystal silicon may indicate the existence of Er–O complexes stimulating electroluminescence. In this context, we suppose that the observed levels *L*5–*L*6 are related to Er–O complexes in the *a*-Si:H matrix; however, the direct extension of these concepts to amorphous hydrogenated silicon meets several difficulties.

On the one hand, it is generally assumed on the basis of the data obtained in [18] that erbium oxide clusters are emitting centers in *c*-Si, *a*-Si:H(Er), and also in *a*-Si:H(Er) when subjected to high-temperature annealing. Mössbauer emission spectroscopy with the ^{169}Er (^{169}Tm) isotope demonstrated that clusters with the structure of Er_2O_3 oxide, similar to those in *c*-Si, are optically active photoluminescence centers, but the clusters somewhat differ in their local surrounding. As follows from SIMS data (Fig. 4), the oxygen content in the Er-enriched layer of amorphous Si is sufficient for similar clusters to be formed.

On the other hand, the analysis of the levels in *a*-Si:H(Er) should take into account the specificity of doping and additional impurity incorporation into the amorphous material. It is known that in amorphous materials there exist “intrinsic tails” of the density of states, induced by fluctuations of bond angles and lengths. Other types of network disordering, such as dangling bonds or impurities, form other types of states in the forbidden band. They affect the intrinsic tails in two ways: their presence enhances the network disordering and broadens the intrinsic tails, and the energy distribution of some states in the gap (in particular, shallow donors) may overlap with the tails. The actual tail is a superposition of these two components [19]. It has been established that, with increasing concentration of shallow dopants, the density of negatively charged dangling bonds in amorphous *n*-Si increases as a square root of the total impurity concentration [20]. In our case, the introduction of Er atoms into the amorphous matrix gives rise to deep levels *L*14 and *L*15 with a con-

centration that far exceeds that of all the levels described above and grows with increasing concentration of introduced Er. Since the activation energies of these levels (0.65 and 0.76 eV) are close to the energies of doubly and singly negatively charged dangling bonds (0.54 and 0.90 eV, respectively) [21], we may suppose that they correspond to dangling silicon bonds (*D*-centers) which favor the resonance energy transfer to an erbium ion [22].

To conclude, we have studied for the first time the electrical properties and characteristics of defect levels in the upper part of the band gap, formed upon introduction of erbium into PECVD-grown amorphous hydrogenated Si to give *a*-Si:H(Er).

REFERENCES

1. M. S. Bresler, O. V. Gusev, B. P. Zakharchenya, *et al.*, Fiz. Tverd. Tela (St. Petersburg) **38**, 1189 (1996) [Phys. Solid State **38**, 658 (1996)].
2. E. I. Terukov, O. I. Kon'kov, V. Kh. Kudoyarova, *et al.*, Fiz. Tekh. Poluprovodn. (St. Petersburg) **32**, 987 (1998) [Semiconductors **32**, 884 (1998)].
3. O. B. Gusev, M. S. Bresler, B. P. Zakharchenya, *et al.*, Fiz. Tverd. Tela (St. Petersburg) **41**, 210 (1999) [Phys. Solid State **41**, 185 (1999)].
4. E. I. Terukov, M. M. Kazanin, O. I. Kon'kov, *et al.*, Fiz. Tekh. Poluprovodn. (St. Petersburg) **34**, 861 (2000) [Semiconductors **34**, 829 (2000)].
5. Y. Gobrecht and D. Hofman, J. Phys. Chem. Solids **27**, 509 (1966).
6. G. F. Garlick and A. F. Gibson, Proc. Phys. Soc. London **60**, 574 (1948).
7. J. T. Randall and M. N. F. Wilkins, Proc. R. Soc. London, Ser. A **184**, 366 (1945).
8. R. A. Cresswell and M. M. Perlman, J. Appl. Phys. **41**, 2365 (1970).
9. S. Libertino, S. Coffa, G. Franzo, and F. Priolo, J. Appl. Phys. **78**, 3867 (1995).
10. J. L. Benton, J. Michel, L. C. Kimerling, *et al.*, J. Appl. Phys. **70**, 2667 (1991).
11. A. H. M. Shousha, Thin Solid Films **20**, 33 (1974).
12. V. S. Lysenko, T. N. Sytenko, V. I. Zimenko, *et al.*, Phys. Status Solidi A **59**, 115 (1980).
13. V. S. Lysenko, I. P. Tyagulski, Y. V. Gomeniuk, *et al.*, J. Phys. D **31**, 1499 (1998).
14. V. S. Lysenko, T. N. Sytenko, V. I. Zimenko, and O. V. Snitko, Phys. Status Solidi A **71**, 619 (1982).
15. S. D. Baranovskii, M. Zhu, T. Faber, *et al.*, Phys. Rev. B **55**, 16 226 (1997).
16. V. V. Emtsev, V. V. Emtsev, Jr., D. S. Poloskin, *et al.*, Fiz. Tekh. Poluprovodn. (St. Petersburg) **33**, 649 (1999) [Semiconductors **33**, 603 (1999)].
17. F. Priolo, G. Franzo, S. Coffa, *et al.*, J. Appl. Phys. **78**, 3874 (1995).
18. V. F. Masterov, F. S. Nasreddinov, P. P. Seregin, *et al.*, Fiz. Tekh. Poluprovodn. (St. Petersburg) **32**, 68 (1998) [Semiconductors **32**, 636 (1998)].
19. J. Tauc, J. Non-Cryst. Solids **97–98**, 149 (1987).
20. V. Stutzman, Philos. Mag. B **53**, L15 (1986).
21. H. Kida, T. Kumada, H. Okumoto, and Y. Hamakawa, Solid State Commun. **59**, 233 (1986).
22. M. S. Bresler, T. Gregorkovich, O. B. Gusev, *et al.*, Fiz. Tverd. Tela (St. Petersburg) **41**, 851 (1999) [Phys. Solid State **41**, 770 (1999)].

Translated by D. Mashovets

Semiconductors, Vol. 35, No. 6, 2001, pp. 627–629. Translated from Fizika i Tekhnika Poluprovodnikov, Vol. 35, No. 6, 2001, pp. 655–657.

II INTERNATIONAL CONFERENCE ON AMORPHOUS AND MICROCRYSTALLINE SEMICONDUCTORS

EXAFS Studies of the Local Atomic Structure of Nanocrystalline GaAs

R. G. Valeev*, A. N. Deev*, Yu. V. Rutz*, Yu. A. Babanov, P. N. Krylov***, V. F. Kobziev***, and S. F. Lomaeva***

** Physicotechnical Institute, Ural Division, Russian Academy of Sciences, ul. Kirova 132, Izhevsk, 426000 Russia*

e-mail: atomic@lasas.fti.udmurtia.su

*** Institute of Metal Physics, Ural Division, Russian Academy of Sciences, ul. S. Kovalevskoi 18, Yekaterinburg, 620219 Russia*

**** Udmurt State University, Krasnoarmeĭskaya ul. 71, Izhevsk, 426034 Russia*

Submitted November 9, 2000; accepted for publication November 15, 2000

Abstract—Conditions were considered for producing GaAs nanocrystalline films by a thermal method on the basis of a UVN-71-P3 modernized vacuum setup using three evaporator types. The extended X-ray absorption fine structure (EXAFS) method was applied to study the local atomic structure of the samples produced. © *2001 MAIK "Nauka/Interperiodica".*

INTRODUCTION

Currently, the production of semiconductor materials with a nanocrystalline structure [1] is being widely studied. As is known, technological problems when producing III–V films are caused by the fact that the components of Group V arsenic and phosphorus are volatile and have a high vapor tension at elevated temperatures. For example, arsenic and phosphorus vapor pressures above GaAs and InP melts are 0.1 MPa (1 atm) and 2.5 MPa, respectively. Therefore, when heated, all phosphides and arsenides lose their volatile components with a higher or lower rate. High temperatures and pressures of toxic and explosive gases drastically increase the cost of III–V compound production.

In this study, nanocrystalline GaAs films were synthesized using a UVN-71-P3 modernized setup. The structure is studied by atomic force microscopy (using a PM-SPM-MDT scanning probe microscope with a silicon cantilever and a tip radius smaller than 10 nm), X-ray diffraction (using a DRON-3 diffractometer), transmission electron microscopy (using a JEM-2000 EX transmission electron microscope), and the extended X-ray absorption fine structure (EXAFS) method (using a RAS-1 X-ray absorption spectrometer based on the DRON diffractometer).

Classical X-ray diffraction methods do not yield information on the short-range order. The EXAFS technique allows the investigation of the local atomic structure, i.e., interatomic distances, coordination numbers, etc., for the closest surroundings. At the same time, mathematical processing of normalized oscillating components isolated from the EXAFS spectra presents difficulties when determining the parameters of local atomic surroundings, especially when elements are sufficiently close in the periodic table. In this case, the conventional Fourier transform technique (widely used when determining the parameters of local atomic structures in the EXAFS method) does not yield accurate data on the local atomic surroundings, since amplitudes and phases of backscattering for gallium and arsenic are virtually identical. Therefore, we employ simulated and experimental normalized oscillating components of EXAFS spectra to study the possibility of gaining information on the local atomic surroundings using a regular method for mathematical processing.

EXPERIMENTAL

A commercial UVN-71-P3 setup does not ensure a uncontaminated residual atmosphere (since it contains oil and water vapors, oxygen, nitrogen, etc.). Therefore, a getter-ion pump was installed in the reaction chamber; this pump included a magnetron sputterer with a titanium target (Fig. 1). The residual pressure in the synthesis chamber was monitored in the course of all experiments.

Semiconductor films were deposited as follows. The reaction chamber was pumped out to 10^{-3} Pa. Then a high-vacuum valve was closed (the throttling mode was turned on) and argon was admitted to an operating pressure of 0.67 Pa (5×10^{-3} Torr). Then the getter-ion pump (magnetron) was turned on, while the high-vacuum valve was closed. A high titanium sorption activity reduced the equilibrium pressure of H_2 and other gases,

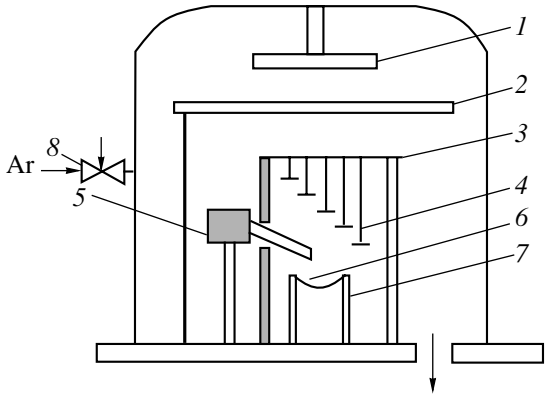

Fig. 1. Schematic of the operating chamber: (*1*) magnetron, (*2*) and (*3*) shields, (*4*) substrates, (*5*) vibration bin, (*6*) evaporator, (*7*) current leads, and (*8*) inlet valve.

CH_4 formation ceased, and the partial residual pressure of chemically active gases was lowered to 10^{-9}–10^{-11} Pa. After that, GaAs was evaporated in an inert gas atmosphere and deposited onto 10×30 mm^2 polyimide substrates placed above the evaporator. The sputtering time was about 10 min. In this time interval, 6 ± 0.3 mg of GaAs powder was poured onto the evaporator from vibration bin *5* (see Fig. 1). Transmission electron microscopy showed that the cluster characteristic size was about 5 nm.

The crystalline GaAs sample was prepared by grinding a GaAs single crystal (used as a substrate in microelectronics) in an agate mortar. The characteristic grain size did not exceed 10–15 μm.

The RAS-1 spectrometer is based on the X-ray transmission scheme using a BSV-27 tube with a molybdenum anticathode. A GUR-9 goniometer with a step motor (the minimum controlled angle was 0.0025°) was used for angular scanning. A $SiO_2(13\bar{4}0)$ single crystal (the lattice constant d is 1.18007 Å at T = 300 K) was used as a monochromator.

The EXAFS spectra for crystalline GaAs at Ga and As *K*-edges and for nanocrystalline GaAs at the Ga *K*-edge were measured in the course of the experiments. The gallium and arsenic spectra (with the absorption edge energies being 10368 and 11865 eV) were measured in the energy ranges from 9997 to 11493 eV and from 11491 to 12992 eV, respectively. The signal-to-noise ratio was about 5%.

RESULTS AND DISCUSSION

Nanocrystallinity of the films produced was confirmed by X-ray diffraction. Peaks typical of crystalline GaAs were broadened significantly. The grain size was diminished by increasing the evaporation rate (in the discrete evaporation method, this means increasing the feed rate of evaporated material), as well as by decreasing the substrate temperature and evaporator–substrate distance. All films are *p*-type with a band gap of 1.4 eV at room temperature.

The local atomic structure of GaAs films was studied by EXAFS spectroscopy. Preliminary processing of the experimental data yielded normalized oscillating components of EXAFS spectra for crystalline GaAs at Ga and As *K*-edges and a normalized oscillating component for nanocrystalline GaAs at the Ga *K*-edge. These are plotted in Fig. 2 in comparison to simulated spectra calculated using a FEFF-7 software package [2] in the multiple scattering approximation. It is evident that the normalized oscillating components measured experimentally somewhat differ from the calculated ones, especially in envelope amplitude. This is caused by the nonuniform thicknesses of both crystalline and nanocrystalline samples. However, this factor has no effect on the calculations of chemical bond lengths and is important only when determining coordination numbers. These data were used to calculate pair correlation

Parameters of pair correlation functions for crystalline and nanocrystalline GaAs

Pair correlation function	Coordination shell no.	Chemical bond length, Å			
		Ga–Ga	Ga–As	As–Ga	As–As
Model	1	4.001	2.450	2.450	4.001
	2	5.658	4.692	4.692	5.658
	3	6.930	6.166	6.166	6.930
Crystal	1	4.002	2.446	2.449	4.010
	2	5.677	4.693	4.695	5.663
	3	6.925	6.184	6.177	6.928
Nanocrystal	1	4.002	2.449	–	–
	2	5.657	4.693	–	–
	3	6.925	6.179	–	–

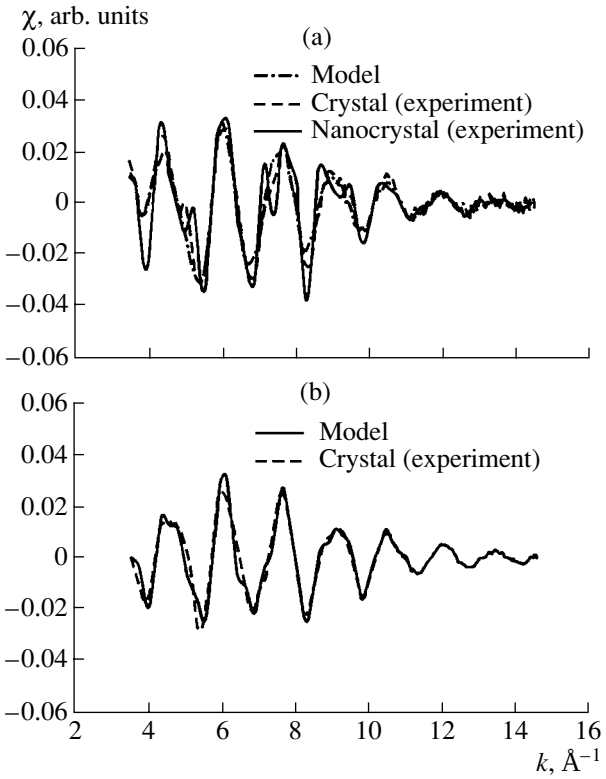

Fig. 2. Normalized oscillating components of EXAFS absorption spectra in comparison to simulated spectra (a) at the Ga *K*-edge in crystalline and nanocrystalline GaAs and (b) at the As *K*-edge in crystalline GaAs.

functions (PCF) by solving the inverse problem by the method outlined elsewhere [3]. The chemical bond lengths found are listed in the table. It is evident that the PCFs and chemical bond lengths of crystalline and nanocrystalline samples do not differ greatly. Hence, the local atomic surroundings of GaAs remains virtually unchanged when going from the crystalline to nanocrystalline state.

Errors in the bond length determination were estimated by solving the inverse problem in model calculations. The errors are 0.004, 0.025, and 0.025 Å for the first, second, and third coordination shells, respectively.

CONCLUSION

Nanocrystalline GaAs films were produced. They were studied by atomic force microscopy, X-ray, and transmission electron microscopy. Comparative EXAFS studies were also carried out for nanocrystalline films and crystalline GaAs. It is shown that irregularity in interatomic distances of the first coordination sphere in nanocrystalline GaAs does not differ significantly from that in the single crystal.

REFERENCES

1. M. G. Mil'vidskiĭ and V. V. Chaldyshev, Fiz. Tekh. Poluprovodn. (St. Petersburg) **32**, 513 (1998) [Semiconductors **32**, 457 (1998)].
2. S. I. Zabinsky, J. J. Rehr, A. Ankudinov, *et al.*, Phys. Rev. B **52**, 2995 (1995).
3. D. I. Kochubeĭ, Yu. A. Babanov, *et al*., *X-ray Spectrum-Analysis Methods for Studying Amorphous Solid-State Structure: EXAFS-Spectroscopy* (Nauka, Novosibirsk, 1988).

Translated by A. Kazantsev

Semiconductors, Vol. 35, No. 6, 2001, pp. 630–636. Translated from Fizika i Tekhnika Poluprovodnikov, Vol. 35, No. 6, 2001, pp. 658–664.

II INTERNATIONAL CONFERENCE ON AMORPHOUS AND MICROCRYSTALLINE SEMICONDUCTORS

Physical Properties of $Si_{20}Te_{80}$ Glasses with Various Structures and Their Use in Acoustooptic Devices

L. A. Kulakova*, B. T. Melekh, É. Z. Yakhkind, N. F. Kartenko, V. I. Bakharev, and Yu. P. Yakovlev

Ioffe Physicotechnical Institute, Russian Academy of Sciences, Politekhnicheskaya ul. 26, St. Petersburg, 194021 Russia

**e-mail: L.Kulakova@shuvpop.ioffe.rssi.ru*

Submitted November 9, 2000; accepted for publication November 15, 2000

Abstract—A method for preparing $Si_{20}Te_{80}$ glasses with various structures is developed. The basic parameters of the material (refractive index, absorption coefficient, density, heat conductivity, specific heat) were determined. Electrical, acoustic, and acoustooptic characteristics, as well as optical absorption spectra of the prepared alloys, were measured in wide ranges of temperatures and frequencies. The properties of heat-treated specimens quenched under different conditions were compared. Possible mechanisms of the phenomena observed are discussed. The synthesized alloy was demonstrated to show considerable promise in the fabrication of high-efficiency acoustooptic devices. A high-efficiency acoustooptic modulator operating in the wide spectral region from 1.87 to 10.6 μm was fabricated and tested. © *2001 MAIK "Nauka/Interperiodica".*

1. INTRODUCTION

The study of physical properties of objects with various degrees of ordering is a current problem in solid-state physics. Various amorphous materials which may contain nanocrystalline and even microcrystalline inclusions are among such objects. These inclusions are of considerable interest, because they may significantly affect the physical properties of the material. This is primarily true for amorphous materials which undergo a glass–crystal phase transition resulting in a change in the short-range order. Prominent examples of such amorphous materials are binary and ternary eutectic-composition compounds of Te with Group III and IV elements. To date, most attention has been concentrated on the formation of glasses of eutectic compositions in such systems [1], as well as on the physicochemical properties of these glasses [2], whereas their physical properties have received little attention. For the most part, some optical and electrical properties of vitreous tellurides were studied [3]. The formation of nanocrystallites that may essentially affect the basic properties of the materials has been left virtually unconsidered.

The study of the physical properties of vitreous tellurides is also of considerable importance in connection with the prospects for their acoustooptic applications, since it has been found [4] that $Si_{20}Te_{80}$ exhibits record-breaking acoustooptic efficiency of the Bragg diffraction at the wavelength $\lambda = 10.6$ μm. However, transmittance of the $Si_{20}Te_{80}$ alloy at $\lambda = 10.6$ μm is noticeably lower than that of single-crystal Ge, which is one of the most efficient and widely used acoustooptic materials for infrared applications. Therefore, it is of vital importance to study the physical properties of the vitreous tellurides and, in particular, to clarify a mechanism for the extremely high optical absorption and search for methods to reduce it.

In this study, we developed methods for the preparation of Si–Te glasses with various structures and examined their physical properties.

2. EXPERIMENTAL

The $Si_{20}Te_{80}$ glasses were synthesized, as a rule, from extra-pure-grade materials. Samples with masses of 2 or 300 g were placed in cells of different configurations: (1) cells with a flattened end about 1 mm in thickness, (2) cylindrical cells 10 to 50 mm in diameter, and (3) conical cells 0.5 to 20 mm in diameter. The melt was quenched either in ice-cold water or air.

We characterized the glass structure by X-ray diffraction in order to (1) reveal whether or not crystallization occurred, (2) determine a phase composition of crystalline inclusions, and (3) estimate the size of particles of a major crystalline phase.

For this purpose, we applied an X-ray diffraction method commonly used in analyzing polycrystalline materials. The X-ray diffraction was measured with a DRON-2 diffractometer (CuK_α radiation). X-ray photographs were taken with an RKSO camera with the use of plane films (CuK and MoK_α radiation, at specimen–film distances of 40 and 70 mm). A specimen was rotated in such a way as to ensure the Bragg geometry for particular reflections. In order to obtain more reliable information, we measured X-ray-diffraction pat-

terns from various areas of the sample surface, since a layer of limited thickness is analyzed by X-ray diffraction.

Specimens for acoustic, optical, and acoustooptic measurements ($4 \times 4 \times 6$ mm in size) were prepared by cutting followed by lapping and optical-grade polishing. The specimens were cooled during cutting.

In acoustooptic measurements, we used the Bragg diffraction of light from acoustic waves. The acoustooptic figure of merit, M_2, was determined by the Dixon method [5]. With this method, not only the intensity of diffracted light, I_l, but also the intensity of transmitted light, I_0, is measured, which excludes the effect of optical absorption on the results. He–Ne and CO_2 gas lasers (λ = 3.39 and 10.6 μm, respectively), as well as semiconductor lasers (λ = 1.87 and 3.3 μm), were used as radiation sources. The measurements were performed at λ = 10.6 μm. Single-crystal Ge was used as a standard. Values of M_2 at other wavelengths were derived from the ratio of the intensity of light diffracted by acoustic waves to the intensity of transmitted light, I_l/I_0, with intensity of sound held constant.

Optical-absorption coefficients α at various wavelengths were calculated from optical-transmission data obtained with a UR-20 spectrometer, as well as by direct measurements of transmittance at corresponding wavelengths.

Acoustic absorption was measured by two methods. High-frequency measurements (acoustic frequency f = 90–700 MHz) were performed by the acoustooptic method (λ = 3.39 μm); and low-frequency measurements (f = 14–150 MHz), by the pulse-echo method. Acoustic waves were excited by resonant piezoelectric transducers made from lithium niobate or piezoceramics, which were cemented to the corresponding face of the specimen with Nonaq Stopcock glue. We used the fundamental frequency (f = 30 MHz for lithium niobate and 14 MHz for piezoceramics) as well as higher harmonics of the transducer. The absorption was measured with an error no larger than 5%.

The data on the velocity of sound were obtained by the microwave-pulse-echo-overlap method [6]. The acoustic velocity, v, was measured with an error of about 2%; and the variation in the acoustic velocity, $\Delta v/v$, with an error of 0.01%.

Temperature dependences of electrical conductivity σ and the acoustic characteristics were measured with the use of a "cold finger", with a specimen being in liquid helium or nitrogen vapor. Acoustooptic measurements of temperature dependences of the acoustic-absorption coefficient were carried out using an evacuated optical cryostat with a "cold finger".

3. RESULTS AND DISCUSSION

The $Si_{20}Te_{80}$ specimens were prepared in the forms of plates 0.8–1 mm in thickness (2 g) and ingots 10–50 mm in diameter (300 g). The specimens showed conchoidal fractures. Examination with a microscope revealed no crystalline inclusions in the glasses.

3.1. X-ray Diffraction Analysis

X-ray diffraction data, obtained with the use of focusing geometry and long exposure times, allow us to conclude with certainty that the quenching conditions have an influence on the alloy structure: the specimens quenched in ice-cold water are amorphous, and the alloys cooled in air contain Te nanocrystalline inclusions in the glass network. No preferential orientation of the crystallites was reveled by the X-ray diffraction measurements. However, the polished specimens were slightly textured. From the (101) reflection of Te (CuK_α radiation), the size of the crystallites was estimated to be (110 ± 20) Å.

The main parameters of the synthesized alloy are listed in Table 1. The refraction index n was calculated from the Brewster angle measured at λ = 10.6 μm.

3.2. Electrical Properties

Temperature dependences of dc electrical conductivity of the $Si_{20}Te_{80}$ glasses (plates) quenched in ice-cold water were measured in the temperature range from 90 to 400 K. It was found that thermal cycling of these specimens to a temperature $T \le T_g$ (T_g is the glass-transition temperature) resulted in the formation of defects in the glass network. Indeed, the $\sigma(1/T)$ curves for the untreated specimens exhibit only two portions with different slopes, whereas the $\sigma(1/T)$ curves for the heat-treated specimens show an additional, low-temperature portion ($\ln\sigma \propto (1/T)^{1/4}$, the activation energy is 0.07 eV). In the context of the Mott model, this portion corresponds to hopping between defect states, which lie close to the Fermi level. Figure 1 shows temperature dependences of σ for the ingots quenched in ice-cold water (curve *1*, diameter of the ingot $\varnothing \approx 10$ mm) and in air (curves *2*, *3*, diameters of the ingots $\varnothing \approx 30$ and 10 mm). At first glance, these dependences should be similar to those for the plates; i.e., the amorphous specimens should show steeper $\sigma(1/T)$ curves; and the spec-

Table 1. Main parameters of the $Si_{20}Te_{80}$ alloy at T = 300 K

v_l, 10^5 cm/s	v_t, 10^5 cm/s	ρ, g/cm^3	κ, cal/(cm s K)	C_p, cal/(g K)	n (λ = 10.6 μm)
2.03	1.16	5.03	1.14×10^{-3}	0.225	3.3

Note: v_l and v_t are the velocities of longitudinal and transverse acoustic waves.

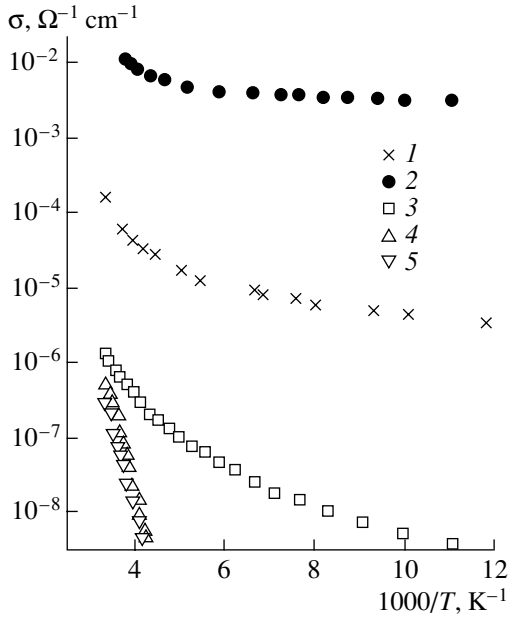

Fig. 1. Temperature dependences of electrical conductivity of the $Si_{20}Te_{80}$ specimens quenched in (*1*, *4*) ice-cold water and (*2*, *3*, *5*) air; (*1*–*3*) before etching, (*4*, *5*) after etching.

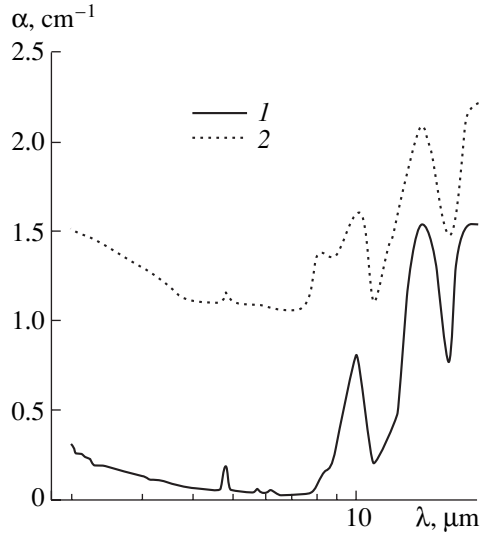

Fig. 2. Optical-absorption spectra of (*1*) the specimens containing nanocrystallites and (*2*) the amorphous specimens.

imens containing nanocrystallites, gentler curves and higher electrical conductivities. However, we found no such correlation. Moreover, the specimens containing nanocrystallites exhibited both low and high conductivities compared to those of the amorphous specimens. This finding was explained by the formation of defects in the surface layer as a result of the mechanical treatment of the specimens. After the specimens were chemically polished, the reproducible results were obtained (Fig. 1, curves *4*, *5*). The electrical conductivities of these specimens are very close, and the activation energy is about 0.45 eV.

3.3. Optical Properties

For both groups of specimens (amorphous alloys and specimens containing nanocrystallites), the optical transmittance varies only slightly from specimen to specimen. Figure 2 shows selected averaged absorption spectra derived from the transmission data on the assumption that the refractive index is independent of λ in the entire spectral region used. The results obtained lead us to the following conclusions.

First, the optical-absorption coefficients of the specimens containing nanocrystallites are considerably lower than those of amorphous specimens and are close to α of single-crystal Ge (see Table 2). Further investigations are required to resolve the question of whether this result may be attributed to different mechanisms of optical absorption or to relatively large defects produced by water quenching, which scatter light and decrease the optical transmittance.

Second, the peak near 5 μm in the spectra of the specimens containing nanocrystallites is much more intense than that in the spectra of the amorphous specimens. This finding may obviously be attributed to the presence of Te nanocrystallites. This mechanism of absorption calls for further investigations.

Third, the optical-absorption edge for the specimens containing nanocrystallites is at a shorter wavelength than that for the amorphous specimens.

3.4. Acoustic Properties

To study the influence of the glass structure on its elastic properties, we measured the temperature and frequency dependences of the acoustic-absorption coefficient α_{ac}, the acoustic velocity v, and its temperature dependences, as well as the nonlinear elastic properties of the alloy.

It is remarkable that the acoustic-absorption coefficients for all the specimens are large and virtually independent of the structure (Fig. 3). For all specimens, α_{ac} varies linearly with frequency and is independent of T in a wide temperature range (30 to 300 K).

A comprehensive analysis [11] of the plausible absorption mechanisms and their quantitative and qualitative consistency with the data obtained shows that all the features observed cannot be explained by Akhiezer's mechanism (interaction of acoustic waves with thermal phonons), which is characteristic of the crystals in this frequency range. As pointed out above, the acoustic-absorption coefficients of the specimens show a linear instead of quadratic (Akhiezer's) frequency dependence (Fig. 3), are independent of temperature, and exceed the absorptivity related to the anharmonicity of the phonon system by 2–3 orders of magnitude. We demonstrated that the acoustic absorp-

tion observed is due to a specific glass structure that contains defects with a wide, almost uniform distribution of relaxation times. These defects are described by double-well potentials with a wide distribution of times of thermally activated relaxation, which results from the wide distribution of the energy barriers ($\Delta V = V_{max} - V_{min} \gtrsim 0.25$ eV). The origin and configurations of these defects invite further investigation.

To study the effect of the Te nanocrystallites on the elastic properties of the glass, we measured the velocity of sound in the specimens. We found that the acoustic velocities and their temperature dependences (Fig. 4) for all the specimens studied coincide within 1%. This suggests that the nanocrystallites affect the linear elastic properties of the glass only slightly. An analysis [12] showed that the contribution of the defects responsible for the acoustic absorption to the temperature dependence of the acoustic velocity is also insignificant because of the wide distribution of relaxation times. Calculations of the anharmonicity contribution (Fig. 4, curve *3*), which arises from the interaction of acoustic waves with thermal phonons, were performed for the averaged Grüneisen constant $\bar{\gamma} = 1.45$ [11]. It is obvious that precisely this interaction is responsible for the observed temperature dependences of the velocity of sound.

In connection with this, the results of the investigation of nonlinear elastic properties are of interest. An analysis [11] of the spatial distribution of acoustic-power density (Fig. 5) shows that the nonlinear elastic constant Γ, which is controlled by the rate of the increase of the second harmonic, is anomalously large for the specimens containing nanocrystallites ($\Gamma \approx 30$), whereas, for the amorphous specimens, $\Gamma \approx 2.77$. Taking into account that the Grüneisen constant for a corresponding phonon mode can be calculated from the nonlinear elastic constant ($\gamma_l = \Gamma/2$ [13]), we obtain $\gamma_l^{(n)} = 15$ for the specimens containing nanocrystallites and $\gamma_l^{(a)} = 1.39$ for the amorphous specimens. Comparing these values of γ_l with the aforementioned value of $\bar{\gamma}$ derived from the $v(T)$ dependence, we may conclude that $\gamma_l^{(a)} \approx \bar{\gamma} \approx 1.4$ is actually a characteristic of the anharmonicity of the phonon system and is scarcely affected by the presence of the nanocrystalline inclusions under study.

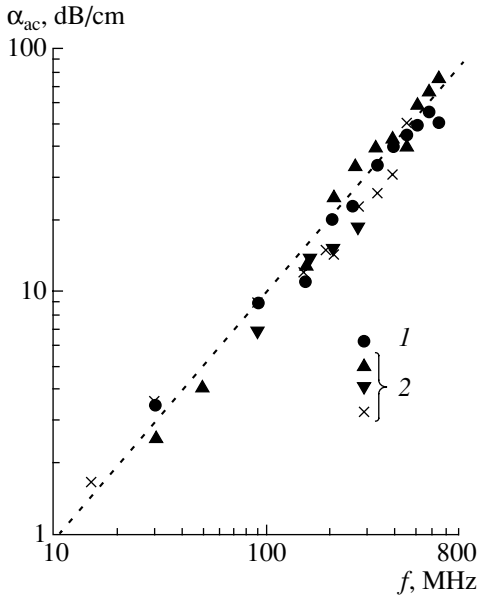

Fig. 3. Acoustic-absorption coefficient as a function of frequency for (*1*) the amorphous specimens and (*2*) the specimens containing nanocrystallites. Dashed line represents the $\alpha_{ac} \propto f$ dependence.

Table 2. Acoustooptic parameters of the $Si_{20}Te_{80}$ alloy and other materials in the infrared spectral region at $T = 300$ K

Material	Transparency region, μm	α, cm^{-1}	α_{ac}, dB/cm ($f = 100$ MHz)	λ, μm	Polarization of light	$(M_2)'$
alloy $Si_{20}Te_{80}$	1.7–13	0.75	8	10.6	∥	3500
				3.39	∥	3200
				1.87	∥	2800
Ge	2–20	0.06	0.3	10.6	∥	540*
As_2Se_3	0.9–11			1.15	∥	700**
a-Se	1–20			1.15	⊥	776***
				10.6	⊥	692***

Note: $(M_2)' = M_2/M_2''$, where $(M_2)'' = 1.56 \times 10^{-18}$ $s^3/g = M_2$ for fused silica. Polarization of light is given relative to the propagation direction of sound.

* From Pinnow [7].

** From Ohmachi *et al.* [8] and Rebrin [9].

*** From Fukuda *et al.* [10].

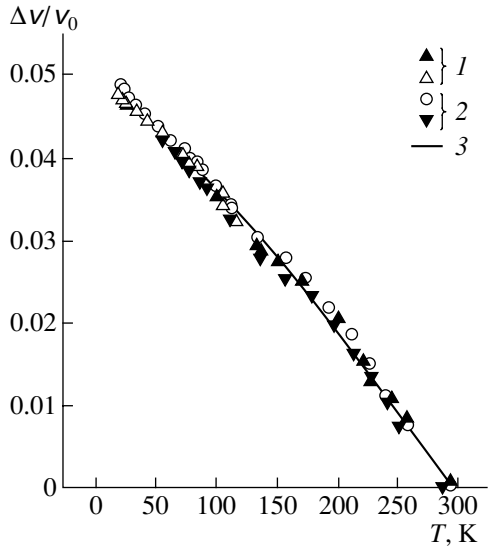

Fig. 4. Temperature dependences of acoustic velocity for (*1*) the amorphous specimens and (*2*) the specimens containing nanocrystallites and (*3*) the calculated dependence for the contribution of phonon modes.

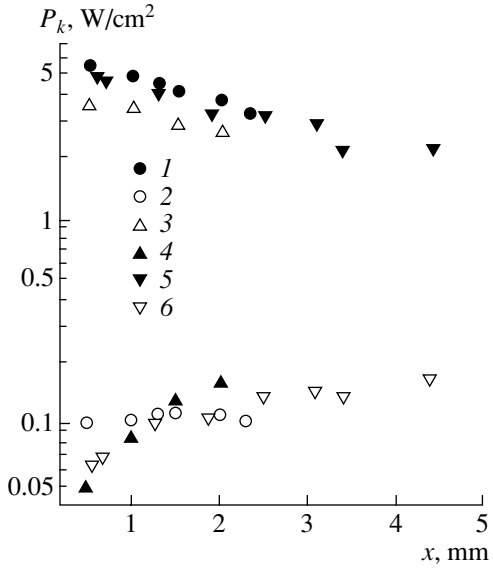

Fig. 5. Intensities of the components of (*1, 3, 5*) the fundamental frequency P_1 and (*2, 4, 6*) the second harmonic P_2 vs. the distance from the transducer for (*1, 2*) the amorphous specimens and (*3–6*) the specimens containing nanocrystallites.

In our opinion, the large Grüneisen constant for the specimens containing nanocrystallites ($\gamma_l^{(n)} = 15$) may be attributed to the anharmonicity of bonding forces at nanocrystallite boundaries. This anharmonicity is responsible for the generation of the second harmonic of acoustic waves; however, its contribution to the value of the averaged Grüneisen constant is insignificant. Similar results were obtained previously for laminar crystals [14].

3.5. Acoustooptic properties

It is well known that the efficiency of the Bragg diffraction of light from ultrasonic waves is determined by the acoustooptic figure of merit, M_2. In a linear mode (low intensity of sound),

$$I_1 = (1/2)I_0M_2P(\pi d/\lambda\cos\theta)^2, \quad (1)$$

$$(M_2)_{ik} = n_i^6 p_{ik}^2/(\rho v_k^3), \quad (2)$$

where P is the intensity of sound; λ is the wavelength of light; d is the width of the acoustic beam; θ is the angle of incidence of light; n_i is the refractive index; p_{ik} are the photoelastic-tensor components; ρ is the crystal density; v_k are the acoustic velocities; and i and $k = 1, 2, 3, 4, 5, 6$ are the polarization and strain indices in the matrix representation.

It can be seen from relation (2) that materials with large refractive indices and low acoustic velocities, which are characteristic of the prepared $Si_{20}Te_{80}$ alloy (Table 1), show the most promise for the fabrication of acoustooptic modulators. Indeed, as pointed out above, $Si_{20}Te_{80}$ shows the record-breaking acoustooptic efficiency of the Bragg diffraction at $\lambda = 10.6$ μm [4] (Table 2). However, the alloy is considerably less transparent in this spectral region than single-crystal Ge (see Table 2) used widely in various devices. Therefore, a topical problem is to measure the photoelastic properties and the optical transmittance of the material at other wavelengths in the infrared region as well as to clarify the mechanism of this strong optical absorption in the glass and search for methods to reduce it.

To determine the photoelastic properties of the $Si_{20}Te_{80}$ glass, we measured the acoustooptic figures of merit in a wide infrared range (λ = 1.87, 3.3, 3.39, 10.6 μm). We found that the $Si_{20}Te_{80}$ glass exhibits record-breaking acoustooptic efficiency in the entire spectral region used (Fig. 6, Table 2) and shows considerable promise for the production of acoustooptic cells.

It should be emphasized that the nanocrystalline inclusions in the glass network have no noticeable effect on the value of M_2.

4. ACOUSTOOPTIC MODULATOR

Based on the results obtained, we fabricated and tested a high-efficiency acoustooptic modulator operating in the spectral range from 1.87 to 10.6 μm.

The modulator consists of an acoustooptic cell about 5 × 5 × 5 mm in size, a resonant piezoelectric transducer (40–150 MHz) bonded to the end of the cell (acoustic-aperture width of about 2.5 mm), and a high-frequency oscillator. As mentioned above, the gas and semiconductor lasers were used as radiation sources. Spe-

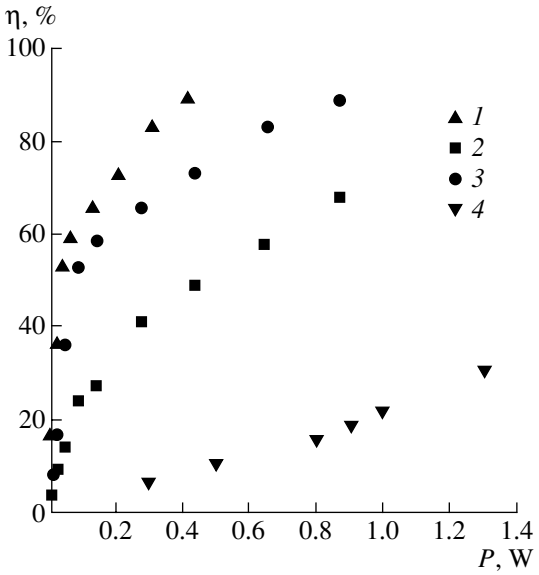

Fig. 6. Depth of modulation as a function of acoustic power for λ = (*1*) 1.87, (*2*) 3.3, (*3*) 3.39, and (*4*) 10.6 μm.

cifically, we used the following. (a) The 10.6-μm CO_2 and 3.39-μm He–Ne gas lasers operating with powers of about 5 W and 100 mW, respectively. (b) A 3.3-μm liquid-nitrogen-cooled InAsSbP/InGaAsSb-heterostructure laser operating with a pulse power of about 40 mW at I = 6 A, τ = 5 μs, and f = 500 Hz; laser radiation was transmitted through an As_2S_3-based optical fiber. (c) A 1.87-μm GaInAsSb/GaAlAsSb-heterostructure laser operating at room temperature with a pulse power of about 1 mW at τ ≈ 1 μs and f = 50 Hz; the heterostructure was grown on a GaSb substrate.

For measurements at the wavelengths mentioned above, we used the following photodetectors: (a) a fast-response *p–i–n* photodiode for λ = 1.87 μm, (b) a liquid-nitrogen-cooled InSb photodiode for λ = 3.3 and 3.39 μm, and (c) a liquid-nitrogen-cooled HgTeCdTe photodiode for λ = 10.6 μm.

Based on direct measurements, the acoustooptic figure of merit was estimated to be $M_2 = 5.46 \times 10^{-15}$ s^3/g at λ = 10.6 μm (Table 2), which exceeds seven to eight times the M_2 for single-crystal Ge used widely in acoustooptics.

At shorter wavelengths (λ = 1.87 and 3.3 μm), M_2 is slightly lower (by 10–30%); however, the modulation depth may be as large as 90% even at an acoustic power of 0.5 W (see Fig. 6), since the efficiency of diffraction increases as $1/\lambda^2$.

Changing the delay time of a modulating acoustic pulse, we can separate a desired portion of an optical pulse. This is of importance when a semiconductor laser operates at large currents, which results in the change of the wavelength during the pulse due to heating of the laser by a current. Additional modulation with the acoustooptic modulator makes it possible to isolate a short pulse of "monochromatic" radiation with a required wavelength within the range determined by the heating of the laser.

Owing to the high acoustooptic efficiency and a fairly short response time (about 0.3 μs), the modulator can be used for the deflection and modulation of continuous radiation as well as for the selection of modes of semiconductor lasers in laser spectroscopy.

5. CONCLUSION

Thus, we found that the cooling conditions affect the alloy structure: the specimens quenched in ice-cold water are amorphous, and the specimens cooled in air contain Te nanocrystalline inclusions in the glass network. The size of the nanocrystallites is, as a rule, about 100 Å.

The measurements of the electrical characteristics of the plate-shaped specimens revealed that the crystallites are not responsible for the change in the electrical conductivity as a result of thermal cycling. For the ingots, we also found no correlation between the temperature dependence of electrical conductivity and the structure of the specimens quenched under different conditions. Further investigations into the cause of the conductivity changes observed are required.

The nanocrystallites do not noticeably affect the acoustooptic efficiency, the absorption, or the velocity of sound. Based on the analysis of the temperature and frequency dependences of the acoustic-absorption coefficient and the velocity of sound, we demonstrated that the averaged Grüneisen constant $\bar{\gamma}$, which characterizes the anharmonicity of the phonon system of the glass network, is $\bar{\gamma} \approx 1.4$ and is scarcely affected by the presence of the nanocrystallites.

The crystalline inclusions have a profound effect on the nonlinear elastic properties. We found an anomalously large anharmonicity of bonding forces at the nanocrystallite boundaries ($\gamma_l^{(n)} \approx 15$). In addition to the scientific importance in understanding the nature of the corresponding bonding forces, this finding has practical significance. The generation of higher harmonics of ultrasonic waves (due to the aforementioned large anharmonicity of bonding forces) makes it possible to detect the presence of nanocrystalline and microcrystalline inclusions in the glass network.

In studying the optical properties of the $Si_{20}Te_{80}$ alloy, we found that the air-quenched specimens, which contained the nanocrystalline inclusions, were considerably more transparent than the amorphous specimens. This result is of great importance, because it opens the way for the preparation of alloys that are comparable to the best infrared materials (e.g., single-crystal Ge) in this parameter. If we recall that the alloy under study exhibits record-breaking acoustooptic efficiency, this finding makes the material particularly

attractive for the production of acoustooptic modulators.

Based on the investigations of the properties of the prepared $Si_{20}Te_{80}$ alloy, we designed a high-efficiency acoustooptic modulator allowing us to deflect and modulate infrared radiation in a wide spectral range as well as to select laser modes.

ACKNOWLEDGMENTS

We are grateful to V.Kh. Kudoyarova for her assistance in the optical-transmittance measurements and A.B. Matveev for supplying the 3.3-μm semiconductor laser.

This study was supported by the Russian Foundation for Basic Research, project no. 98-02-18305.

REFERENCES

1. P. P. Seregin, É. Yu. Turaev, A. A. Andreev, and B. T. Melekh, Fiz. Khim. Stekla **5** (3), 375 (1979).
2. M. S. Ablova, A. A. Andreev, B. T. Melekh, Z. V. Maslova, *et al.*, Fiz. Khim. Stekla **14** (3), 413 (1988).
3. B. T. Melekh, M. S. Ablova, I. B. Berman, *et al.*, in *Proceedings of the Conference "Noncrystalline Semiconductors-89", Uzhgorod, Ukraine, 1989*, Vol. 1, p. 136.
4. Yu. V. Ilisavskiĭ, L. A. Kulakova, B. T. Melekh, and É. Z. Yakhkind, Akust. Zh. **40** (2), 307 (1994) [Acoust. Phys. **40**, 279 (1994)].
5. R. W. Dixon, IEEE J. Quantum Electron. **QE-3** (2), 85 (1967).
6. E. J. Papadakis, J. Acoust. Soc. Am. **42** (5), 1045 (1967).
7. D. A. Pinnow, IEEE J. Quantum Electron. **QE-6**, 223 (1970).
8. Y. Ohmachi and N. Uchida, Appl. Phys. **43** (4), 1709 (1972).
9. Yu. K. Rebrin, *Optical Beam Control in Space* (Sov. Radio, Moscow, 1977).
10. S. Fukuda, T. Shiosaki, and A. Kawabata, Jpn. J. Appl. Phys. **19** (11), 2075 (1980).
11. L. A. Kulakova, Fiz. Khim. Stekla **26** (6), 839 (2000).
12. Yu. V. Ilisavskiĭ, L. A. Kulakova, and V. V. Tikhonov, Fiz. Tverd. Tela (Leningrad) **31** (8), 153 (1989) [Sov. Phys. Solid State **31**, 1363 (1989)].
13. *Physical Acoustics: Principles and Methods*, Vol. 3, Part B: *Lattice Dynamics*, Ed. by W. P. Mason (Academic, New York, 1965; Mir, Moscow, 1968).
14. L. A. Kulakova, Fiz. Tverd. Tela (St. Petersburg) **42** (1), 51 (2000) [Phys. Solid State **42**, 55 (2000)].

Translated by N. Izyumskaya

Semiconductors, Vol. 35, No. 6, 2001, pp. 637–642. Translated from Fizika i Tekhnika Poluprovodnikov, Vol. 35, No. 6, 2001, pp. 665–670.

II INTERNATIONAL CONFERENCE ON AMORPHOUS AND MICROCRYSTALLINE SEMICONDUCTORS

Levels of Structural Modification of Noncrystalline Semiconductors and Limits of Their Applicability

A. I. Popov*, V. A. Vorontsov, and I. A. Popov

Moscow Power Institute (Technical University), Moscow, 111250 Russia

** e-mail: popov@admin.mpei.ac.ru*

Submitted November 9, 2000; accepted for publication November 15, 2000

Abstract—The method for the structural modification of noncrystalline semiconductors consists in controlling the properties of these materials by changing their structure at a fixed chemical composition. It is shown that there exist at least four levels of structural modification distinguished by changes in the material structure: the levels of short- and medium-range order, morphology, and the defect subsystem. Each level of structural modification affects a certain group of properties. The possibility and efficiency of changing the structure at different levels of the above classification is analyzed for covalent semiconducting compounds of elements belonging to Groups IV–VI of the periodic table and some systems on their basis. Based on this analysis, the applicability limits of various levels of structural modification are determined. *© 2001 MAIK "Nauka/Interperiodica".*

TYPES OF STRUCTURAL CHANGES

In the first investigations concerned with noncrystalline semiconductors, B.T. Kolomiets and coworkers established that the most essential feature of these materials is their weak sensitivity to impurities. Even though exceptions to this rule appeared later (e.g., amorphous hydrogenated silicon), the problem of control over the properties of noncrystalline semiconductors and the problem of reproducible synthesis of noncrystalline semiconductors with prescribed properties are still very important.

As an alternative to the control over semiconductor properties by doping, a method for the structural modification of noncrystalline semiconductors has been proposed [1] consisting in controlling the properties by changing the structure of a material at its fixed chemical composition. An analysis of the possibilities of this technique demonstrated that there exist at least four levels of structural modification, distinguished by the effected changes in the material structure: modifications of short-range order (level 1), medium-range order (level 2), morphology (level 3), and the defect subsystem (level 4) (see Table 1).

Modifying the short-range order leads to significant changes in all the basic properties of a material. For example, polymorphic crystalline modifications of carbon (diamond, graphite, carbine) possess fundamentally different physicochemical properties because of the different hybridizations of electron orbitals and different atomic structures at the short-range-order level.

Amorphous carbon films incorporate structural units of different allotropic modifications, with the relative content of these units determined by film growth modes and varying widely for the same preparation method. Correspondingly, the coordination of atoms varies (between 2 and 4) together with other parameters of the first coordination sphere. When films of amorphous hydrogenated carbon (*a*-C:H) are obtained by rf ion-plasma sputtering in an argon–hydrogen atmosphere, merely changing the substrate temperature and discharge power may give films [2] in which the optical gap varies by two orders of magnitude (between 0.02 eV for graphite-like films and 1.85 eV for films with predominance of the diamond-like phase); the dark conductivity, by more than 10 orders of magnitude (between 7 and 2×10^{-10} Ω^{-1} cm^{-1}) (see Fig. 1).

Changing the medium-range order at a fixed short-range order mainly affects the macroscopic properties of a material (viscosity, microhardness, Young modulus, photocontraction of films—see Table 1 and Fig. 2, [3]). At the same time, the properties governed by the electronic structure (electronic spectrum) of the material (conductivity, photoconductivity), mainly depending on the short-range order, change relatively weakly.

Morphological changes affect the properties sensitive to microinhomogeneities [2], whereas changes in the defect subsystem modify the spectrum of localized states in the mobility gap (Fig. 3, [4]), shift the Fermi level, and modify the properties related to the electron subsystem (Table 1).

Despite the wide application of the method of structural modification of properties to various noncrystalline semiconducting materials and devices based on them (chalcogenide vitreous semiconductors [3, 5, 6], *a*-Si:H [4, 7–9], *a*-SiC:H [10], and *a*-C [2, 11]), the issue of the applicability limits of one or another level of structural modification remains open. To answer this question, let us analyze the efficiency of structural changes at the different above-mentioned levels in covalent semiconducting compounds of elements

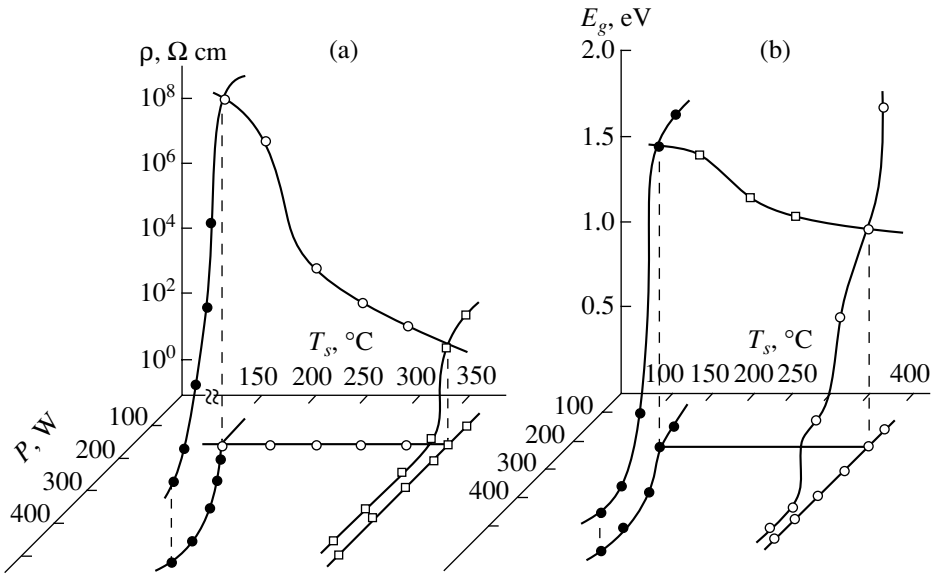

Fig. 1. Resistivity ρ (a) and optical gap E_g (b) of *a*-C:H films in relation to their preparation modes: T_s is the substrate temperature, P is the rf discharge power.

belonging to Groups IV–VI of the periodic table (carbon, silicon, germanium, phosphorus, arsenic, antimony, sulfur, selenium, and tellurium) and also in a number of their systems.

STRUCTURAL CHANGES AT THE SHORT-RANGE-ORDER LEVEL

The first level of structural modification assumes pronounced changes in the short-range order, i.e., changes in the hybridization of electron orbitals of all (or most) atoms constituting the sample. Carbon has long been considered the only (and unique in this respect) element of those considered here existing in allotropic crystalline modifications of diamond (sp^3 hybridization) and graphite (sp^2 hybridization). The discovery of carbines (*sp* hybridization) [12] in 1960 only served as more evidence in favor of the unique properties of carbon. At the same time, it should be noted that there have been reports that the short-range order may change substantially under certain conditions for other elements as well. For example, cubic α and β modifications of crystalline selenium with atom coordination numbers of, respectively, 4 and 6 were obtained in [13, 14] in electron beam–induced crystallization of thin films. However, these reports failed to attract due attention of the scientific community at that time.

The monopoly of carbon on the possibility of existence of forms with different hybridizations of electron

Table 1. Levels of structural modification

Level	Structural changes	Method of treatment	Characterization of sensitive properties	Groups of sensitive properties	Examples of sensitive properties
1	Short-range order	Various methods and modes of preparation	All properties	All properties	All properties
2	Medium-range order	Treatment during preparation or thermal treatments with external factors	Properties associated with rearrangement of structural units	Mechanical properties, phase transitions	Viscosity, hardness, Young modulus, photocontraction of films, temperature and activation energy of crystallization
3	Morphology	Changes in the preparation and treatment modes	Properties dependent on microheterogeneities	Electrical, optical	AC conductivity
4	Defect subsystem	Changes in preparation modes, treatments affecting the defect subsystem	Properties dependent on the distribution of the density of localized states and on the Fermi level position	Electrical, photoelectric	Field dependence of conductivity

orbitals and, consequently, with different atom coordination numbers was cardinally broken up by a series of investigations [7–9]. New forms of silicon were discovered in these studies, appearing under certain conditions in films of amorphous silicon and in *a*-Si:H—silicine with *sp* hybridization of electron orbitals and an atom coordination of 2 and a form with sp^2 hybridization and an atom coordination of 3. True, it should be noted that, in these investigations devoted to silicon and in studies concerned with selenium [13, 14], the new forms were obtained only under certain, rather specific conditions.

Thus, in the considered group of covalent semiconducting materials (periods 2–5, Groups IVA–VIA of the periodic table), structural changes at the short-range-order level are observed for elements belonging to Group IVA, periods 2 and 3 (C, Si), and Group VIA, period 4 (Se) (see Table 2), i.e., for three elements of the considered nine. We should also note the increase in the first coordination number from 2 to 3 in a tellurium melt (at 600°C), with the covalent nature of chemical bonds being preserved [15]. The mentioned elements show no fundamental distinctions in electron shell structure or other parameters from the rest of the considered elements. In view of the aforesaid, it seems reasonable to assume that structural changes at the short-range-order level are not unique to carbon, being characteristic for all of the considered covalent semiconducting materials. Experimental evidence in favor of this assumption has been obtained for carbon, silicon, and selenium, and obtaining it for other elements is only a matter of time and attention devoted to the problem.

STRUCTURAL CHANGES AT THE MEDIUM-RANGE-ORDER LEVEL

At the second level of structural modification, the obtained differences in the atomic structure are due to changes in the medium-range order (distribution of dihedral angles and their signs, degree of molecule polymerization, extent of disorder in alloys, etc.). In this case, the maximum possible structural changes can be evaluated by the criterion of efficiency of structural modification, expressed in a simplified form as [3]

$$\mathrm{CESM} = \frac{\mathrm{VEC} - N}{N(1 - I_c - M)}, \qquad (1)$$

where VEC is the average concentration of valence electrons, N is the average coordination number, I_c is the ionicity of chemical bonds, and M is the degree of bond metallization.

CESM varies between 2 for sulfur and selenium and 0 for silicon. There exist some boundary values of CESM [3] below which it becomes impossible to change the material properties by structural modification at this level. In this connection, the question arises In this connection as to what determines the applicability limit of the structural modification at the medium-range-order level and where it lies.

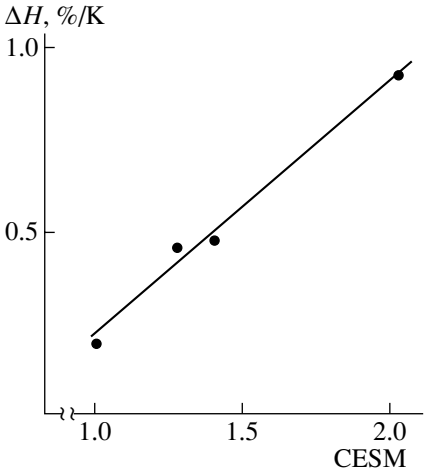

Fig. 2. Change in microhardness of chalcogenide vitreous semiconductors as a result of changes in the thermal history of a material, ΔH, vs. the criterion of efficiency of structural modification (CESM).

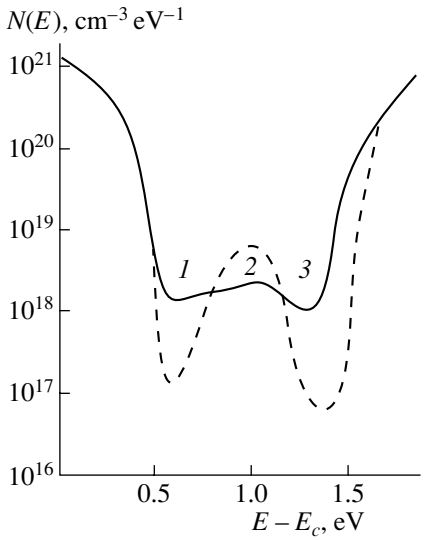

Fig. 3. Energy distribution of the density of localized states, $N(E)$ in the mobility gap of *a*-Si:H before (solid line) and after (dashed line) exposure to UV radiation (dose 10^{19} cm^{-2}) found using (*1*) constant photoconductivity method, (*2*) modeling of the temperature dependence of conductivity, and (*3*) analysis of space-charge-limited currents.

Qualitatively, it may be stated that this limit is determined by the rigidity of the structural network: for changes in the medium-range order to occur, the network must exhibit a certain lability and flexible bonds are to be present. In view of the aforesaid, it seems reasonable to suggest that the limit in question corresponds to the rigidity threshold of the structural network [16–18] at which the average number of force

Table 2. Short-range order level

Periods	Elements					
	IVA	N_1	VA	N_1	VIA	N_1
2	$^{6}_{12}$C	2 3 4				
3	$^{14}_{28}$Si	2 3 4	$^{15}_{31}$P	3	$^{16}_{32}$S	2
4	$^{32}_{72.5}$Ge	4	$^{33}_{75}$As	3	$^{34}_{79}$Se	2 4 6
5			$^{51}_{122}$Sb	3	$^{52}_{128}$Te	3 – melt

Note: N_1 stands for the first coordination number.

constants per atom becomes equal to the number of degrees of freedom. In [17], the critical coordination number was determined corresponding to the rigidity threshold of the structural network for chalcogenide glasses: $N_c = 2.4$. For the systems Ge–Se, Ge–S, As–Se, and As–S, the rigidity threshold is shown by the solid line in Table 3.

However, experimental studies of these systems (see [19] and references therein) have shown that the rigidity threshold actually lies at higher average coordination numbers. It was demonstrated in [20] that the reason for the discrepancy between the calculated and experimental values of the rigidity threshold consists in that the ionic component and metallization of chemical bonds are neglected. The rigidity threshold obtained for the above-mentioned systems with account of the ionicity of chemical bonds is shown in Table 3 by a double solid line. In accordance with this suggestion, the same line is the applicability limit of the second level of structural modification.

STRUCTURAL CHANGES AT THE MORPHOLOGICAL LEVEL

The morphology of films of noncrystalline materials means the presence of microheterogeneities in them (columns, globules, cones, etc.). A certain morpholgy (columnar structure) was observed in *a*-Si:H films in 1979 [21]. Ligachev demonstrated (see [22] and references therein) that the presence of heterogeneities is a characteristic feature of amorphous tetrahedral semiconductors (*a*-Si:H, *a*-C:H, *a*-Si_xC_{1-x}:H) and established a relationship between the averaged morphological parameters (cross dimensions of columns), spectra of electron states, and material properties.

It should be noted that the necessary condition for obtaining any solid noncrystalline material is the thermodynamically nonequilibrium process of its synthesis. In conformity with the basic concepts of the theory of self-organization (synergetics), the nonequilibrium conditions of material formation result in the appearance of heterogeneities (or a certain morphology). Thus, general considerations suggest the presence of microheterogeneities in all of the noncrystalline semiconductors in question. At the same time, while the presence of a certain morphology in films of tetrahedral noncrystalline semiconductors has been firmly estab-

Table 3. Medium-range order and morphological levels

Groups		Systems $A^{IV}_x(A^{V}_x)B^{VI}_{1-x}$, x values							Group
IVA	VA	0.60	0.50	0.40	0.33	0.25	0.20	0.11	VIA
Ge					$GeSe_2$	$GeSe_3$	$GeSe_4$	$GeSe_8$	Se
4					2.66	2.50	2.40	2.22	2
4					2.40	2.30	2.24	2.12	2
Ge			GeS	Ge_2Se_3	GeS_2	GeS_3	GeS_4	GeS_8	S
4			3.00	2.80	2.66	2.50	2.40	2.22	2
4			2.73	2.49	2.30	2.23	2.19	2.10	2
	As	As_2Se_3	AsSe	As_2Se_3	$AsSe_2$	$AsSe_3$	$AsSe_4$	$AsSe_8$	Se
	3	2.60	2.50	2.40	2.33	2.25	2.20	2.11	2
	3	2.53	2.42	2.31	2.25	2.19	2.16	2.09	2
	As	As_3S_2	AsS	As_2S_3	AsS_2	AsS_3	AsS_4	AsS_8	S
	3	2.60	2.50	2.40	2.33	2.25	2.20	2.11	2
	3	2.49	2.38	2.26	2.22	2.17	2.14	2.08	2

Note: Bold line indicates the rigidity threshold for purely covalent bonds; double line corresponds to the rigidity threshold with account of the bond ionicity; upper row: average coordination number, lower row: $N_1(1 - I_c)$, where I_c is the ionicity of chemical bonds and N_1 is the first coordination number.

Table 4. Defect subsystem level

Groups		Systems		Group
IVA	VA	$A_2^VB_3^{VI}$	$A^{VI}B^{VI}$	VIA
C				
Si	P			
Ge	As	As_2S_3	S–Se	S
		As_2Se_3	Se–Te	Se
		As_2Te_3		Te

lished (see references above), a "structureless" smooth surface is commonly observed in vitreous materials. The most likely reason for this contradiction is the indeterminate distinction between "macroheterogeneities" and "microheterogeneities."

Experimental data mostly indicate the occurrence of a certain morphology in films of tetrahedral amorphous semiconductors and the possibility of obtaining homogeneous "structureless" films of vitreous semiconductors. Therefore, it may be assumed that (at least for the time being) the third level of structural modification is applicable to noncrystalline materials with a rigid structural network and that the line corresponding to the rigidity threshold (Table 3) separates its applicability area from that of the second level of structural modification.

STRUCTURAL CHANGES AT THE DEFECT SUBSYSTEM LEVEL

The fourth level of structural modification is associated with changes in the defect subsystem under the action of either sample fabrication conditions or various external factors and is manifested in changes in the spectrum of localized states in the gap, which in turn leads to changes in material properties.

In [23, 24], the effect of amorphous silicon pseudodoping was observed, varying with sample preparation conditions.

In [4], a significant change in the spectrum of localized states in *a*-Si:H, resulting from a change in the relative content of Si–H, Si–H_2, and Si–H_3 complexes, was achieved by treating samples with ultraviolet radiation.

The effect of weak electric and magnetic fields on quasimolecular defects and properties of vitreous selenium, arsenic triselenide, and materials of the selenium–tellurium system was observed in [25, 26]. In [27], these results were extended to sulfur and arsenic trisulfide.

Thus, the fourth level of structural modification is observed experimentally both in a tetrahedral material with rigid covalent structural network (*a*-Si:H) and in vitreous materials of Group VI and in V–VI chalcogenide glasses (Table 4).

The aforesaid suggests that the structural modification at the defect subsystem level is inherent, as is the structural modification at the short-range-order level, in all of the considered noncrystalline semiconducting materials.

CONCLUSION

There exist at least four levels of structural modification of the properties of noncrystalline semiconductors which differ in the resulting structural changes.

Control over properties of noncrystalline semiconductors by changing the structure at the short-range-order level is, in principle, possible for all of the considered materials.

The fourth level of structural modification—control over properties by treating the defect subsystem—is also applicable to all these materials.

Control over properties by changing the medium-range order is possible for vitreous semiconductors having high CESM values, with the applicability limit of this level corresponding to the rigidity threshold of the structural network, calculated with account of the ionicity of chemical bonds. On the other side of this boundary (materials with rigid structural network) lies the area of applicability of the third level of structural modification, involving changes in the morphology of semiconductor films.

REFERENCES

1. A. I. Popov, in *Proceedings of the International Conference "Amorphous Semiconductors-80", Kishinev, 1980*, p. 150.
2. S. N. Stukach, Author's Abstract of Candidate's Dissertation (Moscow, 1996).
3. A. I. Popov, N. I. Michalev, and V. K. Shemetova, Philos. Mag. B **47**, 73 (1983).
4. I. A. Popov, Fiz. Tekh. Poluprovodn. (St. Petersburg) **30**, 466 (1996) [Semiconductors **30**, 258 (1996)].
5. O. V. Luksha, Yu. Yu. Firtsak, P. A. Fennich, and V. P. Ivanitskiĭ, in *Compound Semiconductors (Production, Properties, Application)*, Ed. by D. V. Chepur (Uzhgorod, 1981), p. 121.
6. A. I. Popov, I. A. Domoryad, and N. I. Michalev, Phys. Status Solidi A **106**, 333 (1988).
7. A. F. Khokhlov, A. I. Mashin, and D. A. Khokhlov, Pis'ma Zh. Éksp. Teor. Fiz. **67**, 646 (1998) [JETP Lett. **67**, 675 (1998)].
8. A. I. Mashin and A. F. Khokhlov, Fiz. Tekh. Poluprovodn. (St. Petersburg) **33**, 1001 (1999) [Semiconductors **33**, 911 (1999)].
9. A. I. Mashin, Author's Abstract of Doctoral Dissertation (Nizhni Novgorod, 1999).
10. V. A. Ligachev, N. N. Svirkova, V. A. Filikov, and N. D. Vasil'eva, Fiz. Tekh. Poluprovodn. (St. Petersburg) **30**, 1591 (1996) [Semiconductors **30**, 834 (1996)].

11. V. A. Ligachev, A. I. Popov, and S. N. Stukach, Fiz. Tekh. Poluprovodn. (St. Petersburg) **28**, 2145 (1994) [Semiconductors **28**, 1183 (1994)].
12. A. M. Sladkov, V. V. Korshak, Yu. P. Kudryavtsev, and V. I. Kasatochkin, USSR Discoverer's Certificate No. 107 (1971), Byull. Izobret., No. 6, 3 (1972).
13. A. I. Andrievskiĭ, I. D. Nabitovich, and P. K. Krinyakovich, Dokl. Akad. Nauk SSSR **124**, 321 (1959) [Sov. Phys. Dokl. **4**, 16 (1959)].
14. A. I. Andrievskiĭ and I. D. Nabitovich, Kristallografiya **5**, 465 (1960) [Sov. Phys. Crystallogr. **5**, 442 (1960)].
15. Yu. G. Poltavtsev, *Structure of Semiconductor Melts* (Metallurgiya, Moscow, 1984).
16. J. C. Phillips, Non-Cryst. Solids **34**, 153 (1979).
17. J. C. Phillips, Inst. Phys. Conf. Ser. **3** (21), 705 (1979).
18. J. C. Phillips, Phys. Status Solidi B **101**, 473 (1980).
19. R. L. Capelleti, S. S. Yun, H. Li, *et al.*, Phys. Rev. B **39**, 8702 (1989).
20. A. I. Popov, Fiz. Khim. Stekla **20**, 803 (1994).
21. J. C. Knights and R. A. Lujan, Appl. Phys. Lett. **35**, 244 (1979).
22. V. A. Ligachev, Author's Abstract of Doctoral Dissertation (Moscow, 1998).
23. O. A. Golikova, M. M. Kazanin, V. Kh. Kudoyarova, *et al.*, Fiz. Tekh. Poluprovodn. (Leningrad) **23**, 1737 (1989) [Sov. Phys. Semicond. **23**, 1076 (1989)].
24. O. A. Golikova, Fiz. Tekh. Poluprovodn. (Leningrad) **25**, 1517 (1991) [Sov. Phys. Semicond. **25**, 915 (1991)].
25. S. A. Dembovskiĭ, S. A. Kozyukhin, E. A. Chechetkina, *et al.*, in *Proceedings of the International Conference "Amorphous Semiconductors-84", Gabrovo, 1984*, Vol. 1, p. 88.
26. S. A. Dembovskiĭ, E. A. Chechetkina, and S. A. Kozyukhin, Pis'ma Zh. Éksp. Teor. Fiz. **41**, 74 (1985) [JETP Lett. **41**, 88 (1985)].
27. S. A. Dembovskiĭ, A. S. Zyubin, and F. V. Grigor'ev, Fiz. Tekh. Poluprovodn. (St. Petersburg) **32**, 944 (1998) [Semiconductors **32**, 843 (1998)].

Translated by M. Tagirdzhanov

Semiconductors, Vol. 35, No. 6, 2001, pp. 643–647. Translated from Fizika i Tekhnika Poluprovodnikov, Vol. 35, No. 6, 2001, pp. 671–675.

II INTERNATIONAL CONFERENCE ON AMORPHOUS AND MICROCRYSTALLINE SEMICONDUCTORS

The Effect of Some Organic Addenda on the HOMO–LUMO Gap in C_{60} Fullerene

D. A. Sykmanov*, Yu. F. Biryulin*, L. V. Vinogradova, and V. N. Zgonnik****

** Ioffe Physicotechnical Institute, Russian Academy of Sciences, Politekhnicheskaya ul. 26, St. Petersburg, 194021 Russia*

*** Institute of Macromolecular Compounds, Russian Academy of Sciences, Bol'shoĭ pr. 31, St. Petersburg, 199004 Russia*

Submitted November 9, 2000; accepted for publication November 15, 2000

Abstract—The photoluminescence of solutions of synthesized fullerene-containing star-shaped polystyrenes in toluene was studied at room temperature. The shift of the peaks in the photoluminescence spectra to shorter wavelengths compared to the spectrum of C_{60} solution in toluene was observed. It was established that, in the first approximation, the magnitude of the shift is independent of the type of chemical bonding of fullerene with an addendum (the covalent nonpolar C–C bond or the covalent polar C–H bond); rather, this shift is controlled by the number of broken double bonds at the fullerene and by the corresponding redistribution of electron density. © *2001 MAIK "Nauka/Interperiodica".*

Persistent interest in fullerenes as new carbon clusters is sustained to a large extent by studies of fullerene-containing materials. One line in these studies is concerned with fullerene-containing polymers [1]. Fullerenes may be involved in polymers of different types in two ways: they can play the role of either the framework in the polymer chain or the link between the polymer chains of differing nature. In the second case, the C_{60} molecule may have bonds with several polymer arms and thus form a macromolecule in which fullerene plays the role of the core. The possibility of employing the C_{60} molecule as the core for the formation of macromolecules of a complex architecture was used previously [2] in the synthesis of fullerene-containing polystyrenes (FPSs); it was shown that interaction of C_{60} with polystyryllithium results in the formation of a star-shaped FPS with a different number of polystyrene chains attached to the C_{60} molecule.

In this paper, we discuss the results of studying the photoluminescence (PL) of solutions of star-shaped FPSs in toluene. The objective of this study was to gain insight into the effect of organic addenda on the HOMO–LUMO gap in fullerene (HOMO stands for the highest occupied molecular orbital; LUMO, for the lowest unoccupied molecular orbital).

The objects of the study were macromolecules with a C_{60} fullerene core and a various number (from one to six) of polystyrene (PS) chains attached to this core. Attachment of a PS chain is accompanied by opening of the double C=C bond at the fullerene. As a result, the PS chain is attached to one end of the broken double bond and forms a nonpolar covalent C–C bond, whereas (depending on whether water or deuteromethyl iodide is used to terminate the reaction) either hydrogen with the formation of polar covalent C–H bond [2] or the CD_3 group with the formation of nonpolar covalent C–C bond [3] is attached to the other end. A third variant of attachment of addendum to the second end of the broken double bond (attachment of the second PS chain) was accomplished by a method described recently [3]. We studied the solutions of all the aforementioned FPS types, whose characteristics are listed in the table.

We studied PL at a temperature of 300 K using an MDR-2 grating monochromator. The PL was excited by an argon laser at a wavelength of λ = 488 nm; the output laser power was ~100 mW. We used the modulation method for measuring the PL spectra with subsequent synchronous phase detection. The laser beam was amplitude-modulated at a frequency of 135 Hz and was focused onto the object to be studied. The excited recombination radiation, after passing through the monochromator, was converted to an electric signal by a photomultiplier; this signal was amplified with a

The structure of studied star-shaped polystyrenes

Sample no.	The number of broken double bonds	The number of attached PS chains	Addenda at the second end of broken double bond
1	1, 2, 4	1, 2, 4	1, 2, 4–H
2	1, 2, 4	1, 2, 4	1, 2, 4–CD_3
3	6	6	6–H
4	6	6	6–CD_3
5	1, 2, 4	(1, 2, 4) + 2	2–(Ph)C(OH)PS
6	6	6 + 4	4–(Ph)C(OH)PS

Note: (Ph) stands for the phenyl ring, and PS stands for polystyrene. The samples were obtained using the methods described in [2, 3].

1063-7826/01/3506-0643$21.00 © 2001 MAIK "Nauka/Interperiodica"

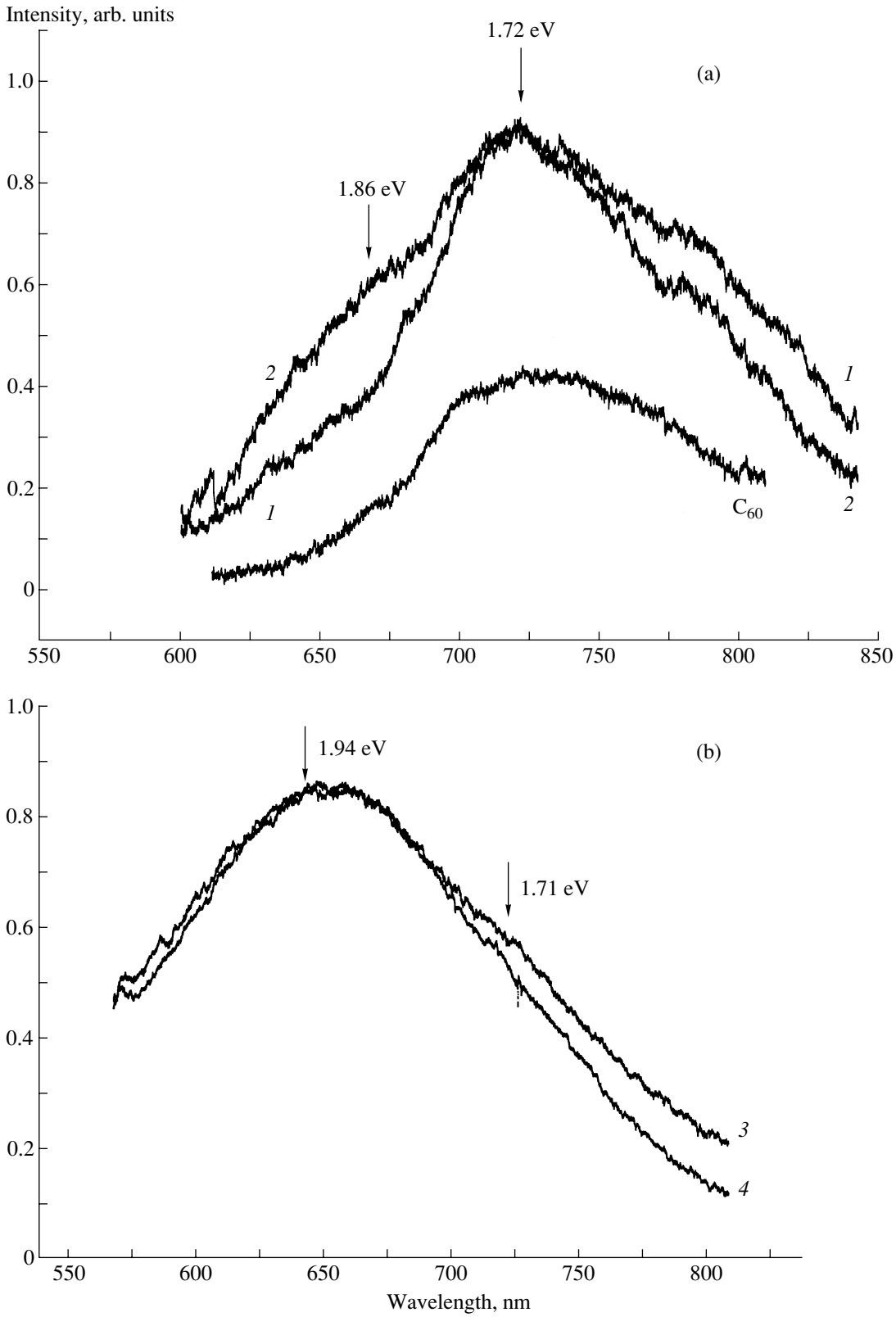

Fig. 1. Photoluminescence spectra of fullerene-containing polystyrene samples with (a) one, two, and four chains of polystyrene and (b) six chains of polystyrene. The addenda are (*1*, *3*) H and (*2*, *4*) CD_3. The luminescence spectrum of C_{60} is shown for the sake of comparison. The numbers at the curves correspond to the sample numbers in the table.

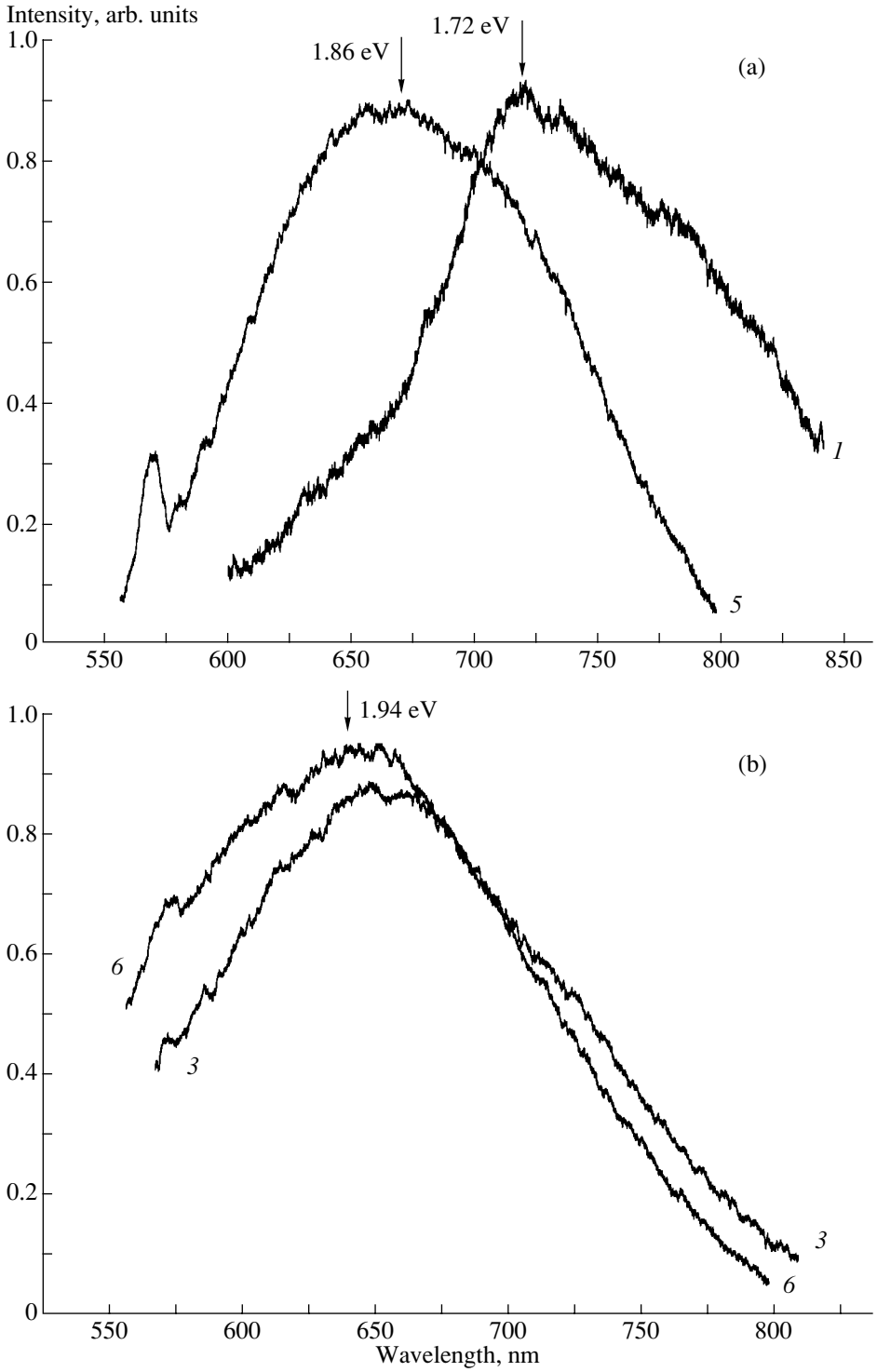

Fig. 2. Photoluminescence spectra of fullerene-containing polystyrene samples with (a) one, two, and four polystyrene chains and (b) six polystyrene chains. The addenda were (*1*, *3*) H and (*5*, *6*) CD_3 and PhC(OH)PS. The curves are numbered in accordance with the sample numbers in the table.

selective amplifier at the modulation frequency and was then detected by a phase detector. Such a processing method substantially enhanced the signal-to-noise ratio and made it possible to record the PL spectrum even if there were only traces of the substance of interest in the sample. The signal from the phase detector was digitized with an analog-to-digital converter and was then fed to a computer, where this signal was stored on a hard disk. Computer processing of the PL spectra was accomplished using the ORIGIN software package.

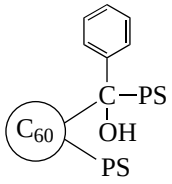

Fig. 3. Spatial formula of the fullerene-containing polystyrene molecule with addendum in the form of the (Ph)C(OH)PS group.

We studied six samples (see table); their PL spectra are shown in Figs. 1 and 2. The reference spectrum of a solution of C_{60} fullerene in toluene served as a starting point in the analysis of PL spectra (Fig. 1a). The main peak of this spectrum is located at $\lambda = 725$ nm (1.7 eV). It was shown previously [1, 4] that a steady shift of the PL spectrum peak to shorter wavelengths occurred as more and more PS chains were attached to C_{60}. In the first approximation, this shift is directly proportional to the number of attached PS arms N and can be described by the empirical formula $\Delta E = 0.04N$, where ΔE is measured in electronvolts [1, 4].

It should be emphasized that, both here and in [1], the studies were performed in the spectral region corresponding to the recombination radiation at C_{60} fullerene, because polystyrene does not luminesce at a wavelength of 488 nm.

The shift of the peak in the C_{60} PL spectrum is caused by a shift of energy levels that belong to the C_{60} HOMO and LUMO molecular orbitals and are responsible for radiative transitions. These levels shift in such a way that the energy gap between them increases. It was ascertained previously [1, 4] that, in the case of covalent attachment of various addenda to C_{60}, the shifts of the C_{60} HOMO and LUMO energy levels were primarily affected by the type of chemical bonding of the attached fragments to C_{60} rather than by the type of these fragments.

Further studies were related to the necessity for clarifying the role of the type of addenda at the second end of the C_{60} broken double bond in the widening of the HOMO–LUMO energy gap. It should be found whether this phenomenon results from the appearance of the C–C covalent bond between the fullerene and the PS chain or whether it is a result of the combined effect of C–C and C–addendum (H or C) bonds on the energies of C_{60} molecular orbitals; the third possibility is that the shift is caused only by the very event of the breaking of the double C=C bond at fullerene, with the electron-density redistribution being such that the bonding type is of minor importance.

In order to verify these assumptions, we compared the PL spectra of the pairs of the following samples: 1 and 2, 3 and 4, 3 and 6, and 1 and 5 (Figs. 1, 2).

The first pair of the samples (Fig. 1a) corresponds to the FPS solutions with one, two, and four PS chains attached (according to the chromatography data). The mixture in the samples of the fractions with one-, two-, and four-armed FPSs is a result of statistical processes in the corresponding synthesis during the reaction while adding the "live" polymer (polystyryllithium) to C_{60} [2]. Since an attachment of a single PS chain causes the shift of the PL-spectrum peak by ~0.04 eV, we are inclined to attribute the short-wavelength shoulders of the spectrum to the two- and four-armed FPS fractions present in the solution. The distinction between samples 1 and 2 consists in the fact that hydrogen is attached to the second end of the broken C=C double bond in sample 1, whereas the CD_3 (deuteromethyl) group is attached in sample 2. In spite of such a distinction, the spectra of these samples have identical characteristic special features; i.e., the wavelength positions of the shoulders and main peaks in the spectra coincide. Certain distinctions between the intensities of the short- and long-wavelength wings in the spectra are explained by a different balance between the intensities of lines corresponding to relevant fractions that form the overall envelope of these lines. Most probably, there were more four-armed FPSs (on a percentage basis) in sample 2 than in sample 1.

The PL spectra of samples 3 and 4 that are the solutions of six-armed FPSs (according to the chromatography data) are shown in Fig. 1b. The distinction between the samples (as in the previous case) is related to the addendum at the second end of the broken C=C double bond at the fullerene; this addendum is hydrogen in sample 3 and deuteromethyl in sample 4. It follows from Fig. 1b that these solutions are much "purer"; i.e., they contain less FPS components with the number of arms different from six, as is shown by the smooth shape of the spectrum envelope, which is nearly free of inflections and shoulders. The shift of peaks in both spectra in reference to the position of the main peak in the pure C_{60} spectrum amounts to ~0.25 eV, which confirms that six-armed FPSs are predominantly present in the solution [1, 2, 4]. In general, these spectra virtually coincide.

The next pairs of compared PL spectra (Figs. 2a, 2b) correspond to the samples in which a portion of polar covalent C–H bonds is changed to nonpolar covalent C–C bond by replacing the two hydrogen atoms (for sample 5) and four hydrogen atoms (for sample 6) by PS chains in samples 1 and 3, respectively. The PS chains were attached to C_{60} via the –(Ph)C(OH)– group and formed the spatial configuration shown in Fig. 3.

As shown above, the spectra of the samples with complete replacement of the C–H bond by C–CD_3 bond are almost the same. However, distinctions are observed if the C–H bonds are partially replaced by the C–C(PS) bonds, although these distinctions are small. Thus, for the pair of samples 3 and 6 (Fig. 2a), which differ only in the fact that four out of six C–H bonds are replaced by C–C(PS) bonds, an insignificant shift of the peak (within the range of 0.02–0.03 eV) to higher ener-

gies is observed. This is also indirectly confirmed by the ratio of the intensities of the short- and long-wavelength slopes of the PL spectra. In other words, there is a shift substantially exceeding the measurement error (±0.003 eV). This fact indicates that we observed the effect of the second order of smallness; i.e., it is about an order of magnitude smaller than in the case of a simple break of a C–C double bond at fullerene. To put it differently, the nearest surroundings of the second C–C bond also affect the changes in the electron density at fullerene; however, the magnitude of this effect is nearly an order of magnitude smaller. In this case, we believe that the effect of the second order of smallness is caused by the impact of oxygen, which draws off a fraction of the electron density from the fullerene. This does not occur if the addendum is hydrogen or deuteromethyl.

A more complex situation is illustrated in Fig. 2b. The replacement of two C–H bonds of fullerene in sample 1 by the bonds of the C–C(PS) type (sample 5) was attempted. Replacement of H by a PS chain was accomplished using a multistage reaction, in one of the stages of which a live polymer (polystyryllithium) was added. It is not inconceivable that, in addition to replacement of H, this reagent broke other double bonds at C_{60} with the formation of a multiarm star. This effect did not manifest itself in sample 6, because the FPS synthesis with the use of live polymers does not make it possible to synthesize the FPSs with a number of arms larger than six, as has been shown experimentally [2, 3]. The idea that double bonds at C_{60} are broken in the course of sample 5 synthesis is corroborated by the position of the main PL peak (Fig. 2b). The shape of this peak suggests that the sample is a mixture of four- and six-armed FPSs; these probably include all the possible types of aforementioned FPSs with various addenda at the second ends of the broken double bonds at C_{60}. We do not mention the isomers of the above combinations here, which may result in broadening and certain shift of the bands.

The low-intensity peaks in the vicinity of $\lambda \approx$ 575 nm appear as a result of entry of background laser radiation into the monochromator.

Thus, we may state with a large degree of confidence that the shifts of energy levels of the C_{60} molecular orbitals are primarily affected (by an order of magnitude of the HOMO–LUMO shift) by opening the C–C double bond at the C_{60} fullerene and by the attachment of a PS chain to one of its ends.

We believe that the surroundings, at least at the second end of the C–C bond (i.e., the type of addenda at this bond), give rise to the effects of changing the HOMO–LUMO gap of the second order of smallness compared to the effect of an increase in this gap when the double bond at C_{60} is broken.

ACKNOWLEDGMENTS

This study was supported by the Russian Foundation for Basic Research (project no. 98-02-03b327) and was performed in the framework of the Russian Scientific-Technological Program “Topical Lines of Research in the Physics of Condensed Media” (the subprogram “Fullerenes and Atomic Clusters,” the project “Polimer-2”).

REFERENCES

1. A. N. Aleshin, Yu. F. Biryulin, N. B. Mironkov, *et al.*, Fullerene Sci. Technol. **6** (3), 545 (1998).
2. V. N. Zgonnik, E. Yu. Melenevskaya, L. S. Litvinova, *et al.*, Vysokomol. Soedin., Ser. A **38** (2), 203 (1996).
3. L. V. Vinogradova, E. Yu. Melenevskaya, E. E. Kever, and V. N. Zgonnik, Vysokomol. Soedin., Ser. A **42** (2), 213 (2000).
4. Yu. F. Biryulin, V. S. Vikhnin, and V. N. Zgonnik, Fiz. Tverd. Tela (St. Petersburg) **42** (1), 188 (2000) [Phys. Solid State **42**, 197 (2000)].

Translated by A. Spitsyn

Semiconductors, Vol. 35, No. 6, 2001, pp. 648–655. Translated from Fizika i Tekhnika Poluprovodnikov, Vol. 35, No. 6, 2001, pp. 676–683.

II INTERNATIONAL CONFERENCE ON AMORPHOUS AND MICROCRYSTALLINE SEMICONDUCTORS

Cooperative Generation of Coherent Phonons by Localized Excitations in Glasses

A. M. Andriesh, N. A. Yenaki, V. I. Korol, P. I. Bardetskiĭ, and I. P. Kulyak

Institute of Applied Physics, Academy of Sciences of Moldova, MD-2028 Chisinau, Moldova

Submitted November 9, 2000; accepted for publication November 15, 2000

Abstract—The cooperative generation of phonon pulses in semiconductors by groups of inverted quasi-equidistant multilevel bound excitations (electrons and excitons) is studied. Such systems with equidistant spectra exist in chalcogenide glasses with a fractal structure. The cooperative generation of nonequilibrium localized phonons (fractons) can be observed in an experimental study of the relaxation of groups of excited atoms after passing a short laser pulse through the sample. An increase in the absorption coefficient in glass excitation by a short laser pulse of comparatively low power is due to the generation of nonequilibrium coherent localized phonons during the relaxation of nonequilibrium excitations. These coherent nonequilibrium localized phonons essentially change the random-potential topology and, consequently, open up a new channel for interband absorption of light. These transitions simultaneously involve photons and localized phonons. Kinetic equations describing the relaxation of localized electrons are obtained for two cases. The first describes the behavior of bound electrons in shallow quantum wells. The second is related to deep quantum wells. The relaxation process strongly depends on the dynamic symmetry of the bound electron–phonon (or exciton–phonon) system. The solutions of these equations are in agreement with experimental data. *© 2001 MAIK "Nauka/Interperiodica".*

1. INTRODUCTION

Under excitation of a vitreous semiconductor (As_2Se_3, AsSe) by laser pulses giving rise to electron transitions in the vicinity of the conduction band bottom, the light absorption coefficient strongly depends on temperature (at a given frequency). Presumably, this is due to changes in the random-potential topology with a changing number of thermalized phonons with a wavelength on the order of the distance between nonuniformities (random potential wells). This result can be formally expressed as

$$\alpha = \alpha_0 + \beta n, \tag{1}$$

where n is the number of localized (and nonlocalized) phonons (fractons), which can alter the random-potential topology, thus increasing the absorption coefficient (1). The spectrum of these phonons is rather broad and, in all probability, the absorption coefficient (1) can be rewritten as

$$\alpha = \alpha_0 + \sum_k \beta_k n_k, \tag{2}$$

where n_k is the number of phonons of the k-th mode, causing a change in the absorption coefficient, with weight factor β_k.

What occurs under the strong excitation of a vitreous semiconductor by laser pulses? Apparently, the number of nonequilibrium phonons increases during electron (hole) relaxation. This means that a stronger alteration of the random-potential topology occurs in this case and the interband absorption coefficient increases faster:

$$\alpha = \alpha_0 + \sum_k \beta_k [n_k^0 + \Delta n_k(t)], \tag{3}$$

where $\Delta n_k(t)$ is the number of nonequilibrium phonons generated via the relaxation of electrons or holes.

Let us consider a model for the relaxation of these excitations. We assume that excited electrons most probably relax to lower-lying bound states, so that the relaxation can be described in terms of a two-level system [1]. During such relaxation, each electron (hole) spontaneously generates a phonon. Apparently, a well in which the excitation (electron or hole) relaxes has random depth and width, determined by the local topology of the random potential. In other words, the spacing between the levels in the two-level systems in question varies and, therefore, the generated phonons have different frequencies. Since the wavelengths of the phonons generated exceed 100–1000 Å, an adequate amount of local quasi-equidistant states can be found in a volume of this size.

In this situation, we can classify the local states into spectral subgroups. Each subgroup can be considered as an independent equivalent excited two-level system that can cooperatively generate a phonon pulse at the frequency ω_k. This pulse, resembling the Dicke superradiant pulse, was observed for the first time in the cooperative generation of phonons in a Rb crystal for "acoustic" transitions of the Cr^{3+} impurity, corresponding to the inversion $\bar{E}\,(^2E)$–$2\bar{A}\,(^2E)$ [2]. The possibility

of the coherent generation of phonons and their effect on the absorption coefficient in the process of propagation of pulses through thin films of *a*-As_2Te_3 and polyacetylene was reported in [3]. The oscillations observed of photoinduced absorption were attributed directly to the propagation of coherent phonon pulses between the film surfaces. A similar generation of coherent phonons and their effect on the absorption coefficient in As_2Se_3, AsSe, $GeSe_2$, and $As_{22}Se_{33}Ge_{45}$ have been observed experimentally in a wide temperature range 70–300 K [4, 5]. Returning to our phonon subgroups, we notice that the build-up of each phonon mode (group of phonons) strongly depends on the frequency of these phonons ω_k, the number N_e^k of excited electrons (or holes) that can transit to a coherent phonon generation mode, the spontaneous-transition probability $1/\tau_0^k$, and even the geometric arrangement of electron excitation. This build-up time is named the phonon pulse delay time in the theory of cooperative relaxation. It can be readily concluded that a group of excited electrons in deeper wells can generate higher-frequency phonon pulses with shorter build-up times. This follows from the dependence of the delay time $t_0^k = \tau_0^k/N_k \ln(2N^k)$ on the frequency and the number of excitations. Since the spontaneous relaxation time τ_0^k is inversely proportional to the cube of the transition frequency ω_k, the coherent build-up of the high-frequency phonon amplitude is faster than that for low-frequency phonon modes.

This effect can be observed experimentally during propagation through a thin film of pulses with the same energy but varied duration. With short pulses, only high-frequency phonon modes have time to build up, and only these modes contribute to the absorption coefficient:

$$\alpha = \alpha_0 + \beta n_{\text{thermal}} + \beta \Delta n_k^{hf}(t). \qquad (4)$$

In the case of propagation of longer pulses, low-frequency coherent modes with a longer build-up have enough time to contribute to absorption involving phonons. In other words, by varying the duration of optical pulses, we can probe the temporal pattern of phonon generation over the spectrum (see Fig. 1). It was established experimentally that the absorption energy of pulse *1* is less than that for pulse *2*. This absorption effect can be accounted for in terms of our model, since only high-frequency phonons contribute to the absorption coefficient in the case of pulse *1*

$$\alpha_1 = \alpha_0 + \beta n^0 + \beta_{k_1} \Delta n_{k_1}(t).$$

For pulse *2*, the absorption coefficient increases

$$\alpha_2 = \alpha_0 + \beta n^0 + \beta_{k_1} \Delta n_{k_1}(t) + \beta_{k_2} \Delta n_{k_2}(t).$$

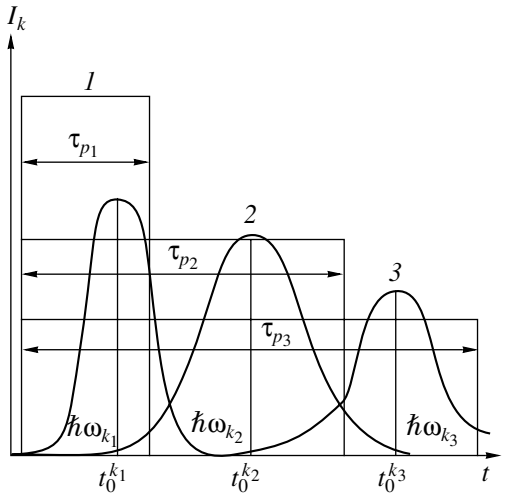

Fig. 1. Excitation of coherent phonon modes by laser pulses of the same power and different durations: $\tau_{p_1} < \tau_{p_2} < \tau_{p_3}$, where $\tau_{p_1} \approx t_0^{k_1}$, $\tau_{p_2} \approx t_0^{k_2}$, $\tau_{p_3} \approx t_0^{k_3}$.

In the case of pulse *3*, all the three groups contribute to the absorption coefficient

$$\alpha_3 = \alpha_0 + \beta n^0 + \sum_{i=1}^{3} \beta_{k_i} \Delta n_{k_i}(t).$$

It should also be noted that the coefficient β in (1) can be found by measuring the absorption coefficient α at two different temperatures [4, 5]

$$\alpha(T_1) = \alpha_0 + \beta n_0(T_1)$$

and

$$\alpha(T_2) = \alpha_0 + \beta n_0(T_2).$$

By eliminating α_0 from these expressions, we obtain

$$\beta = \frac{\alpha(T_1) - \alpha(T_2)}{n_0(T_1) - n_0(T_2)}.$$

Taking into consideration that the main contribution to the light absorption comes from localized phonons with wavelength $\lambda \approx d_m$, where $d_m \approx 1$ nm is the mean distance between the spatial nonuniformities in a chalcogenide vitreous semiconductor (CVS) sample, β can be determined from $\alpha(T_1)$, $\alpha(T_2)$ and $n_0(T_1)$, $n_0(T_2)$ as functions of temperature. The mean number of localized phonons can be found using the Bose distribution

$$n_0(T) = [\exp(\hbar\omega_s/k_B T) - 1]^{-1},$$

where k_B is the Boltzmann constant, $\omega_s \approx sk_m$; s is the velocity of sound in a CVS ($s \approx 10^5$ cm/s); and $k_m \approx 2\pi/d_m$. Substituting into the expressions for $\alpha(T)$ and $n_0(T)$ the appropriate CVS parameters [4–6], we find that $\beta \approx 6 \times 10^3$ cm^{-1}.

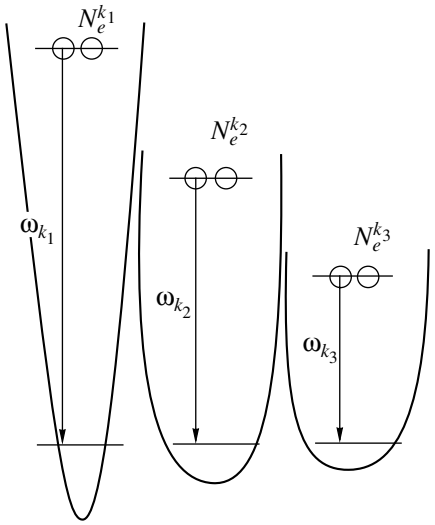

Fig. 2. System of two-level excitations in glasses with random transition energies. $N_e^{k_i}$ is the number of excitations of the *i*th subgroup; $\omega_{k_1} > \omega_{k_2} > \omega_{k_3}$.

The main aim of this study is to show how excited electrons in random-potential quantum wells (QWs) can generate correlated localized phonons (fractons). These correlated localized excitations decay to give acoustic phonons propagating through the CVS sample.

2. MODEL OF THE COOPERATIVE GENERATION OF PHONONS AND THEIR EFFECT ON THE ABSORPTION COEFFICIENT

The mechanism of excitation of localized electron–hole pairs by a laser pulse and the generation of nonequilibrium coherent phonons can be described by the following set of equations

$$\frac{1}{c}\frac{dI_s(t,z)}{dt} + \frac{dI_s(t,z)}{dz} = -(\alpha_0 + \beta n)I_s(t,z),$$

$$\frac{dN_e^k}{dt} = -\frac{N_e^k}{\tau_0^k} + (\alpha_0 + \beta n)\frac{V_0 I_s(t,z)}{\hbar\omega_0}\rho^k - \frac{N_e^k N_g^k}{\tau^k} - \frac{n_k}{\tau_0^k}(N_e^k - N_g^k), \quad (5)$$

$$\frac{dN_g^k}{dt} = \frac{N_e^k}{\tau_0^k} + \frac{N_e^k N_g^k}{\tau^k} + \frac{n_k}{\tau_0^k}(N_e^k - N_g^k),$$

$$\frac{dn}{dt} = \frac{1}{\tau_f}(n - n_0) + \sum_k \frac{dN_g^k}{dt},$$

where N_e^k and N_g^k are, respectively, the average numbers of excited electrons and electrons in the ground state for the *k*-th subgroup (see Fig. 2); *k* enumerates the equidistant subgroups of two-level systems, $k = 1, 2, 3, \ldots, N_s$; V_0 is the volume excited by laser pulse in the CVS sample; I_s is the light intensity in the CVS sample; ρ^k is the density of distribution over subgroups, possessing the property

$$\sum_{k=1}^{N_s} \rho^k = 1;$$

$n_k = n\rho^k$; τ^k/N^k is the time of cooperative decay of the *k*-th subgroup; $N^k = N_g^k + N_e^k$; τ_f is the time in which phonons move away from the domain of active localization of acoustic phonon modes. This set of equations can be derived from the Maxwell–Bloch equations when the laser pulse is much longer than the electronic polarization relaxation time in the CVS. A cooperative effect is possible if the localized phonon wavelength is on the order of the distance between the QWs of the *k*th subgroup.

Let us consider the case when the pulse duration τ_p is on the order of the relaxation times of localized electrons and phonon subsystems. Then we can find an asymptotic time-independent solution for the absorption coefficient $\alpha(I_s) = -dI_s(z)/I_s dz$ using the stationarity conditions $dI_s/dt = dn/dt = dN_e/dt = 0$:

$$\alpha(I_s) = \alpha_0 + \beta\frac{n_0 + \tau_f V_0 \alpha_0 I_s(z)/\hbar\omega_0}{1 - \tau_f V_0 \beta I_s(z)/\hbar\omega_0}. \quad (6)$$

It is noteworthy that the absorption coefficient grows with increasing light intensity. Such an increase in the absorption coefficient was observed experimentally in [4, 5]. A time-dependent solution of the set of equations (5) leads to a hysteretic dependence of the light intensity at the output on the input intensity.

When the laser pulse is much shorter than the localized electron relaxation time, the exciting pulse can be approximated by the delta function: $I_s(z, t) = I_{s0}\tau_p\delta(t)$. In this case, the number of electrons excited during the time of pulse propagation has the form

$$N_e^k = \tau_p V_0 \frac{I_{s0}}{\hbar\omega_0}(\alpha + \beta n)\rho^k = 2j^k, \quad (7)$$

where $2j^k$ is the number of localized excited centers (electrons and holes) in the *k*-th subgroup. An equation for the decay kinetics of the inversion parameter $\langle D_z^k \rangle =$

$(N_e^k - N_g^k)/2$ can be obtained from the second and third equations of the set (5):

$$\frac{d\langle D_z^k\rangle}{dt} = -\frac{1}{\tau_0^k}(\langle D_z^k\rangle + j^k) - \frac{2}{\tau_0^k}\bar{n}_0\langle D_z^k\rangle + \frac{1}{\tau^k}[\langle D_z^k\rangle^2 - (j^k)^2]. \quad (8)$$

Here, $\bar{n}_0$ is the mean number of phonons of the external thermalized field;

$$\bar{n}_0 = [\exp(\hbar\omega_0/k_B T) - 1]^{-1}.$$

Let us analyze the behavior of the proposed system in the quasi-stationary case, when $dn/dt \ll (n - n_0)/\tau_f$. Then it follows from the fourth equation of set (5) that

$$n = n_0 - \tau_f \sum_k \frac{d\langle D_z^k\rangle}{dt}, \quad (9)$$

where $\langle D_z^k\rangle$ can be found by solving (8),

$$\langle D_z^k\rangle = \frac{\tau^k}{2\tau_0^k}(1 + 2\bar{n}_0) - d^k \ln\left[\frac{d^k}{\tau^k}(t - t_0)\right], \quad (10)$$

where

$$t_{0k} = \frac{\tau^k}{d^k}\ln\sqrt{\frac{d^k - \frac{\tau^k}{2\tau_0^k}(1 + 2\bar{n}_0) + j^k}{d^k + \frac{\tau^k}{2\tau_0^k}(1 + 2\bar{n}_0) - j^k}}$$

is the delay time for the subgroup k, given by

$$d^k = \sqrt{\left(\frac{\tau^k}{2\tau_0^k}\right)^2(1 - 2\bar{n}_0)^2 + \left(\frac{j^k}{\tau^k} + \frac{1}{\tau_0^k}\right)j^k\tau^k}. \quad (11)$$

In this case, the time-independent solution for the nonlinear absorption coefficient takes the form

$$\alpha = \alpha_0 + \beta\left(n_0 - \tau_f\sum_k \frac{d\langle D_z^k\rangle}{dt}\right) = \alpha_0 + \beta\left\{n_0 + \tau_f\sum_k \frac{d^{k2}}{\tau^k}\mathrm{sech}^2\left[\frac{d^k}{\tau^k}(t - t_{0k})\right]\right\}. \quad (12)$$

Formula (12) describes the relaxation of the nonlinear absorption coefficient after propagation of a delta pulse through the CVS sample. It should be noted that the relaxation data were also considered in [4, 5]. It follows from (12) that the relaxation process depends on the law of cooperation between electrons. Each function $\mathrm{sech}^2(x)$ in expression (12) peaks at the point $t = t_{0k}$. Summing over k takes account of all the subgroups of equidistant two-level states having different delay times. In this situation, the relaxation function of the absorption coefficient may be broader than that for a single group of equidistant two-level states. This broadening depends on the explicit form of the subgroup distribution ρ^k.

3. MODEL FOR THE DESCRIPTION OF DEEP QWs

In this section we consider another case, with random-potential QWs deep enough for a localized excitation to have more than two states, say, M energy states. For simplicity we restrict ourselves to the case when the spectrum of a single localized state can be considered a quasi-equidistant spectrum of a nonlinear oscillator with the energy spacing $\hbar\omega_f$ between neighboring levels [7]. Such a nonlinear oscillator may be equivalent to excited electrons in solids in which exciton–exciton interaction is taken into account [8]. Similarly to the case of shallow QWs, all deep QWs can be distributed over subgroups with equal energy spacings between neighboring levels $\hbar\omega_{fk}$. Let us assume that a short laser pulse creates in a CVS sample a localized excitation belonging to the subgroup k so that, during the relaxation of this localized excitation down the M-level equidistant spectrum, $M - 1$ correlated localized phonons (fractons) are generated. Let us also assume that the excitation energy in a separate QW is E_0. The conservation law for the spontaneous decay process reads

$$E_0 = E_{el} + E_f, \quad (13)$$

where E_{el} is the energy of a localized electron (hole), and E_f is the energy of emitted phonons. These energies can be expressed in terms of the mean number of electrons (excitons), $\langle a_j^+ a_j\rangle$, at the level j and the mean number of fractons, n, as follows:

$$E_{el} = \sum_j \hbar\omega_f j\langle a_j^+ a_j\rangle, \quad E_f = \hbar\omega_f n.$$

From the conservation law (13) we obtain

$$\frac{dn}{dt} = -\frac{d}{dt}\langle D_z\rangle. \quad (14)$$

Here, $\langle D_z\rangle = \sum_j j\langle a_j^+ a_j\rangle$.

In the case when a localized electron–hole excitation decays via an equidistant spectrum, various dynamic symmetries related to the decay law may take place. For instance, a relaxation process may occur during which the spontaneous decay is only accelerated or only decelerated [7]. On the other hand, relaxation is possible when acceleration or deceleration of the spontaneous decay follow one another [7]. Below, we consider three dynamic symmetries, one of which is the harmonic oscillator symmetry, and the other two are

$SU(2)$ and $SU(1, 1)$. Depending on which dynamic symmetry we have, D_z takes different forms:

$$D_a = \begin{cases} A^+A, \\ J_z, \quad SU(2), \\ R_z, \quad SU(1,1), \end{cases} \qquad D^+ = \begin{cases} A^+, \\ J^+, \quad SU(2), \\ R^+, \quad SU(1,1), \end{cases}$$

$$D^- = [D^+]^+.$$

Let us consider three further situations for the relaxation of a localized electron down the equidistant spectrum in the QW:

(i) $d_{s,\,s-1} = d_0\sqrt{s}$,
(ii) $d_{s,\,s-1} = d_0[(j+m)(j-m+1)]^{1/2}$;
(here, $j = (M-1)/2$, $m = s-j-1$),
(iii) $d_{s,\,s-1} = d_0[(p-I)(p+I-1)]^{1/2}$;
(here, $p - I = s$, $I = 0, 1, 2, \ldots$),

where $d_{s,\,s-1}$ is the matrix element of the dipole transition between levels s and $s-1$, $2j$ is the number of excited states of the anharmonic oscillator in the case of $SU(2)$ symmetry, and I is the group parameter for $SU(1, 1)$, which can be found from the experimental data on the decay law. In case (i), when the number of electron levels M is large, the following collective operators can be introduced:

$$A = \sum_{s=1}^{M-1} \sqrt{s}\, a_s^+ a_{s+1}, \quad A^+ = \sum_{s=1}^{M-1} \sqrt{s}\, a_{s+1}^+ a_s, \qquad (15)$$

satisfying the commutation relation:

$$[A, A^+] = \sum_{s=1}^{M} a_s^+ a_s - M a_M^+ a_M. \qquad (16)$$

The first term in the right-hand side of (16) is unity ($\sum_{s=1}^{M} a_s^+ a_s = 1$). Since we study the decay of an oscillator in the state $|K\rangle$ lying below the state $|M\rangle$, we can also neglect the second term in the right hand side of (16). Within this approximation, A and A^+ are Bose operators and the system behaves like a harmonic oscillator.

In the second case (ii) the following collective cascade transition operators can be introduced:

$$J^- = \sum_{m=-j+1}^{j} [(j+m)(j-m+1)]^{1/2} a_{m+j}^+ a_{m+j+1},$$

$$J^+ = \sum_{m=-j+1}^{j} [(j+m)(j-m+1)]^{1/2} a_{m+j+1}^+ a_{m+j}, \qquad (17)$$

$$J_z = \sum_{m=-j}^{j} m a_{m+j+1}^+ a_{m+j+1},$$

where $2j + 1 = M$ is the number of equidistant electronic levels in the QW.

These new operators generate the $SU(2)$-algebra and, therefore, have conventional properties of the angular momentum [7–12]. The result of the action of the J^+, J^-, and J_z operators on the ket vector corresponding to the $SU(2)$-algebra is defined by the following relations [7, 8]:

$$J^+|j, m\rangle = [(j-m)(j+m+1)]^{1/2}|j, m+1\rangle,$$

$$J^-|j, m\rangle = [(j+m)(j-m+1)]^{1/2}|j, m-1\rangle, \qquad (18)$$

$$J_z|j, m\rangle = m|j, m\rangle.$$

Now we can determine the transition dipole moment $d_{s,\,s-1}$ in relation to the level number s in the cascade equidistant ladder. As follows from (18), this dependence can be represented for large M values in the simple form

$$d_{s,\,s-1} \approx d_0\sqrt{s(M-s)}.$$

There also occurs another case, when the dynamics of transitions from $|M\rangle$ excited states differs fundamentally from that described above. The $SU(1, 1)$ symmetry of transitions can be used in this situation. Indeed, if we consider case (iii), the collective transition operators can be introduced

$$\bar{R}^+ = \sum_{p=0}^{M-1} [p(2I+p-1)]^{1/2} a_{p+1}^+ a_p,$$
$$\bar{R}^- = \sum_{p=0}^{M-1} [p(2I+p-1)]^{1/2} a_p^+ a_{p+1}, \qquad (19)$$

satisfying the following commutation relation:

$$[\bar{R}^+, \bar{R}^-] = -2\sum_{p=0}^{M} (p+I-1) a_p^+ a_p + M(2I+M-1) a_M^+ a_M \qquad (20)$$

or

$$\tilde{R}^+ = \sum_{p=-M+1}^{0} [p(p-2I+1)]^{1/2} a_{p+M+1}^+ a_{p+M},$$
$$\tilde{R}^- = \sum_{p=-M+1}^{0} [p(p-2I+1)]^{1/2} a_{p+M} a_{p+M+1}^+. \qquad (21)$$

When M takes large values and higher-lying localized electron levels are unpopulated, the new transition operators satisfy the commutation relation for the $SU(1, 1)$ algebra [7, 8, 13–18]:

$$[R^+, R^-] = -2R_z, \quad [R_z, R^\pm] = \pm R^\pm, \qquad (22)$$

where R_z can be defined in the following form

$$\bar{R}_z = \lim_{M\to\infty}\sum_{p=1}^{M}(p+I-1)a_p^+a_p,$$
$$\tilde{R}_z = \lim_{M\to\infty}\sum_{p=-M+1}^{0}(p-I)a_{p+M}^+a_{p+M} \quad (23)$$

for the upper and lower sheets of the hyperboloid of rotation, respectively. Then we have a new integral of motion

$$R^2 = R_z^2 - R_y^2 - R_x^2. \quad (24)$$

Here, $R_y = (R^+ - R^-)/2i$, $R_x = (R^+ + R^-)/2$ for the "bar" and "tilde" operators. The hyperboloid of rotation corresponding to the classical pseudoangular momentum vector (24) is presented in Fig. 3. It is seen from Fig. 3 and expressions (19), (21), and (23) that the bar and tilde operators are related, respectively, to the upper and lower sheets of the hyperboloid of rotation. It should be noted that the change in the matrix element of the transition dipole moment with the state number s strongly depends on the parameter I and a hyperboloid sheet. In this case, normalized ket vectors corresponding to the upper sheet of the hyperboloid of rotation take the form [7]

$$|I, p\rangle = \left[\frac{(2I-1)!}{(p-I)!(p+I-1)!}\right]^{1/2}(\bar{R}^+)^{(p-I)}|I, I\rangle, \quad (25)$$
$$p = I, I+1, I+2, \ldots$$

and those for the lower sheet

$$|I, p\rangle = \left[\frac{(2I-1)!}{(|p|-I)!(|p|+I-1)!}\right]^{1/2}(\tilde{R}^-)^{(|p|-1)}|I, -I\rangle, \quad (26)$$
$$p = -I, -I-1, -I-2, \ldots$$

In this situation, the action of the group generators on the state $|I, p\rangle$ should be expressed as follows:

$$R^+|I, p\rangle = \sqrt{(p-I+1)(p+I)}|I, p+1\rangle,$$
$$R^-|I, p\rangle = \sqrt{(p+I-1)(p-I)}|I, p-1\rangle, \quad (27)$$
$$R_z|I, p\rangle = p|I, p\rangle, \quad |p| \geq I.$$

Using these properties, we can establish the dependence of the matrix elements of the transition dipole moment $d_{s,s+1}$ on the state number s and the group parameter I. We have for the upper and lower sheets of the hyperboloid of rotation

$$d_{s,s+1} \approx d_0\sqrt{s(2I+s)} \quad (28)$$

and

$$d_{s,s+1} \approx d_0\sqrt{(M-s)(2I+M-s)}, \quad (29)$$

respectively. It should be noted that for the upper sheet the moment $d_{s,s+1}$ grows with increasing s and this increase changes from linear for $I \ll 1$ to square-root at large I. For the lower sheet, a decrease in the transition moment with increasing s is observed at the same dependence on the parameter I as that for the upper sheet. Therefore, we can vary the decay process rate by choosing an optimal value of the parameter I in accordance with experimental data.

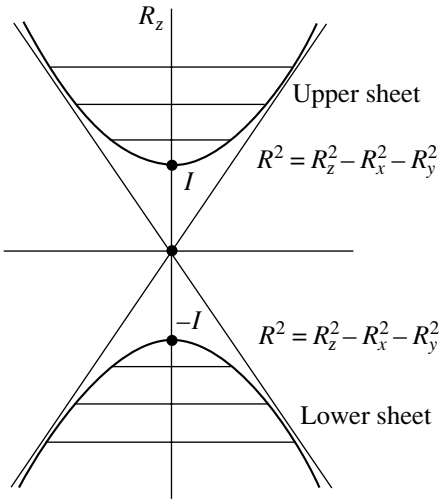

Fig. 3. Upper and lower sheets of the hyperboloid of rotation for the $SU(1, 1)$ symmetry of transitions.

Since the D^+ and D^- centers in chalcogenide glasses can appear and disappear simultaneously [6], it is natural to assume that the relaxation of such bicenters may be accompanied by the creation of a single localized oscillation (fracton). Within the framework of our interpretation, this process is related to the $SU(1, 1)$ symmetry of transitions between localized states in glasses. If two localized centers create a single fracton, the interaction Hamiltonian can be represented as

$$H_{\text{int}} \propto g(a^{+2}b + a^2b^+),$$

where $a^+(a)$ is the localized center creation (annihilation) operator, and $b^+(b)$ is the fracton creation (annihilation) operator. In this case the collective operators for the symmetry $SU(1, 1)$ are given by

$$R^+ = (a^+)^2/2, \quad R^- = a^2/2, \quad R_z = (aa^+ + a^+a)/4.$$

The physical aspects of the higher and lower sheets of the $SU(1, 1)$ symmetry of transitions were discussed in more detail in [7].

Let us consider the case when electronic transitions obey the $SU(2)$ algebra. Then, using the conservation law for the operator of the total angular momentum, J^2, and commutation relations for the collective operators of this group, we can derive the following equation for

the electronic population in the semiclassical approximation $\langle J_z^2 \rangle \approx \langle J_z \rangle^2$:

$$\frac{d\langle J_z \rangle}{dt} = -2\gamma[j(j+1) - \langle J_z \rangle^2 + \langle J_z \rangle] - 4\gamma\bar{n}_0\langle J_z \rangle, \quad (30)$$

where $2\gamma = 1/\tau_0$ and τ_0 is the spontaneous relaxation time for a single electron. When $\bar{n}_0 = 0$, the solution of this equation in the limit $j \gg 1$ reads

$$\langle J_z(t) \rangle = -j\tanh\frac{1}{2\tau_r}(t - t_0'). \quad (31)$$

Here, $1/\tau_r = 2j/\tau_0$ is the reciprocal of the cooperative emission time, and $t_0' = (\tau_0/2j)\ln 4j$ is the delay time for Mth phonon pulse. As mentioned above, this solution is obtained in the semiclassical approximation, so that the population fluctuation $\sigma_{zz} \ll 1$.

Similarly, using the conservation law for the squared total pseudoangular momentum operator R^2 (24) and the commutation relations (22) in the semiclassical approximation, we have for the $SU(1, 1)$ transition symmetry:

$$\frac{d\langle R_z \rangle}{dt} = -2\gamma[-I(I-1) + \langle R_z \rangle^2 - \langle R_z \rangle] + 4\gamma\bar{n}_0\langle R_z \rangle. \quad (32)$$

In the case when the electron is initially in the excited state $|K\rangle$ ($K = I + M$) of the upper hyperboloid sheet, the following solution of this equation can be obtained at $\bar{n}_0 = 0$ for $I \gg 1$:

$$\langle \bar{R}_z(t) \rangle = I\coth\frac{1}{2\tau_r'}(t + \bar{t}_0), \quad (33)$$

where $1/\tau_r' = 2I/\tau_0$ is the reciprocal of the cooperative emission time,

$$\bar{t}_0 = (\tau_0/2I)\ln(K+I)/(K-I).$$

It can be readily seen that in this case the decay rate decreases with time. If the initial excited state corresponds to the highest state of the lower sheet of the hyperboloid of rotation, then another solution can be obtained for the electron occupancy

$$\langle \tilde{R}_z(t) \rangle = I\coth\frac{1}{2\tau_r'}(t - \tilde{t}_0'). \quad (34)$$

Here, $\tilde{t}_0' = (\tau_0/2I)\ln 4I$.

It should be noted that, with the occupancy fluctuations neglected, we can obtain closed Eqs. (30) and (32) for the level occupancy for transition symmetries $SU(2)$ and $SU(1, 1)$, respectively. Solving these equations in the absence of an electromagnetic field, $\bar{n}_0 = 0$, we can obtain an explicit solution for the occupancies: (31) for $SU(2)$ and (33) and (34) for $SU(1, 1)$. It can be readily seen that the solution for the $SU(2)$ symmetry resembles the corresponding solution for Dicke's model of superradiance of $(M-1)$ inverted atoms, whereas in the case of the $SU(1, 1)$ symmetry the decay process is fundamentally different.

If the nature of the random potential is such that there is a great number of quasi-equidistant nonlinear oscillators (excitons) in the CVS, the behavior of such a system can be described by analogy with the case of shallow QWs. Indeed, since the spectrum of the M-level localized excitations can be divided into a spectrum of quasi-equidistant subgroups, two kinds of cooperation are possible. One of these is the cooperation between localized excitations belonging to different spatially separated quasi-equidistant nonlinear oscillators. Such cooperation is only possible if the wavelength of localized phonons is on the order of the distance between the localized oscillators of the k-th group. The second kind is the cooperation taking place during the relaxation of a single quasi-equidistant oscillator from an excited to the ground state [7]. In this case, the set of equations (5) is modified by introducing new equations describing the relaxation of electron–hole pairs belonging to the k-th group of the M-level equidistant spectrum. Thus, the set of equations describing the process of nonlinear interband absorption of light in glasses in the presence of these kinds of cooperation reads as follows:

$$\begin{aligned}
\frac{dI_s(t,z)}{dt} &= -c\left[\frac{dI_s(t,z)}{dz} + (\alpha_0 + \beta n)I_s(t,z)\right],\\
\frac{d\langle D_z^k \rangle}{dt} &= -\frac{1}{\tau^k}\langle D_k^+ D_k^- \rangle - \frac{2}{\tau_0^k}n^k(t)\langle D_z^k \rangle G\\
&\quad + (\alpha_0 + \beta n)\frac{V_0 I_s(t,z)}{\hbar\omega_f}\rho^k,\\
\frac{d\langle D_k^+ D_k^- \rangle}{dt} &= -\frac{1+n^k}{\tau_0^k}\langle D_k^+ D_k^- \rangle\\
&\quad + \frac{G}{\tau^k}\langle D_k^+ D_k^- \rangle\langle D_z^k \rangle - \frac{G^2}{\tau_0^k}\langle D_z^k \rangle n^k(t),\\
\frac{dn}{dt} &= -\sum_k \frac{d}{dt}\langle D_z^k \rangle - \frac{1}{\tau_f}(n - n_0).
\end{aligned} \quad (35)$$

In this system, $G = 1$ for the $SU(2)$ symmetry and $G = -1$ for the $SU(1, 1)$symmetry.

Let us now consider the case when the symmetry of the dipole transitions of localized excitations in deep QWs is $SU(1, 1)$ [see (28)]. In this situation the equa-

tion for the occupancy D_z can be written by analogy with the case of shallow QWs

$$\frac{d\langle D_z^k\rangle}{dt} = -\frac{1}{\tau_0^k}(-\langle D_z^k\rangle + I^k) + \frac{2}{\tau_0^k}\bar{n}_0\langle D_z^k\rangle + \frac{1}{\tau^k}[-\langle D_z^k\rangle^2 + (I^k)^2]. \quad (36)$$

The solution of this equation reads:

$$\langle D_z^k\rangle = \frac{\tau^k}{2\tau_0^k}(1+2\bar{n}_0) + \bar{d}^k \coth\left(\frac{\bar{d}^k}{\tau^k}t + \ln\sqrt{\frac{\bar{d}^k - \frac{\tau^k}{2\tau_0^k}(1+2\bar{n}_0) + I^k}{\bar{d}^k + \frac{\tau^k}{2\tau_0^k}(1+2\bar{n}_0) - I^k}}\right), \quad (37)$$

where

$$\bar{d}^k = \sqrt{\left(\frac{\tau^k}{2\tau_0^k}\right)^2(1+2\bar{n}_0)^2 + \left(\frac{I^k}{\tau^k} - \frac{1}{\tau_0^k}\right)I^k\tau^k}. \quad (38)$$

With the use of this solution, an expression can be readily obtained for the nonlinear absorption coefficient in the case of the *SU*(1, 1) symmetry of the localized excitations in deep QWs:

$$\alpha = \alpha_0 + \beta\left[n_0 + \tau_f\sum_k \frac{(\bar{d}^k)^2}{\tau^k} \times \operatorname{cosech}^2\left(\frac{\bar{d}^k}{\tau^k}t + \ln\sqrt{\frac{\bar{d}^k - \frac{\tau^k}{2\tau_0^k}(1+2\bar{n}_0) + I^k}{\bar{d}^k + \frac{\tau^k}{2\tau_0^k}(1+2\bar{n}_0) - I^k}}\right)\right]. \quad (39)$$

It is noteworthy that in this situation the nonlinear absorption coefficient α decreases with time and tends in the course of relaxation to the equilibrium value $\alpha = \alpha_0 + \beta n_0$, whereas in the case of the *SU*(2) symmetry the absorption coefficient behaves similarly to the corresponding case of shallow QWs.

4. CONCLUSION

As can be seen from Eqs. (12) and (39), the coefficient of nonlinear induced light absorption, α, strongly depends on the law of relaxation of localized excitations of the random potential. This law is determined by the form of the random potential and by the dynamic symmetry of the system relaxation. Equation (12) implies that for shallow QWs, and also for the *SU*(2) symmetry in the case of deep QWs, the nonlinear absorption coefficient $\alpha \propto \operatorname{sech}^2 t$ resembles Dicke's superradiant pulse. In the case of the *SU*(1, 1) symmetry for deep QWs, it can be seen from Eq. (39) that the nonlinear absorption coefficient $\alpha \propto \operatorname{cosech}^2 t$ fundamentally differs from Dicke's superradiance case, which, in turn, gives deeper insight into the results of experimental studies [2–5].

REFERENCES

1. P. W. Anderson, B. I. Halperin, and C. M. Varma, Philos. Mag. **25**, 1 (1972).
2. M. H. Overwijk, J. I. Dijkhuis, and H. W. de Wijn, Phys. Rev. Lett. **65**, 2015 (1990).
3. C. Thomsen, J. Strait, Z. Vardeny, *et al.*, Phys. Rev. Lett. **53**, 989 (1984).
4. A. M. Andriesh, O. I. Bogdan, N. A. Enaki, *et al.*, Izv. Akad. Nauk, Ser. Fiz. **56**, 96 (1992).
5. A. M. Andriesh, N. A. Enaki, I. A. Kozhkar', *et al.*, Pis'ma Zh. Tekh. Fiz. **14**, 1985 (1988) [Sov. Tech. Phys. Lett. **14**, 860 (1988)].
6. N. F. Mott and E. A. Davis, *Electronic Processes in Non-Crystalline Materials* (Clarendon Press, Oxford, 1979; Mir, Moscow, 1982).
7. N. A. Enaki and V. I. Koroli, J. Phys. B **31**, 3583 (1998).
8. P. I. Bardetskii, N. A. Enaki, and D. Michalache, Zh. Éksp. Teor. Fiz. **110**, 1186 (1996) [JETP **83**, 653 (1996)].
9. L. C. Biedenharn and J. D. Louck, *Angular Momentum in Quantum Mechanics* (Addison-Wesley, Reading, 1981; Mir, Moscow, 1984).
10. J. M. Radcliffe, J. Phys. A **4**, 313 (1971).
11. F. T. Arecchi, E. Courtens, R. Gilmore, and H. Thomass, Phys. Rev. A **6**, 2211 (1972).
12. S. S. Hassan, G. P. Hildred, R. R. Puri, and R. K. Bullough, J. Phys. B **15**, 2635 (1982).
13. C. C. Gerry, Phys. Rev. A **37**, 2683 (1988).
14. A. M. Perelomov, *Generalized Coherent States and Their Applications* (Nauka, Moscow, 1987; Springer, Berlin, 1980).
15. V. Buzeek, Phys. Rev. A **39**, 3196 (1989).
16. K. Wodkiewicz and J. H. Eberly, J. Opt. Soc. Am. B **2**, 458 (1985).
17. C. C. Gerry, Phys. Rev. A **31**, 2721 (1985).
18. M. Ban, J. Opt. Soc. Am. B **10**, 1347 (1993).

Translated by S. Ktitorov

Semiconductors, Vol. 35, No. 6, 2001, pp. 656–658. Translated from Fizika i Tekhnika Poluprovodnikov, Vol. 35, No. 6, 2001, pp. 684–686.

II INTERNATIONAL CONFERENCE ON AMORPHOUS AND MICROCRYSTALLINE SEMICONDUCTORS

Influence of *a*-Si:H Band Tails on the Occupation of Dangling-Bond States and on Photoconductivity

S. V. Kuznetsov* and E. I. Terukov**

** Moscow State University, Vorob'evy gory, Moscow, 119899 Russia*

*** Ioffe Physicotechnical Institute, Russian Academy of Sciences, Politekhnicheskaya ul. 26, St. Petersburg, 194021 Russia*

e-mail: eug.terukov@pop.ioffe.rssi.ru

Submitted November 9, 2000; accepted for publication November 15, 2000

Abstract—The results of numerical calculation are presented for the temperature dependence of photoconductivity and occupation of dangling-bond states of *a*-Si:H with various doping levels. The calculations show that the energy position of traps influences substantially the temperature dependences of photoconductivity. This influence is due not only to the participation of traps in recombination at low temperatures, but also to the influence of dangling-bond states on occupation. It was found that the concentration of neutral dangling bonds (D^0 centers) for *p*-type *a*-Si:H in the region of medium and low temperatures is independent of the Fermi level. This feature was shown to be the consequence of asymmetry in the position of the D^0 centers and the *D* centers (negatively charged dangling bonds) rather than of asymmetry in the arrangement of traps in the band gap with respect to the edges of allowed energy bands. © *2001 MAIK "Nauka/Interperiodica".*

1. INTRODUCTION

A great number of experimental results and numerical calculations devoted to the properties of *a*-Si:H and photoconductivity (σ_{ph}), in particular, have been published. However, until now, there was no model that could satisfactorily explain all the features of σ_{ph}. Among the problems under discussion is the interpretation of the asymmetric dependence of σ_{ph} on the Fermi level position ($E_F - E_V$). Previously, it was shown that the photoconductivity of *p*-type *a*-Si:H depends only slightly on an $E_F - E_V$ value [1, 2] and on the dangling-bond (*D*-center) concentration in contrast to σ_{ph} for *n*-type *a*-Si:H [2]. Asymmetry in the band tails, which leads to a significant distinction between the nonequilibrium and equilibrium occupancies of *D*-centers [2] was proposed to explain this weak dependence. In this paper, we report the results of a numerical calculation of the influence of the energy position of traps in the bond tails on the form of temperature dependence of photoconductivity for *p*-type *a*-Si:H.

2. MODEL

For testing recombination models that interpret experimental results, computer simulation is often used. As a rule, the numerical calculations are fulfilled for a simplified density of states in the mobility gap and take into account only the main recombination and emission fluxes in the model under consideration. The model for the density of states used in our calculations is illustrated in Fig. 1. As can be seen from Fig. 1, instead of a continuous distribution of density of states in the mobility gap, we consider four discrete levels: E_{tp}, E_D, $E_D + U$, and E_{tn}. The levels E_{tp} and E_{tn} with a state concentration of N_{tp} and N_{tn} are the effective levels in the valence- and conduction-band tails, respectively. The levels E_D and $E_D + U$ are the energy levels of the positively correlated dangling-bond states. In the phenomenological description of recombination in semiconductors, the localized states are classified as recombination levels and traps depending on their position with respect to the demarcation levels. As a rule, the tail states act as traps; therefore, we will use the terms "traps for holes" and "traps for electrons" for the levels E_{tp} and E_{tn}, respectively. In this study, we consider two possible channels of recombination in correspondence with Fig. 1: the direct capture of free electrons and holes by *D*-centers (fluxes U_1, U_2, U_5, and U_6) and the tunnel recombination between the electrons captured at the conduction-band-tail states and the holes captured at the valence-band-tail states (U_{13}). In the previous paper [3], we cited the arguments in favor of the choice of such a recombination model and wrote the corresponding kinetic equations. In the following section, the numerical solutions to these equations are presented for the same values of parameters involved in them when varying $E_F - E_V$, E_{tp}, and E_{tn}.

3. RESULTS OF NUMERICAL CALCULATION AND DISCUSSION

In Fig. 2, we show the calculated temperature dependences of photoconductivity for $E_F - E_V = 0.75$ eV (a lightly doped *p*-type *a*-Si:H) corresponding to three different relations between positions of traps: (1) symmetric shallow-level traps $E_{tp} - E_V = E_C - E_{tn} =$

0.1 eV (curve *3*); (2) symmetric deep-level traps $E_{tp} - E_V = E_C - E_{tn} = 0.3$ eV (curve *1*); and (3) asymmetric traps $E_{tp} - E_V = 0.3$ eV and $E_C - E_{tn} = 0.1$ eV (curve *2*). In Fig. 2, we also plot the temperature dependence of dark conductivity σ_d and the temperature dependence of photoconductivity for a density of states without traps; i.e., $E_{tp} - E_V = E_C - E_{tn} = 0$ (curve *4*). For the optical-generation rate (G) and the D-center concentration (N_D), the following values were taken: $G = 10^{19}$ cm^{-3} s^{-1} and $N_D = 10^{16}$ cm^{-3}. It follows from Fig. 2 that the influence of traps on photoconductivity increases with decreasing temperature and with increasing values of $E_{tp} - E_V$ and $E_C - E_{tn}$. In this case, according to the calculations, the traps can become recombination states (for curves *1* and *2*). In contrast, at high temperatures with $\sigma_d > \sigma_{ph}$, the influence of traps on the temperature dependence of photoconductivity is negligible. In the region of moderate temperatures, the temperature dependence of photoconductivity is of the activation type with an activation energy of $E_A = 0.05$ and 0.15 eV for curves *3* and *2*, respectively [i.e., $E_A = 0.5(E_{tp} - E_V)$] and $E_A = 0.2$ eV (curve *1*). Irrespective of the relation between $E_{tp} - E_V$ and $E_C - E_{tn}$, the equality $p_t = N_D f^0$ is valid in this temperature range; here, p_t is the concentration of holes captured at a hole trap, f^0 is the probability of finding a dangling bond in the neutral state (D_0-state), and N_D is the concentration of D centers in the D_0 state (the D_0-center concentration). As was previously shown [2], this relationship is derived from the electroneutrality condition and means that the nonequilibrium positive charge in *p*-type *a*-Si:H is localized at the valence-band-tail states under illumination conditions, whereas the nonequilibrium negative charge is localized at the D centers. It should be noted that the recharging of D-centers under illumination ($D^+ + e \longrightarrow D^0$ and $D^0 + e \longrightarrow D^-$) in the case of asymmetric traps leads to the thermal quenching of photoconductivity (Fig. 2, curve *2*). At temperatures below the region of thermal quenching of photoconductivity, the slope of the temperature dependence of photoconductivity is 0.09 eV, which is close to the value of $E_C - E_{tn} = 0.1$ eV.

We now consider how the trap parameters influence the occupation of the D centers. In Fig. 3, the dependences of $N_D f^0$ on the Fermi level ($E_F - E_V$) at $T = 250$ K are shown for various relations between $E_{tp} - E_V$ and $E_C - E_{tn}$. It follows from Fig. 3 that the dependence of $N_D f^0$ on $E_F - E_V$ is asymmetric irrespective of trap parameters: for the Fermi levels lying in the upper half of the mobility gap, a D_0-center concentration differs only negligibly from the equilibrium one; in contrast, for the Fermi levels in the range of $E_F - E_V = 0.5$–0.75 eV (corresponding to *p*-type *a*-Si:H), the concentration of $N_D f^0$ is independent of $E_F - E_V$ and differs significantly from the equilibrium one. In this case, it should be noted that the value of $N_D f^0$ in *p*-type *a*-Si:H

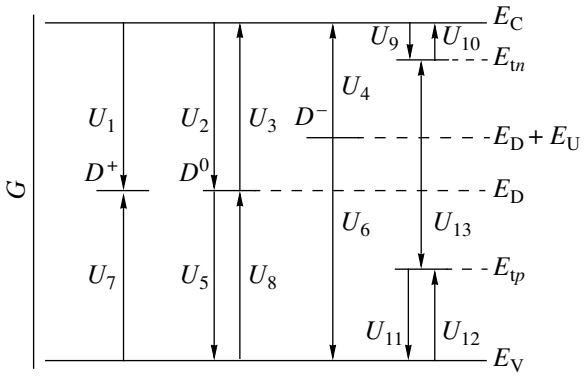

Fig. 1. Schematic representation of electron transitions for the simplified model of density of states in the *a*-Si:H mobility gap.

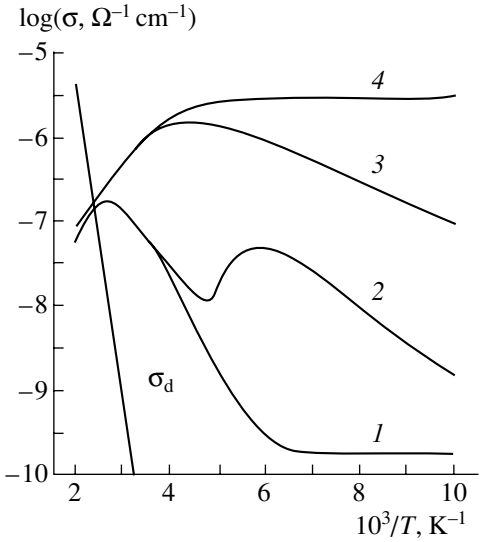

Fig. 2. Temperature dependences of photoconductivity (*1*–*4*) for $E_F - E_V = 0.75$ eV and different relations between $E_{tp} - E_V$ and $E_C - E_{tn}$. See details in the text.

is mainly governed by the value of $E_{tp} - E_V$ instead of $E_C - E_{tn}$.

We consider the dependence $N_D f^0$ ($E_F - E_V$) at $T = 150$ K (Fig. 4). From Fig. 4, it follows that the symmetric (with respect to $E_D + U/2$) dependences $N_D f^0$ ($E_F - E_V$) correspond to symmetric traps, while the asymmetric dependence $N_D f^0$ ($E_F - E_V$) corresponds to asymmetric traps. As can be seen from Figs. 3 and 4, the relation between $E_{tp} - E_V$ and $E_C - E_{tn}$ only influences the value of $N_D f^0$ for *p*-type *a*-Si:H but does not affect the $N_D f^0$ ($E_F - E_V$) dependence. It should be noted that the asymmetric traps lead to a higher charge rate of the D-centers than the symmetric ones.

The analysis of these calculations enables us to conclude that the asymmetry of the $N_D f^0$ ($E_F - E_V$) dependence at $T = 250$ K is the consequence of asymmetry in

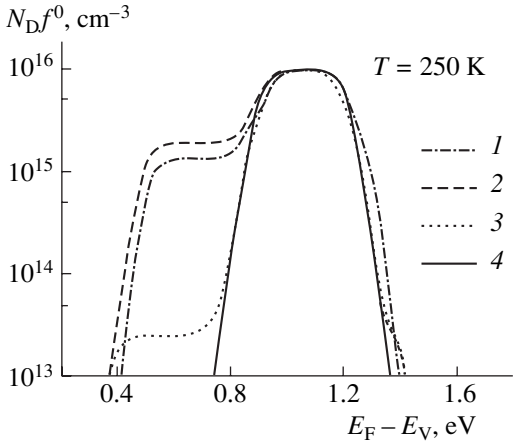

Fig. 3. Numerical calculation of the D_0-center concentration at T = 250 K (*4*) in dark and (*1–3*) under illumination conditions depending on the Fermi level position and the following relations between $E_C - E_{tn}$ and $E_{tp} - E_V$, in eV: (*1*) $E_C - E_{tn} = E_{tp} - E_V = 0.3$; (*2*) $E_C - E_{tn} = 0.1$, $E_{tp} - E_V = 0.3$ and (*3*) $E_C - E_{tn} = E_{tp} - E_V = 0.1$.

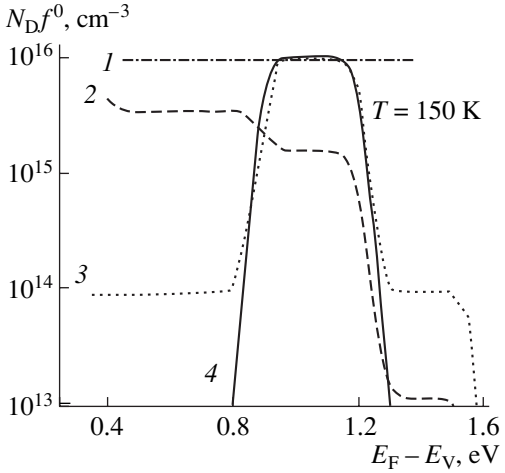

Fig. 4. Numerical calculation of the D_0-center concentration at T = 150 K as a function of the Fermi level position. The numbers at the curves correspond to the same conditions as those in Fig. 3.

the position of the levels E_D and $E_D + U$ with respect to the mobility midgap rather than of the asymmetry in the position of the traps with respect to band edges E_C and E_V.

The independence of $N_D f^0$ on $E_F - E_V$ for *p*-type *a*-Si:H leads to the independence of photoconductivity σ_{ph} on the doping level if we assume that, in the region of moderate temperatures, the main channel of recombination is the direct capture of free carriers via *D*-centers. This type of recombination is corroborated by the experimental results that indicate the presence of the effect of temperature quenching of photoconductivity for a lightly boron-doped *p*-type *a*-Si:H [2, 4], because the maximum of photoconductivity in the region of temperature quenching of photoconductivity is associated with changing the tunnel recombination or the "band–tail" recombination [5] for the recombination of free carriers via the dangling bonds in the case of increasing temperature.

4. CONCLUSION

In summing up the aforesaid, we can conclude that the independence of photoconductivity in *p*-type *a*-Si:H is an immanent property of this material and is specified by the distribution of the density of states in the mobility gap, which, under illumination, leads to a substantially nonequilibrium concentration of the D_0 centers representing the main recombination centers.

ACKNOWLEDGMENTS

We thank A.G. Kazanskiĭ for his useful participation in discussions of the results.

REFERENCES

1. P. E. Vanier, Sol. Cells **9**, 85 (1983).
2. S. V. Kuznetsov, Fiz. Tekh. Poluprovodn. (St. Petersburg) **34**, 748 (2000) [Semiconductors **34**, 723 (2000)].
3. S. V. Kuznetsov, J. Non-Cryst. Solids (in press).
4. H. Fritzsche, M. Q. Tran, B.-G. Yoon, and D.-Z. Chi, in *Proceedings of ICAS 14, Garmisch-Partenkirchen, 1991*.
5. F. Vaillant, D. Jousse, and J.-C. Bruyere, Philos. Mag. B **57**, 649 (1988).

Translated by V. Bukhanov

Semiconductors, Vol. 35, No. 6, 2001, pp. 659–660. Translated from Fizika i Tekhnika Poluprovodnikov, Vol. 35, No. 6, 2001, pp. 687–689.

II INTERNATIONAL CONFERENCE ON AMORPHOUS AND MICROCRYSTALLINE SEMICONDUCTORS

The Meissner Effect in Copper-Containing Fullerides

A. V. Prikhod'ko and O. I. Kon'kov

St. Petersburg State Technical University, Politekhnicheskaya ul. 29, St. Petersburg, 195251 Russia

Submitted November 9, 2000; accepted for publication November 15, 2000

Abstract—The existence of the Meissner effect in polycrystalline copper-containing fullerides produced by a new technology is experimentally established. The critical temperature of superconducting transition is determined to be 110 K. © *2001 MAIK "Nauka/Interperiodica".*

A basic property of the superconductor is magnetic field expulsion from its volume at temperatures below the critical one, i.e., the Meissner effect. It is a basic test for superconductivity and is usually demonstrated by experiments with a magnet suspended above the surface of low- and high-temperature superconductors [1]. To measure the force acting on the magnet, various balances are used, as well as compensation methods, for example, the electromagnetic one. Such experiments include the study of low-frequency conductance oscillations during the levitation of a microspherical magnet between high-temperature superconductor (HTSC) plates [2]. A magnetized body in a nonuniform magnetic field is subject to a force directed toward the greatest magnetic induction gradient and proportional to the magnetic susceptibility χ and the volume V [3],

$$F = AV\chi,$$

where $A = BdB/dr$ and B is the magnetic induction.

This principle is put into the basis of the forcemetric method for measuring the magnetic susceptibility (the Faraday method) of low-magnetic samples. For example, let a sample be an elongated parallelepiped whose ends are in fields with magnetic inductions B_1 and B_2. Then it is subject to the force directed to the higher induction B_2,

$$F = (1/2)S\chi(B_2^2 - B_1^2),$$

where S is the sample cross-sectional area.

A similar situation can take place in the experiment with a suspended magnet when the magnetic induction B_2 exists only at the surface (in a layer of thickness equal to the field penetration depth); the magnetic induction B_1 inside the superconducting sample is zero. Thus, the magnet is pushed out toward the higher magnetic induction. As the temperature (T) approaches the critical one (T_c), the penetration depth tends to infinity. The magnetic field penetrates deeper and deeper into the superconductor and the magnet levitation effect disappears. In this paper, we suggest an experiment in which the superconducting sample remains fixed, while the magnet is pushed out due to the Meissner effect in the sample bulk. We study copper-containing fullerene polycrystals. Previously [4], we concluded that such materials can exhibit superconducting properties.

This study is aimed at detecting the Meissner effect in copper-containing fulleride samples.

We study polycrystalline samples prepared using a modified sublimation process of initial fullerene powder (10 mg) and fine-grained copper (10 mg) in a small thermal chamber [5]. The average copper content in the sample does not exceed 10^{-2} wt %.

The sample diameter and thickness are 8 and 2 mm, respectively. The diameter and maximum length (through the entire membrane thickness at its center) of individual crystals do not exceed 0.2 and 2 mm, respectively.

Temperature dependences of the expulsion force of polycrystals and (for comparison) superconducting ceramics $YBa_2Cu_3O_{7+\delta}$ samples were measured using a modified thickness meter [6] based on disbalance in the frequencies of quartz oscillators (the generation frequency of each was 1 MHz). The relative frequency change df/f depends linearly on the quartz mass [6]. Therefore, quartz was used as an indicator of contact with a "levitating" magnet. The experimental scheme is illustrated in Fig. 1. A thin ferromagnetic film on Mylar, 12 μm thick, 6 mm long, and 0.1 mm wide, magnetized in a constant field of 59 mT is used as a magnet. As the expulsion force arises in sample *1*, ferromagnetic film *2* comes into contact with quartz surface *3*, and the frequency increases. The setup is calibrated as follows. Let there be a liquid nitrogen layer between the quartz surface and a metal ball (standard) (see the inset in Fig. 2). The ball is in the gravitational field normal to the quartz surface. As the nitrogen layer is freely evaporated, the ball falls onto the quartz surface due to gravity and the frequency changes. Figure 2 shows the temperature dependence of the relative frequency change df/f for a ball with diameter 4.8 mm and mass of 450 mg. Thus, the value $F = 4.4 \times 10^{-2}$ dyne corresponds to the frequency change $df/f = 2.2$. The region of signal instability near $T = 100$ K is caused by the active boiling of liquid nitrogen.

1063-7826/01/3506-0659$21.00

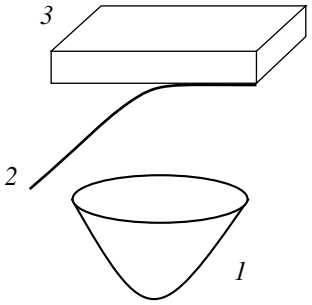

Fig. 1. Schematic of the measuring setup: (*1*) sample, (*2*) ferromagnet, and (*3*) quartz.

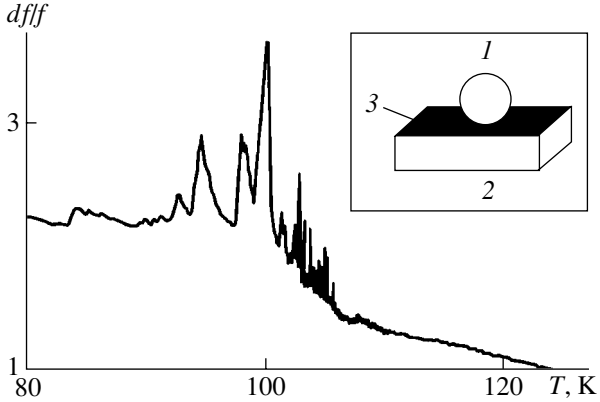

Fig. 2. Temperature dependence of df/f for a metal ball. The inset shows ball position *1* above quartz *2* surface and liquid nitrogen layer *3* between them.

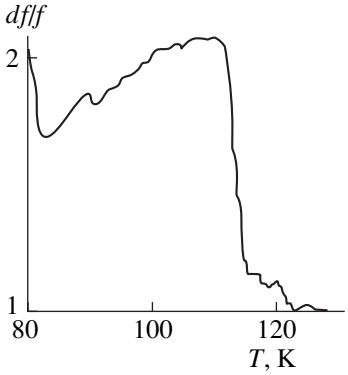

Fig. 3. Temperature dependence of df/f for the copper-containing fulleride sample.

The results of the main experiment are plotted in Fig. 3. The critical temperature T_c of superconducting transition is 110 K for the copper-containing fulleride sample. The value T_c for HTSC ceramics is 91 K, which is consistent with known critical temperatures for ceramics of similar composition. The value T_c found for the copper-containing fulleride corresponds to those measured by other methods [7]. The frequency behavior below the critical temperature is comparable to the data of magnetic experiments. For example, the measurements of dynamic magnetic susceptibility [7] have detected a wide "diamagnetic well" at temperatures 80–98 K in samples of thickness not exceeding 0.5 mm. In our case, the frequency decrease, which can be related to a magnetic susceptibility change, is observed in the temperature range T = 80–110 K. We now estimate the sample volume involved in the expulsion force origination. At the magnetic susceptibility $\chi = -6 \times 10^{-5}$ cm^3/g measured by the Faraday method [7], taking into account the sample sizes, ferromagnetic field induction $BdB/dx = 2.5 \times 10^6$ G^2/cm, and formula (1), the sought-for sample volume is 2.9×10^{-4} cm^3. An individual crystal volume is 6.28×10^{-5} cm^3. Thus, approximately five individual crystals are involved in inducing the repulsive force rather than the entire sample. Since the entire sample volume is 10^{-1} cm^3, approximately one-thousandth of the sample volume or 0.1 wt % contributes to the Meissner effect. A fraction of each individual crystal is 0.01%, which corresponds approximately to the copper percentage in the sample.

Thus, the existence of the Meissner effect in copper-containing fullerides produced by the new technology has been experimentally established. The critical temperature is T_c = 110 K.

ACKNOWLEDGMENTS

This study was supported by the Federal Programs "Fullerenes and Atomic Clusters" (the "Gradient" project no. 98063), and "Russian Universities–Basic Research."

REFERENCES

1. A. P. Malozemoff, in *Physical Properties of High Temperature Superconductors*, Ed. by D. M. Ginsberg (World Scientific, Singapore, 1989; Mir, Moscow, 1990).
2. R. Grosser, J. Jager, J. Betz, and W. Schoepe, Appl. Phys. Lett. **67** (16), 2400 (1995).
3. E. N. Chechurina and A. P. Shchelkin, Zavod. Lab. **45** (10), 901 (1979).
4. V. F. Masterov, A. V. Prichodko, and O. I. Konkov, Fullerene Sci. Technol. **6** (3), 481 (1998).
5. V. F. Masterov, A. V. Prikhod'ko, O. I. Kon'kov, and V. Yu. Davydov, RF Patent No. 2135648, Byull. No. 24, 1999.
6. B. Huner, P. Klinkhachorn, and E. B. Overton, Rev. Sci. Instrum. **59** (6), 983 (1988).
7. V. F. Masterov, A. V. Prikhodko, V. V. Romanov, *et al.*, in *Abstracts of the 4th Biennial International Workshop "Fullerenes and Atomic Clusters", IWFACT99, St. Petersburg, 1999*, p. 204.

Translated by A. Kazantsev

Semiconductors, Vol. 35, No. 6, 2001, pp. 661–665. Translated from Fizika i Tekhnika Poluprovodnikov, Vol. 35, No. 6, 2001, pp. 690–694.

II INTERNATIONAL CONFERENCE ON AMORPHOUS AND MICROCRYSTALLINE SEMICONDUCTORS

X-ray Studies of Nanoporous Carbon Powders Produced from Silicon Carbide

É. A. Smorgonskaya*, R. N. Kyutt*, A. V. Shchukarev, S. K. Gordeev***, and A. V. Grechinskaya*****

** Ioffe Physicotechnical Institute, Russian Academy of Sciences, Politekhnicheskaya ul. 26, St. Petersburg, 194021 Russia*

*** "Mekhanobr–Analit" Analytical Center, St. Petersburg, Russia*

**** Central Research Institute of Structural Materials, nab. Monastyrki 1, St. Petersburg, 193167 Russia*

Submitted November 9, 2000; accepted for publication November 15, 2000

Abstract—X-ray diffraction, small-angle X-ray scattering, and X-ray photoelectron spectroscopy were used to study the structure of nanoporous carbon powders produced directly by chlorination of polycrystalline α-SiC powders with various degrees of dispersion. Small-angle scattering data were used to derive the distribution function for scattering inhomogeneities with respect to inertia radii $m(R_g)$. It is shown that the mean sizes and the fraction of large inhomogeneities increase with increasing size of grains in the starting powder. As follows from the diffraction patterns, the degree of "graphitization" of nanocluster structure increases simultaneously, which is attributed to longer times required for carbonization of coarser grains. An analysis of photoelectron spectra for 1*s* electrons of carbon atoms shows that, for most of the C–C bonds (>65%), the hybridization of valence bonds is intermediate between those for graphite and diamond (sp^x, where $2 < x < 3$), which is indicative of the bending of graphene-like layers in nanoclusters. © *2001 MAIK "Nauka/Interperiodica".*

1. INTRODUCTION

The chlorination chemical reaction at a high temperature makes it possible to obtain a carbon material with a high porosity (nanoporous carbon) from polycrystalline carbide compounds, in particular, from hexagonal silicon carbide (α-SiC). Compacted (bulk) nanoporous carbon samples, which have the required mechanical strength and an overall porosity as high as 65–70 vol %, are obtained as a result of a preliminary heat treatment of the starting carbide powders under pressure in a methane atmosphere with subsequent chlorination [1, 2]. According to adsorption measurements and estimations, ~45 vol % of the sample obtained from polycrystalline α-SiC is occupied by nanopores with a typical size of ~8 Å and a high degree of uniformity in size.

In recent years, prospects of using nanoporous carbon for technical applications have stimulated intensive structural studies of this class of materials by physical methods, including X-ray diffraction [3], small-angle X-ray scattering [3, 4], X-ray photoelectron spectroscopy (XPS) [5], and the Raman spectroscopy [6]. However, most of the available results refer to the bulk nanoporous carbon samples, the composition of which includes binding pyrolytic carbon as a result of aforementioned heat treatment of carbide powders. At the same time, the structural base of nanoporous carbon (i.e., the porous carbon skeleton) has remained unexplored so far, although it is this skeleton that primarily specifies the attractive physical and physicochemical properties of nanoporous carbon. In this context, the objective of this study was to gain insight into the structure of nanoporous carbon powders with various degrees of dispersion; the samples were obtained by chlorination of α-SiC powders with different degrees of dispersion (with grain sizes of 10–10^3 μm) without a preliminary heat treatment in methane. The results based on X-ray diffraction, small-angle X-ray scattering, and XPS are reported in this paper. As is known, these methods make it possible to judge the structure of the short-range order in a system, typical sizes of the scattering fragments, distribution in sizes for these fragments, and the special features of hybridization of the valence bonds.

2. EXPERIMENTAL

All the measurements for the nanoporous carbon powders were performed under the same experimental conditions as those reported previously for the bulk samples [3–5]. We studied three types of the samples (denoted henceforth as F20, F80, and F600) with grain sizes of the starting α-SiC being D = 800–1000, 180–200, and 8–10 μm, respectively. The intensities of X-ray diffraction and small-angle X-ray scattering were measured with a double-crystal diffractometer; CuK_α radiation (a wavelength of λ = 1.54 Å) and a monochromator made of a structurally perfect Ge crystal [the (111) reflection] were used, which ensured the incident-beam angular divergence of 20″. Angular dependences of the intensity $I(2\theta)$, where 2θ is the diffraction (scattering) angle, were measured under the conditions when the beam passed through the sample (the 2θ-scanning mode); the angular resolution was

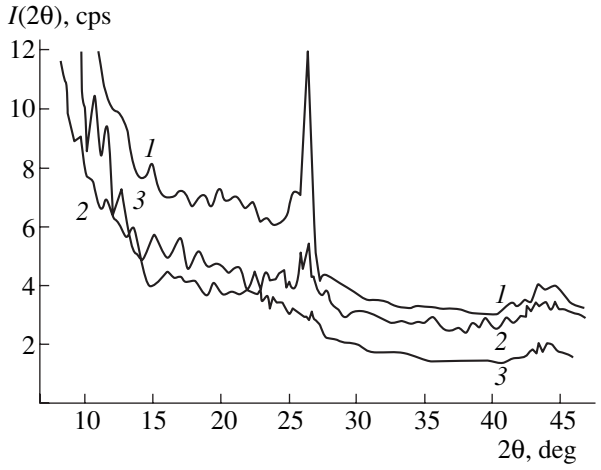

Fig. 1. Diffraction patterns for nanoporous carbon powders obtained from α-SiC powders of fractions (*1*) F20, (*2*) F80, and (*3*) F600. The grain size *D* was equal to (*1*) 800–1000, (*2*) 180–200, and (*3*) 8–10 μm.

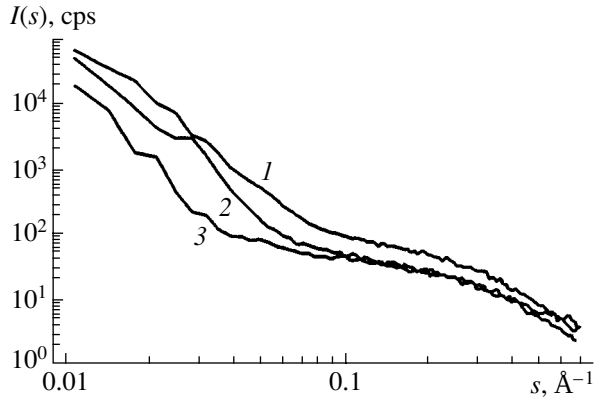

Fig. 2. The curves of small-angle X-ray scattering for nanoporous carbon films obtained from the α-SiC powders of fractions (*1*) F20, (*2*) F80, and (*3*) F600. The grain size *D* was equal to (*1*) 800–1000, (*2*) 180–200, and (*3*) 8–10 μm.

0.16°. The XPS spectra were measured using a PHI 5400 spectrometer calibrated with the standard Au $4f_{7/2}$ line (the binding energy of 84.0 eV). In order to excite the C 1*s*(*K*) carbon line, we used the AlK_α radiation, which is nearly monochromatic. The spectra were analyzed using the standard programs for decomposition of the spectra into components; these programs were built into the spectrometer.

3. RESULTS AND DISCUSSION

3.1. X-ray Diffraction

In Fig. 1, we show the diffraction patterns for the three nanoporous carbon powders. In all three cases, one can see the features in the vicinity of $2\theta \approx 26°$ and 44°; these correspond closely to the (0002) reflections for (100) and (101) graphite or (111) diamond. The "graphite" (0002) reflection is found to be the most intense and narrowest for sample F20 with coarsest grains. As the grain size decreases, the intensity of (0002) reflection decreases sharply in amplitude and the peak broadens, mainly on the side of smaller angles 2θ. Estimations of the correlation length (of the ordered-region sizes) $L_\perp$ in the direction normal to the graphene planes yield the values of 450 and 80 Å for samples F20 and F80, respectively (see table); the estimates were based on the data on the (0002) peak half-width. For the F600 powder having finest grains, the (0002) peak manifests itself only as a slight excess of the signal over the background in a wide range of angles $2\theta = 20°–27°$. Thus, we may infer that coarse-grained nanoporous carbon powders contain rather large graphite-like nanoclusters, whereas these nanoclusters are virtually absent in a fine-grained powder.

The parameters of the reflection in the vicinity of 44° are nearly independent of the grain sizes; thus, it should be interpreted as the type (111) reflection and be related to other structural fragments, more precisely, to the deformed diamond-like clusters with the atom coordination almost corresponding to the tetrahedral one. Needless to say, we also do not rule out the contribution of (100) type reflections from large graphite-like clusters to the reflection at ~44°, which is more important for coarse-grained powders.

3.2. Small-Angle X-ray Scattering

In Fig. 2, the experimental curves of the small-angle X-ray scattering $I(s)$ ($s = 4\pi\sin\theta/\lambda$) are shown on the log–log scale for the same powders of nanoporous carbon. By processing these curves according to the Guinier model for polydisperse systems, we obtained the approximate distribution functions for scattering inhomogeneities with respect to the inertia radii $m(R_g)$ (Fig. 3); the Guinier model has been previously applied to the bulk samples [3]. The function $m(R_g)$ specifies the ratio between the volumes occupied by inhomogeneities with different sizes ($\sim 2R_g$). As it follows from the shape of the curves of the small-angle X-ray scattering (Fig. 2) and from the form of the distribution functions $m(R_g)$ (Fig. 3), two subsystems of inhomogeneities (the small-scale inhomogeneities with $R_g < 20$ Å and the large-scale inhomogeneities with $R_g > 20$ Å) can be distinguished in a system of structural inhomogeneities in all the powders; the former occupies a much larger fraction of the volume than the latter. A similar situation also takes place in the bulk material [3]. At the same time, it can be seen from Fig. 3 that the typical sizes of small-scale inhomogeneities decrease as the grain sizes decrease: the distribution $m(R_g)$ narrows, whereas the peak R_g^{max} shifts to smaller R_g (see table). In addition, as the grain sizes decrease, the fraction of the small-scale inhomogeneities increases compared to

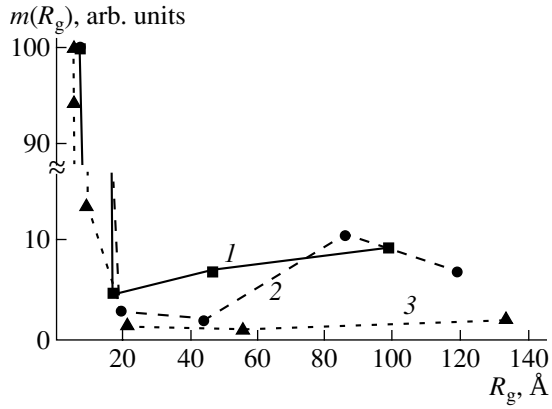

Fig. 3. The distribution functions for nanoinhomogeneities in reference to the inertia radii $m(R_g)$ on the basis of the data of the small-angle X-ray scattering for nanoporous carbon powders obtained from α-SiC of fractions (*1*) F20, (*2*) F80, and (*3*) F600. The grain sizes *D* were equal to (*1*) 800–1000, (*2*) 180–200, and (*3*) 8–10 μm.

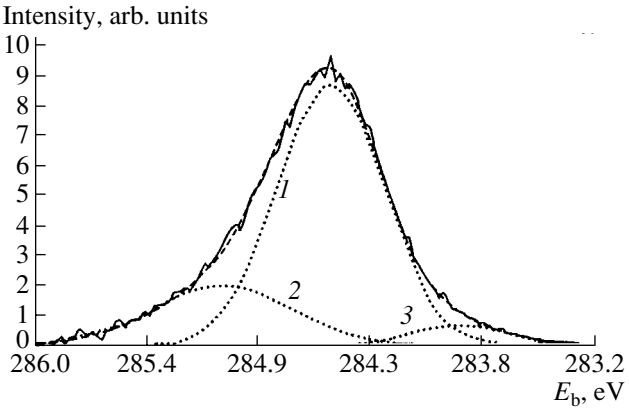

Fig. 4. Photoelectron spectrum of 1*s* states of carbon atoms in a nanoporous carbon powder obtained from α-SiC powder with the grain size of 800–1000 μm (F20) (the solid line). Decomposition of the line into components *1*, *2*, and *3* corresponding to different coordination (different type of hybridization of the valence bonds) of carbon atoms and the sum of these components (the dashed lines) are shown.

that of the large-scale inhomogeneities. Thus, in powders F20 and F80, scattering fragments with R_g = 80–90 Å amount to approximately 10% of the volume occupied by the fragments with the most probable R_g^{max}, whereas this fraction is less than 2% in powder F600 (Fig. 3). Thus, the results of the small-angle X-ray scattering qualitatively agree with the data obtained by X-ray diffraction.

3.3. X-ray Photoelectron Spectroscopy

According to the full-range XPS spectra measured in the binding-energy range of E_b = 0–1000 eV using the MgK_α radiation, the carbon content in the powders under study is no higher than 98 at. %. About 1 at. % of oxygen was detected; this oxygen forms double or bridge bonds with carbon and is also contained in adsorbed water or in the carbon-linked hydroxyl group OH.

Careful studies of the intense 1*s* line of carbon showed that nanoporous carbon powders differ slightly from one another in the position and shape of this line. As is the case with compacted samples [5], the line is broad and its position yields the binding energy E_b, which is intermediate between the values of 284.3 and 285.0 eV corresponding to graphite and diamond with the sp^2 and sp^3 hybridizations of the valence bonds, respectively (see table). As an example, Fig. 4 shows the C 1*s* spectrum of powder F20. Assuming that the broadening is inhomogeneous, we decomposed this spectrum into components, which made it possible to determine the partial contributions of carbon atoms with a different hybridization of bonds or, in other words, with a different coordination of the short-range order. The results of such a procedure for all the samples (namely, the binding energies for 1*s* states of carbon atoms E_b^i in the *i*th structural configuration and the fraction of atoms in this configuration S^i) are also listed in the table. It can be seen from the table that at least two-thirds of carbon atoms in the 1*s* state and *i* = 1 configuration have the binding energy E_b^1, which is slightly higher than that in the trigonal coordination of ideal graphene layer but substantially lower than that in tetrahedrally coordinated diamond. This means that, for the structural configuration under consideration, the σ states (of the sp^2 type) and the π states (of the *p* type) of the valence electrons are partially mixed, so that their hybridization corresponds to the sp^{2+x} and s^yp types. As it was discussed for the bulk nanoporous carbon [5], the parameters of rehybridization $x < 1$ and $y < 1/3$ describe the local curvature of the surface in which the atom's σ bonds in the configuration under consideration lie [7]. For example, according to theoretical estimates, we have $x = 0.278$ and $y = 0.081$ or 0.085 for C_{60} fullerene [7]; the experimental value of E_b is ~284.7 eV for this fullerene [8].

It can be seen from the table that, as the grain size in the powder decreases, the value of E_b^1 approaches that for graphite, which at first glance contradicts the aforementioned data obtained by the X-ray diffraction and small-angle X-ray scattering. In fact, a decrease in the curvature of graphene-like layers in a sequence of the F20, F80, and F600 powders, which follows from the XPS data, is accompanied by a decrease in the sizes of graphite-like nanoclusters (according to the data obtained by the X-ray diffraction) rather than by an increase of these sizes. However, it must be recalled that the estimates based on the X-ray diffraction data refer to the thickness of graphite-like clusters $L_\perp$ in the direction perpendicular to the layer planes rather than to the extent $L_\parallel$ of the layers themselves. Nevertheless,

The structure parameters of nanoporous carbon powders with different degrees of dispersion

The powder type		F20	F80	F600
D, μm		800–1000	180–200	8–10
$L_\perp$, Å		450	80	–
R_g^{max}, Å		5.7	5.6	4.6
E_b, eV		284.56	284.51	284.42
$i = 1$	E_b^1, eV/S^1, at. %	284.52/73.58	284.47/65.79	284.43/74.68
$i = 2$	E_b^2, eV/S^2, at. %	285.06/21.70	284.95/30.26	284.97/20.89
$i = 3$	E_b^3, eV/S^3, at. %	283.87/4.72	283.81/3.95	283.73/4.43

it is reasonable to expect that the dimensions $L_\perp$ and $L_\parallel$ correlate with each other and that very small nanoclusters are indeed predominant in the most disperse F600 powder. In this context, the structure of these nanoclusters may be conceived as consisting of "broken" and almost flat graphene-like formations or their small fragments with the graphite-like 3-coordinated nearest neighbors of inner atoms. For example, such structures exist in the so-called "rigid" (ungraphitizable) carbon [9]. The above reasoning is qualitatively corroborated by a decrease in the fraction of the large-scale inhomogeneities in reference to that of the small-scale inhomogeneities, which was observed by small-angle X-ray scattering in a sequence of the F20, F80, and F600 powders. However, this corroboration is indirect because the data of small-angle X-ray spectroscopy may refer to nanopores rather than to graphite-like nanoclusters.

In the C 1*s* spectra of all the powders under consideration, there is a fairly intense component corresponding to the binding energy E_b^2, which nearly coincides with that for tetrahedrally (sp^3) coordinated carbon. However, one cannot draw an unambiguous inference about the presence of diamond-like clusters in the structure of powders on the basis of the above data, because carbon atoms in hydrocarbons (most likely adsorbed at the surface of nanoporous carbon grains from atmosphere) have virtually the same binding energy. Using the aforementioned results of X-ray diffraction and taking into account a fairly high content (20–30 at. %) of carbon atoms with sp^3-hybridized bonds (see table), we may assume that diamond-like fragments do exist in the structure of the powders under consideration. Evidence for tetrahedral structures in nanoporous carbon has recently been obtained by studying the Raman spectra of compacted samples [6].

4. CONCLUSION

Thus, the size of grains in the powder of the starting silicon carbide noticeably affects both the degree of graphitization of carbon skeleton in nanoporous carbon and the ratio between the numbers of small and large nanoclusters (possibly, between the contents of small and large nanopores). In our opinion, this effect of the grain sizes is caused by an enhanced content of macrodefects and an increased surface-to-volume ratio in the fine-grained α-SiC powder compared to those in the coarse-grained powder, which, in turn, are related to the procedure of mechanical grinding of the crystals grown. The coarse α-SiC grains have a more perfect structure of crystalline carbon planes (0001), which is conducive to partial preservation of preferential orientation of the (0002) layers parallel to the initial (0001) planes in nanoporous carbon subjected to carbonization; this was established for nanoporous carbon obtained from a 6*H*-SiC single crystal [3]. In addition, due to the smaller surface-to-volume ratio, the carbonization rate for coarse-grained powders is much lower than that for fine-grained powders; as a result, larger graphite-like fragments may form with a higher probability during the reaction. Gross structural imperfections in fine-grained starting α-SiC powders present an obstacle both to growth and the correlated arrangement of large graphene-like layers in the forming nanoporous carbon even if the samples are kept at a high temperature for a long time in the reactor; still, due to the latter procedure, the structure corresponding to the short-range order approaches that of graphite for most ($\gtrsim$65 at. %) of carbon atoms. The considered special structural features of the carbon skeleton should manifest themselves in the bulk material obtained from the α-SiC powders with different degrees of dispersion. In particular, the large graphite-like clusters with bended graphene-like layers in compacted samples that were studied previously [2–6] and contained pyrolytic carbon may constitute structural elements not only of pyrolytic carbon inclusions but also of nanoporous framework itself.

ACKNOWLEDGMENTS

This study was supported by the Russian Foundation for Basic Research (project no. 99-02-17984), the

Ministry of Science of the Russian Federation (Program "Fullerenes and Atomic Clusters," subprogram "Plenka-2"), and AOZT "Karbid" (St. Petersburg). We thank the "Skeleton Technologies Group" (Sweden) for support and making available to us the silicon carbide powders. We are indebted to Yu.A. Kukushkina for chlorination of the samples.

REFERENCES

1. S. K. Gordeev and A. V. Vartanova, Zh. Prikl. Khim. (St. Petersburg) **66** (7), 1080 (1994); **66** (9), 375 (1994).
2. S. K. Gordeev, A. V. Vartanova, S. G. Zhukov, I. N. Gran', V. V. Sokolov, T. I. Mazaeva, and R. G. Avarbe, RF Patent No. 2026735, Byull. No. 2 (1995).
3. R. N. Kyutt, É. A. Smorgonskaya, S. K. Gordeev, *et al.*, Fiz. Tverd. Tela (St. Petersburg) **41** (5), 891 (1999) [Phys. Solid State **41**, 808 (1999)]; Fiz. Tverd. Tela (St. Petersburg) **41** (8), 1484 (1999) [Phys. Solid State **41**, 1359 (1999)].
4. É. A. Smorgonskaya, R. N. Kyutt, S. K. Gordeev, *et al.*, Fiz. Tverd. Tela (St. Petersburg) **42** (6), 1141 (2000) [Phys. Solid State **42**, 1176 (2000)].
5. S. K. Gordeev, A. V. Grechinskaya, A. M. Danishevskiĭ, *et al.*, in *Abstracts of the 4th Biennial International Workshop "Fullerenes and Atomic Clusters", IWFACT99, St. Petersburg, 1999*; Mol. Mater. **13**, 355 (2000).
6. A. M. Danishevskiĭ, É. A. Smorgonskaya, S. K. Gordeev, and A. V. Grechinskaya, Fiz. Tverd. Tela (St. Petersburg) **43** (1), 130 (2001) [Phys. Solid State **43**, 137 (2001)].
7. R. C. Haddon, Philos. Trans. R. Soc. London, Ser. A **343** (1667), 53 (1993).
8. M. A. Khodorkovskii, A. L. Sakhmin, and N. B. Leonov, Fiz. Tverd. Tela (St. Petersburg) **36**, 626 (1994) [Phys. Solid State **36** (3), 345 (1994)].
9. E. Buiel and J. R. Dahn, Electrochim. Acta **45**, 121 (1999).

Translated by A. Spitsyn

Semiconductors, Vol. 35, No. 6, 2001, pp. 666–668. Translated from Fizika i Tekhnika Poluprovodnikov, Vol. 35, No. 6, 2001, pp. 695–697.

II INTERNATIONAL CONFERENCE ON AMORPHOUS AND MICROCRYSTALLINE SEMICONDUCTORS

Effective Control over the Photoelectric Properties of Triphenylamine-containing Polyimides

L. P. Kazakova*,[1], E. L. Aleksandrova, and A. V. Chernyshev***

** Ioffe Physicotechnical Institute, Russian Academy of Sciences, Politekhnicheskaya ul. 26, St. Petersburg, 194021 Russia*

*** Vavilov State Optical Institute, All-Russia Scientific Center, St. Petersburg, 199034 Russia*

[1] e-mail: kazakova@pop.ioffe.rssi.ru

Submitted November 9, 2000; accepted for publication November 15, 2000

Abstract—Photoconductivity, the quantum yield of photogeneration, and carrier drift mobility have been studied in electric fields $F = (0.1–10) \times 10^5$ V/cm in thin films of polyimide organic semiconductors, both unsensitized and sensitized with a dye. The introduction of dye leads to a substantial increase in photoconductivity (by 2–3 orders of magnitude) and in the drift mobilities of holes and electrons. The electron mobility grows to its maximum extent, becoming as high as $\sim 10^{-3}$ cm^2/(V s) at room temperature and at $F \approx 10^4$ V/cm. © *2001 MAIK "Nauka/Interperiodica".*

Despite the progress in developing light-emitting diodes based on organic polymeric semiconductors, research is continuing into new materials of this kind, which possess high thermal stability, for use as both emitting and transport layers. The choice of material with high electron and hole mobilities is not sufficiently wide. In this context, a search for a means of controlling the carrier mobility in organic polymers is a topical task. Research into materials exhibiting high photosensitivity is also of much interest.

This study is concerned with the drift mobility, photoconductivity, and quantum yield of carrier photogeneration in thin layers of organic materials based on polyimides (PI). Triphenylamine (TPA) molecules were used as donor fragments of the polyimide monomer unit [1]. Sensitization was done with a dye of the triphenylmethane class, Malachite Green (MG), used in 1% concentration, having maximum spectral sensitivity at 647 nm. Polymide layers were deposited by the "hanging meniscus" method or by centrifugation from a 6.5% solution in tetrachloroethane onto glass substrates with an electrically conducting In_2O_3 or SnO_2 coating serving as a bottom electrode. The layer thickness was $L = 0.2–3$ μm.

Drift mobility was studied in samples with a "sandwich" structure by the time-of-flight technique [2, 3]. Semitransparent aluminum film deposited onto the PI layers by vacuum evaporation served as the top electrode. Excess carrier concentration in a sample was created by a light pulse (wavelength 0.337 μm, pulse duration ~8 ns) generated by an LGI-21 nitrogen laser. A voltage pulse of length ~1 ms was applied to the samples. Depending on the polarity of the applied voltage, electrons or holes moved in the sample. The measurements were carried out under minor charge drift conditions in electric fields $F = (0.1–2) \times 10^5$ V/cm.

The quantum yield of photogeneration was measured by a method described in [4] in the electrographic mode in the spectral region of the highest photosensitivity at $F = (1–10) \times 10^5$ V/cm. A drop of mercury was used as the second electrode in the photoconductivity measurements.

The investigations performed demonstrated that the introduction of a sensitizing agent reduced the sample resistance by two orders of magnitude [from $\sim 10^9$ to $\sim 10^7$ Ω at top electrode area of $(3–5) \times 10^{-2}$ cm^2]. As can be seen from Fig. 1, the photoconductivity of PI layers increases by 2–3 orders of magnitude on sensitization with a dye. In this case, the quantum yield η of photogeneration changed by no more than an order of magnitude and reached a value of $\sim 10^{-1}$ at $F \approx 10^6$ V/cm.

Drift mobility measurements revealed that only hole drift is observed in unsensitized films, whereas in films sensitized with a dye both holes and electrons are mobile carriers. The drift mobility was determined from the time of carrier flight through the sample (t_T) using the formula: $\mu = L/t_T F$. The time t_T was found from transient photocurrent oscillograms $I(t)$ corresponding to electron or hole drift. Oscillograms $I(t)$ taken for films with and without dye exhibited a constant-current portion ("plateau") followed by gradual current decay over time. The instant of time corresponding to the transition from the "plateau" to further decay of $I(t)$ was taken to be the time t_T.

It should be noted that the presence of the "plateau" in the $I(t)$ curves indicates the nondispersive nature of the transport. At the same time, the prolonged current decay at $t > t_T$ points to the strong spatial spreading of the carrier packet, characteristic of dispersive transport. Such $I(t)$ dependences have been observed previously

in a number of chalcogenide glassy semiconductors [3, 5]. The observed behavior has been attributed to specific features of the energy spectrum of localized states controlling the drift mobility [6] or to a mobility distribution of carriers, resulting from the existence of inhomogeneities in the films [7]. It is quite probable that the films under study also have inhomogeneities whose appearance may be associated with the technology of their fabrication, which, e.g., involves sample heating to remove the solvent.

The investigations performed demonstrated that the introduction of a sensitizing agent makes the drift mobilities of both holes and electrons higher (Fig. 2), with the increase being the most pronounced for electrons. At room temperature and electric field strength $F = 2 \times 10^4$ V/cm the drift mobility of holes in unsensitized PI films was about 1.5×10^{-4} cm^2/(V s); the drift mobilities of electrons and holes in sensitized films were ~1.6×10^{-3} and ~4×10^{-4} cm^2/(V s), respectively. The carrier drift mobility became higher with increasing electric field strength. Figure 2 presents in the coordinates $\log\mu = f(F^{0.5})$ the dependences of the drift mobility on the electric field strength, taken for holes (curves *1* and *2*) and electrons (curve *3*) in the films under study. It can be seen that the dependence $\mu(F)$ is stronger in sensitized samples. An approximation of the $\mu(F)$ dependence for dye-free films at electric fields $F > 10^5$ V/cm by the Poole–Frenkel law gave a coefficient $\beta = 3.5 \times 10^{-4}$ eV(V/cm)$^{-0.5}$ virtually coinciding with the value characteristic of anthracene-based PI [8]. However, the carrier drift mobilities in these materials were much lower (by approximately 2 or 3 orders of magnitude), compared with the PI with TPA obtained in this study. As is known [9], monomer units of PI are donor–acceptor complexes. In this case, TPA molecules having the lowest ionization potentials $I_D = 6.9$ eV among aromatic compounds [10] act as donor fragments, and dyimide fragments (-O-) with electron affinity $A_A = 1.12$ eV [9] act as acceptors. The introduction of MG dye leads to the appearance, in addition, of acceptor fragments ClO_4^- with $A_A = 1.6$ eV and donor fragments with $I_D = 6.7$ eV [10]. The fact that PI with TPA is characterized by higher drift mobilities than anthracene-based PI [8] is in agreement with the data indicating that transport characteristics are improved on addition of TPA to PI [9]. Since the carrier mobility in PI may be governed by hopping via donor and acceptor fragments of the molecules, it is quite possible that the appearance of additional donor and acceptor fragments on introducing the MG dye into PI leads to a higher hopping probability and, consequently, to higher drift mobilities of electrons and holes.

Thus, the study performed revealed the following:

(1) The hole drift mobility in polyimide films with triphenylamine is ~10^{-4} cm^2/(V s) in an electric field $F \approx 10^4$ V/cm at temperature $T \approx 300$ K.

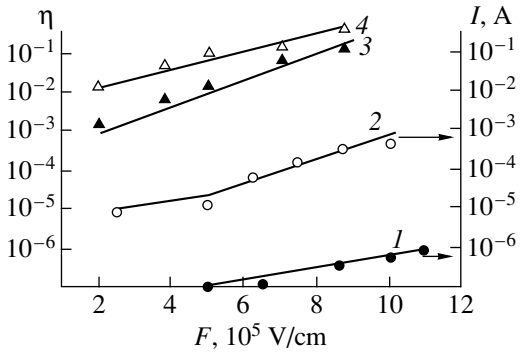

Fig. 1. Photocurrent (*1*, *2*) and quantum yield of photogeneration (*3*, *4*) vs. electric field strength for PI + TPA films without (*1*, *3*) and with (*2*, *4*) Malachite Green dye.

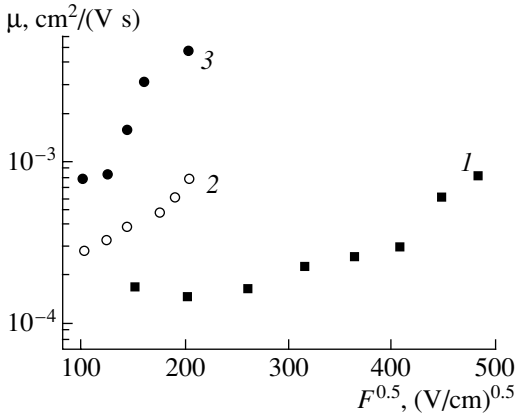

Fig. 2. Drift mobilities of holes (*1*, *2*) and electrons (*3*) vs. electric field strength in PI + TPA films without (*1*) and with (*2*, *3*) Malachite Green dye; $T \approx 300$ K.

(2) Film sensitization with Malachite Green dye makes both the electron and the hole drift mobilities higher, with the increase in electron mobility to ~10^{-3} cm^2/(V s) at $F \approx 10^4$ V/cm and $T \approx 300$ K being the most pronounced.

(3) The photoconductivity and conductivity of the films increase by two orders of magnitude upon sensitization.

The results obtained demonstrate that dye introduction allows effective control over the electrical properties of the films, improving the transport and photoelectric properties of polyimide-based polymers. This indicates that these polymers show promise as transport layers in polymeric light-sensitive and light-emitting devices.

ACKNOWLEDGMENTS

We thank N.A. Vasilenko and B.V. Kotov for providing us with PI samples, K.D. Tsendin for his helpful participation in discussions, É.A. Lebedev for his

encouragement, and E.K. Kuznetsova and P.S. Yakovlev for their assistance in the experiments.

REFERENCES

1. N. A. Vasilenko, G. A. Rybalko, and B. V. Kotov, in *Proceedings of the III All-Union Conference "Nonsilverhalide and Unusual Photoprocesses. Electrophotography", Vilnius, 1980*, p. 59.
2. W. E. Spear, J. Non-Cryst. Solids **1**, 197 (1969).
3. L. P. Kazakova, B. T. Kolomiets, É. A. Lebedev, and S. A. Tauraĭtene, Fiz. Tekh. Poluprovodn. (Leningrad) **21**, 274 (1987) [Sov. Phys. Semicond. **21**, 166 (1987)].
4. E. L. Aleksandrova and Yu. A. Cherkasov, Opt. Spektrosk. **64** (5), 1047 (1988) [Opt. Spectrosc. **64**, 624 (1988)].
5. É. A. Lebedev and L. P. Kazakova, in *Electron Phenomena in Chalcogenide Vitreous Semiconductors*, Ed. by K. D. Tséndin (Nauka, St. Petersburg, 1996), Chap. 4, p. 141.
6. V. I. Arkhipov, L. P. Kazakova, É. A. Lebedev, and A. I. Rudenko, Fiz. Tekh. Poluprovodn. (Leningrad) **21** (4), 724 (1987) [Sov. Phys. Semicond. **21**, 442 (1987)].
7. V. I. Arkhipov, É. A. Lebedev, and A. I. Rudenko, Fiz. Tekh. Poluprovodn. (Leningrad) **15** (4), 712 (1981) [Sov. Phys. Semicond. **15**, 405 (1981)].
8. A. R. Tameev, V. I. Berendyaev, A. A. Kozlov, *et al.*, Zh. Nauchn. Prikl. Fotogr. **42** (2), 3842 (1997).
9. B. M. Rumyantsev, V. I. Berendyaev, N. A. Vasilenko, and B. V. Kotov, Vysokomol. Soedin., Ser. A **39** (4), 720 (1997).
10. L. V. Gurvich, G. V. Karachevtsev, and V. N. Kondrat'ev, *Energy of Chemical Bond Breakage, Ionization Potentials and Electron Affinity* (Nauka, Moscow, 1974).

Translated by M. Tagirdzhanov

Semiconductors, Vol. 35, No. 6, 2001, pp. 669–673. Translated from Fizika i Tekhnika Poluprovodnikov, Vol. 35, No. 6, 2001, pp. 698–702.

II INTERNATIONAL CONFERENCE ON AMORPHOUS AND MICROCRYSTALLINE SEMICONDUCTORS

Low-Temperature Plasma-Enhanced Chemical Vapor Deposition of Carbon Films and Their Emission Properties

A. Ya. Vinogradov*,[1], A. N. Andronov, A. I. Kosarev*, and A. S. Abramov***

** Ioffe Physicotechnical Institute, Russian Academy of Sciences, Politekhnicheskaya ul. 26, St. Petersburg, 194021 Russia*

[1] e-mail: vinogradov@aik.ioffe.rssi.ru

*** St. Petersburg State Technical University, ul. Politekhnicheskaya 29, St. Petersburg, 195251 Russia*

Submitted November 9, 2000; accepted for publication November 15, 2000

Abstract—Carbon films prepared by the plasma-enhanced chemical gas deposition from a mixture of hydrogen and hexane vapor at a substrate temperature of 150–200°C on silicon tip emitters and flat substrates were investigated. Coatings improving the emission efficiency of tip and flat emitters were deposited under various conditions of hydrogen-plasma etching of a growing film. The films deposited on flat substrates and tip emitters had a high optical transparency; a low electrical conductivity; and a polymer-like structure with a high concentration of the C–C sp^2 bonds differ in electronic structures, carbon-atom surroundings in the lattice, microdensity, and hydrogen content in the film. *© 2001 MAIK "Nauka/Interperiodica".*

INTRODUCTION

Carbon coatings including those produced at temperatures lower than 300°C can be deposited onto the tip field emitters [1]. In this case, the emission current increases and the threshold electric-field strength at the onset of emission decreases. Furthermore, such films are widely investigated as a material potentially feasible for fabricating flat field emitters [2]. It was noted that the coatings enhancing the emission current and reducing the threshold voltage at the onset of emission of tip emitters and the films on flat substrates having a large number of emission centers require different conditions of deposition and, as a consequence, are likely different in composition and structure.

This study is devoted to investigating the features of the process of growth and etching of carbon films at low substrate temperatures and also to studying the distinctions in composition and structure of materials deposited on tip emitters and flat substrates.

EXPERIMENTAL

The carbon films were prepared by high-frequency (56 MHz) plasma-enhanced chemical deposition from a mixture of hydrogen (H_2) and hexane (C_6H_{14}) vapor on flat *p*-Si crystalline substrates at 150–250°C. The film thickness was measured with a laser interferometer during film growth or etching. In the same setup, we carried out the experiments aimed at clarifying the laws of the process of low-temperature deposition of carbon films.

The structure of films was investigated by the infrared (IR) and Auger spectroscopy as well as by the electron characteristic energy loss (ECEL) spectroscopy.

The emission properties of samples were characterized by the integral current–voltage (*I–V*) characteristics recalculated into dependences of the emission-current density *J* on the electric-field strength *F* and by the emission-center distribution measured in a diode-type system. The emission efficiency was estimated from the values of emission current and threshold field at the onset of emission as well as from the distribution uniformity and density of emitting centers over the emitter surface.

RESULTS

When depositing carbon coatings, we varied the working-mixture composition, the procedure of pretreatment of substrates, and technological parameters of the coating-deposition process. The most important of these parameters turned out to be the high-frequency (HF) power and the substrate temperature. Therewith, it was noted that the parameters of the process of depositing carbon coatings enhancing the emission current and reducing the threshold voltage at the onset of emission for tip emitters [1] differ from the parameters of depositing the carbon films on a flat substrate because these films showed a large number of emission centers.

Moreover, it was noted that the rate of deposition of a carbon film increases with an HF power and depends only slightly on the substrate temperature but falls abruptly to zero above a certain critical temperature. Such a behavior of the film-deposition rate was observed in the case of depositing carbon films on sili-

1063-7826/01/3506-0669$21.00 © 2001 MAIK "Nauka/Interperiodica"

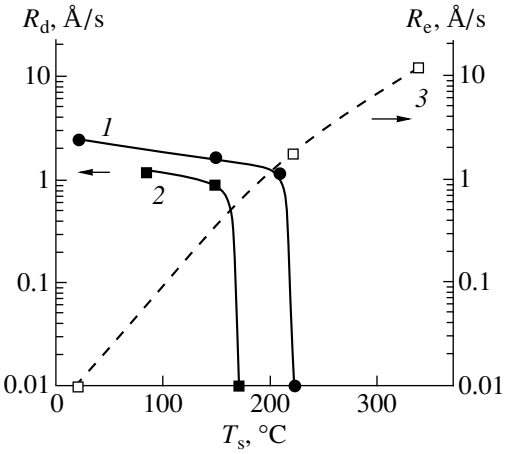

Fig. 1. Dependences of a deposition rate (R_d) and an etching rate (R_e) of a carbon film on the substrate temperature (T_s). (*1*) deposition from C_6H_{14}; (*2*) deposition from a mixture of 7%C_6H_{14} and 93%H_2; and (*3*) etching in H_2.

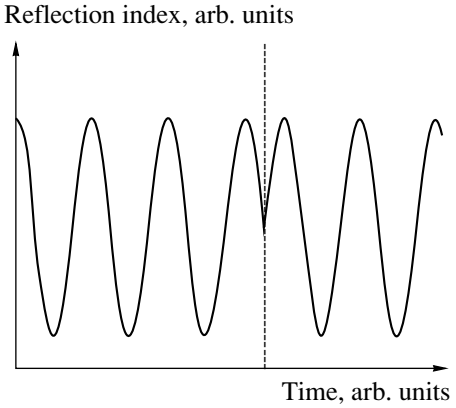

Fig. 2. Interferogram with changing the deposition of a film (to the left of the dotted line) to etching (to the right of the dotted line).

con, ceramic, and metal substrates at frequencies of 13.56 and 56 MHz using a mixture of methane with argon, hexane vapor, and their mixtures with hydrogen. However, we encountered no published data on the existence of a critical temperature for deposition of carbon films, i.e., the temperature above which the film deposition ceases.

In Fig. 1, we display the carbon-film-deposition rate (R_d) and its hydrogen-plasma etching rate (R_e) as functions of a substrate temperature (T_s). The etching was performed under conditions close to those of film deposition: a frequency f = 56 MHz, a working-mixture flow Q = 25 sccm, a reactor pressure P = 30 mTorr, and an HF power W = 50 W.

As can be seen from Fig. 1, the hydrogen-plasma etching rate of a growing film begins to exceed the deposition rate at a temperature $T_s \approx 200$°C in the case of depositing a film from hexane vapor and at a temperature $T_s \approx 150$°C in the case of depositing from a mixture of 7%C_6H_{14} and 93%H_2. In fact, a change of interferogram-sweep run to the reversed one (see Fig. 2) proves that, at substrate temperatures above the critical one, the film deposition changes to the etching with hydrogen even for depositing a film from hexane vapor undiluted with hydrogen. In the last case, the amount of hydrogen produced as a result of dissociation of hexane molecules turns out to be sufficient for an efficient etching of the carbon film.

A hydrogen-plasma etching rate of a carbon film is negligible at room temperature and grows with the substrate temperature. For this reason, we may assume that the carbon films deposited at high temperatures (close to the critical one) are etched more efficiently by hydrogen radicals during growth than the films grown at lower temperatures. The films deposited at room temperature or close to it undergo no etching during their growth.

Previously, we showed in study [1] the following.

(1) The coatings enhancing the emission current and reducing the threshold voltage at the onset of emission from tip emitters require deposition conditions providing an efficient hydrogen etching of the film during its growth; i.e., the films are deposited at substrate temperatures close to the critical one. Moreover, a pretreatment of a tip emitter is necessary; this treatment consists in the hydrogen-plasma etching with subsequent treatment in the hexane plasma heavily diluted with hydrogen at a constant positive bias at the HF electrode.

(2) The coatings providing an improvement in the tip-emitter efficiency are not continuous; rather, they are flakelike (type 1 at the photograph in [1]).

(3) A continuous smooth coating (type 2 at the photograph in [1]) deposited under the conditions providing a moderate etching of a growing film (the substrate temperature is below the critical one and no pretreatment of the substrates is used) does not improve the emission properties of the tip emitter.

Later [2], we showed that carbon coatings of type 1 deposited on flat silicon substrates manifested the presence of field emission with the following parameters: an emission-current density of up to 1 mA/cm^2 and a threshold electric-field strength lower than 1 V/μm. The emission was of a pronounced activation type (it manifested itself and became stable after the multiple application of an electric field). In this case, the number of emission centers was extremely small (a few individual spots). The films of type 1 had an optical transparency of 93%, an electrical conductivity of 10^{-12}–10^{-14} Ω^{-1} cm^{-1} at 400°C, and an electrical-conductivity activation energy of 1.2–1.6 eV.

The investigation of a surface of films using Auger spectroscopy (Fig. 3a) revealed a small Auger-peak shift for a film material (curve *1*) to higher energies from the graphite peak (curve *3*), although the shapes of

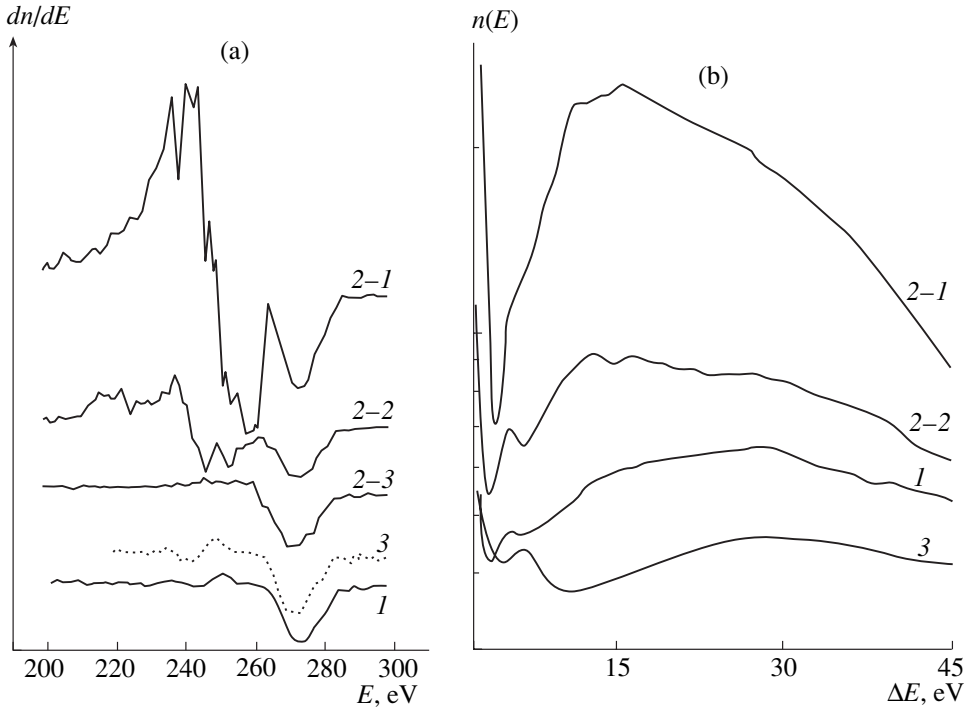

Fig. 3. (a) Auger spectra and (b) ECEL spectra at the primary-beam energy of 125 eV: (*1*) film of type 1; (*2–1*) film of type 2 in the region of a maximum emission-center concentration; (*2–2*) film of type 2 in the region with a moderate emission-center concentration; (*2–3*) film of type 2 in the region without emission centers; and (*3*) graphite. ΔE is the electron energy loss.

these peaks are similar. The ECEL spectroscopy showed the peaks at 284 and 291 eV shifted compared with the graphite peaks (283 and 289 eV) in the film-material spectra. Thus, the shape of the ECEL spectrum of the carbon films, like the Auger spectrum, turned out to be close to the graphite spectrum but shifted approximately by 1 eV to higher energies. The similar shift in the binding energy for the 1s level of carbon was observed, for example, in the C_2H_4 and C_2H_2 molecules [3]. We believe that an ECEL-peak shift for carbon films is caused by the presence of a significant quantity of hydrogen chemically bonded with the lattice. According to the IR-spectroscopy data, its concentration in the films under investigation is equal to [H] $\approx 1 \times 10^{23}$ cm^{-3}.

From the ECEL spectra in the energy range of 5–50 eV (Fig. 3b), we determined the plasmon energy $\hbar\omega_p$, the valence-electron concentration n, and the microdensity ρ of the carbon films. The values of these parameters for the films under investigation and for diamond and graphite are listed in the table. On the basis of the data on the microdensity and surface carbon concentration, we estimated the hydrogen content on the surface of the films as 65–70 at. %.

The similarity of the Auger spectra to the ECEL spectra, and the material characteristics determined from the low-energy region of the ECEL spectra for the films under investigation and graphite, along with the optical and electrical properties of the films, can be explained by the fact that the films have a polymer-like structure with a high concentration of the C–C sp^2 bonds.

The deposition of carbon films on flat silicon substrates at temperatures below the critical one (under conditions of a moderate etching of the growing film by hydrogen that are identical to the conditions of depositing a continuous smooth coating on a tip emitter) resulted in obtaining flat emitters of type 2 for which high emission-current densities (up to 10 mA/cm^2) and a much larger number of emission centers (up to 10^3 cm^{-2}) compared to the films of type 1 were observed. In this case, the appearance of the region of a uniform distribution of emission centers was accompanied by an emission-current jumplike increase by several orders of magnitude, which can be seen from the shape of curve *1* in Fig. 4, and by a short-time increase in pressure in the measurement chamber. The distribution of emission centers at the film of type 2 is shown in Fig. 5.

Plasmon energy $\hbar\omega_p$, the valence-electron concentration n, and the microdensity ρ of carbon films under investigation, diamond, and graphite

Material	$\hbar\omega_p$, eV	n, 10^{23} cm^{-3}	ρ, g/cm^3
Carbon films	28.5	5.8	2.73
Diamond [4]	34.5	8.6	4.3
Graphite	26	5.3	2.63

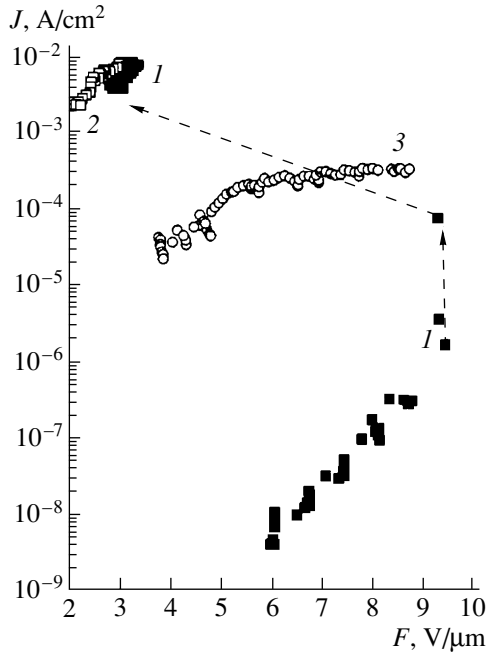

Fig. 4. Emission characteristics of carbon films deposited on flat substrates under conditions of a moderate hydrogen etching: (*1*) film of type 2 with increased electric field; (*2*) film of type 2 with reduced electric field, and (*3*) film of type 3.

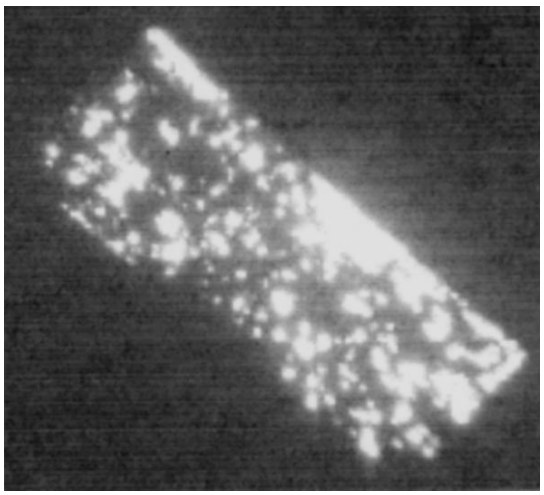

Fig. 5. Distribution of emission centers over the films of type 2 at E = 2 kV/200 μm.

A decrease in a thickness of the film deposited under moderate-etching conditions made it possible to obtain the samples of type 3 differing from the above-described by the fact that the same uniform distribution of the emission centers was attained without jumps in current and pressure for current densities of ~0.3 mA/cm^2.

The dependences of the emission-current density on an electric-field strength for the carbon films deposited onto flat substrates under conditions of moderate hydrogen etching of growing films (types 2 and 3) are shown in Fig. 4.

The films of types 2 and 3 had the same optical transparency as the films of type 1 and even higher resistivity. According to the data of Auger spectroscopy and ECEL spectroscopy shown in Fig. 3, films 2 and 3 (like film 1) had a polymer-like structure with a high concentration of the sp^2 bonds in the atomic carbon lattice. However, the shape of Auger spectra and ECEL spectra for these films (curves *2–1*) differed significantly from those for the films of type 1 (curves *1*).

The distinction of the Auger spectra of the films of type 2 from the spectra of the films of type 1 consists in the presence of additional peaks in the region of 200–250 eV, which, as we assume, is indicative of a different electron structure and a change in the surroundings of carbon-lattice atoms, for example, due to an increase in the hydrogen amount. A distinction of the ECEL spectra of the films of type 2 from those of the films of type 1 consists in a large shift of the peak to lower energies, which means that the microdensity decreases and the hydrogen concentration possibly increases in the film.

A noticeable distinction is observed between the Auger spectra and the ECEL spectra for the films of type 2 measured in the region of a maximum emission-center concentration (curves *2–1*), in the region with a moderate emission-center concentration (curves *2–2*), and in the region without emission centers (curves *2–3*). The Auger spectra and the ECEL spectra measured in the region of the highest emission-center concentration differ most markedly from the graphite spectra (curves *3*), while the spectra measured in the region without emission centers repeat the shape of the graphite spectra.

The question about what structural and chemical modifications in the film material lead to such changes in the Auger spectra and ECEL spectra can be conclusively answered only after additional investigations.

CONCLUSION

(i) The behavior of the growth rate for a carbon film at low substrate temperatures indicates that the hydrogen-plasma etching of a growing carbon film is an important factor determining the process of depositing the film at a low substrate temperature.

(ii) Conditions for obtaining carbon films enhancing the emission efficiency are different for tip emitters and flat coatings. The tip-emitter coatings were deposited under conditions providing an efficient etching of a growing film with hydrogen, while the coatings on flat substrates were deposited under conditions of moderate etching.

(iii) All the obtained carbon films had a high optical transparency, a low electrical conductivity, and their

Auger spectra and ECEL spectra were similar to those of graphite. This fact enables us to conclude that the film material has a polymer-like structure with a high concentration of the C–C sp^2 bonds.

(iv) A distinction of the films on flat substrates with a high number of emission centers from the films enhancing the emission efficiency of tip emitters, according to the data of the Auger spectroscopy and the ECEL spectroscopy, are likely caused by the difference in electronic structure, surroundings of carbon atoms in lattice, microdensity, and hydrogen concentration in the film.

(v) A convincing answer to the question as to what structural and chemical modifications in the film material lead to the modifications in the Auger spectra and the ECEL spectra requires additional investigations.

ACKNOWLEDGMENTS

This work was supported by the INTAS, grant no. 97-1754.

REFERENCES

1. A. I. Kosarev, V. V. Zhirnov, A. J. Vinogradov, *et al.*, Mater. Res. Soc. Symp. Proc. **509**, 130 (1998).
2. A. I. Kosarev, A. S. Abramov, A. N. Andronov, *et al.*, in *Proceedings of the 4th International Symposium on Diamond Films and Related Materials, ISDF-4, Kharkov, 1999*, p. 209.
3. D. A. Shirley, Adv. Chem. Phys. **23**, 85 (1973).
4. J. Schäfer, J. Ristein, R. Graupner, *et al.*, Phys. Rev. B **53**, 7762 (1996).

Translated by V. Bukhanov

Semiconductors, Vol. 35, No. 6, 2001, pp. 674–676. Translated from Fizika i Tekhnika Poluprovodnikov, Vol. 35, No. 6, 2001, pp. 703–706.

II INTERNATIONAL CONFERENCE ON AMORPHOUS AND MICROCRYSTALLINE SEMICONDUCTORS

Current Instability in *a*-Si:H Solar Cells after Their Exposure to Light

É. N. Voronkov

Moscow Power Engineering Institute, ul. Krasnokazarmennaya 14, Moscow, 111250 Russia

e-mail: edward@b14s1nt.mpei.ac.ru

Submitted November 9, 2000; accepted for publication November 15, 2000

Abstract—It is shown that the illumination of amorphous silicon solar cells produces changes in dark current. The current relaxation after turning off the light depends on the intensity and duration of the illumination. If the latter is sufficiently long, a current instability occurs, manifesting itself in chaotic oscillations increasing with time and followed by their abrupt disappearance. The observed effect can be explained by assuming that an intense illumination produces changes in the equilibrium among the various types of defects in *a*-Si:H films, and the defects blocking the existing channels of current leakage through the barrier become dominant. In the dark, the equilibrium attained during the illumination is changed, and the blocking defects disappear with time. At the moments when the concentration of these defects becomes close to the values determining the percolation threshold through the channels, chaotic oscillations occur with the amplitude increasing in the vicinity of a threshold value. When the channels are partially or completely recovered, the oscillations disappear. The chaotic behavior of oscillations is explained by the randomness of the processes of variation in the number and the configuration of the channels. *© 2001 MAIK "Nauka/Interperiodica".*

Studies of *a*-Si:H solar cells revealed a change in the magnitude of a dark current after turning off the illumination relative to the current observed prior to illumination. With time, the magnitude of dark current tends to a constant value. The time and the character of the relaxation of a current to a steady-state value depend on the intensity and duration of the illumination. A specific feature of the observed effect is that a certain exposure to light produces a current instability in the form of increasing chaotic oscillations followed by their abrupt disappearance.

The purpose of this study is to explain the observed effect.

Solar cells on a metal foil with an area of 3 cm^2 prepared according to the technology of the ECD firm (Troy, USA) were used as the samples. The characteristics measured under illumination and in the dark were typical for the cells of this type [1], with the efficiency measured with the aid of a solar radiation simulator under the AM1 conditions being equal to 8%. An incandescent lamp with a quartz envelope was used as a light source. The samples were illuminated through a water filter. The illuminance of a sample during the exposure was 5000 lx. The initial illumination was performed on solar cells which had not been previously exposed to intense light.

A circuit for measuring the current from the sample *I* consisted of an operational amplifier, analog-to-digital converter, and a computer. The results of the measurements were accumulated for 300 s as an experimental data array consisting of 6000 points. Then, the array was written to a file, and the accumulation of the data was repeated once again during the next time interval. The time of writing to a file separating the sequence of experimental points did not exceed 5 s. The measurements of a transient process stopped when the current was stabilized around the magnitude existed prior to the illumination.

The results of the measurements are shown in the figure. All measurements were performed in the dark under the forward bias of 0.5 V. Curve *1* represents the change in current *I* with time for the sample that has not been exposed to light. It can be seen that, during the entire period of measurements, the mean value of a current remains constant (we denote it by I_0). The current contains a small noise component.

Curve *2* corresponds to a sample illuminated for two minutes. The illumination causes a slight increase in current without any noticeable increase in the level and change in the character of the noise. With time, the current gradually approaches its initial magnitude.

Curves *3–1* and *3–2* correspond to the samples illuminated for 10 min. These curves are plotted on the basis of two successive samplings: the array of points obtained during the initial 300 s and the array of points obtained during the succeeding 300 s (the time delay between two arrays did not exceed 5 s). The comparison of curve *2* with curves *3–1* and *3–2* shows that, in spite of a seemingly slight increase in exposure, the character of the relaxation of a current to a steady-state value changes markedly. After turning off the illumination, the current initially changes during the first 10 s in the same way as after the illumination for 1 min. Then, it decreases, with the rate of decrease being signifi-

1063-7826/01/3506-0674$21.00

cantly higher than that for curve *2*. When the magnitude of a current becomes lower than I_0, a chaotically oscillating component arises with the amplitude increasing with time. Approximately 200 s (for the second sampling *3–2*) after the illumination has been turned off, an abrupt rise in current occurs; its magnitude approaches I_0; and after several oscillations with a small amplitude, the current stabilizes at the level existed prior to illumination.

At longer illumination times, the oscillating component disappears and the magnitude of a steady-state current reduces.

Here are some experimental facts worth mentioning.

(1) The relaxation times observed in the experiments are too long for the electron processes in the bulk and are typical of the formation of defects in *a*-Si:H [2].

(2) Short exposures of a nonilluminated sample to light (curve *2*) slightly increase the forward current through a solar cell.

(3) The increase in the exposure time beyond a certain value t_1 results in the appearance of a chaotic oscillations in the current relaxation curves (curves *3–1* and *3–2*), and the current can attain the value I_0 in an abrupt manner.

(4) With the increase in the exposure time beyond a certain value t_2 ($t_2 > t_1$), the total interval of oscillations shortens and the oscillations become discontinuous (a telegraph noise). For long exposure times, the oscillations completely disappear and the magnitude of a current becomes lower than I_0 and tends to a constant value with a very long time constant (hundreds of minutes).

(5) The values of t_1 and t_2 are not fixed; rather, they are random variables for different samples and measurements.

(6) Prior to the range of current instability, there can exist a smooth part in the relaxation curve with a current higher or lower than the I_0 value.

The effect of exposure to light on the dark current relaxation behavior has been observed previously in polycrystalline solar cells [3] and has been explained by the interaction of photoexcited charge carriers with defects at the grain boundaries. The dark current relaxation curve was described by several exponents with the constants characterizing the times of existence of various photoexcited defects. The curves were monotone and well-reproducible in the experiments, although they could differ for various samples. The specific feature of *a*-Si:H solar cells is that, along with a slow monotone change in the current during the relaxation process, a relatively fast-oscillating component can be observed. We think that in our case, as in the case considered in [3], the relaxation of the reverse current is determined by the change in equilibrium between the defects of various types in the course of illumination.

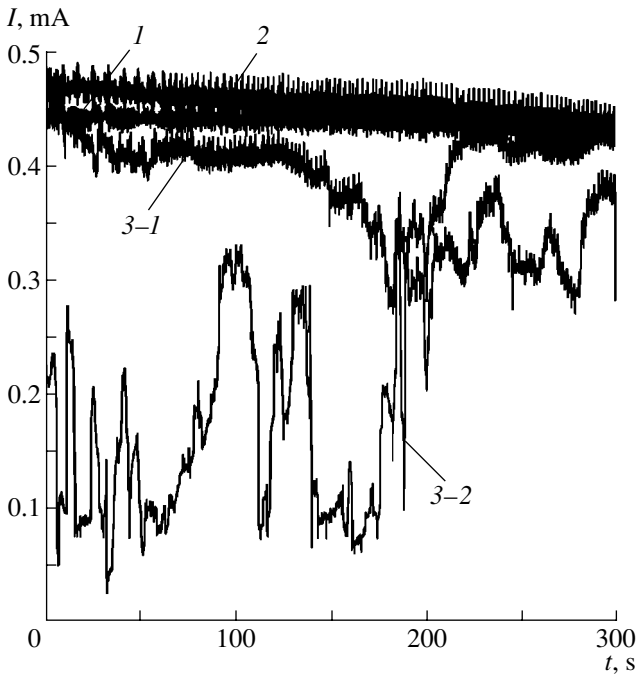

Effect of illumination on the time-dependent current through the *p–i–n* structure of an *a*-Si:H solar cell: (*1*) prior to exposure; (*2*) after the exposure for 2 min; (*3–1*) after the exposure for 10 min (the first array of experimental points); and (*3–2*) after the exposure for 10 min (the second array of experimental points).

We now consider the nature of large-amplitude chaotic oscillations which were not observed in [3]. One of the features of amorphous silicon solar cells with a large surface area is their high conductivity that shunts the barrier along the channels with an enhanced recombination rate; it is these channels that control the dark current. The illumination reduces the current and, consequently, the number of channels. The channels are formed by the clusters of defects that have a large cross section for capturing both electrons and holes, blocking the *i*-layer, and playing the role of effective recombination centers. Illumination intensely generates the electron–hole pairs which stimulate reactions between defects and shift the equilibrium, thus reducing the number of effective recombination centers as well as the number of channels and the magnitude of leakage current. After the illumination is turned off, the processes directed to the recovery of the initial equilibrium come into action, the concentration of effective recombination centers increases, and the conditions for their clusterization and creation of channels become favorable. A channel becomes unblocked abruptly when the concentration of recombination centers in a cluster reaches a critical value [4]. Since the clusters shunting the barrier have various concentrations and densities of defects, the instants of activation of the channels are widely spread about some characteristic time corresponding to a certain critical concentration of defects involved in the recombination.

If the exposure times exceed a critical value t_2, the major portion of channels is blocked and the formation and disappearance of a relatively small number of channels do not affect the current. If the exposure times are shorter than t_2, the number of defects blocking the existing channels becomes small and the conditions for disappearance of a permeable cluster are not met (the concentration of defects is lower than a critical one necessary for blocking the channels). When the concentration of channel-creating defects approaches a critical value, the probability of a through current decreases and, at the moment when a critical concentration is reached, the variance of probability for disappearance–formation of channels increases; therefore, the amplitude of current oscillations attains a maximum [4, 5].

In a hydrogenated amorphous silicon, the spectrum of metastable defects is very broad [2] and the study of kinetics of such defects is far from being completed. Nevertheless, it is established that the dominant types of metastable defects in *a*-Si:H are the dangling silicon bonds (DB), the major part of which contains hydrogen (DBH). In addition, there exist such defects as the interacting valence alternative pairs (IVAP) formed in the course of capture of an electron or a hole by dangling bonds; these pairs serve as effective recombination centers.

The generation of electrons and holes by light and their subsequent capture by defects result in a disbalance of equilibrium. The leading part in the transformation of DB into DBH and IVAP is played by the atoms of the metastable hydrogen (MH) formed by illumination [6]. The IVAP centers are most likely responsible for the creation of channels. The structure of these centers conducive to the cluster formation, the absence of barrier for their formation [2], and the fact that they are effective recombination centers—all these factors favor the above idea. Generation of these defects can occur according to the following scheme:

$$h + e + (\mathrm{Si} - \mathrm{H}) + (\mathrm{Si} - \mathrm{Si})$$

$$\longrightarrow \{\mathrm{Si}^- + (\mathrm{Si} - \mathrm{H} - \mathrm{Si})^+\}.$$

At the intermediate stage of the decay, an active role is played by the metastable hydrogen, which reduces the energy of the reaction:

$$\{\mathrm{Si}^- + (\mathrm{Si} - \mathrm{H} - \mathrm{Si})^+\}$$

$$\longrightarrow \{\mathrm{Si}^- + (\mathrm{H}^+ - \mathrm{Si} - \mathrm{Si})\} \longrightarrow (\mathrm{Si} - \mathrm{H}) + (\mathrm{Si} - \mathrm{Si}).$$

The concentration of the metastable hydrogen depends on the quality of a material and on the intensity and duration of the illumination. According to [5], for a material of the "device" quality exposed to light with intensity close to that in our experiments, the time t_1 required for the MH concentration to reach the values that can affect the formation of defects should be about 100 s. During the time interval $t < t_1$, the formation of new light-induced defects (DB, DBH, IVAP) in *a*-Si:H is possible; however, their decay involving MH is hardly probable since the concentration of MH increasing with time at the initial stages is small. Therefore, for short exposures, the increase in shunting effect of the channel can be observed due to the increase in the number of light-induced DBs and to generation of IVAPs (curve *2* in the figure). As exposure becomes longer, the concentration of MHs increases and the simultaneous generation and decay of defects occurs. In this process, the redistribution of DBH and IVAP defects among the hydrogen-containing defects occurs: the concentration of DBHs increases, while the concentration of IVAPs decreases. Correspondingly, the number of channels reduces and the leakage current decreases. After the illumination is switched off, the recovery of the equilibrium existed prior to the illumination occurs due to the residual metastable hydrogen. The recovery rate is proportional to the concentration of MHs. If the *i*-region of a solar cell does not contain the metastable hydrogen or its concentration is too small, the channels are not recovered (or they are recovered very slowly) after switching off the light.

The above mechanism is verified by the calculations performed in [5], according to which the durations of illumination sufficient for MH to be effective in the formation of defects approximately correspond to the times observed experimentally. It is shown [5] that these times are very sensitive to the initial concentration of defects. Thus, the effect considered in here can be used to study the kinetics of formation and decomposition of photoinduced defects in *a*-Si:H, to estimate the quality of the *i*-region of *a*-Si:H solar cells, and to predict their possible degradation.

REFERENCES

1. A. L. Fahrenbruch and R. H. Bube, *Fundamentals of Solar Cells. Photovoltaic Solar Energy Conversion* (Academic, New York, 1983; Énergoatomizdat, Moscow, 1987).
2. H. Yang and G. Lucovsky, Jpn. J. Appl. Phys. **37**, 1082 (1998).
3. É. N. Voronkov, A. E. Sharonov, and V. V. Kolobaev, Fiz. Tekh. Poluprovodn. (St. Petersburg) **33**, 481 (1999) [Semiconductors **33**, 461 (1999)].
4. B. I. Shklovskiĭ and A. L. Efros, *Electronic Properties of Doped Semiconductors* (Nauka, Moscow, 1979; Springer-Verlag, New York, 1984).
5. V. G. Golubev, V. Yu. Davydov, A. V. Medvedev, and A. B. Pevtsov, Fiz. Tverd. Tela (St. Petersburg) **39** (8), 1335 (1997) [Phys. Solid State **39**, 1197 (1997)].
6. K. Morigaki and H. Hikita, Solid State Commun. **114**, 69 (2000).

Translated by A. Zalesskiĭ

Semiconductors, Vol. 35, No. 6, 2001, pp. 677–679. Translated from Fizika i Tekhnika Poluprovodnikov, Vol. 35, No. 6, 2001, pp. 707–709.

II INTERNATIONAL CONFERENCE ON AMORPHOUS AND MICROCRYSTALLINE SEMICONDUCTORS

High-Temperature Superconductivity in Chalcogenide Vitreous Semiconductors

A. V. Prikhod'ko*, K. D. Tséndin,[1], and B. P. Popov***

** St. Petersburg State Technical University, St. Petersburg, 195251 Russia*

*** Ioffe Physicotechnical Institute, Russian Academy of Sciences, Politekhnicheskaya ul. 26, St. Petersburg, 194021 Russia*

[1] e-mail: tsendin@pop.ioffe.rssi.ru

Submitted November 9, 2000; accepted for publication November 15, 2000

Abstract—Relevant experimental data are discussed and the possibility is revealed of the occurrence of high-temperature superconductivity in vitreous Se in samples having the form of globules of the well-known high-temperature superconductor $Y_1Ba_2Cu_3O_7$ embedded in vitreous Se. The possible superconducting state occurs in Se channels several micrometers long, appearing between $Y_1Ba_2Cu_3O_7$ globules as a result of switching. The parameters of the Se channels, determined for the normal and possible superconducting states, are in good agreement with the values predicted by the model of negative-*U* centers. *© 2001 MAIK "Nauka/Interperiodica".*

A study of the superconducting properties of a sample prepared from a 1 : 6 mixture of a high-temperature superconductor (HTS) $Y_1Ba_2Cu_3O_7$ and vitreous Se was reported in [1]. The samples were fabricated by melting a small amount of Se (~1 mm^3) mixed with HTS microcrystals and placed between two crossed tungsten wires 50 μm in diameter. Selenium melting and suction of the mixture into the gap between the wires was achieved by passing current through them. Since the HTS concentration was low, the samples studied in [1] were, in fact, separate HTS globules embedded in a continuous Se matrix. Figure 1 shows a map of the element distribution over the sample cross section, obtained by means of X-ray microanalysis. It can be seen that, the concentration of HTS being low, its globules do not form uninterrupted paths connecting the opposite electrodes. The samples studied were of two types—with low and high resistance.

Current–voltage (*I–V*) characteristics of the low-resistance samples, taken at $T = 297$ and 77 K, are presented in Fig. 2a. In these samples, the interelectrode gap is the narrowest (~1 μm). Since the characteristic size of HTS globules is also several micrometers (see Fig. 1), then, with the cross-sectional area of the conducting region taken to be $S \approx 10$ μm^2, for the conductivity σ we have a value of ~10^3 S/cm, characteristic of $Y_1Ba_2Cu_3O_7$ at room temperature. Hence it follows that the interelectrode space in low-resistance samples is shorted by one or several HTS globules. This conclusion is also confirmed by the critical current of 6×10^{-8} A (Fig. 2a): we have a value of ~2 A/cm^2 for the critical density, which is characteristic of a low-density granulated HTS medium [2].

The *I–V* characteristics of the high-resistance sample, also measured at $T = 297$ and 77 K, are presented in Fig. 2b. In these samples, the interelectrode gap was wider than that in low-resistance samples, so that the room-temperature resistance was determined by the resistance of one or several Se layers. Let as take, for estimation purposes, the total Se thickness to be ~10 μm (see Fig. 1). Then, considering the cross-sectional linear dimension of the conducting region to be equal to the diameter of a tungsten wire, we get the room-temperature conductivity of this region to be ~10^{-4} S/cm. This value is many orders of magnitude higher than the conductivity of pure vitreous Se (~10^{-12} S/cm [3]), but lower than the conductivity of crystalline Se (~10^{-3} S/cm [3]). It is known that the conductivity of vitreous Se increases dramatically upon introducing an oxygen impurity or subjecting the material to thermal treatment. Therefore, it can be assumed that in the samples under study, prepared in air with heating sufficient for Se melting, the oxygen concentration is high and gives rise to the observed high conductivity. It is also possible that some Se is in the crystalline state and the effective thickness of vitreous Se is much less than 10 μm. It should be emphasized that, in any case, the room-temperature resistance of the high-resistance samples is not determined by the HTS material.

The superconducting transition temperature (T_c) of the high-resistance samples virtually coincides with the transition temperature in pure $Y_1Ba_2Cu_3O_7$ [1]. This can also be seen from Fig. 2b, indicating that at $T = 77$ K the superconducting state in high-resistance samples disappears at a critical current of ~10^{-8} A. Hence the conclusion was made in [1] that Josephson contacts are formed between HTS globules embedded in the selenium matrix, made possible through superconducting transport in the samples. In Fig. 1, the possible path

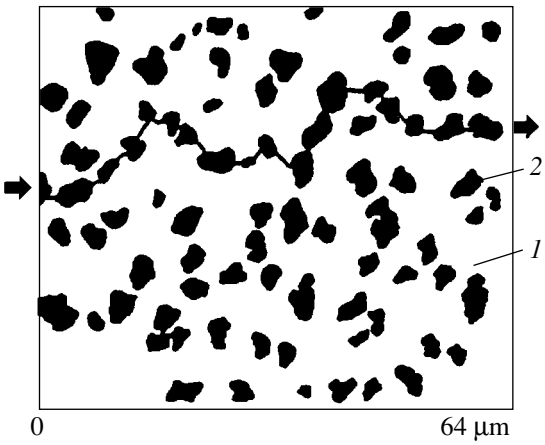

Fig. 1. Distribution of elements over the sample cross section, obtained by means of X-ray microanalysis (reproduced from [1]). (*1*) Selenium and (*2*) HTS. The broken line showing the path of the current represents a set of superconducting Se channels connecting adjacent HTS globules.

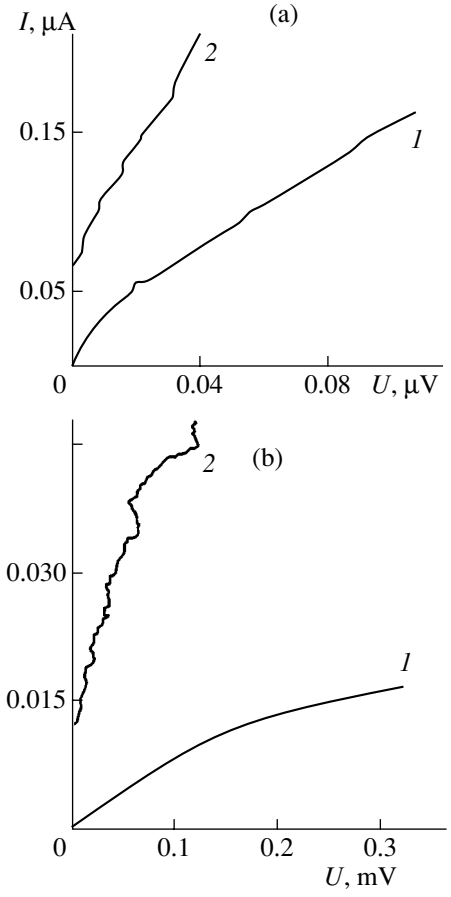

Fig. 2. *I–V* characteristics of (a) low- and (b) high-resistance samples at temperatures T = (*1*) 297 and (*2*) 77 K.

of such a channel connecting the left- and right-hand electrodes (thick black arrows) is depicted by a solid broken line.

The most important fact we emphasize in this communication consists in the following. It is now known that the correlation length in HTS materials (ξ) is small and equal to 10–15 Å [4, 5]. Consequently, the thickness of the Josephson contacts must be of the same order of magnitude. At the same time, it can be seen from Fig. 1 that the spaces between HTS globules, filled with selenium, have linear dimensions of several micrometers, i.e., 10^3 times ξ. Hence, it follows that the superconducting properties of the sample as a whole can only be accounted for under the assumption that the vitreous Se in the spaces between the globules also possesses superconducting properties with a transition temperature not lower than that of $Y_1Ba_2Cu_3O_7$. To be sure, such an assumption does not refer to the entire volume of selenium known not to exhibit high-temperature superconductivity. We mean here only the channels appearing between the HTS globules in the electric field as a result of switching, shown schematically by the broken line in Fig. 1. It is known that the transition of a thin Se layer from the state with high resistance to that with low resistance (switching effect) occurs in an electric field with a strength on the order of 10^5–10^6 V/cm [6]. At the same time, the field strength in [1] did not exceed 10^2 V/cm, even with the effective thickness of the Se layer taken to be ~0.1 μm. Thus, it can be assumed that vitreous Se present between HTS globules has unusual properties and is switched in weak electric fields.

It is for channels of this kind, appearing as a result of switching in chalcogenide vitreous semiconductors (CVS), of which Se is a representative, that a model of superconductivity has been recently proposed [7], based on the concept of centers having negative effective electron correlation energy U (negative-U centers).

At present, it is considered a well-established fact that the negative-U centers are the predominant type of native defects in chalcogenide vitreous semiconductors. With U being negative, electrons (holes) are effectively attracted when residing on a defect and thus form electron or hole bipolarons, which are bosons. It was assumed in [7] that, at a sufficiently high concentration of negative-U centers, their states may form bands of delocalized electron or hole bipolarons, whose Bose condensation gives rise to superconductivity. Only the simplest CVS (vitreous Se) was considered in [7] as an example. Figure 3 shows schematically the band of electron bipolarons, the $D(-)$ band.

The parameters of negative-U centers in vitreous Se can be found from the drift mobility measurements. The thermal activation energy of hole drift in the valence band is 0.14 eV [3], which corresponds to the capture of holes into states of the electron bipolaron with the subsequent thermal excitation of holes. Therefore, it can be assumed that the center of the $D(-)$ band lies at 0.14 eV above the top of the Se valence band. The same figure shows the expected energy of optical ionization of the $D(-)$ states, which, according to the

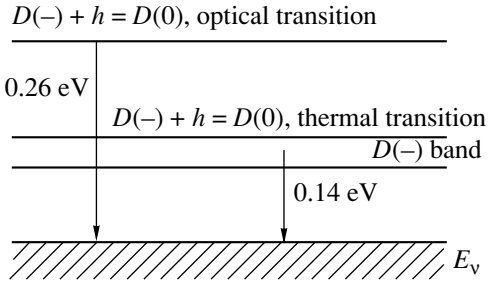

Fig. 3. Band energy diagram of vitreous Se near the valence band edge E_v. The arrows show the thermal and optical transitions of holes from the $D(-)$ state of the negative-U center. Two closely lying horizontal lines delimit the band of bipolarons [$D(-)$ band] whose Bose condensation is responsible for the superconductivity.

simple theory of negative-U centers, must be twice the thermal ionization energy.

Thus, the Bose condensation of electron bipolarons in the $D(-)$ band arising from the $D(-)$ level may be thought of as being responsible for the superconducting properties of the selenium channel connecting the HTS globules.

It was believed in [7] that the superconducting channel appearing upon switching in CVS samples with electrodes made of nonsuperconducting metals exists only in strong electric fields. By contrast, in the case in question, it should be considered that the channels between the HTS globules arise in samples prepared from a mixture of HTS and Se immediately following the application of a weak measuring field. This distinction suggests that the role played by globules located at the channel ends consists in reducing the field strength necessary for superconductivity to appear in the vitreous Se channel.

It was suggested in [7] that a situation similar to that observed in CVS may arise in organic polymers, in which negative-U centers also, possibly, exist. The results of recent studies [8, 9] confirm this assumption. In these investigations, as in the present study, the superconducting state was observed in channels of organic polymers connecting electrodes made of superconducting metals.

ACKNOWLEDGMENTS

A.V. Prikhod'ko thanks the Scientific Council on "Fullerenes and Atomic Clusters" (project no. 98063, task "Gradient") and the Scientific Program of the Ministry of Education "Universities of Russia—Basic Research."

REFERENCES

1. A. V. Prikhod'ko, S. V. Kozyrev, and V. F. Masterov, Sverkhprovodimost: Fiz., Khim., Tekh. **3**, 1130 (1990).
2. I. É. Graboĭ, A. R. Kaul', and Yu. G. Metlin, Itogi Nauki Tekh., Ser.: Khim. Tverd. Tela **6**, 143 (1989).
3. G. B. Abdullaev and D. Sh. Abdinov, *Physics of Selenium* (ÉLM, Baku, 1975), p. 259.
4. T. K. Worthington, W. J. Gallagher, and T. R. Dinger, Phys. Rev. Lett. **59**, 1160 (1987).
5. L. Forro, J.Y. Henry, C. Ayache, and P. Stamp, Phys. Lett. A **128**, 283 (1988).
6. A. V. Prikhod'ko, A. A. Chesnis, and V. A. Bareĭkis, Fiz. Tekh. Poluprovodn. (Leningrad) **15**, 536 (1981) [Sov. Phys. Semicond. **15**, 303 (1981)].
7. B. P. Popov and K. D. Tséndin, Pis'ma Zh. Tekh. Fiz. **24** (7), 45 (1998) [Tech. Phys. Lett. **24**, 265 (1998)].
8. A. N. Ionov and V. A. Zakrevskiĭ, Pis'ma Zh. Tekh. Fiz. **26** (20), 34 (2000) [Tech. Phys. Lett. **26**, 910 (2000)].
9. A. N. Ionov, V. A. Zakrevskiĭ, and I. M. Lazebnik, Pis'ma Zh. Tekh. Fiz. **25** (17), 36 (1999) [Tech. Phys. Lett. **25**, 691 (1999)].

Translated by M. Tagirdzhanov

Semiconductors, Vol. 35, No. 6, 2001, pp. 680–683. Translated from Fizika i Tekhnika Poluprovodnikov, Vol. 35, No. 6, 2001, pp. 710–713.

II INTERNATIONAL CONFERENCE ON AMORPHOUS AND MICROCRYSTALLINE SEMICONDUCTORS

Photonic Crystals with Tunable Band Gap Based on Filled and Inverted Opal–Silicon Composites

V. G. Golubev*, V. A. Kosobukin, D. A. Kurdyukov, A. V. Medvedev, and A. B. Pevtsov

Ioffe Physicotechnical Institute, Russian Academy of Sciences, ul. Politekhnicheskaya 26, St. Petersburg, 194021 Russia

** e-mail: golubev@gvg.ioffe.rssi.ru*

Submitted November 29, 2000; accepted for publication November 30, 2000

Abstract—Three-dimensional opal–silicon composites both with a direct (with different extent of the opal voids filling with Si) and inverted structure were synthesized, and their structural analysis was carried out. The spectra of specular reflection from (111) growth surfaces of the synthesized composites were measured in the wavelength range from 400 to 900 nm. The features observed in the spectra are analyzed theoretically and interpreted as manifestations of the photonic band gap in the direction [111]; the band gap position and width can be tuned in the visible and near-infrared spectral range. *© 2001 MAIK "Nauka/Interperiodica".*

Recently, growing attention has been focused on the studies of the photonic crystals, the structures where the dielectric constant is spatially modulated with the period on the order of the wavelength of light [1]. In these structures, the Bragg diffraction of the Bloch-type electromagnetic eigenstates at the Brillouin zone boundary results in the appearance of the forbidden band for radiation, the photonic band gap [2, 3]. In the photonic crystals with a complete band gap, propagation of light in any direction is prohibited within the spectral region of the gap. This is especially important for the possible applications of photonic crystals (in the optical communication systems [4, 5], laser technology [6], and quantum computers [7]). Synthetic opals are believed to have promising photonic-crystal properties. This is related both to their easy fabrication and to the possibility of considerable variation of their optical properties [8–12].

The structure of synthetic opals is formed by closely packed amorphous SiO_2 spheres 150–1000 nm in diameter arranged in an fcc lattice [13, 14]. The voids between the silica spheres may comprise up to 26% of the total volume of the opal material (under the conditions of point contact between the spheres). This makes it possible to change the optical contrast coefficient ($\eta = \sqrt{\varepsilon_v/\varepsilon_s}$, where $\sqrt{\varepsilon_s}$ and $\sqrt{\varepsilon_v}$ are the bulk refractive indices within the SiO_2 spheres and outside them, respectively [15]) by filling the voids with different substances. According to the theoretical estimations [15], a complete band gap may exist for $\eta \geq 2.8$. In pure opals, where η is considerably lower, the formation of the complete photonic band gap is, apparently, impossible [15]. Therefore, the materials with a high dielectric constant should be used to fill the voids, in particular, semiconductors such as InP, Si, and Ge (hereafter, the composites formed after filling the voids are called "direct opals"). η can be increased still further by inverting the opal structure, which means the removal of SiO_2 from the prepared direct opal–semiconductor composite [14, 15]. This operation yields a three-dimensional semiconductor lattice occupying up to 26% of the total volume of the material and surrounded by a matrix of air spheres that occupy the remaining 74% of the volume. Among other semiconductors, Si is especially attractive as a filling substance due to the prospects of the integration of Si photonic crystals into conventional microelectronics technology [4].

The purpose of this study is to synthesize opal–silicon composites with direct and inverted structure and to examine the possibilities of using them for the fabrication of photonic crystals with a band gap whose width and spectral position can be tuned in a broad range of wavelengths. The band gap tuning in synthetic composite structures can be achieved by varying the contrast and the average dielectric constant. To verify this, we carried out experimental investigations of the reflection spectra of the synthesized composites and established the existence of the characteristic spectral features. These features were interpreted as manifestations of the photonic band gap for the one-dimensional (1D) propagation of the light wave along the high-symmetry directions of the periodic dielectric structure (namely, the direction normal to the (111) plane in the case considered here).

Commercially available opal with the SiO_2 sphere diameter of 230 nm was used as a matrix for composite synthesis. The samples possess a polydomain structure, with the size of a single domain with highly ordered arrangement of SiO_2 spheres being 30–100 μm. The analysis by scanning-electron microscopy (SEM) (see Fig. 1a) demonstrates that point contact between the adjacent spheres exists and that the volume of the voids that can be filled is about 26% of the total volume. Silicon was deposited in the opal matrix voids by thermal

decomposition of the gas mixture of 5% silane with argon (the technology is described in detail in our previous publications [16–18]). This process results in the formation of a Si film of uniform thickness on the surface of the SiO_2 spheres. The fraction of the filled volume of the voids can be varied from 0 to 100% by changing the parameters of the technological process. The region with complete filling can be as thick as 0.4 mm. Samples with the filling profile varying over the thickness of the structure can be fabricated by this technology as well. The samples were further annealed in air at 800°C temperature and 1 Torr pressure. It was demonstrated by X-ray, electron-microscopy, and Raman studies that the silicon film has mixed amorphous–nanocrystalline phase composition [16, 18]. SEM images of (111) surface of an unfilled opal and an inverted structure are shown in Fig. 1. Inverted structures were fabricated from an opal–Si composite material by etching off the SiO_2 with the hydrofluoric acid aqueous solution, as described in [19]; a similar procedure for the fabrication of inverted structures from Si-filled opals was used in [14]. The samples selected for further studies have a dimension of $5 \times 5 \times 0.4$ mm. The optical contrast in inverted structures is $\eta \approx 3.5$. It was already noted that the technology developed makes it possible to gradually vary the fraction of the void volume filled with silicon. We intend to use this possibility in the future to optimize the photonic properties of inverted structures. In particular, the calculation indicates that, in the case of partial filling of the opal voids with silicon, a twofold increase in the complete band gap width can be achieved [15].

When analyzing the optical properties of the opal-based structures, we assume that the eigenstates of the electromagnetic field are the Bloch waves due to the periodic modulation of the dielectric characteristics. In the specular reflection experiment, we are concerned with the state that is excited for a given wavelength of the incident light and which is responsible for the reemission in the specular direction. Similar to the treatment of the light transmission [20], the 1D nature of the light reflection process makes it possible to consider the photonic crystal as a dielectric superlattice analogously to the Kronig–Penney model for electrons [21]. In the case of an infinite structure, this approach yields the dispersion equation

$$\cos(qd) = \cos(k_1 a)\cos(k_2 b) - \frac{1}{2}\left(\sqrt{\frac{\varepsilon_1}{\varepsilon_2}} + \sqrt{\frac{\varepsilon_2}{\varepsilon_1}}\right)\sin(k_1 a)\sin(k_2 b) \quad (1)$$

for the electromagnetic Bloch states with quasi-wavevector q (cf. the theory of the optical filters [22]). Here, $k_i = \sqrt{\varepsilon_i}(\omega/c)$ ($i = 1, 2$); the dielectric constant is assumed to be equal to ε_1 in the layer of thickness a and ε_2 in the layer of thickness b, with the period of the structure being $d = a + b$.

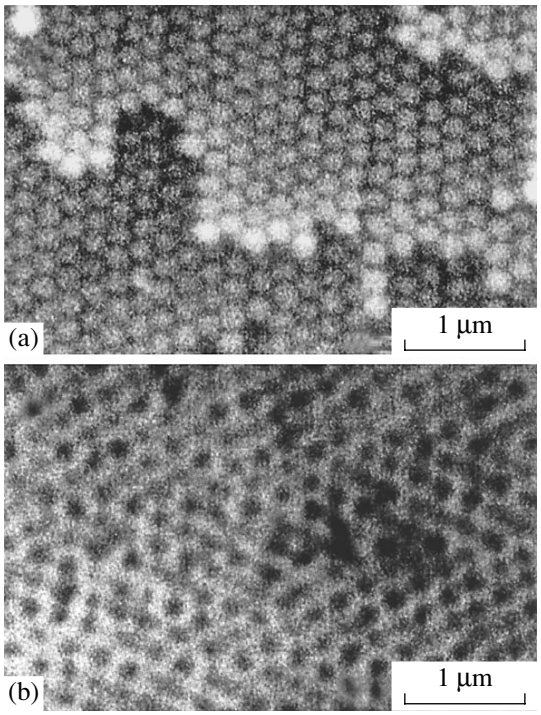

Fig. 1. SEM images of (111) surfaces of (a) unfilled opal and (b) inverted structure obtained by etching off the SiO_2 spheres from the opal–Si composite.

One of the difficulties encountered by the theory is related to the fact that the long-wavelength approximation of "effective medium" cannot be applied to the photonic crystals with $d \sim 2\pi c/\omega$. This means that, although the dielectric constants (or refractive indexes) of the components of the photonic crystal are well defined, the significance of the spatially averaged values is limited. This is related to the deep modulation of the electromagnetic field within the unit cell. However, in spite of these limitations, it is convenient to use the "mean" values of the dielectric parameters to illustrate the behavior of the width and position of the band gap in the spectrum of the electromagnetic states in a photonic crystal.

Keeping this in mind, when considering the reflection of light along the normal to the (111) growth surface of opal-based composites, we characterize the properties of a medium by the averaged dielectric constant that varies with the coordinate z normal to the sample surface; i.e.,

$$\bar{\varepsilon}(z) = \varepsilon_s S(z) + \varepsilon_v [1 - S(z)]. \quad (2)$$

Here, ε_s and ε_v characterize the material of the spheres and the voids, respectively; if these volumes are filled nonuniformly, the volume-averaged values are used. The opal structure is defined by the radius r of the spheres and their arrangement in the fcc lattice. The function $S(z)$ represents the fraction of the cross-section plane (determined by coordinate z) occupied by the

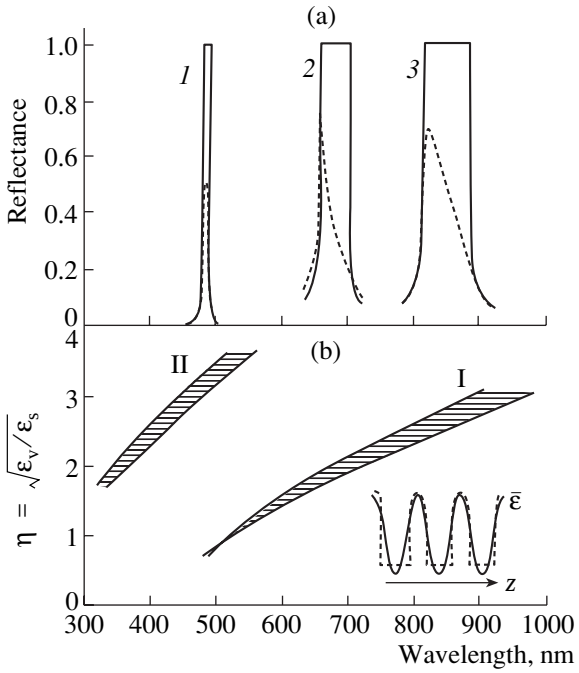

Fig. 2. (a) Calculated normal-incidence reflection coefficient for the (111) growth surface of the opal-based composites: (*1*) unfilled opal, (*2*) opal with voids partially filled with silicon (average refractive index $\sqrt{\varepsilon_{Si}} = 3.7$), and (*3*) opal with voids completely filled with silicon (refractive index $\sqrt{\varepsilon_{Si}} = 3.5$); reflection at the vacuum–opal boundary was disregarded. The spectral curves shown by solid lines were calculated with absorption disregarded; the curves shown by dashed lines were calculated with absorption taken into consideration: the bulk absorption coefficient of the filling substance was assumed to be 0, 0.1, and 0.24 in the cases *1*, *2*, and *3*, respectively. (b) Calculated widths and spectral positions of the two low-energy forbidden bands (marked I and II) in relation to the parameter $\eta = \sqrt{\varepsilon_v/\varepsilon_s}$ ($\sqrt{\varepsilon_v}$ is the bulk refractive index of the filling substance, and $\sqrt{\varepsilon_s} = 1.37$ is that of the SiO_2 spheres). The inset illustrates schematically the principle of approximation of the dielectric constant profile in the absence of absorption.

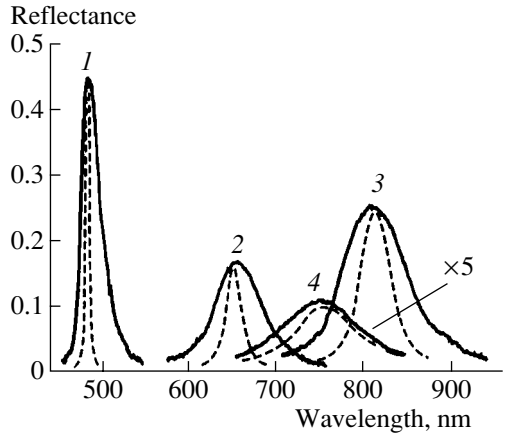

Fig. 3. The measured and calculated normal-incidence spectra (solid and broken lines, respectively) of reflection from the (111) surface of the opal-based composites: (*1*) unfilled opal, (*2*) opal with voids partially filled with silicon, (*3*) opal with voids completely filled with silicon, and (*4*) inverted opal. The vacuum–opal boundary was disregarded in the calculations. For (*1–3*), the measurements were carried out on specially prepared polished surfaces by optical microscopy technique [24]; for (*4*), unpolished surface was studied. Background related to the diffuse component of the reflected light was eliminated from the experimental curves.

spheres. A further qualitative analysis was carried out on the basis of Eq. (1) with the parameters ε_i derived from the function $\bar{\varepsilon}(z)$ (given by (2)) for a specified ratio between *a* and *b* taking into account that, for the [111] direction in the opal structure, $d = r\sqrt{8/3}$. In this approximation, we used the transfer matrix technique (the problem is formulated similar to [23]) to calculate the band spectrum and such optical parameters as the light reflection and transmission coefficients, which can be measured experimentally.

First, we examined theoretically the effect of the bulk index of refraction $\sqrt{\varepsilon_v}$ of the filling substance on the spectral behavior of the reflection coefficient (Fig. 2a) and on the position and width of the forbidden bands (Fig. 2b). For $\sqrt{\varepsilon_v}$ in silicon, we adopt the known complex refractive index of the bulk material, with the strong dispersion in the spectral region under consideration taken into account. For the SiO_2 spheres in the opal, we adopt $\sqrt{\varepsilon_s} = 1.37$. Clearly, the existence of the band gap is evidenced by the shape of the calculated spectra of reflection along the normal to the (111) surface (Fig. 2a) (only the spectral features related to the first band gap are shown). The total reflection originating from the existence of the band gap for the propagation of light is shown in the spectra calculated for the case of negligibly low absorption (solid curves). When the absorption is taken into account, the shape of the spectra is modified (dashed curves) but the position and the width of the spectral features remain approximately the same within the corresponding band gap regions. A general idea of the photonic band structure can be visualized from Fig. 2b, where the variation of the width and position of the two low-energy forbidden bands with the parameter $\eta = \sqrt{\varepsilon_v/\varepsilon_s}$ are shown for the case of negligible absorption.

To verify these estimates experimentally, the spectra of the specular reflection of light from the (111)-oriented surface of the synthesized materials were measured. To eliminate the influence of the polydomain structure of the samples under study on the recorded signal, optical microscopy was employed [24]. The light from an incandescent lamp was focused by a microobjective on the sample under the normal angle of incidence. The same objective was used to collect the

reflected light and to image the sample surface with a magnification of about ×50 onto the intermediate slit oriented perpendicularly to the entrance slit of the spectrometer. The aperture angle did not exceed 6°. The intermediate slit plane was imaged onto the plane of the spectrometer entrance slit by a silica optical fiber. Changing the widths of the mutually perpendicular slits, we could select a single-domain region to be studied on the sample surface. Figure 3 displays the reflection spectra experimentally obtained for an unfilled opal, a partially and completely Si-filled opal, and an inverted opal. With an increase in optical contrast, the spectral bands broaden and shift to longer wavelengths, in agreement with the calculations. The calculated spectra are shown in Fig. 3 by dashed lines. They were fitted to the experimental spectra by slightly varying the imaginary part of the dielectric constant across the thickness of the structure; this procedure can be interpreted in terms of taking into account the scattering of light in photonic-crystal structures, which makes an additional contribution to the extinction coefficient. The qualitative agreement between the experimental and theoretical curves enables us to conclude that the observed reflection peaks do originate from the existence of photonic band gaps in the structures under study.

To summarize, the comparison of experimental data with the theory predicting the existence of a "one-dimensional" band gap indicates that peaks observed in the reflection spectra result from the Bragg diffraction of electromagnetic waves on the 1D-periodic dielectric structure in the samples investigated. We also demonstrated that the degree of void filling in crystalline opals can be controlled with a high accuracy by the technique developed in this study. This makes it possible to produce photonic crystals with the desired width and spectral position of the band gap.

ACKNOWLEDGMENTS

We thank M.V. Zamoryanskaya and A.V. Naschekin for carrying out the electron microscopy studies.

This study was supported by the Russian Foundation for Basic Research (project no. 00-02-16924) and the Program of the Ministry of Science "Physics of the Solid-State Nanostructures" (project no. 97-2016).

REFERENCES

1. *Photonic Band Gap Materials*, Ed. by C. M. Soukoulis (Kluwer, Dordrecht, 1996), NATO ASI Ser., SER. E **315** (1996).
2. E. Yablonovitch, Phys. Rev. Lett. **58**, 2059 (1987).
3. S. John, Phys. Rev. Lett. **58**, 2486 (1987).
4. J. D. Joannopoulos, P. R. Villeneuve, and S. Fan, Nature **386**, 143 (1997).
5. J. G. Fleming and Shawn-Yu Lin, Opt. Lett. **24**, 49 (1999).
6. Y. Yamamoto and R. E. Slusher, Phys. Today **46**, 66 (1993).
7. S. Ya. Kilin, Usp. Fiz. Nauk **169**, 507 (1999).
8. V. N. Bogomolov and T. M. Pavlova, Fiz. Tekh. Poluprovodn. (St. Petersburg) **29**, 826 (1995) [Semiconductors **29**, 428 (1995)].
9. A. van Blaaderen, R. Ruel, and P. Wiltzius, Nature **385**, 321 (1997).
10. H. Míguez, C. López, F. Meseguer, *et al.*, Appl. Phys. Lett. **71**, 1148 (1997).
11. Yu. A. Vlasov, V. N. Astratov, A. V. Baryshev, *et al.*, Phys. Rev. E **61**, 5784 (2000).
12. S. G. Romanov, H. M. Yates, M. E. Pemble, and R. M. De La Rue, J. Phys.: Condens. Matter **12**, 8221 (2000).
13. V. N. Bogomolov, D. A. Kurdyukov, A. V. Prokof'ev, and S. M. Samoĭlovich, Pis'ma Zh. Éksp. Teor. Fiz. **63**, 496 (1996) [JETP Lett. **63**, 520 (1996)].
14. A. Blanco, E. Chomski, S. Grabtcak, *et al.*, Nature **405**, 437 (2000).
15. K. Bush and S. John, Phys. Rev. E **58**, 3896 (1998).
16. V. N. Bogomolov, V. G. Golubev, N. F. Kartenko, *et al.*, Pis'ma Zh. Tekh. Fiz. **24** (8), 90 (1998) [Tech. Phys. Lett. **24**, 326 (1998)].
17. V. N. Bogomolov, N. A. Feoktistov, V. G. Golubev, *et al.*, J. Non-Cryst. Solids **266–269**, 1021 (2000).
18. V. N. Bogomolov, N. A. Feoktistov, V. G. Golubev, *et al.*, in *Abstracts of the Symposium "Amorphous and Heterogeneous Silicon Thin Films-2000"*, A. 24.4.1.
19. V. G. Golubev, V. A. Kosobukin, D. A. Kurdyukov, and A. B. Pevtsov, in *Abstracts of the 25th International Conference on Physics of Semiconductors, Osaka, Japan, 2000*, p. 1000.
20. Yu. A. Vlasov, M. A. Kalitievskii, and V. V. Nikolaev, Phys. Rev. B **60**, 1555 (1999).
21. E. M. Lifshitz and L. P. Pitaevskiĭ, *Course of Theoretical Physics*, Vol. 5: *Statistical Physics* (Nauka, Moscow, 1978; Pergamon, New York, 1980), Part 2.
22. A. Yariv and P. Yeh, *Optical Waves in Crystals: Propagation and Control of Laser Radiation* (Wiley, New York, 1984; Mir, Moscow, 1987).
23. V. A. Kosobukin, Fiz. Tverd. Tela (St. Petersburg) **34**, 3107 (1992) [Sov. Phys. Solid State **34**, 1662 (1992)].
24. Yu. A. Vlasov, M. Deutsch, and D. J. Norris, Appl. Phys. Lett. **76**, 1627 (2000).

Translated by M. Skorikov

Semiconductors, Vol. 35, No. 6, 2001, pp. 684–687. Translated from Fizika i Tekhnika Poluprovodnikov, Vol. 35, No. 6, 2001, pp. 714–717.

II INTERNATIONAL CONFERENCE ON AMORPHOUS AND MICROCRYSTALLINE SEMICONDUCTORS

Self-Organization Processes and Optical Activation of the Er^{3+} Ions in Amorphous Hydrogenated Er-Doped Silicon Films

M. M. Mezdrogina, G. N. Mosina, E. I. Terukov, and I. N. Trapeznikova

Ioffe Physicotechnical Institute, Russian Academy of Sciences, Politekhnicheskaya ul. 26, St. Petersburg, 194021 Russia

Submitted November 29, 2000; accepted for publication November 30, 2000

Abstract—The formation of the optically active centers in the *a*-Si:(H,Er) films obtained by the method of magnetron sputtering of the mosaic target containing Er with the O impurity was investigated. The microstructure of the films was investigated by electron microscopy, and crystallites from 5 to 50 nm in size depending on the Er concentration were found. It was assumed that not only the local surroundings of the Er ion but also the self-organization processes affect the intensity of the photoluminescence band in the vicinity of 1.54 μm.

INTRODUCTION

The problem of optical activation of erbium ions (Er^{3+}) in the Si matrix is of great interest. On the basis of this material, it is possible to develop the emitters at the wavelength $\lambda = 1.54$ μm, which are used in fiber links.

According to [1], the optically active centers in the films of Er-doped amorphous hydrogenated Si (*a*-Si:(H,Er)) are the [Er–O] clusters with the local symmetry of the Er^{3+} surroundings similar to that one in Er_2O_3. However, the local symmetry of Er surroundings in the [Er–O] clusters in amorphous and crystalline Si is somewhat distinct, which is explained by different structures of matrices.

It was also demonstrated that annealing *a*-Si:(H,Er) films does not affect the local structure in the previously formed [Er–O] clusters. This is possible if a large enough cluster with a size close to the unit cell parameter of Er_2O_3 is formed. It is known that the unit cell parameter of Er_2O_3 in the cubic crystal system is equal to 10.548 Å.

The formation of optically active centers in the *a*-Si:(H,Er) films obtained by various deposition techniques was investigated recently [2]. It was demonstrated that the dependence of the intensity of the photoluminescence (PL) band $\lambda = 1.54$ μm on the Er content is observed only if the magnetron sputtering of the mosaic target containing Er with the O impurity (no less than 0.10–0.12%) is used. No dependence on the concentration is observed if Er of extra-purity grade is used. It was also demonstrated that the formation of the [Er–O] complexes in the gas phase is highly improbable, and the magnetron sputtering technique is advantageous because of a large growth rate of the films. In addition, if the mosaic target with sufficiently high O content is used, the formed [Er–O] complexes exist. The PL spectrum in the region $\lambda = 1.54$ μm for the optimal Er concentration, at which the highest PL intensity is observed, includes a series of the peaks. It should be noted that the peak of the PL band at $\lambda = 1.54$ μm shifts nonmonotonically with the variation in the concentration. More specifically, the peak shifts to shorter wavelengths as the Er content increases to 1.08% and to longer wavelengths with even higher contents.

The set of the data obtained by us suggests that not only the local surroundings of the Er ion but also the cluster size affects the PL intensity at $\lambda = 1.54$ μm.

The purpose of this study was to gain insight into the effect of the cluster size (self-organization process) during the formation of the [Er–O] complexes on the optical activation of the Er^{3+} ions in the *a*-Si:(H,Er) films.

The effect of the nanowire size from 9.5 nm to several hundreds of nanometers in diameter on the shift of the PL peak with increasing diameter, which was explained by the existence of the quantum-well effect in nanowires, was considered recently [3]. It is noteworthy that the PL spectra [3] have no specific features and peaks as the PL peak shifts from 624 nm (1.99 eV) to 783 nm (1.58 eV), with the full-width at half-maximum (FWHM) of the peak being equal to 160 nm for 1.99 eV.

For the optimal Er content, which provided the highest intensity of the PL band at 1.54 μm, FWHM was equal to 23 nm [2].

Thus, it was assumed [2, 3] that size effects affect the optical activation of the Er^{3+} ions in the *a*-Si:(H,Er) films.

1063-7826/01/3506-0684$21.00

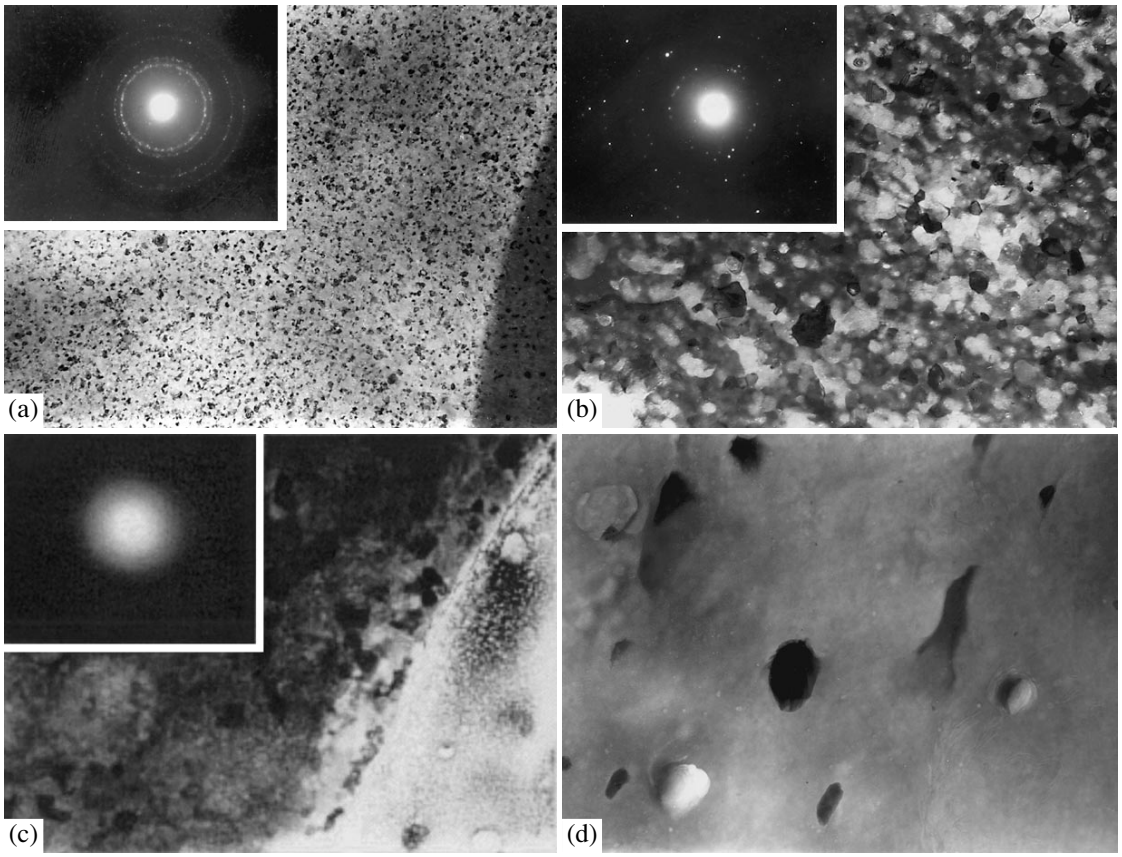

Fig. 1. Microstructure of the *a*-Si:(H,Er) films with the Er content C_{Er} of (a) 1.08, (b) 0.79, and (c, d) 0.34%. In insets, the microdiffraction patterns are shown.

EXPERIMENTAL

The microstructure of the *a*-Si:(H,Er) films was investigated using the transmission-electron microscopy. The microstructure and X-ray diffraction patterns of the *a*-Si:(H,Er) films with various Er contents are shown in Fig. 1. The dependences of the intensity of the PL band at $\lambda = 1.54$ μm on the Er content C_{Er} are shown in Fig. 2.

The microstructure of the *a*-Si:(H,Er) films with the Er content $C_{Er} = 1.08\%$ is shown in Fig. 1a. It can be seen that a fine-crystalline second phase is present in the amorphous film. The crystallite size varies from 5 to 50 nm. The X-ray diffraction pattern of this structure (see the inset in the upper part of Figs. 1a–1c) comprises the set of rings. An interpretation of the diffraction pattern demonstrated that the interplanar spacings *d* in it correspond to interplanar spacings for Er_2O_3 (see table). The average particle density is $\sim 5 \times 10^{10}$ cm^{-2}.

The microstructure of the *a*-Si:(H,Er) films with the Er content $C_{Er} = 0.79\%$ is illustrated in Fig. 1b. In this case, the *a*-Si:(H,Er) film has a cellular structure. The new phase, which repeats the cell shape, crystallizes in the cells. The particle size varies from 50 to 250 nm, and their density is 5×10^9 cm^{-2}. The reflections of the Er_2O_3 phase are also present in the microdiffraction pattern of this film (table).

The microstructure of the *a*-Si:(H,Er) films with the Er content $C_{Er} = 0.34\%$ is shown in Fig. 1c. As compared to the films described above with the Er content

Interplanar spacings according to the transmission electron microscopy data

$C_{Er} = 1.08\%$		$C_{Er} = 0.79\%$		$C_{Er} = 0.34\%$	
d, Å	$d(Er_2O_3)$, Å	*d*, Å	$d(Er_2O_3)$, Å	*d*, Å	*d*(Si), Å
2.59	2.631	2.6	2.631	3.20	3.138
2.23	2.243	2.466	2.48	0.95	0.9599
1.526	1.521	2.24	2.243		
1.50	1.49	1.526	1.521		
1.343	1.349	1.51	1.490		
		1.343	1.349		

Note: *d* are the experimental values obtained from the X-ray diffraction patterns, $d(Er_2O_3)$ are the tabulated data for the cubic Er_2O_3 with the unit cell parameter 10.548 Å, and *d*(Si) are the tabulated data for cubic Si.

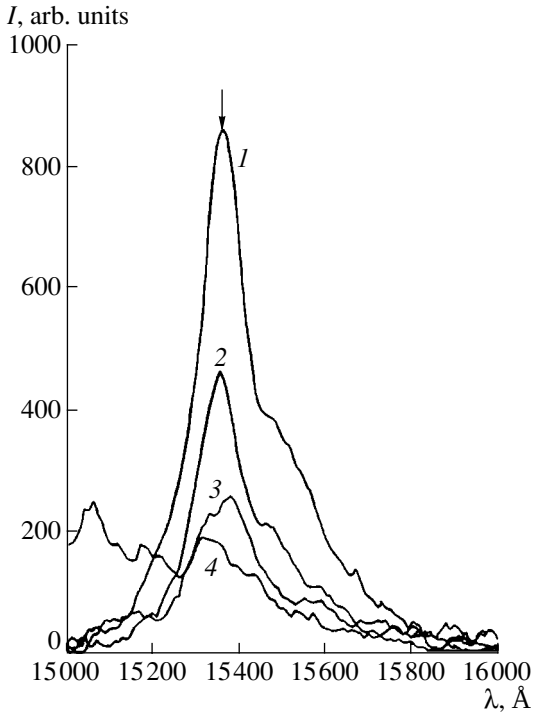

Fig. 2. Variation in the PL intensity at 300 K for the *a*-Si:(H,Er) films with the Er content C_{Er} of (*1*) 1.08, (*2*) 0.79, (*3*) 0.34, and (*4*) 1.42%.

of C_{Er} = 1.08 and 0.79%, this film has larger pores. Against the background of the pores, the poorly pronounced formation of the second phase is observed. The low-contrast crystallites with dimensions close to 50–250 nm are clear in Fig. 1. Crystallites do not contribute to the microdiffraction pattern, since only two diffuse rings from the amorphous phase are observed in it (table).

The microstructure type of the films correlates with the shape of the PL spectra at $\lambda = 1.54$ μm rather well. This can be seen from the comparison of Figs. 1 and 2: an increase in the crystallite size leads to an increase in the PL intensity.

RESULTS AND DISCUSSION

The mechanism of transfer of the excitation energy to Er ions was considered recently [4] using the time-resolved PL and exciton spectroscopy techniques. As a result, the phenomenological model of the excitation was suggested. Omitting the details of this complex model, let us dwell on one of its major conclusions that microcrystallites should be necessarily present. It is known that the specific features of the presence of microcrystallites are the unusual electrical and magnetic characteristics, which are determined by large surface-to-volume ratios. According to the model suggested [4], the excitation energy is transferred from excitons in nanocrystallites to the Er^{3+} ion, where radiative recombination occurs. As a result of the recombination, the intracenter transition to the unoccupied 4*f* shell of Er takes place and PL at $\lambda = 1.54$ μm is observed.

In the *a*-Si:(H,Er) films investigated in this study, the most probable mechanism of the crystallite formation when oxygen-containing Er is used is as follows. The [Er–O] complexes arriving at the substrate directly from the target have a low mobility over the surface by virtue of the relatively low substrate temperature (300°C), large size of complexes, and incomplete saturation of dangling bonds. The SiH^{3-} complexes with completely saturated bonds have the highest mobility over the substrate surface. However, their concentration is relatively low for a large deposition rate, which is characteristic of magnetron sputtering. All reactions occurring on the substrate surface [5] will lead to the formation of the [Si–O] complexes and erbium silicides ([Er–Si] complexes). The lowest energy of formation and the highest probability of the process are typical of the former complexes, whereas the higher energy of formation is typical for the latter complexes. The rate-determining factor for these processes is related to the fact that the surface of the growing film contains O atoms which can escape into the gas phase because of the reactions with the atomic H arriving at the surface of the growing film from the plasma discharge.

It is obvious that the type of Si–O bonds in the *a*-Si:(H,Er) film also changes with the variation in the O content; namely, instead of the Si–O–Si bonds, which are characteristic of the *a*-Si:(H,Er) films, the O–Si–O bonds, which are characteristic of the $Si_{1-x}O_x$ compounds, should be observed. The crystallite size is controlled by the magnitudes of surface energies and component concentrations. If we consider the high-rate processes of the film deposition, specifically, dc magnetron sputtering and radio-frequency sputtering, the first method is obviously preferable for the formation of the optically active centers. With the use of a magnetron, no bombardment of the growing film occurs at a high deposition rate in contrast to radio-frequency sputtering. Thus, magnetron sputtering with the optimal Er and O concentrations in the target is that at which the self-organization processes (i.e., the order–disorder transition caused by the structural instability which is accompanied by a decrease in the entropy) play an important role. It was demonstrated that the self-organization process is the sequence of nonequilibrium phase transitions arising with a nonadditive decrease in one or several bifurcation parameters [6]. It is known that the surface energy for oxides of the $Si_{1-x}O_x$ or $Er_{1-x}O_x$ type exceeds the surface energy for $Si_{1-x}Er_x$ silicides, Si, and Er. The crystallite size presumably varies in accordance with the difference in the surface energy [7, 8]. We may assume that the [Er–O] and [Si–O] complexes have the largest size, whereas the [Er–Si] complexes have the smallest size in this series of com-

pounds. It seems likely that the [Si–Er] complexes, which are of the smallest size, possess the exciton energy necessary and sufficient for the energy transfer [4]. Thus, these complexes serve as certain triggers initiating a complicated process of energy transfer to Er^{3+} ions in the case of their optimal concentration. As this takes place, the role of the [Si–O] oxides consists only in forming the optimal concentration and size of the [Er–O] complexes. According to [9], the nearest surroundings of Er in the *a*-Si:(H,Er) films consist of O atoms, and the second coordination shell is formed by Si atoms. It was also demonstrated that the average coordination number increases with the increasing O concentration. If we consider the nearest surroundings of Er^{3+} ions, the [Er^{3+}–O] complexes have lower symmetry compared to the 6-coordinated [Er^{3+}–Si] complex. The [Er^{3+}–O] complexes are weakly bonded to the disordered structural network because of the presence of the strong internal bond. Thus, a large intensity of the PL band at $\lambda = 1.54$ μm and a weak temperature quenching of PL are observed.

For the realization of the problem of injection pumping, it is necessary to solve the complex technology problem of optimization of the concentrations of the complexes mentioned.

REFERENCES

1. V. F. Masterov, F. S. Nasredinov, P. P. Seregin, *et al.*, Fiz. Tekh. Poluprovodn. (St. Petersburg) **32**, 709 (1998) [Semiconductors **32**, 636 (1998)].
2. M. M. Mezdrogina, M. P. Annaorazova, E. I. Terukov, and I. N. Trapeznikova, Fiz. Tekh. Poluprovodn. (St. Petersburg) **33**, 1260 (1999) [Semiconductors **33**, 1145 (1999)].
3. Y. F. Zhang, Y. H. Tang, H. Y. Peng, and N. Wang, Appl. Phys. Lett. **75** (13), 1842 (1999).
4. G. Franzo, V. Vinciduerro, and F. Priolo, Appl. Phys. A: Mater. Sci. Process. **A69** (1), 3 (1999).
5. M. M. Mezdrogina, A. F. Bardamid, O. A. Golikova, *et al.*, Neorg. Mater. **27**, 667 (1991).
6. I. Prigogine, *From Being to Becoming: Time and Complexity in the Physical Sciences* (Freeman, San Francisco, 1980; Nauka, Moscow, 1985).
7. A. G. Khachaturyan, *The Theory of Phase Transitions and the Structure of Solids Solutions* (Nauka, Moscow, 1974), p. 122.
8. A. Piamonteze, A. C. Juigiez, and L. R. Tesler, Phys. Rev. Lett. **81** (21), 4652 (1998).
9. N. N. Ledentsov, V. M. Ustinov, V. A. Shchukin, *et al.*, Fiz. Tekh. Poluprovodn. (St. Petersburg) **32** (4), 385 (1998) [Semiconductors **32**, 343 (1998)].

Translated by N. Korovin

Semiconductors, Vol. 35, No. 6, 2001, pp. 688–689. Translated from Fizika i Tekhnika Poluprovodnikov, Vol. 35, No. 6, 2001, pp. 718–719.

ATOMIC STRUCTURE AND NONELECTRONIC PROPERTIES OF SEMICONDUCTORS

Polycrystalline Films of Gallium Nitride Grown by Magnetron Sputtering

A. N. Blaut-Blachev

Institute of Physical Chemistry, Russian Academy of Sciences, Leninskiĭ pr. 31, Moscow, 117915 Russia

Submitted October 14, 2000; accepted for publication November 21, 2000

Abstract—Using radio-frequency magnetron sputtering, polycrystalline GaN films were fabricated on Si and polycrystalline Al_2O_3 substrates. When applied during fabrication, the negative bias increased the degree of crystallinity of the film. © *2001 MAIK "Nauka/Interperiodica".*

At present, GaN thin films are widely used for the preparation of semiconductor devices [1]. This semiconductor material has a wide band gap, direct band-to-band transitions, and high carrier mobilities. This permits the use of this material for the fabrication of semiconductor lasers, light-emitting devices, and high-gain transistors.

Typically, GaN thin films are fabricated by the chemical gas-phase deposition [2]. This technique has a number of drawbacks, particularly the use of corrosive media and high temperatures. The reactive magnetron sputtering, in which the target composed of Ga or GaN is sputtered in the N_2 atmosphere or in the $Ar + N_2$ mixture, may be an alternative method for fabricating the GaN films. Using magnetron sputtering, large-area films (dozens of square centimeters) may be deposited on the substrates from crystalline and amorphous materials, metals, and insulators; in this case, the film properties depend only slightly on the substrate material.

The application of magnetron sputtering for fabrication of the GaN films was described previously [3–6]. However, according to the X-ray diffraction data, the crystal structure of the films obtained is considerably less perfect as compared to the structure of the films grown by the chemical gas-phase deposition. In this study, we attempted to select the conditions of magnetron sputtering in order to improve the quality of the films obtained.

The GaN films were fabricated by radio-frequency magnetron sputtering in the installation described elsewhere [7] using a target with a diameter of 88 mm from the GaN powder. The films were sputtered in the $Ar + N_2$ atmosphere. The $Ar : N_2$ ratio was 50 : 50, and the pressure of the gas mixture was 2×10^{-2} Pa. The distance between the target and the substrate was 35 mm,

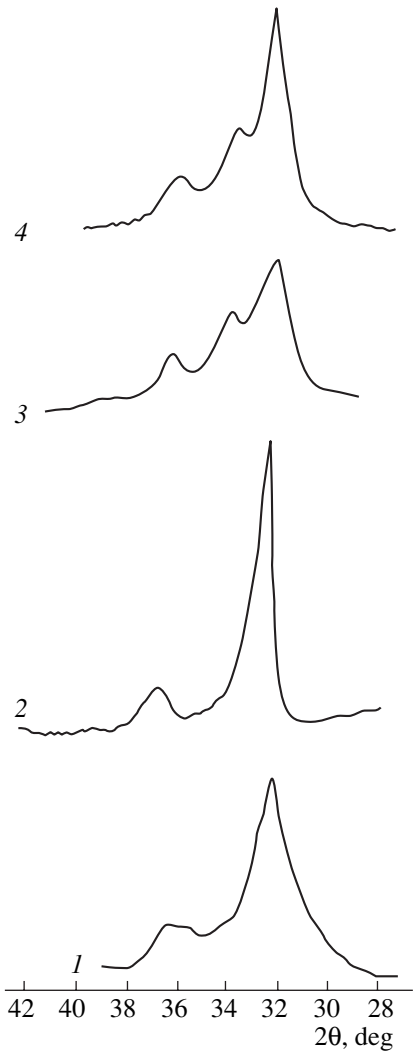

Fig. 1. X-ray diffraction patterns of the GaN films grown on Si(100) at biases of (*1*) –50, (*2*) –100, (*3*) –150, and (*4*) –200 V.

the substrate temperature was 600°C, and the radio-frequency power supplied was 150 W. The single-crystal Si or polycrystalline Al_2O_3 polished wafers were used as the substrates. The film thickness, which was measured using an MII-4 two-beam interferometer, was ~1 μm for the films described. The growth rate of the films was 0.2–0.3 μm/h. The X-ray diffraction analysis of the films obtained was carried out using a DRON-2 diffractometer (Cu radiation).

The specific feature of our method of growing the GaN films is the negative bias up to 200 V, which is applied to the substrate.

The X-ray diffraction patterns for the angular range $2\theta = 28°–42°$ for the films deposited on the Si(100) substrates are shown in Fig. 1. Various negative biases were applied to the substrate during different deposition runs. Three peaks at 32.2° (0.01), 34.4° (0.02), and 36.7° (1.01), which are characteristic of hexagonal GaN, are observed in Fig. 1. An increase in the bias leads to the change of the preferential crystallite orientation in the film. The optimal bias exists (–100 V) when the X-ray diffraction peak is the most intense and narrowest. The relatively large peak width is indicative of the small size of the crystallites in the films.

A characteristic feature of the film deposition by magnetron sputtering is the almost complete absence of tangential growth. For this reason, the films deposited on both single-crystal and amorphous substrates have the same orientation. The X-ray diffraction pattern for the GaN film, which was grown on the polycrystalline Al_2O_3 substrate under the reverse bias of –100 V, is shown in Fig. 2. Three narrow bands from the substrate and one broad band peaked at 32.2° from the GaN polycrystalline film can be seen in Fig. 2.

Based on the above data, we may assume that the film orientation depends on the energy of the particles arriving at the substrate. The particle energy may be controlled by varying the composition or pressure of the gas mixture and the target–substrate distance. This makes it possible to choose deposition modes superior to those used previously and to obtain the films having a crystal structure of a higher quality.

The electrical conduction is observed in the films obtained. The resistance of the films grown on polycrystalline Al_2O_3 is as high as 500 kΩ at room temperature, which corresponds to the resistivity of ~50 Ω cm.

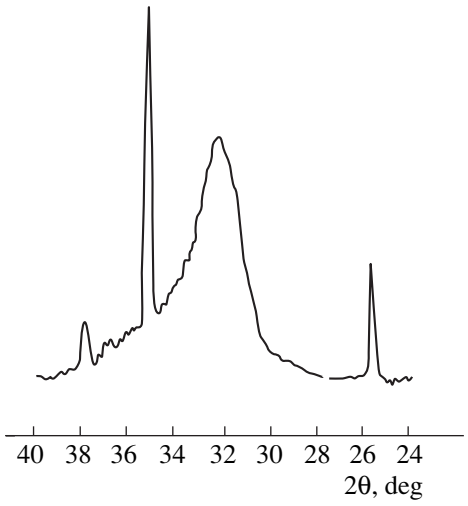

Fig. 2. X-ray diffraction pattern of the GaN film grown on polycrystalline Al_2O_3 at a bias of –100 V.

Based on the results obtained, it is possible to conclude that the GaN polycrystalline films may be grown on Si and polycrystalline Al_2O_3 substrates by radio-frequency magnetron sputtering with reverse bias.

ACKNOWLEDGMENTS

This work was supported by the INTAS Program, grant no. 97-1754.

REFERENCES

1. S. J. Pearton, J. C. Zolper, R. J. Shul, and F. Ren, J. Appl. Phys. **86** (1), 1 (1999).
2. J. Cryst. Growth **189–190** (1998).
3. T. L. Tasley, R. J. Egan, and S. C. Horrigan, Thin Solid Films **164**, 441 (1988).
4. S. Nonomura, S. Kobayashi, T. Gotoh, *et al.*, J. Non-Cryst. Solids **198–200**, 174 (1996).
5. C.-W. Wang, J.-Y. Liao, C.-L. Chen, *et al.*, J. Vac. Sci. Technol. B **17** (4), 1545 (1999).
6. W. T. Young, S. R. P. Silva, J. V. Anguita, *et al.***,** Diamond Relat. Mater. **9**, 456 (2000).
7. A. F. Belyanin, P. V. Pashchenko, and A. P. Semenov, Prib. Tekh. Éksp., No. 3, 220 (1991).

Translated by N. Korovin

Semiconductors, Vol. 35, No. 6, 2001, pp. 690–694. Translated from Fizika i Tekhnika Poluprovodnikov, Vol. 35, No. 6, 2001, pp. 720–724.

ELECTRONIC AND OPTICAL PROPERTIES OF SEMICONDUCTORS

An Analysis of the Temperature Dependence of the Electron Mobility in the $CdGeAs_2$ Single Crystals

S. I. Borisenko*, V. Yu. Rud', Yu. V. Rud'***, and V. G. Tyuterev***

** Kuznetsov Siberian Physicotechnical Institute, Tomsk, 634050 Russia*

*** St. Petersburg State Technical University, St. Petersburg, 195251 Russia*

**** Ioffe Physicotechnical Institute, Russian Academy of Sciences, St. Petersburg, 194021 Russia*

Submitted July 3, 2000; accepted for publication November 20, 2000

Abstract—The experimental temperature dependence of the Hall mobility of the degenerate electron gas in the $CdGeAs_2$ single crystals was analyzed. For this purpose, the drift mobility was calculated by numerically solving the Boltzmann equation in the effective mass and isotropic continuum approximation with consideration for the complicated character of the polar phonon spectrum. Agreement with the experiment in the liquid-nitrogen temperature region was achieved taking into account the electron scattering by a single-charged native defects of the Coulomb type. An agreement of theory and experiment at room temperature was achievable only if electron scattering by the plasma vibrations was considered. © *2001 MAIK "Nauka/Interperiodica".*

1. INTRODUCTION

Adding complexity to the atomic composition of the diamond-like semiconductors is one of the main lines in the development of contemporary semiconductor material science [1]. A transition to studies of ternary analogues of the binary III–V semiconductors results in discovery of crystals with record-breaking nonlinear polarizability d_{36} [2, 3] which belong to a group of ternary compounds with the chalcopyrite lattice. These crystals are considered to be the best nonlinear-optical materials. Among these materials, $CdGeAs_2$ crystals have the largest value of d_{36} = 236 pm/V; thus, they have the greatest prospect for development of highly efficient converters of the CO_2-laser radiation [2–4]. However, the high optical absorption in the $CdGeAs_2$ transparency region is a barrier for implementing these devices [4, 5]. It is well known that one of the criteria for the semiconductor quality is a high Hall mobility of carriers. Recently, great progress in the growth technology of $CdGeAs_2$ has been achieved. Due to development of the method of low-temperature crystallization from nonstoichiometric solutions–melts, single crystals were grown with electron mobility unprecedentedly high for this material [6].

In this paper, the temperature dependence of the electron mobility in $CdGeAs_2$ is analyzed on the basis of the theoretical concepts concerning the electron and phonon spectra of this compound [7, 8]. In contrast to the calculations carried out previously [9], we calculated mobility for the samples with degenerate electron gas with regard to scattering by the plasma vibrations. Scattering by nonpolar optical phonons is disregarded due to the insignificance of this effect [10]. Anisotropy and nonparabolicity of the electron energy spectrum are also ignored, as is the anisotropy of scattering by the polar phonons (due to averaging of characteristics over the angles). The iteration method described in [11] was used for numerical solution of the linearized Boltzmann equation. Results of calculation are compared with the experimental temperature dependences of the Hall mobility for the sample from [6].

2. MOBILITY CALCULATION METHOD

The procedure for calculating the electron mobility in $CdGeAs_2$ in the temperature region from 77 to 300 K involves the consideration of both nonelasticity of polar scattering by the long-wavelength optical phonons (PO), which exists in semiconductors of this type [8], and degeneracy of the electron gas in samples from [6]. To satisfy the requirements mentioned above, the Boltzmann equation in the low-field approximation was reduced to the functional equation for nonequilibrium addition to the distribution function; this equation was numerically solved by the iteration method. For a combined scattering which includes elastic scattering and PO-scattering, the functional equation can be written according to [11] as

$$\tau(\varepsilon) = \tau_0(\varepsilon)\left\{1 + \sum_{\nu}[S_\nu^+(\varepsilon)\tau(\varepsilon + \hbar\omega_\nu) + S_\nu^-(\varepsilon)\tau(\varepsilon - \hbar\omega_\nu)]\right\}, \quad (1)$$

1063-7826/01/3506-0690$21.00 © 2001 MAIK "Nauka/Interperiodica"

where $\tau(\varepsilon)$ is a function of the electron energy ε which has the dimension of the relaxation time and determines the nonequilibrium addition to the distribution function expressed by the conventional equation

$$g(k) = e\frac{\partial f_0}{\partial \varepsilon}\tau(\varepsilon)E v_k. \quad (2)$$

Here, $f_0(\varepsilon)$, E, v_k, $\hbar\omega_\nu$ are equilibrium Fermi–Dirac function, electric field strength, the electron velocity with the wave vector k and energy $\varepsilon = \hbar^2k^2/2m^*$ with angle-averaged effective mass m^*, and energy of the long-wavelength polar phonon with number ν, respectively;

$$1/\tau_0(\varepsilon) = 1/\tau_{so}(\varepsilon) + \sum_i 1/\tau_i(\varepsilon), \quad (3)$$

where $\tau_i(\varepsilon)$ is the relaxation time of the ith elastic scattering mechanism;

$$1/\tau_{so}(\varepsilon) = \sum_\nu \{S^+_{o\nu}(\varepsilon) + S^-_{o\nu}(\varepsilon)\}$$

is the function corresponding to a nonelastic polar scattering,

$$S^\pm_\nu(\varepsilon) = A_\nu\left[N_\nu + \frac{1}{2} \pm \frac{1}{2} \mp f_0(\varepsilon)\right]\frac{f'_0(\varepsilon')}{f'_0(\varepsilon)} \times \frac{(\varepsilon' + \varepsilon + 2\eta^2)}{\varepsilon\sqrt{\varepsilon}}S(\varepsilon, \varepsilon')\Big|_{\varepsilon' = \varepsilon \pm \hbar\omega_\nu},$$

$$S^\pm_\nu(\varepsilon) = A_\nu\left[N_\nu + \frac{1}{2} \pm \frac{1}{2} \mp f_0(\varepsilon)\right] \times \frac{2}{\sqrt{\varepsilon}}S_o(\varepsilon, \varepsilon')\Big|_{\varepsilon' = \varepsilon \mp \hbar\omega_\nu},$$

$$S(\varepsilon, \varepsilon') = \ln\left[\frac{(\sqrt{\varepsilon'} + \sqrt{\varepsilon})^2 + \eta^2}{(\sqrt{\varepsilon'} - \sqrt{\varepsilon})^2 + \eta^2}\right] - \frac{4\sqrt{\varepsilon\varepsilon'}[(\varepsilon' - \varepsilon)^2 + 3\eta^2(\varepsilon' + \varepsilon) + 2\eta^4]}{(\varepsilon' + \varepsilon + 2\eta^2)[(\varepsilon' - \varepsilon)^2 + 2\eta^2(\varepsilon' + \varepsilon) + \eta^4]}, \quad (4)$$

$$S_o(\varepsilon, \varepsilon') = \ln\left[\frac{(\sqrt{\varepsilon'} + \sqrt{\varepsilon})^2 + \eta^2}{(\sqrt{\varepsilon'} - \sqrt{\varepsilon})^2 + \eta^2}\right] - \frac{4\sqrt{\varepsilon\varepsilon'}\eta^2}{(\varepsilon' - \varepsilon)^2 + 2\eta^2(\varepsilon' + \varepsilon) + \eta^4},$$

$$f'_0(\varepsilon) = \frac{\partial f_o(\varepsilon)}{\partial \varepsilon}, \quad \eta^2 = \frac{\hbar^2\alpha^2_\infty}{2m^*},$$

$$A_\nu = \frac{\sqrt{2m^*}e^2\omega_\nu}{32\pi\varepsilon_0\hbar}C_{\mathrm{PO}_\nu},$$

where α_∞ is a reciprocal screening length of high-frequency electric oscillations, $C_{\mathrm{PO}_\nu} = \tilde{S}^2_\nu/\omega^2_\nu$ is the coupling constant of the electron–phonon interaction, $\tilde{S}^2_\nu$ is the angle-averaged squared oscillator strength of optical phonon [9], $N_\nu = 1/[\exp(\hbar\omega_\nu/k_0T) - 1]$ is the Bose–Einstein function, and ε_0 is the dielectric constant.

The electron scattering by plasmons, which is one of the possible scattering mechanisms in semiconductors with a high concentration of free carriers, can be described, according to [12], by a mechanism similar to PO-scattering if we replace the phonon frequency ω_ν in formulas (3) and (4) by the plasma frequency ω_{PL} and constant of the electron interaction with phonon C_{PO} by constant of the electron interaction with plasmon C_{PL}, where

$$\omega_{\mathrm{PL}} = \sqrt{\frac{e^2n}{\varepsilon_0\varepsilon_\infty m^*}}, \quad C_{\mathrm{PL}} = \frac{1}{\varepsilon_\infty}, \quad (5)$$

n is the electron concentration, and ε_∞ is the high-frequency relative permitivity.

The relaxation time for scattering by the impurity ions was calculated using the well-known Brooks–Herring formula:

$$\tau_I = \frac{16\pi\sqrt{2m^*}\varepsilon_0^2\varepsilon_s^2}{e^4N_I[\ln(1 + \beta) - \beta/(\beta + 1)]}\varepsilon^{3/2}, \quad (6)$$

where $\beta = 8m^*\varepsilon/\hbar^2\alpha_s^2$; α_s is the reciprocal screening length of low-frequency electric fields; and N_I and ε_s are concentration of the single-charged impurity ions and static dielectric constant of semiconductor, respectively.

The scattering of acoustic vibrations by the deformation potential (DA) was regarded as elastic, and the relaxation time was calculated by the well-known formula

$$\tau_{\mathrm{DA}} = \frac{\pi\hbar^4\tilde{c}_L}{\sqrt{2}(m^*)^{3/2}\tilde{D}_c^2k_0T}\varepsilon^{-1/2}. \quad (7)$$

For II–IV–V_2 crystals in the isotropic continuum approximation, $\tilde{D}_c$ is the angle-averaged deformation potential constant which corresponds to the bottom of the conduction band and

$$\tilde{c}_L = \frac{1}{5}(2c_{11} + c_{33}) + \frac{2}{15} \times [(2c_{13} + c_{12}) + 2(2c_{44} + c_{66})] \quad (8)$$

is the modulus of elasticity for longitudinal acoustic vibrations. Formula (8) was obtained from the angle-averaging component of the equation of state for elastic anisotropic continuum with the chalcopyrite symmetry along the wave vector of longitudinal acoustic vibrations.

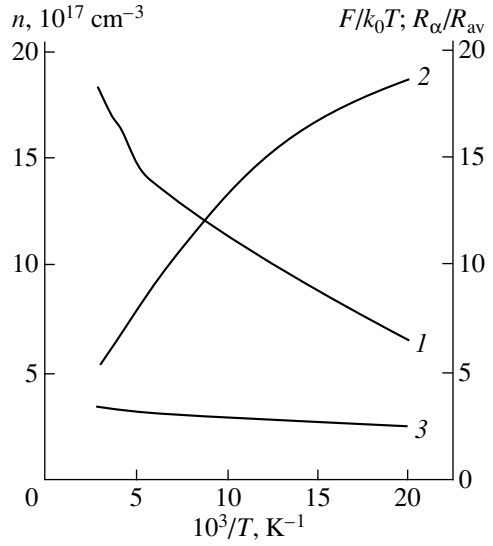

Fig. 1. The temperatures dependences of some parameters of the electron gas in the $CdGeAs_2$ single crystals: (*1*) the electron concentration *n*, (*2*) the reduced electron energy at the Fermi level F/k_0T, and (*3*) the ratio of R_α/R_{av} (see text).

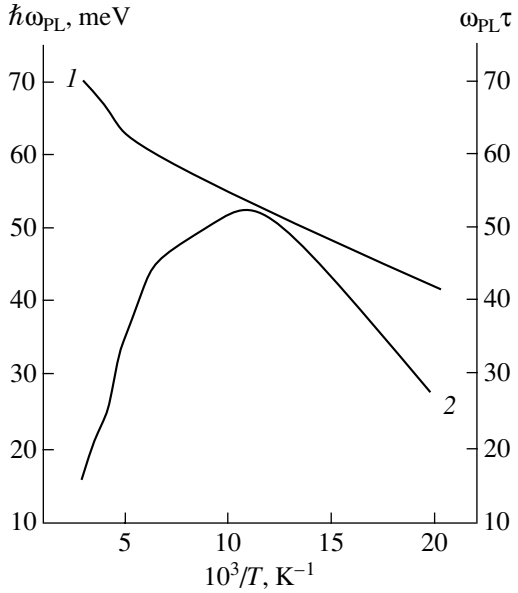

Fig. 2. Characteristics of the plasma vibrations of the electron gas in $CdGeAs_2$: (*1*) $\hbar\omega_{PL}$, and (*2*) $\omega_{PL}\tau$.

3. COMPARISON OF THE RESULTS OF CALCULATION WITH EXPERIMENTAL DATA

Values of the $CdGeAs_2$ parameters which were used in the analysis of the temperature dependence of the electron mobility are listed in the table. The electron–phonon interaction coupling constants for PO phonons with similar frequencies and with Γ_4 and Γ_5 symmetries are combined. It should be noted that the electron–phonon interaction constant is an order of magnitude less than the electron–plasmon interaction constant.

$CdGeAs_2$ parameters used in calculation

Designation	Value	Source
m^*	$0.034m_0$	[13]
ε_s	18.1	[14]
ε_∞	15.3	[14]
$\tilde{c}_L$	11.2×10^{12} N/m^2	[15]*
$\tilde{D}_c$	14.5 eV	[16]**
$\hbar\omega_1$	12 meV	[14]
$\hbar\omega_2$	20 meV	[14]
$\hbar\omega_3$	25 meV	[14]
$\hbar\omega_4$	33 meV	[14]
C_{PO1}	0.0008	[14]
C_{PO2}	0.0012	[14]
C_{PO3}	0.0052	[14]
C_{PO4}	0.0049	[14]
C_{PL}	0.065	[14]

* Value is calculated by formula (8).

** Value is obtained as arithmetic average of the deformation potential constants in the binary analogues InAs and GaAs.

Mobility was calculated in the temperature range from 50 to 350 K. The temperature dependence of the electron concentration *n* of the sample under study (curve *1*) calculated from the temperature dependence of the Hall coefficient [6], as well as the temperature dependences of the reduced Fermi energy F/k_0T (curve *2*) and the ratio of the screening length R_α to the halved average distance between a single-charged defects of donor type indicated as R_{av} (curve *3*), is shown in Fig. 1. We will refer to the above defects as the impurity ions. Calculation of the Fermi level was performed in the effective mass approximation on the assumption that the electron concentration is equal to concentration of the impurity ions ($n = N_I$). In order to calculate the screening length, we used the Debye formula for a degenerate electron gas. According to Fig. 1, the electron gas is degenerate in the entire temperature range in the crystals studied in [6] and the screening length R_α is larger than R_{av} by a factor of 2–3. The latter result suggests that the approximation of one-particle electron scattering by ions in the sample under study is not valid, and in this case the conventional Debye formula for calculation of the screening length is incorrect. It should be noted that we failed to explain an occurrence of high concentration of electrons in samples near liquid-nitrogen temperature on the assumption that, in such a material, only simple impurity centers of a donor type with positive activation energy and

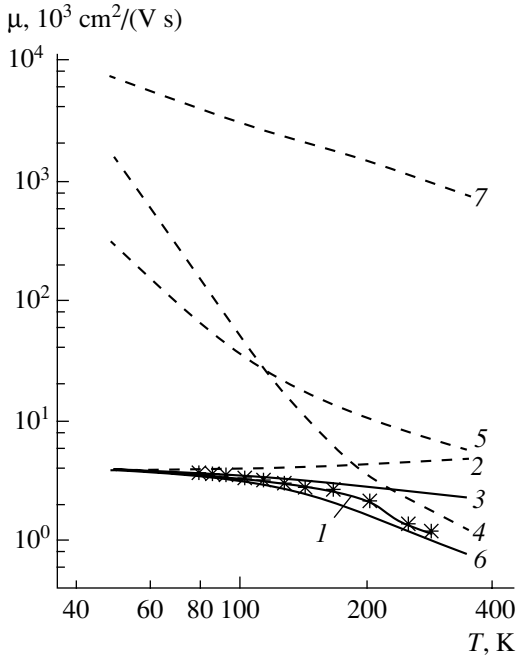

Fig. 3. Experimental (curve *1*, [6]) and calculated temperature dependences of the electron mobility in the $CdGeAs_2$ single crystals in which the following scattering mechanisms are considered: (*2*) scattering by the impurity ions (ION), (*3*) ION + PO (polar scattering by optical phonons), (*4*) PL (by plasma vibrations), (*5*) PO, (*6*) ION + PO + PL, and (*7*) DA (deformation potential scattering by acoustic phonons).

a low density of states at the bottom of the conduction band exist.

The temperature dependence of the plasmon energy $\hbar\omega_{PL}$ (curve *1*) calculated by formula (5), as well as dependence of the product of plasma frequency by the energy-averaged momentum relaxation time $\omega_{PL}\tau$ (curve *2*), the value of which characterizes the condition for the plasmon existence [12], are shown in Fig. 2. These values are calculated with regard to the experimental temperature dependences of the electron concentration and the Hall mobility (see Fig. 1 in [6]). It can be seen from Fig. 2 that plasmons may occur over the entire temperature range ($\omega_{PL}^2\tau^2 \gg 1$) and that their energy is higher than the maximum PO-phonon energy (see table), although these energies are comparable in magnitude.

Results of calculation of the drift mobility temperature dependence with consideration for different scattering mechanisms (curves *2–7*) and the experimental data on the Hall mobility (curve *1*) are shown in Fig. 3. As was to be expected, the basic scattering mechanism at temperatures near the liquid-nitrogen one is scattering by the impurity ions (single-charged defects). The Brooks–Herring formula yields a good agreement with experimental data in this temperature region on the assumption that the screening length equals the average distance between ions (curve *2*). Consideration of combined scattering by the impurity ions and by PO-phonons in the room temperature region (curve *3*) yields a mobility which is considerably higher than the experimental value. A more intense actual electron scattering in the sample can be related, as we believe, to the plasmon scattering (curve *4*), which is more important at room temperature than scattering by PO-phonons (curve *5*) in terms of the electron–plasmon interaction model. Taking into account the PL-scattering combined with scattering by the impurity ions and by PO-phonons (curve *6*) in the room temperature region yields a rather good agreement with experimental data. Interaction of electrons with PO-phonons and plasmons was screened in the same way as interaction with the impurity ions. It should be noted that the electron scattering by DA-phonons (curve *7*) has a low intensity in the temperature region under consideration and, therefore, can be neglected.

4. CONCLUSION

An analysis of the experimental temperature dependences of the Hall mobility in $CdGeAs_2$ with a degenerate electron gas suggests that in the liquid-nitrogen temperature region the dominant scattering mechanism is scattering by ionized centers of the Coulomb type related to the native defects in the $CdGeAs_2$ single crystals. At room temperature, such a mechanism could involve scattering by plasmons or combined electron–phonon and electron–electron scattering. As our results show, an analysis of these mechanisms is urgent for compound semiconductors. At the same time, an important problem for further studies is the analysis of the temperature dependence of the Hall coefficient. The purpose of this analysis is to clarify the cause of such a high electron concentration at liquid-nitrogen temperature and to determine the nature of the native lattice defects of donor type in the $CdGeAs_2$ single crystals with unprecedentedly high electron mobility.

REFERENCES

1. N. A. Goryunova, *The Chemistry of Diamond-like Semiconductors* (Leningr. Gos. Univ., Leningrad, 1963; Chapman and Hall, London, 1965).
2. N. A. Goryunova, S. M. Ryvkin, I. M. Fishman, *et al.*, Fiz. Tekh. Poluprovodn. (Leningrad) **3**, 1525 (1968) [Sov. Phys. Semicond. **2**, 1834 (1969)].
3. F. P. Kesamanly and Yu. V. Rud', Fiz. Tekh. Poluprovodn. (St. Petersburg) **27**, 1761 (1993) [Semiconductors **27**, 969 (1993)].
4. M. C. Ohmer and R. Pandey, MRS Bull. **23**, 16 (1998).
5. P. G. Schunemann, K. L. Schepler, and P. A. Budni, MRS Bull. **23**, 45 (1998).

6. I. K. Polushina, V. Yu. Rud', Yu. V. Rud', and T. N. Ushakova, Fiz. Tverd. Tela (St. Petersburg) **41**, 1190 (1999) [Phys. Solid State **41**, 1084 (1999)].

7. A. S. Poplavnoĭ, Yu. I. Polygalov, and V. A. Chaldyshev, Izv. Vyssh. Uchebn. Zaved., Fiz., No. 7, 17 (1970).

8. A. S. Poplavnoĭ and V. G. Tyuterev, Izv. Vyssh. Uchebn. Zaved., Fiz., No. 6, 39 (1978).

9. S. I. Borisenko, G. F. Karavaev, and V. G. Tyuterev, Fiz. Tekh. Poluprovodn. (Leningrad) **16**, 432 (1982) [Sov. Phys. Semicond. **16**, 274 (1982)].

10. S. I. Borisenko, G. F. Karavaev, S. I. Skachkov, and V. G. Tyuterev, Fiz. Tekh. Poluprovodn. (Leningrad) **17**, 2198 (1983) [Sov. Phys. Semicond. **17**, 1406 (1983)].

11. S. I. Borisenko, Fiz. Tekh. Poluprovodn. (St. Petersburg) **35** (3), 313 (2001) [Semiconductors **35**, 298 (2001)].

12. A. S. Davydov, *Theory of Solid State* (Nauka, Moscow, 1976), Chap. 4, p. 90.

13. S. I. Borisenko and G. F. Karavaev, Izv. Vyssh. Uchebn. Zaved., Fiz., No. 4, 101 (1988).

14. G. D. Holah, A. Miller, W. D. Dunnett, and G. W. Iseler, Solid State Commun. **23**, 75 (1977).

15. Tu Hailing, G. A. Saumbers, W. A. Lambson, and R. S. Teigelson, J. Phys. C **15**, 1399 (1982).

16. S. I. Borisenko and G. F. Karavaev, Izv. Vyssh. Uchebn. Zaved., Fiz., No. 5, 117 (1988).

Translated by I. Kucherenko

Semiconductors, Vol. 35, No. 6, 2001, pp. 695–699. Translated from Fizika i Tekhnika Poluprovodnikov, Vol. 35, No. 6, 2001, pp. 725–730.

ELECTRONIC AND OPTICAL PROPERTIES OF SEMICONDUCTORS

Fine Structure of the Edge Ultraviolet Luminescence of GaN:Mg Films Activated in a Nitrogen Plasma and the Electroluminescence of a ZnO–GaN:Mg Heterostructure Based on These Films

A. N. Georgobiani*, A. N. Gruzintsev[,1], M. O. Vorob'ev*, U. Kaiser***, W. Richter***, and I. I. Khodos****

** Lebedev Physical Institute, Russian Academy of Sciences, Leninskiĭ pr. 53, Moscow, 117924 Russia*

*** Institute of Microelectronic Technology and Ultrahigh-Purity Materials, Russian Academy of Sciences, Chernogolovka, Moscow oblast, 142432 Russia*

[1] e-mail: gran@ipmt-hpm.ac.ru

**** Institute of Solid State Physics, Friedrich-Shiller-Universität, Jena, D-07743, Germany*

Submitted November 10, 2000; accepted for publication November 21, 2000

Abstract—Studies of the effect of annealing in a nitrogen plasma of GaN films doped with Mg on their photoluminescence and photoconductivity spectra and on the type of conductivity were carried out. A number of narrow emission bands that peaked at 3.06, 3.17, and 3.27 eV in the ultraviolet (UV) spectral region in GaN:Mg are observed after low-temperature annealing in a nitrogen plasma. The ZnO–GaN:Mg heterostructures are obtained with electroluminescence peaks in the UV excitonic region of GaN at an energy of 3.44 eV and in the edge region of GaN at an energy of 3.26 eV. *© 2001 MAIK "Nauka/Interperiodica".*

INTRODUCTION

Fabrication of high-quality gallium nitride films of *n*- and *p*-type conductivity permitted the production of efficient photodiodes and semiconductor lasers for the blue spectral region [1–3]. One should note that in this case, native point defects of GaN, which form the deep energy levels in the material band gap, serve as a main channel of radiative recombination [4, 5]. The improvement of the stoichiometry and crystallinity of GaN films will allow one not only to shift the emission peak to the region of the ultraviolet (UV) exciton luminescence of GaN, but also to enhance considerably the efficiency of electroluminescent structures. In our previous study [6], we established the donor–acceptor nature of the blue emission with a peak at 2.8 eV, with the nitrogen vacancy in one of its charge states being a donor. Consequently, annealing in a nitrogen atmosphere is required for stoichiometry improvement. It is worthwhile to note that a short-term high-temperature annealing in a nitrogen atmosphere does not result in the desired situation due to the fracture of the film surface and the volatilization of nitrogen from GaN [7, 8]. An increase in the effective pressure of atomic nitrogen above a GaN film with simultaneous lowering of the annealing temperature is needed to reduce the material evaporation. This is possible by annealing the film in a nitrogen plasma when the fraction of atomic nitrogen is considerably lower (by 4–5 orders of magnitude) than during annealing in a nitrogen atmosphere under the same conditions.

This annealing allows one not only to reduce the number of native donor defects, which provide the blue emission, but to affect also the film conductivity. Doping GaN during growth with acceptor impurities (Mg or Zn) results only in the formation of a high-resistivity material due to the compensation effect of these impurities. Only the use of electron-beam irradiation after the growth of GaN:Mg films allowed Nakamura *et al*. [4] to obtain the low-resistivity material of *p*-type conductivity. It was found [4] that annealing of initially insulating GaN:Mg films at a temperature of T_a = 700°C in a nitrogen atmosphere also results in the formation of hole conductivity. This effect was attributed [4] to the decomposition of the electrically inactive Mg–Hg complexes (formed in the process of film growth by MOCVD) with the origination of isolated Mg acceptor centers, which provide the efficient hole conductivity necessary for producing the semiconductor structures.

It is of interest to study the effect of the acceptor impurity activation processes on the properties of film luminescence. Due to a lower hole mobility, the radiative recombination of carriers in a photodiode structure occurs in a *p*-type region. Thus, it is the emission of a film doped with acceptors that determines the spectral characteristics of devices. Li *et al.* [9] have observed this increase in the blue emission band in GaN:Mg films after a short-term high-temperature annealing. Similar annealing of the undoped films in a nitrogen atmosphere [7] resulted in a reduction of the impurity luminescence intensity and in an increase in the exciton

1063-7826/01/3506-0695$21.00 © 2001 MAIK "Nauka/Interperiodica"

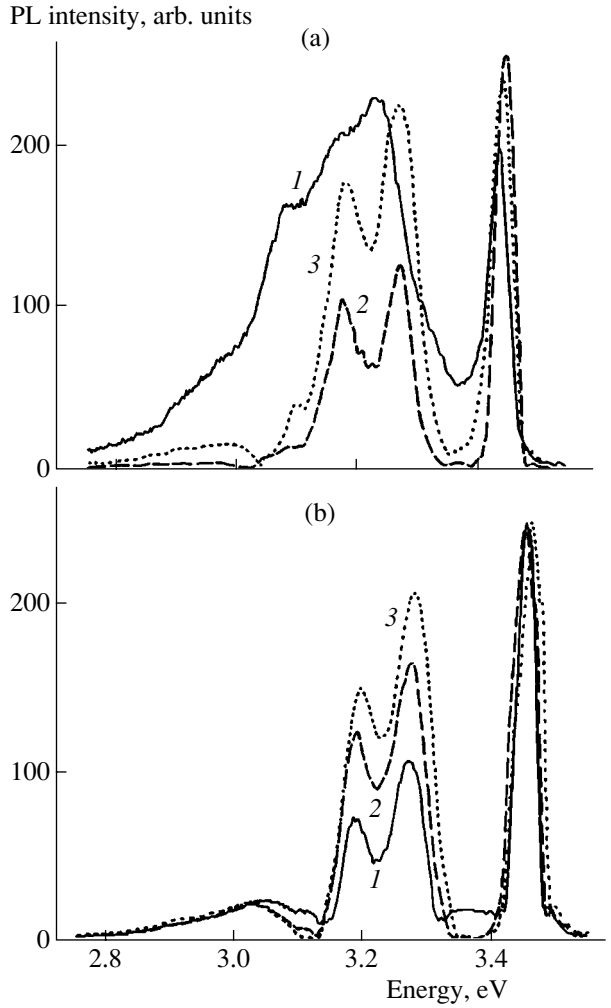

Fig. 1. Photoluminescence (PL) spectra of GaN:Mg films at a temperature of 80 K. (a) Unannealed samples (*1*) and the samples annealed in a nitrogen atmosphere (*2*) and a nitrogen plasma (*3*) at a temperature T_a = 700°C. (b) The samples annealed in a nitrogen plasma at temperatures T = (*1*) 400, (*2*) 500, and (*3*) 600°C.

luminescence intensity. This was considered [7] as evidence of the crystallinity enhancement and the improvement in the film morphology in the process of annealing accompanied by the simultaneous modification of the film stoichiometry. According to [8], annealing under the same conditions, on the contrary, worsened the film morphology and resulted in an increase in the intensity of all the emission bands.

Here, we are interested in the effect of annealing in a nitrogen plasma at various temperatures on the *p*-type conductivity activation and emission spectra (as well as the photoconductivity) in doped GaN:Mg films. Employing nitrogen plasma allows the film stoichiometry to shift drastically in the direction of the nitrogen excess and to improve its crystalline structure at comparatively low annealing temperatures. The ZnO–GaN:Mg diode heterostructures were obtained on the basis of annealed *p*-GaN:Mg films. The similarity between the crystalline and band structures of these two materials with hexagonal symmetry allows us to expect that this type of structure may contribute much to the development of electroluminescent devices.

EXPERIMENTAL

We studied *p*-GaN:Mg films with the hole concentration $p = 5 \times 10^{15}$ cm^{-3}, resistivity $\rho = 5.6 \times 10^4$ Ω cm, and thickness 0.1 μm. The Hall measurements showed that the carrier mobility was 100–150 cm^2/(V s) in the unannealed films. The films under study were grown by molecular-beam epitaxy (MBE) on sapphire substrates with (0001) orientation. The layers of zinc oxide were obtained by the oxidation of Zn films of thickness 0.5 μm on the surface of GaN at 550°C in an oxygen atmosphere. The annealing of the GaN:Mg films for 2 h at temperatures in the range T_a = 300–700°C in a nitrogen plasma was carried out in the radical-beam epitaxy setup that was described in detail previously [10]. The nitrogen plasma obtained using a high-frequency field was passed through a strong constant magnetic field for removing the plasma ionic component. Thus, the annealing was performed in an atmosphere of nitrogen neutral atoms (radicals). The concentration of neutral nitrogen atoms in this method exceeded by 4–5 orders of magnitude their concentration in the inactivated atmosphere under the same pressures and annealing temperature.

An ILGI-503 pulsed nitrogen laser with the radiation wavelength 337.1 nm and a pulse duration of 10 ns (the mean radiation power was 10 kW) was used for the photoluminescence (PL) excitation. The spectra were analyzed with the use of an MDR-6 double monochromator controlled by a computer, which yielded a spectral resolution no worse than 1 meV for the slits used. In the photoconductivity measurements, the planar platinum contacts were deposited onto the film. The nonrectifying properties of the contacts were tested by measurements of the forward and reverse portions of the current–voltage (*I–V*) characteristic. The photoconductivity was excited by a halogen lamp with a power of 100 W modulated by a chopper and was passed through an MDR-12 high-aperture monochromator. The samples were mounted in an optical cryostat at liquid- nitrogen temperature.

In studies of the effect of annealing on the crystallinity and morphology of the GaN:Mg film surface, a JEOL-2000 transmission electron microscope was used.

RESULTS

The PL spectra of GaN:Mg films prior to and after annealing in an atmosphere of inactivated and activated nitrogen at various temperatures are shown in Fig. 1. One should note the good initial stoichiometry of our

films, as evidenced by a practical absence of the blue band peaking at 2.88 eV (Fig. 1a, curve *1*), which is associated with nitrogen vacancies in GaN. A broad red band that peaked at 3.23 eV and a narrow band of bound excitons with a peak at 3.44 eV are observed in the emission spectrum of unannealed films. It is worthwhile to point out the presence of a weakly pronounced structure in the form of several shoulders in the edge emission in the long-wavelength region. This indicates the presence of several overlapping elementary bands associated with the various acceptor centers in this emission region.

Annealing in a nitrogen atmosphere results in a considerable narrowing of the edge luminescence due to a decrease in the intensity of its long-wavelength components (Fig. 1b). In this case, the intensity of the excitonic emission increases, which indicates that the crystalline structure improves during annealing. After the annealing of GaN:Mg films, three peaks at 3.06, 3.17, and 3.27 eV are well pronounced in the edge region of the PL spectrum. With the temperature increase of annealing in a nitrogen plasma (Fig. 1b), the intensities of the first two luminescence bands increase, whereas the intensity of the band peaked at 3.06 eV remains practically constant. The intensity of the exciton peak also remained practically unchanged.

Annealing in a nitrogen plasma in our experiments shifts the stoichiometry of GaN toward the nitrogen excess; i.e., acceptor type defects become predominant. Therefore, one should expect an increase in the *p*-type conductivity of the GaN:Mg films under study after annealing. The resistivities of the films prior to and after annealing in the plasma at various temperatures are listed in the table. It can be seen that the high-temperature annealing enhances the conductivity of the material almost by an order of magnitude. It is of interest to study the effect of annealing on the photoconductivity of GaN:Mg films. The photoconductivity spectra of unannealed and annealed films are shown in Fig. 2. In the unannealed material, one can separate a broad extrinsic photoconductivity band peaked at 1.55–2.07 eV. A low-temperature annealing (Fig. 2a) at T_a = 400°C causes the emergence of an intense narrow peak at 3.53 eV associated with the interband carrier transitions in GaN. As the annealing temperature increases (Fig. 2b), this peak disappears, possibly caused by the degradation of the film surface morphology [11]. In this case, the increase in the photosensitivity of GaN:Mg films in the red region of the spectrum at 1.38–1.46 eV occurs.

As was stated above, annealing results in the enhancement of the conductivity of GaN:Mg films. The predominance of the UV luminescence bands in films of such a type allows one to hope that the UV light-emitting diode structures based on these films can be produced. As the layer of *n*-type conductivity, we used low-resistivity layers of zinc oxide 0.5 μm thick obtained by oxidation of Zn deposited onto the

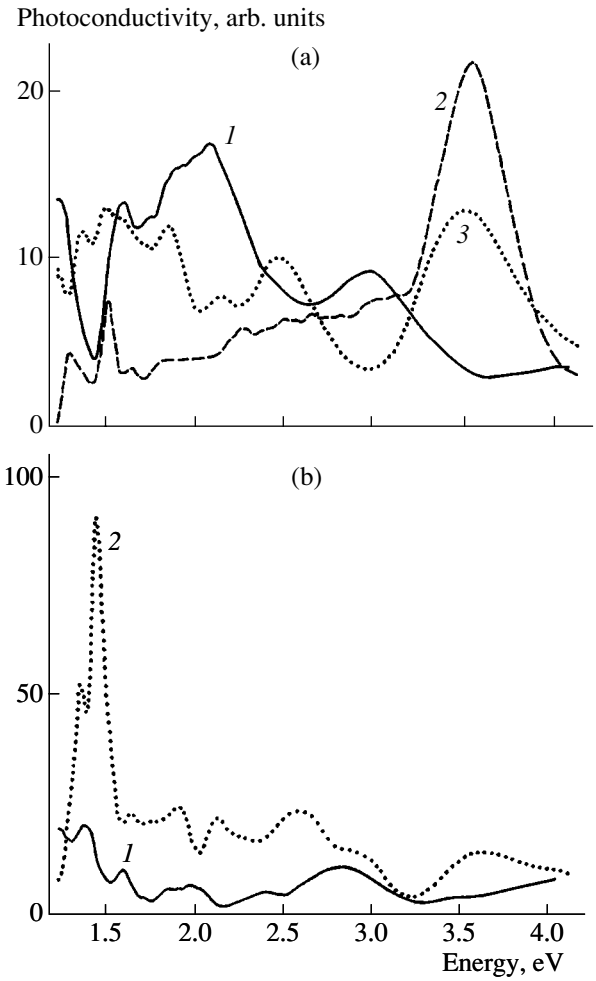

Fig. 2. Photoconductivity spectra of GaN:Mg films at a temperature T = 300 K. (a) (*1*) Unannealed samples and the samples annealed in a nitrogen plasma at temperatures T_a = (*2*) 400 and (*3*) 500°C. (b) The samples annealed in a nitrogen plasma at temperatures T_a = (*1*) 600 and (*2*) 700°C.

GaN:Mg film surface. The oxide layers had perfect crystallinity and had only narrow lines of bound excitons in the emission spectra. If a constant positive voltage was applied from the GaN side and a negative voltage was applied from the zinc oxide, electroluminescence (EL) of the diode structure was observed. The EL spectrum of these structures measured at a voltage of 10 V and at liquid-nitrogen temperature is shown in Fig. 3. The UV emission bands characteristic of GaN:Mg films are observed; these are excitonic bands peaked at 3.44 eV, and edge bands with peaks at 3.17 and 3.27 eV. This indicates that the radiative recombination of carriers occurs mainly in the region of the hole conductivity of GaN, although the peak of green emission at 2.30 eV with a rather low intensity can be associated with the luminescence of zinc oxide layers optically excited by UV radiation.

A study of *I–V* characteristics of the diode structures obtained indicates that there is a Schottky barrier in the

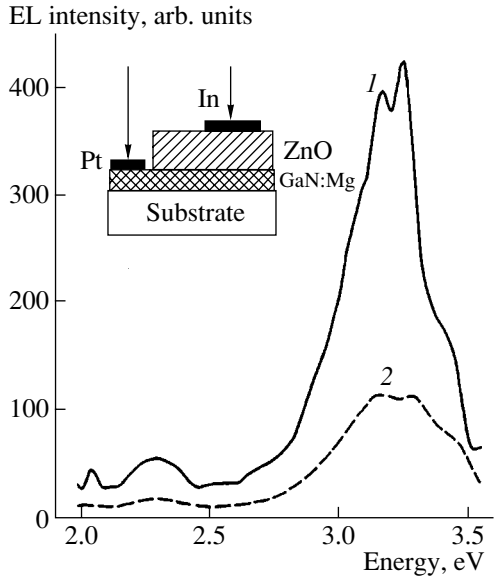

Fig. 3. Electroluminescent spectra of ZnO–GaN:Mg diode heterostructures at temperatures T = (*1*) 80 and (*2*) 300 K. In the inset, the schematic representation of a diode structure is given.

region of a *p–n* junction, which explains the rather high (–10 V) operating voltages of the obtained EL sources of UV emission. However, the low preparation temperatures of zinc oxide layers of *n*-type conductivity allow one to avoid interdiffusion of heterolayer components; this is evidenced by the similarity between the PL spectra of GaN:Mg films and the EL of a corresponding heterostructure.

DISCUSSION OF THE RESULTS

The results obtained testify that annealing GaN:Mg films in a nitrogen plasma affects the properties of point defects more strongly than annealing in a vacuum or in nitrogen vapor. Previously, Li *et al*. [9] observed in heavily-doped GaN:Mg films UV luminescence that peaked at 3.455 eV for the excitons line and at 3.285 eV for the red line, the intensity of which drastically decreased after short-term high-temperature annealing at T_a = 700°C in a nitrogen-enriched ambiance. Such an emission was believed [9] to be caused by the carrier recombination from the conduction band at the Mg acceptor level. However, the edge emission has a broad band with a pronounced structure, which indicates that several acceptor centers are present in GaN:Mg. The width of the lines and the positions of the peaks, as a rule, depend on the film growth conditions, and, in our studies (Fig. 1), on the annealing temperature, as the properties of point defects in the semiconductor depend on these two factors.

Dependence of the GaN : Mg film resistivity on the annealing temperature in a nitrogen plasma

Sample no.	T_a, °C	ρ, 10^4 Ω cm
1	(as-grown)	5.6
2	300	5.5
3	400	5
4	500	2.3
5	600	1.3
6	700	0.58

As the annealing temperature increases, the enhancement of the acceptor center concentration and the intensity of the luminescence bands associated with them is observed (Fig. 1). Taking into account that a nitrogen plasma provides the highest partial pressure of atomic nitrogen at the film surface, the nitrogen vacancies are filled with nitrogen atoms when these vacancies reach the surface. Actually, only by annealing under these conditions, can the stoichiometry of GaN shift toward the nitrogen excess. The number of native acceptors (Ga vacancies) begins to increase. In the edge region, the UV emission has three clearly pronounced peaks at 3.06, 3.17, and 3.27 eV (Fig. 1b). A Mg impurity and Ga vacancy in two different charge states can probably be involved in the formation of corresponding emission centers.

An isolated defect (Mg at the Ga site, Mg_{Ga}) yields an acceptor level located near the valence band. Therefore, the UV red luminescence band peaked at 3.27 eV can be caused by electron transitions from the conduction band to the Mg acceptor level. In this case, by analogy with the wide-gap compound CdS, which also has a hexagonal crystal lattice, the near-band edge luminescence can be caused not only by isolated acceptors but also by their complexes with native defects when the latter occupy the neighboring lattice sites [12]. However, the acceptor level determines the emission peak position. Acceptors associated with the Ga vacancies yield deeper electrically inactive levels in GaN:Mg. Therefore, in the PL spectrum, the longer wavelength lines of the edge emission peaked at 3.06 and 3.17 eV can be associated with them.

Here, it is worthwhile to note that we previously [11] attributed the UV peak of the edge luminescence at 3.30 eV (T = 80 K) of the heavily doped GaN:Zn films (6×10^{19} cm^{-3}) to the radiative transitions of electrons from the conduction band to the level of the isolated Zn. In our case, the recombination mechanism is similar, although the acceptor level is caused by the Mg impurity and Ga vacancy. The situation obtained by doping GaN films with acceptors of Group II is of interest. An increase in the doping dose or activating annealing in a nitrogen excess (plasma) [13] quenches the blue emission at 2.88 eV and results in UV edge luminescence. Consequently, the optimum light-emitting diode structures based on GaN have to yield not a blue but a UV emission with a peak in the region of 3.18–3.26 eV.

The increase in the number of levels of isolated Zn acceptors in the GaN band gap after high-temperature annealing in a nitrogen plasma results in the predominance of red bands with peaks at 1.38–1.46 eV in the photoconductivity spectra (Fig. 2). These bands can be caused by hole transitions from the valence band to deep acceptor centers. In this case, the material photosensitivity in the extrinsic region increases almost by an order of magnitude compared to the unannealed films. Until now, the use of GaN in photodetectors of UV radiation was only known with a wavelength lower than 350 nm. However, our studies have shown that the GaN:Mg films also demonstrate photosensitivity bands in the visible spectral region. The positions of the band peaks are consistent with the energy distance of the corresponding levels of native and impurity defects from the valence band. By controlling material stoichiometry in the course of annealing, one can vary the photosensitivity in the extrinsic region of the spectrum. At high annealing temperatures, the photoconductivity peaks associated with the interband transitions disappear due to the degradation of the GaN:Mg film surface.

CONCLUSION

Thus, we showed that the annealing in a nitrogen plasma of GaN:Mg films results in the GaN stoichiometry shift toward nitrogen excess. In this case, the decrease in the number of donor–acceptor pairs occurs with the participation of a N vacancy as a donor, which gives rise to the blue emission band of GaN:Mg peaked at 2.88 eV. The recombination of electrons directly from the conduction band at the Mg_{Ga} acceptor levels responsible for the UV red luminescence band peaked at 3.27 eV and at the acceptor levels (Ga vacancies) becomes predominant; this gives rise to bands with peaks at 3.06 and 3.17 eV. This is the edge emission, which determines the shortest emission wavelength of ZnO–GaN:Mg diode structures based on GaN heavily doped with an acceptor impurity.

It is shown here that, due to acceptor activation during annealing in nitrogen plasma, the films remain a *p*-type material and their conductivity increases (see table). In this case, their photoconductivity in the extrinsic region of the spectrum increases. The photosensitivity of GaN:Mg is found not only in the UV, but also in the visible spectral region due to electron transitions from the local levels to the valence band.

It is shown the activating annealing of GaN:Mg films in a nitrogen plasma with subsequent deposition of zinc oxide layers on their surface allows one to produce diode EL structures with an UV emission spectrum. The intensity of the UV luminescence of the GaN:Mg films annealed in a nitrogen plasma is considerably higher than that after short-term high-temperature annealing in nitrogen-enriched atmosphere [10], which is important for the development of a number of light-emitting structures.

REFERENCES

1. S. Nakamura, S. Nagahama, N. Iwasa, *et al.*, Appl. Phys. Lett. **68**, 2105 (1996).
2. S. Nakamura, S. Nagahama, N. Iwasa, *et al.*, Appl. Phys. Lett. **68**, 3269 (1996).
3. S. Nakamura, S. Nagahama, N. Iwasa, *et al.*, Appl. Phys. Lett. **69**, 1477 (1996).
4. S. Nakamura, N. Iwasa, M. Senoh, and T. Mukai, Jpn. J. Appl. Phys. **31**, 1258 (1992).
5. S. Nakamura, M. Senoh, and T. Mukai, Jpn. J. Appl. Phys. **31**, L139 (1992).
6. U. Kaiser, A. N. Gruzintsev, I. I. Khodos, and W. Richter, Neorg. Mater. **36** (6), 720 (2000).
7. J. C. Zolper, M. Hagerott, J. Grawtord, *et al.*, Appl. Phys. Lett. **68**, 200 (1996).
8. N. I. Katsavets, G. M. Laws, I. Harrison, *et al.*, Fiz. Tekh. Poluprovodn. (St. Petersburg) **32**, 1175 (1998) [Semiconductors **32**, 1048 (1998)].
9. Y. Li, Y. Lu, H. Shen, *et al.*, Mater. Res. Soc. Symp. Proc. **395**, 369 (1996).
10. T. V. Butkhuzi, A. N. Georgobiani, E. Zade-Uly, *et al.*, Tr. Fiz. Inst. Akad. Nauk SSSR **182**, 140 (1987).
11. A. N. Georgobiani, A. N. Gruzintsev, U. A. Aminov, *et al.*, Fiz. Tekh. Poluprovodn. (St. Petersburg) **35** (2), 149 (2001) [Semiconductors **35**, 144 (2001)].
12. A. N. Georgobiani, A. N. Gruzintsev, A. V. Zayats, and I. M. Tiginyanu, Semicond. Sci. Technol. **6**, 165 (1991).
13. M. Ilegems and R. Dingle, J. Appl. Phys. **44**, 4234 (1973).

Translated by T. Galkina

Semiconductors, Vol. 35, No. 6, 2001, pp. 700–702. Translated from Fizika i Tekhnika Poluprovodnikov, Vol. 35, No. 6, 2001, pp. 731–733.

ELECTRONIC AND OPTICAL PROPERTIES OF SEMICONDUCTORS

Bi Impurity in PbSe

S. A. Nemov and P. A. Osipov

St. Petersburg State Technical University, Politekhnicheskaya ul. 29, St. Petersburg, 195251 Russia

Submitted November 27, 2000; accepted for publication November 27, 2000

Abstract—Doping with Bi and self-compensation in PbSe were studied. Dependences of the carrier concentration on the Bi content and excess amount of Se have been determined for metal–ceramic samples from Hall data. The comparison of the experimental data with calculation results shows that the donor effect of Bi is compensated for by doubly ionized lead vacancies. At a high impurity content, $N_{Bi} > 0.5$ at. %, the compensation is deeper than that predicted by the theory. This effect is accounted for by the formation of (impurity atom)–vacancy complexes and the redistribution of Bi between the cation and anion sublattices of PbSe. © *2001 MAIK "Nauka/Interperiodica".*

Bismuth impurity in lead chalcogenides has been poorly studied. It is only known that it acts as donor, but this effect is unstable. The amphoteric behavior observed in [1] presumably indicates that Bi is located on both cation and anion sublattices. It is noteworthy that these studies were performed using film samples the analysis for which was complicated by the existence of nonequilibrium point defects. As far as we know, no systematic detailed study of the bismuth impurity in thermodynamically equilibrium bulk PbSe samples has been done till now.

We studied bulk equilibrium samples fabricated by hot-pressing (at a temperature of 350°C and a pressure of 1–2 ton/cm^2) with subsequent homogenizing annealing at 650°C for 100 h. The average grain size in the samples obtained was $d \approx 0.1$ mm.

The goal was to analyze Bi doping and self-compensation in PbSe. The charge carrier concentration (n for electrons and p for holes) was determined from room-temperature Hall constant R as $n = (eR)^{-1}$.

Let us consider the results obtained. Figure 1 shows maximal electron concentrations in several series of PbSe:Bi samples with a fixed Bi impurity content. It can be seen that for small Bi content (<0.5 at. %), the electron concentration corresponds to the amount of the introduced Bi impurity. In this range, the dependence of the electron concentration on the Bi content is a straight line with a slope of unity.

According to commonly accepted ideas, Bi, by belonging to Group V and substituting Pb—a Group IV element—in the cation sublattice, acts as a donor, supplying one electron per impurity atom to the conduction band [2]. This is in agreement with the experimental data obtained. At the same time, at higher contents of bismuth ($N_{Bi} > 0.5$ at. %) its donor effect is unstable. In a number of samples, the electron concentration was substantially (by an order of magnitude or more) lower than the amount of bismuth introduced. This can be accounted for under the assumption that some Bi atoms are bound into complexes, and may also occupy other positions in the crystal lattice. It seems possible that Bi can be located in the anion sublattice (substituting Se, a group VI element), thus acting as an acceptor. In this case, the transition of some Bi atoms from the cation to anion sublattice strongly suppresses the donor action of Bi (this effect may be called "impurity self-compensation").

Additional information concerning the doping action of an impurity and the defect formation in a crystal can be obtained by studying the self-compensation effect. This effect is caused by the introduction of a doping impurity that stimulates the formation of electrically active intrinsic defects in a semiconductor, compensating for the doping action of the impurity. For an experimental study of the self-compensation, several sets of samples were prepared whose composition corresponded to the chemical formula $Pb_{1-x}Bi_xSe_{1+y}$. The

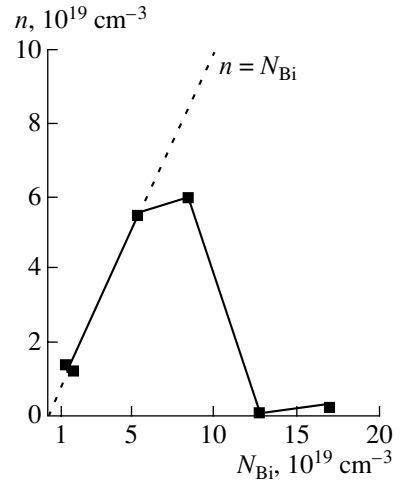

Fig. 1. Maximum electron concentration vs. Bi content in several sets of quasi-stoichiometric $Pb_{1-x}Bi_xSe$ samples.

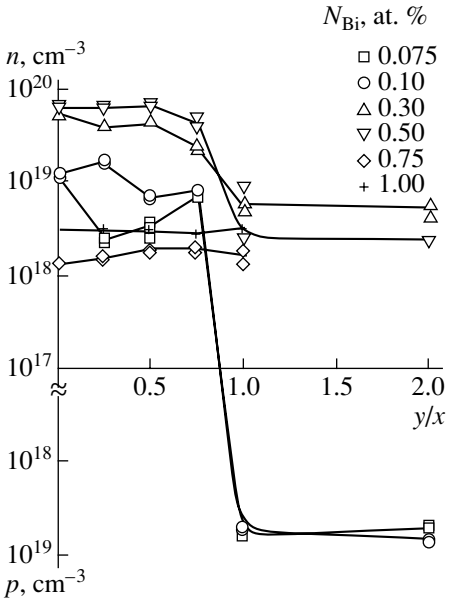

Fig. 2. Free carrier concentration in $Pb_{1-x}Bi_xSe_{1+y}$ samples vs. the excess of Se, y/x, for several impurity concentrations, N_{Bi}.

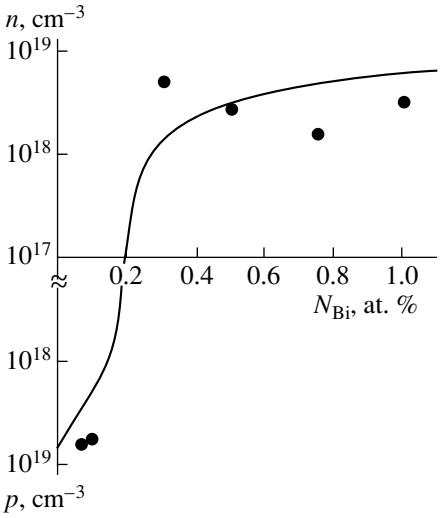

Fig. 3. Carrier concentration vs. Bi content for samples fully saturated with Se. Points: experiment, lines: calculation in terms of the self-compensation theory (by the model of compensation by doubly charged donor vacancies of lead with enthalpy of formation H_V = 0.75 eV at an annealing temperature of 650°C).

bismuth content x was 0.075, 0.1, 0.3, 0.5, 0.75, and 1.0 at. %, and the ratio of the excess selenium to bismuth content was y/x = 0, 0.25, 0.5, 0.75, and 1.2.

The boundary of the homogeneity range was determined from the point of changeover from one type of dependence $n(y/x)$ of the free carrier concentration n on the excess of selenium in relative units, y/x, to another (Fig. 2). It can be seen that these dependences are complicated. Indeed, for high selenium content the curves show a break and tend to level off. For a small excess of selenium, the samples exhibit n-type conduction. Adding selenium to the stock favors the formation of acceptor vacancies of lead, compensating for the donor action of bismuth. This leads to a decrease in the electron concentration in the conduction band and even to the inversion of the conduction type at a bismuth content of $N_{Bi} < 0.3$ at. %. The experimental data obtained show that the limiting concentration of the compensating defects grows with increasing bismuth content, this being evidence of self-compensation. According to a variety of data, a value of $\sim 1.2 \times 10^{19}$ cm^{-3} corresponds to the boundary of the homogeneity range on the Se excess side, and in the series of samples with a Bi content of 0.1 at. % ($N_{Bi} = 1.7 \times 10^{19}$ cm^{-3}) we observed overcompensation of Bi donors by acceptor defects. It should also be noted that at the Bi content $N_{Bi} > 0.75$ at. % the concentration and type of carriers in the samples studied are independent of the amount of introduced Se.

As follows from the theory of self-compensation, developed in [3], further information on defect formation processes can be obtained from the dependence of carrier concentration on the bismuth impurity content (points in Fig. 3) for samples fully saturated with selenium (which was achieved by introducing excess selenium into the mixture and homogenizing isothermal annealing in a selenium vapor). In this case, the carrier concentration can be calculated using the theory of impurity self-compensation by isolated vacancies [3]. The line in Figure 3 represents the calculation results. It can be seen that for low Bi content the experimental data are in agreement with the theoretical predictions and the donor Bi impurity is compensated by doubly charged Pb acceptor vacancies. For a higher bismuth content, the experimental pattern becomes more complicated: the experimental values of the electron concentration are less than half the calculated value, which means a deeper compensation of impurities than that predicted by the theory. To account for this, it is necessary to consider the more complicated behavior of the Bi impurity in PbSe, in particular, the possible formation of complexes including an impurity and a Pb vacancy and also the transition of some Bi atoms to the Se sublattice (where Bi acts as an acceptor).

Thus, it was found that at small (<0.5 at. %) Bi impurity contents, Bi is mainly located on the Pb sublattice of PbSe. In this position, bismuth acts as a donor and supplies one electron per impurity atom to the conduction band.

The experimental pattern becomes complicated at a Bi content over 0.5 at. %. The observed features of PbSe doping with Bi can be accounted for by the formation of complexes including Bi atoms and Pb vacancies (both neutral and charged), and also by the redistribution of Bi atoms between the cation and anion sublat-

tices of the compound. The last assumption is confirmed by nonmonotonous dependences of the electron concentration in the conduction band on the excess of Se, observed in samples with a Bi content of 0.075 and 0.1 at. % (see Fig. 2).

ACKNOWLEDGMENTS

We are indebted to V.A. Zykov for his helpful participation in discussions and to V.I. Proshin for his assistance in the experiments and participation in discussions.

REFERENCES

1. V. A. Zykov, T. A. Gavrikova, and S. A. Nemov, Fiz. Tekh. Poluprovodn. (St. Petersburg) **29** (2), 309 (1995) [Semiconductors **29**, 154 (1995)].
2. Yu. I. Ravich, B. A. Efimova, and I. A. Smirnov, *Semiconducting Lead Chalcogenides* (Nauka, Moscow, 1968; Plenum, New York, 1970).
3. V. I. Kaĭdanov, S. A. Nemov, and Yu. I. Ravich, Fiz. Tekh. Poluprovodn. (St. Petersburg) **28** (3), 369 (1994) [Semiconductors **28**, 223 (1994)].

Translated by D. Mashovets

Semiconductors, Vol. 35, No. 6, 2001, pp. 703–707. Translated from Fizika i Tekhnika Poluprovodnikov, Vol. 35, No. 6, 2001, pp. 734–738.

ELECTRONIC AND OPTICAL PROPERTIES OF SEMICONDUCTORS

Temperature Dependence of Plasma-Reflection Spectra of Bismuth–Antimony Crystals

V. M. Grabov* and N. P. Stepanov**

** Russian State Pedagogical University, St. Petersburg, 191186 Russia*

*** Transbaikal State Pedagogical University, Chita, 672000 Russia*

Submitted November 29, 2000; accepted for publication November 29, 2000

Abstract—The temperature dependence of plasma-reflection spectra of $Bi_{0.93}Sb_{0.07}$ single crystals doped with tin acceptor impurity was studied in the temperature range of $T = 4$–300 K. A nonmonotonic shift of the plasma frequency ω_p with increasing temperature and a substantial increase in the reflection coefficient R in the high-frequency region of the spectrum for the frequencies $\omega \gg \omega_p$ were observed. It is shown that the observed effects are caused by passage of the chemical-potential level through the direct energy gap E_{gL} at the L point of the Brillouin zone. It is in this case that the concentration of free charge carriers and the plasma frequency are found to be the lowest. In addition, the reflection spectrum cannot be described by the Drude dielectric function, because, in the situation under consideration, $\hbar\omega_p \approx E_{gL}$ and direct band-to-band transitions contribute significantly to the interaction of electromagnetic radiation with crystal. Calculation of dielectric function in terms of a model which accounts for the contributions of the plasma of free charge carriers and band-to-band transitions to this function makes it possible to satisfactorily describe the experimental reflection spectra and also to determine a number of parameters that specify the interaction of electromagnetic radiation with charge carriers in $Bi_{1-x}Sb_x$ crystals. © *2001 MAIK "Nauka/Interperiodica".*

The reflection spectra of bismuth and bismuth–antimony crystals have a shape characteristic of plasma reflection in the far-infrared region [1, 2]: the reflection coefficient decreases drastically in the vicinity of the plasma frequency $\omega_p^2 = 4\pi Ne^2/m^*\varepsilon_\infty$, where N is the concentration of free charge carriers, m^* is their effective mass, and ε_∞ is the high-frequency dielectric constant for $\omega \gg \omega_p$. In undoped bismuth-crystals and crystals doped lightly with an acceptor impurity of tin, the plasma frequencies are close to the frequencies of direct band-to-band transitions at the L point of the Brillouin zone: $\hbar\omega_p \approx E_{gL} + 2E_F$ [3, 4]. In the crystals doped with donor impurity of tellurium to the concentrations exceeding 0.1 at. %, the aforementioned frequencies diverge considerably, $\hbar\omega_p < E_{gL} + 2E_F$; as a result, the behavior of optical functions in the vicinity of the plasma frequency is adequately described by the classical Drude model [5]. Optical functions of the bismuth–antimony single crystals doped with the tin acceptor impurity have been analyzed previously [6, 7]. It has been shown [7] that the frequently observed deviations of the behavior of optical functions from the Drude model are caused by a contribution of the band-to-band transitions to the dielectric constant of the crystal.

The objective of this study was to gain insight into the shape of reflection spectra of the bismuth–antimony crystals in a wide temperature range of $T = 4.2$–300 K. Particular attention was given to crystals doped with the tin acceptor impurity; in these crystals, as temperature increases, the Fermi level leaves the valence band and passes into the conduction band through a narrow direct energy gap at the L point of the Brillouin zone ($E_{gL} \approx$ 10 meV).

We consider the temperature dependences of the plasma-reflection spectra for the $Bi_{1-x}Sb_x$ ($x = 0.07$) with the tin content of 0.01, 0.05, and 0.15 at. %. The $Bi_{0.93}Sb_{0.07}$ solid-solution single crystals were obtained by the zone-melting recrystallization. The concentrations of components in the crystals were determined using a CAMEBAX electron-probe microanalyzer; the nonuniformity in the distribution of antimony over the sample was no higher than 0.5 at. %. We measured the resistivity and the Hall coefficient at the liquid-nitrogen temperature for all the samples.

The reflection spectra were measured in the temperature range of $T = 4$–300 K using an AFS-01 automated Fourier spectrometer at the Institute of Metal Physics (Yekaterinburg). The spectra were obtained under the conditions when the nonpolarized light was reflected from the basal plane perpendicular to the $\mathbf{C}_3$ optical axis of the crystal. The angle of incidence of light on the sample was 45°. As a detector, we used a narrow-gap semiconductor crystal immersed in liquid helium. Additional measurements of the reflection spectra in the temperature range of $T = 78$–300 K were performed using a Bruker IFS-113V Fourier spectrometer according to [7].

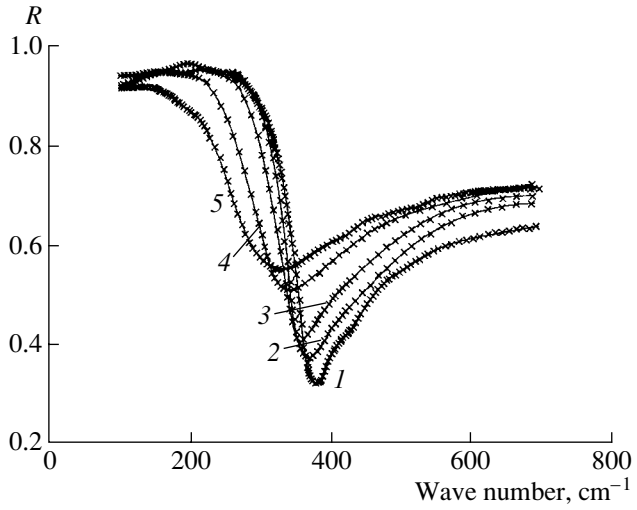

Fig. 1. The reflection spectra of $Bi_{0.93}Sb_{0.07}$ crystals doped with 0.15 at. % of Sn; the measurements were performed at T = (*1*) 4.2, (*2*) 37, (*3*) 55, (*4*) 93, and (*5*) 110 K.

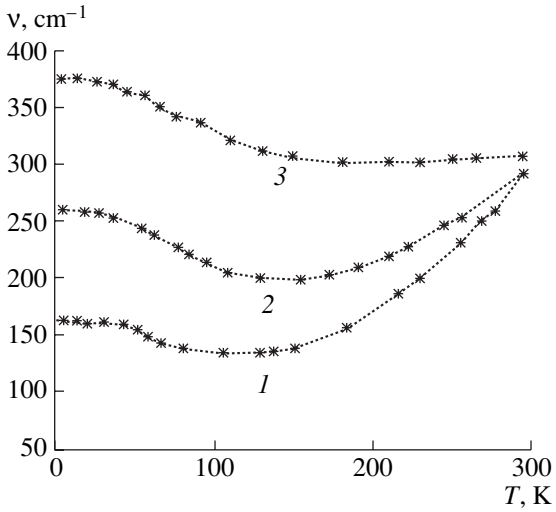

Fig. 2. Temperature dependences of the plasma-reflection minimum in the $Bi_{0.93}Sb_{0.07}$ crystals doped with Sn with the content of (*1*) 0.01, (*2*) 0.05, and (*3*) 0.15 at. %.

In Fig. 1, we show the temperature dependence of the reflection spectra for one of the studied $Bi_{0.93}Sb_{0.07}$ crystals doped with 0.15 at. % of Sn. A similar temperature dependence of the spectrum shape is also observed for other $Bi_{0.93}Sb_{0.07}$ crystals doped with tin. An increase in the reflection coefficient at the plasma minimum and a decrease in the slope of the plasma edge with increasing temperature are caused by an increase in the intensity of the charge-carrier scattering by the lattice vibrations. Special attention must be given to an increase in the reflection coefficient in the high-frequency region of the spectrum with increasing temperature in the spectra of the crystals doped with tin

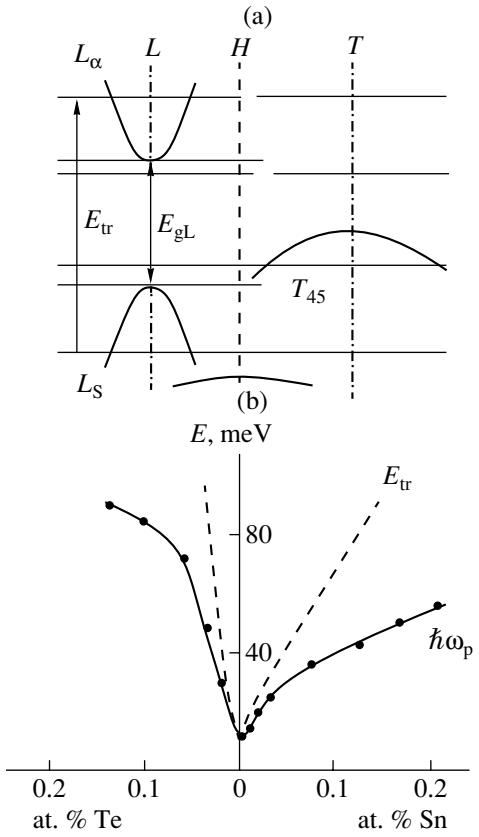

Fig. 3. (a) The energy-band diagram for $Bi_{0.93}Sb_{0.07}$ crystals with approximate position of chemical potential in the bands indicated and (b) the energies of the plasma oscillations $\hbar\omega_p$ and the band-to-band transitions E_{tr} in relation to the content and type of the dopant at T = 80 K.

(Fig. 1); at the same time, in the reflection spectra of the crystals doped with tellurium, the reflection coefficient is virtually temperature-independent in the high-frequency region of the spectrum [5].

A change in the frequency (the wave number ν) corresponding to the minimum of the plasma reflectivity in the $Bi_{0.93}Sb_{0.07}$:Sn crystals in the studied temperature range is illustrated in Fig. 2. For all crystals, as the temperature increases, the plasma minimum shifts first to lower frequencies and then to higher frequencies. A nonmonotonic temperature dependence of the plasma-minimum frequency is caused by the fact that the density of electron states in the valence band (the T and L extrema) in the vicinity of the chemical-potential level in the $Bi_{1-x}Sb_x$ crystals is much higher than in the conduction band (the L extrema) (Fig. 3). Doping of the crystals with an acceptor impurity of tin brings about a shift of the chemical potential deeper into the valence band and an increase in the hole concentration and in the corresponding plasma frequencies (Fig. 2). As the temperature increases, the chemical-potential level shifts to the conduction band. The lowest plasma-minimum frequency corresponds to the position of the

chemical-potential level within the E_{gL} gap (Fig. 3a) and to the lowest concentration of the charge carriers in the L extrema of the valence and conduction bands; in these extrema, the charge carriers have small effective masses. A further increase in temperature results in an increase in the charge-carrier concentration in the L extrema of the conduction band and an increase in the plasma frequencies. An inference about the emergence of an electron component of electrical conductivity (in the crystals doped lightly with tin) with increasing temperature is supported by the results of studying the temperature dependences of the Hall coefficient and resistivity [6].

In order to analyze the reflection spectra shown in Fig. 1 in more detail, we processed them using the Kramers–Kronig dispersion relations, which made it possible to determine the plasma frequency ω_p and the relaxation time τ_p. The obtained values of the parameters were used as the initial ones in the calculation of the reflection spectra in terms of the Drude model according to the following expressions for the real and imaginary parts of the dielectric function:

$$\varepsilon'(\omega) = \varepsilon_\infty\left(1 - \frac{\omega_p^2}{\omega^2 - \tau^{-2}}\right); \quad \varepsilon''(\omega) = \varepsilon_\infty\frac{\omega_p^2}{\omega^3\tau_p}. \quad (1)$$

The results of calculations are shown in Fig. 4 together with experimental data. It can be seen that the Drude model does not adequately describe all the special features of the experimental reflection spectra. The sharpest deviations are observed in the short-wavelength region of the spectrum. In addition, a substantial increase in the high-frequency dielectric constant from 80 to 140 is observed as the temperature increases from 4 to 110 K; this cannot be explained in the context of the concept of redistribution of free charge carriers in the allowed bands (Fig. 3a) as the temperature is varied.

This indicates that there is another mechanism (in addition to the plasma-related one) for the interaction of radiation with the crystal.

We can gain insight into the nature of this mechanism by analyzing the plot in Fig. 3b. The plasma-oscillation energies $\hbar\omega_p$ obtained from experimental spectra and the interband-transition (at the L point of the Brillouin zone) energies E_{tr} calculated in terms of the two-band model taking into account the Burstein–Moss shift ($E_{tr} = E_{gL} + 2E_F$) are shown in Fig. 3b in relation to the type and content of dopant at $T = 80$ K. As can be seen, the energy of the band-to-band transitions in the studied $Bi_{0.93}Sb_{0.07}$:Sn_y crystals (y = 0.05, 0.10, and 0.15 at. %) is close to the energy characteristic of the high-frequency region of the studied spectral range. Obviously, the relation between the plasma-oscillation energy $\hbar\omega_p$ and the energy of the band-to-band transitions $E_{tr} = E_{gL} + 2E_F$ changes as the temperature is varied. This results in the variation of relative contributions of these energies to the shape of the reflection spectra. As can be seen from Fig. 1, the magnitude of the effect of the band-to-band transitions on the spectra increases with increasing temperature, which manifests itself in a sharp increase in the reflection coefficient in the high-frequency region of the spectrum.

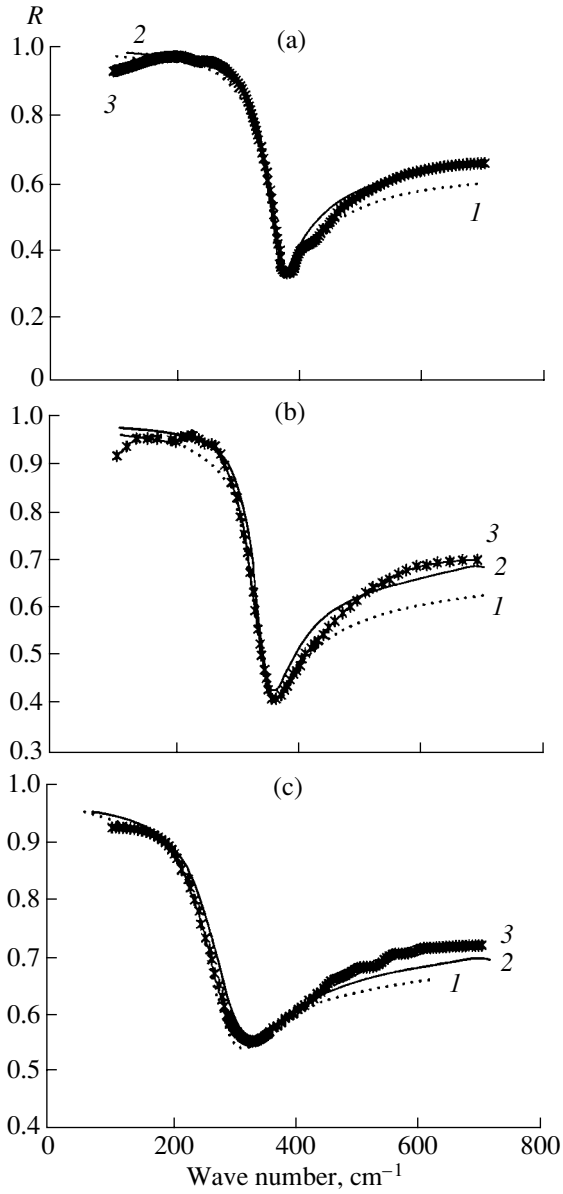

Fig. 4. Spectral dependences of the reflection coefficient for a $Bi_{0.93}Sb_{0.07}$ crystal doped with 0.15 at. % of Sn at T = (a) 4.2, (b) 55, and (c) 110 K. Curves *1* and *2* were calculated according to models (1) and (2), and curve *3* is experimental.

The dielectric function $\varepsilon(\omega)$ of the narrow-gap semiconductors has been previously calculated [8, 9] taking into account the additive contributions of free charge carriers $\varepsilon_{intra}(\omega)$, the band-to-band transitions $\varepsilon_{inter}(\omega)$, and the lattice vibrations $\varepsilon_{ph}(\omega)$. The bismuth–antimony alloys feature a small value of $\varepsilon_{ph}(\omega)$ due to the

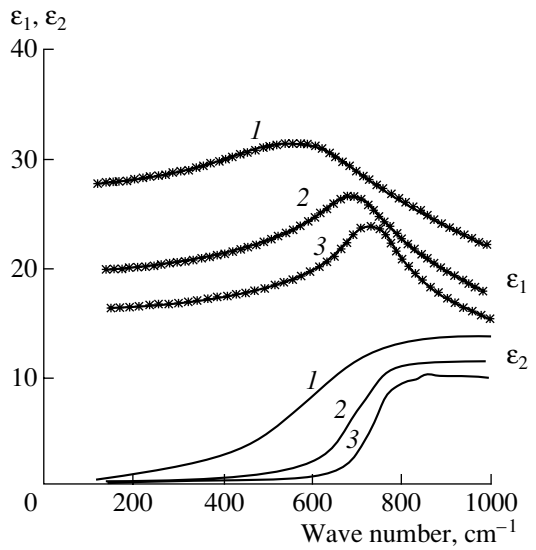

Fig. 5. The real (ε_1) and imaginary (ε_2) parts of the dielectric function $\varepsilon_{inter}(\omega)$ that describes the contribution of the band-to-band transitions to the spectra shown in Fig. 4. Calculations were performed in terms of model (2) for T = (*1*) 110, (*2*) 55, and (*3*) 4.2 K.

fact that the chemical bonds are nonpolar; nevertheless, if the plasma and optical-phonon frequencies (the latter correspond to a wave number of 100 cm^{-1}) are close to each other, it is impossible to calculate the optical functions without taking the lattice vibrations into account [10]. In the case under consideration in this study, the plasma frequencies differ markedly from the optical-phonon frequencies; therefore, we used the following formula to calculate the dielectric function:

$$\varepsilon(\omega) = \varepsilon'_\infty + \varepsilon_{intra}(\omega) + \varepsilon_{inter}(\omega). \quad (2)$$

Here, ε'_∞ is the high-frequency dielectric constant that accounts for all transitions with energies differing widely from those of the plasma frequencies, except for the transition $L_S \longrightarrow L_\alpha$. The contribution of intraband transitions in the conduction band is described in the terms of the Drude model as given by expression (1).

The behavior of the frequency dependence $\varepsilon_{inter}(\omega)$ for the band-to-band transitions has been obtained as a result of considering the dielectric function in the random-phase approximation (see [9] for details) and is described by the expression

$$\varepsilon_{inter}(\omega) = \frac{\sqrt{2}e^2(m_c^* m_0)^{1/2}}{\pi\hbar(1+p)}\int G(E)F(E,\omega)dE, \quad (3)$$

where

$$G(E) = f(-pE) - f(E), \quad (4)$$

$$F(E,\omega) = \frac{E^{-1/2}}{E - \hbar(\omega + i\gamma)/(1+p)} + \frac{E^{-1/2}}{E + \hbar(\omega + i\gamma)/(1+p)}, \quad (5)$$

and $f(E)$ is the Fermi–Dirac distribution function given by

$$f(E) = \left[1 + \exp\left(\frac{E - E_F}{kT}\right)\right]^{-1}. \quad (6)$$

Here, γ is the parameter accounting for the transition damping and $p = m_c^*/m_v^*$, with m_c^* and m_v^* standing for the density-of-state effective masses in the valence and conduction bands.

The real and imaginary parts of the function $\varepsilon_{inter}(\omega)$ calculated for the samples whose data are represented in Fig. 4 are shown in Fig. 5. In calculations, we used the charge-carrier parameters at the L point of the Brillouin zone that were determined previously [11] and corresponded to the McClure dispersion law [12].

Experimental and theoretical wave-number dependences of the reflection coefficient calculated both in terms of the Drude model (1) and in terms of the additive model described by (2) are shown in Fig. 4. Figure 4a indicates that experimental spectra obtained at a low (liquid-helium) temperature are adequately described by model (2). At higher temperatures (Figs. 4b, 4c), although the experimental spectra are described in terms of the additive model much better than in terms of the Drude model, a close agreement with experiment is not attained, which is indicative of the increasing role of indirect $T_{45} \longrightarrow L_\alpha$ transitions that were disregarded in model (2).

The dielectric-function calculation based on the condition for the closest agreement between the experimental and model curves with an allowance made for

The parameters obtained by simulating the optical functions of the $Bi_{0.93}Sb_{0.07}$ solid solution doped with 0.15 at. % of Sn

T, K	The Drude model			The model described by $\varepsilon(\omega) = \varepsilon'_\infty + \varepsilon_{intra}(\omega) + \varepsilon_{inter}(\omega)$			
	ω_p, 10^{13} s^{-1}	τ_p, 10^{13} s	ε_∞	γ	E_{tr}	ε'_∞	m_c^*/m_0
4	6.76	1.1	112	30	740	65	0.25
55	6.44	0.9	161	60	700	70	0.35
110	5.3	0.6	183	120	600	75	0.6

$L_S \longrightarrow L_\alpha$ direct band-to-band transitions makes it possible to determine a number of parameters, such as the transition energies and damping, and to estimate the density-of-state effective mass at the Fermi level and the value of the high-frequency dielectric constant. The parameters obtained by simulation are listed in the table. The value of the density-of-state effective mass ($0.6m_0$) obtained in terms of model (2) for the $Bi_{0.93}Sb_{0.07}$ alloy doped with 0.15 at. % of Sn substantiates the conclusion that the fraction of heavy charge carriers in the H extremum is large in the Bi–Sb solid solutions doped heavily with acceptor impurity (Fig. 3a). The most important result for the further study of optical properties of bismuth–antimony crystals consists in the fact that explicit consideration of the interband-transition contribution makes it possible to correctly determine such an important parameter as ε_∞ and also the contribution of plasma of free charge carriers to the dielectric constant. This extends the scope of using the plasma-reflection method for determination of effective masses for studying the dispersion law for the charge carriers.

REFERENCES

1. E. Gerlach, P. Grosse, M. Rautenberg, and M. Senske, Phys. Status Solidi B **75**, 553 (1976).
2. V. D. Kulakovskiĭ and V. D. Egorov, Fiz. Tverd. Tela (Leningrad) **15** (7), 2053 (1973) [Sov. Phys. Solid State **15**, 1368 (1973)].
3. T. M. Lifshits, A. B. Ormont, E. G. Chirkova, and A. Ya. Shul'man, Zh. Éksp. Teor. Fiz. **72** (3), 1130 (1977) [Sov. Phys. JETP **45**, 591 (1977)].
4. N. P. Stepanov, V. M. Grabov, and B. E. Vol'f, Fiz. Tekh. Poluprovodn. (Leningrad) **23** (7), 1312 (1989) [Sov. Phys. Semicond. **23**, 817 (1989)].
5. V. M. Grabov and A. S. Mal'tsev, in *Proceedings of the VI All-Union Symposium "Narrow-Gap Semiconductors and Semimetals"* (L'vovsk. Gos. Univ., Lvov, 1983), Part 1, p. 231.
6. M. I. Belovolov, V. S. Vavilov, V. D. Egorov, and V. D. Kulakovskiĭ, Izv. Vyssh. Uchebn. Zaved., Fiz., No. 2, 5 (1976).
7. V. M. Grabov, N. P. Stepanov, B. E. Vol'f, and A. S. Mal'tsev, Opt. Spektrosk. **69** (1), 134 (1990) [Opt. Spectrosc. **69**, 82 (1990)].
8. J. G. Broerman, Phys. Rev. B **5** (2), 397 (1972).
9. M. Grynberg, R. Le Toulles, and M. Balkanski, Phys. Rev. B **9** (2), 517 (1974).
10. N. P. Stepanov and V. M. Grabov, Opt. Spektrosk. **84** (4), 581 (1998) [Opt. Spectrosc. **84**, 515 (1998)].
11. V. M. Grabov, V. V. Kudachin, and A. S. Mal'tsev, in *Proceedings of the VII All-Union Symposium "Narrow-Gap Semiconductors and Semimetals"* (L'vovsk. Gos. Univ., Lvov, 1986), Part 2, p. 167.
12. J. W. McClure and K. H. Choi, Solid State Commun. **21**, 1015 (1977).

Translated by A. Spitsyn

Semiconductors, Vol. 35, No. 6, 2001, pp. 708–713. Translated from Fizika i Tekhnika Poluprovodnikov, Vol. 35, No. 6, 2001, pp. 739–744.

ELECTRONIC AND OPTICAL PROPERTIES OF SEMICONDUCTORS

Changes in the Optical-Absorption Spectra of Transmutation-Doped GaAs as a Result of Annealing

V. N. Brudnyĭ*, N. G. Kolin[,1], D. I. Merkurisov**, and V. A. Novikov****

** Kuznetsov Siberian Physicotechnical Institute, Tomsk, 634050 Russia*

e-mail: brudnyi@ic.tsu.ru

*** Karpov Institute of Physical Chemistry Research Center (Obninsk Branch), Obninsk, Kaluga oblast, 249020 Russia*

[1] e-mail: fci@meteo.ru

Submitted November 28, 2000; accepted for publication November 29, 2000

Abstract—The optical-absorption spectra of GaAs irradiated with pile neutrons (with integrated fluxes of up to $D = 2 \times 10^{19}$ cm^{-2}) at temperatures of 70, 350–390, and 850°C were studied after subsequent isochronous annealing at temperatures as high as 1100°C. It is shown that the free charge carriers with a concentration of $n \gtrsim 10^{17}$ cm^{-3} appear after an annealing at temperatures of about 400–550°C. The quality of transmutation-doped material was assessed in relation to the conditions of irradiation and the temperature of the subsequent thermal annealing. © *2001 MAIK "Nauka/Interperiodica".*

1. INTRODUCTION

The transmutation-assisted (nuclear) doping of semiconductors by irradiation with thermal neutrons has attracted the attention of researchers because this method ensures the controlled introduction of a chemical impurity in the crystal by varying the integrated flux of neutron radiation and makes it possible to obtain the material with a high degree of uniformity of electrical parameters. The main disadvantage of this method consists in the formation of high concentrations of structural defects in the semiconductor lattice; these defects to a large extent control the properties of the material immediately after irradiation. This necessitates the elimination of these defects either by postirradiation annealing or by high-temperature irradiation. Thus, a high-temperature treatment of the material constitutes an integral part of the transmutation doping. All these issues have been adequately studied for transmutationally doped Si. For semiconductors with a complex structure (in particular, GaAs), these problems are still under investigation.

In this paper, we report the results of studying the doping of GaAs as a result of reactor irradiation. As the main method for studying the properties of irradiated material, we used the analysis of the optical-absorption spectra both after irradiation with pile neutrons and after the subsequent isochronous annealing of the material. Up to now, most of the data on the properties of transmutation-doped GaAs were obtained from electrical measurements and from studying the photoluminescence (PL); at the same time, the data on the optical-absorption spectra of irradiated material are lacking.

2. EXPERIMENTAL

The starting *n*- and *p*-GaAs crystals (whose parameters are listed in the table) grown by the Czochralski method were irradiated with total-spectrum neutrons in a VVR-Ts reactor (a water-cooled and water-moderated cylindrical reactor) at the Karpov Institute of Physical Chemistry Research Center (Obninsk Branch) at temperatures of $T_{irr} \approx 70$, 350–390, and 850°C with a thermal-neutron flux density of $(1–5) \times 10^{13}$ cm^{-2} s^{-1} and a cadmium ratio of ten (the energy $E > 0.3$ MeV). The temperature at which the irradiation was performed was attained owing to the "self-heating" of the samples due to an increase in the mass of irradiated material. After the decay of induced radioactivity, the samples were introduced into a chamber for measurements and subsequent annealing in the temperature range of $T_{ann} = 20–1100$°C. The samples were annealed for 20 min in a vacuum chamber at temperatures of up to $T_{ann} = 500$°C; at higher temperatures, the irradiated samples were annealed in the quartz cells under the equilibrium pressure of As vapor. In order to eliminate the surface effects, we removed the 50- to 100-μm-thick layer from each side of the sample by lapping after a high-temperature annealing.

3. RESULTS AND DISCUSSION

3.1. Electrical Properties

Bombardment with pile neutrons brings about an accumulation of Ge (40%) and Se (60%) chemical elements in the GaAs lattice owing to nuclear transmutations of Ga and As, respectively; this is used to obtain

n-GaAs. Simultaneously, a high concentration of radiation defects is formed in the GaAs lattice mainly due to fast neutrons; a high-temperature annealing of transmutation-doped material (or irradiation at elevated temperatures) is needed to eliminate these defects and activate the chemical impurities introduced by irradiation. The choice of optimal annealing temperature (or the irradiation temperature) is especially important for GaAs, because both the thermal stability of radiation defects in this compound and the acceptor formation (characteristic of gallium arsenide at high temperatures) should be taken into account.

It is known that irradiation of GaAs with pile neutrons reduces electrical conductivity to $\sigma \approx 10^{-9}\ \Omega^{-1}\ cm^{-1}$ (at a temperature of $T = 300$ K [2]) as a result of capturing the free charge carriers by deep-level traps of irradiation-related origin; the spectrum of these traps has been studied previously [3, 4]. In such a material, the Fermi level is pinned in the vicinity of $E_v + 0.6$ eV. This ultimate (steady-state) position of the Fermi level is close to the calculated position of the local-electroneutrality level in this material and is preserved when the sample is irradiated further [5]. Subsequent irradiation ("reirradiation") of such a material with neutrons brings about the formation of low-resistivity samples as a result of the origination of hopping conduction of the charge carriers over the localized states of radiation defects [2, 6].

Electrical parameters of the studied samples before irradiation, after irradiation with the highest integrated fluxes (D) of pile neutrons, and after subsequent annealing at temperatures of $T_{ann} = 900$ and 1100°C are listed in the table.

Variation in electrical conductivity of irradiated samples as a result of subsequent isochronous annealing in the temperature range of $T_{ann} = 20$–1100°C is illustrated in Fig. 1. Three stages of variations in σ at annealing temperatures of 200–300, 400–600, and 750–850°C characteristic of neutron-irradiated GaAs [6] are clearly observed. The relation of these annealing stages to the healing of deep-level radiation point defects has been discussed in a number of publications (see, for example, [4]). Variations in conductivity at $T_{ann} = 200$–300°C are attributed to annealing-out of the

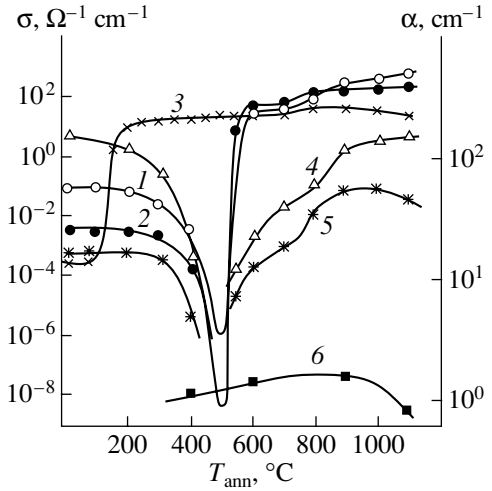

Fig. 1. Variation in (*1–3*) electrical conductivity σ and (*4–6*) optical-absorption coefficient α at a wavelength of 9 μm as a result of isochronous annealing (for 20 min at each temperature T_{ann}) of GaAs transmutation-doped samples (*1*, *4*) G1, (*2*, *5*) G2, and (*3*, *6*) G5. Measurements were performed at a temperature of 295 K.

point radiation defects, more precisely, of the so-called *E* and *H* traps that constitute the main compensating centers in gallium arsenide irradiated with gamma-ray quanta or electrons. Variations in the vicinity of T_{ann} = 400–600°C are attributed to the disappearance of more complex defects (the so-called *P* centers), whereas the higher temperature stages of recovery of electrical conductivity are attributed to the annealing of complex defects of unknown origin. For crystals irradiated at high temperatures (sample G5, $T_{irr} = 850$°C), the main stage of recovery of σ is observed at T_{ann} = 150–220°C; this stage is related to annealing of the *E* and *H* point defects that were introduced into the sample during its storage after the pile-neutron irradiation owing to "self-irradiation" of the material with gamma-ray quanta and beta-particles emitted during radioactive decay of ^{70}Ge, ^{72}Ge, and ^{76}As nuclei [7]. The absence of a high-temperature stage of recovery of electrical conductivity for

Conditions of irradiation and annealing and the parameters of GaAs samples at $T = 295$ K

Samples	σ, Ω^{-1} cm^{-1}	T_{irr}, °C	D, 10^{17} cm^{-2}	σ, Ω^{-1} cm^{-1}	n, cm^{-3}	μ, cm^2 V^{-1} s^{-1}	n*, cm^{-3}	n, cm^{-3}	μ, cm^2 V^{-1} s^{-1}	n*, cm^{-3}
	before irradiation			after irradiation	T_{ann} = 900°C			T_{ann} = 1100°C		
G1(*n*)	10^{-7}	70	200	6.8×10^{-2}	1.6×10^{18}	1490	2.8×10^{18}	1.7×10^{18}	1840	3.0×10^{18}
G2(*p*)	10^{1}	350–390	90	3.0×10^{-3}	9.2×10^{17}	2170	1.3×10^{18}	1.0×10^{18}	2030	1.4×10^{18}
G5(*n*)	10^{-2}	850	5	2.0×10^{-4}	8.0×10^{16}	4140	1.4×10^{17}	4.8×10^{16}	3650	1.0×10^{17}

Note: The values of *n** were estimated from the optical-absorption spectra using the data reported previously [1].

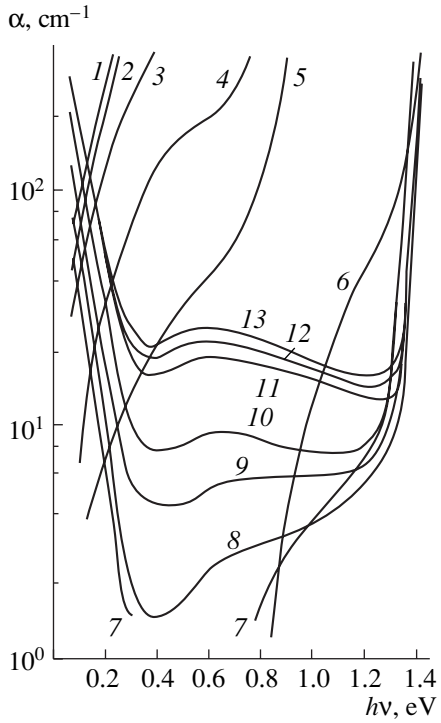

Fig. 2. Variations in the spectra of optical-absorption coefficient α as a result of isochronous annealing (for 20 min) of transmutation-doped GaAs, sample G1. The annealing temperatures were T_{ann} = (*1*) 20, (*2*) 200, (*3*) 300, (*4*) 370, (*5*) 450, (*6*) 500, (*7*) 550, (*8*) 600, (*9*) 700, (*10*) 800, (*11*) 900, (*12*) 1000, and (*13*) 1100°C. The spectra were measured at T = 295 K.

sample G5 (T_{irr} = 850°C) indicates that there is no build-up of complex defects in such a material during pile-neutron irradiation.

These studies show that heat treatment of neutron-irradiated material at T_{ann} > 900°C does not result in significant changes in its electrical parameters.

3.2. Optical Absorption

In the samples irradiated with pile neutrons, significant optical absorption is observed in the extrinsic region of the spectrum, i.e., for the photon energies lower than the band gap ($h\nu < E_g$) (Fig. 2). The magnitude of this absorption is proportional to the integrated flux of neutrons; the origin of the absorption in GaAs samples irradiated with fast neutrons has been studied repeatedly (see, for example, [6]). Postirradiation annealing of such samples results in the disappearance of irradiation-induced extrinsic absorption; after an annealing at $T_{ann} \approx 550$°C, optical measurements indicate that free charge carriers manifest themselves in two wavelength ranges characteristic of GaAs: in the range of λ = 4–10 μm (the free-carrier absorption) and in the range of λ = 1–4 μm (as an absorptivity step caused by optical transitions between different subbands in the conduction band). It should be noted that the annealing temperature of $T_{ann} \approx 550$°C is critical for GaAs irradiated with pile neutrons, because it is in the vicinity of this temperature that not only do free electrons make themselves evident (according to the measurements of the optical-absorption spectra) but also the lattice constant, density, and microhardness of GaAs irradiated with pile neutrons are recovered [8].

Variation in the absorption coefficient α (λ = 9 μm) as a result of annealing of irradiated samples (see Fig. 1) coincides qualitatively with variation in electrical conductivity of the samples and corresponds to a decrease in the concentration of optically active radiation defects that act as compensating centers for electrical conductivity. An increase in α (at λ = 9 μm) at $T_{ann} \gtrsim 550$°C is caused by the emergence of free electrons owing to doping of GaAs with hydrogen-like impurities (Ge and Se) and by a decrease in the concentration of deep-level radiation defects. The results of both optical and electrical measurements show that the annealing temperature of $T_{ann} \approx 900$°C is sufficient for activation of chemical impurity and for annealing of a large fraction of radiation damage in transmutation-doped GaAs. Moreover, an increase in the annealing temperature to 1100°C leads to a decrease in the concentration of free electrons in lightly and moderately doped crystals (samples G2 and G5), which is consistent with the results of electrical studies and indicates that acceptor-type compensating centers are formed at high annealing temperatures (Fig. 1). In the heavily irradiated material (sample G1), the absorption coefficient α (at λ = 9 μm) continues to increase as a result of heat treatment at temperatures as high as 1100°C in spite of the thermal generation of acceptors in GaAs at these temperatures, which indicates that annealing of radiation defects is incomplete in the heavily irradiated material.

The data shown in Fig. 2 for sample G1 and similar studies of samples G2 and G5 were used to estimate the free-electron concentration in annealed samples. According to [1], in the samples doped with hydrogen-like donors, the value of α/n (here, n is the free-electron concentration) varies in the range of $(4.2–7.5) \times 10^{-18}$ cm^2 for the wavelength of λ = 2 μm and in the range of $(3–8) \times 10^{-17}$ cm^2 for λ = 9 μm (at 300 K) when the free-electron concentration varies from 1×10^{17} to 7×10^{18} cm^{-3}. This makes it possible to use optical measurements to estimate the free-electron concentration in the studied samples for annealing temperatures of T_{ann} = 900 and 1100°C (see table). The data obtained from optical measurements are close to the corresponding values obtained from electrical measurements, although they exceed the latter by a factor of about 1.5, which is caused by an error in estimating the cross section of optical absorption by free electrons.

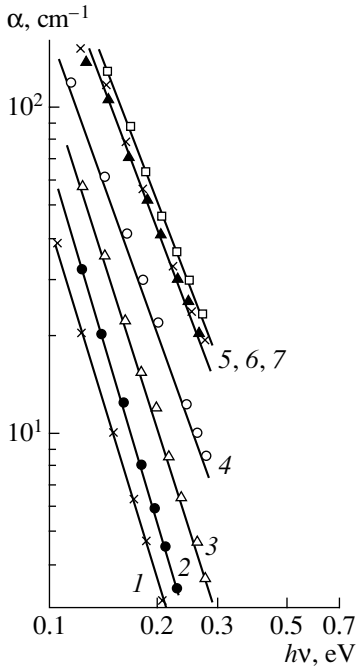

Fig. 3. Spectral dependences of the optical-absorption coefficient α in the wavelength range of 4–10 μm for sample G1 after isochronous annealing (for 20 min) at T_{ann} = (*1*) 550, (*2*) 600, (*3*) 700, (*4*) 800, (*5*) 900, (*6*) 1000, and (*7*) 1100°C. The absorption coefficient was measured at T = 295 K.

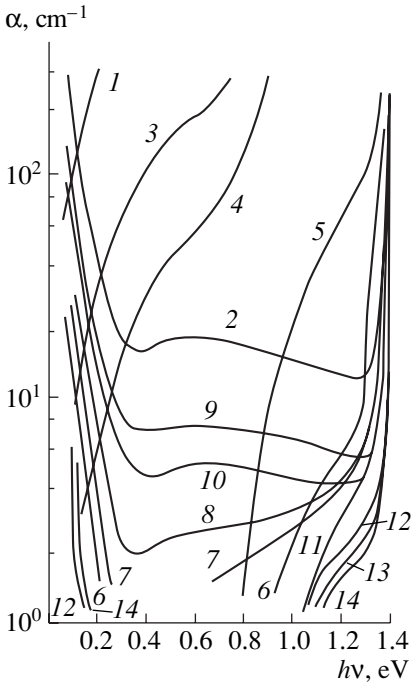

Fig. 4. The effect of temperature during reactor-neutron irradiation T_{irr} on the variation in the optical-absorption spectra of GaAs as a result of subsequent isochronous annealing (for 20 min). Sample G1: T_{irr} = 70°C; T_{ann} = (*1*) 20 and (*2*) 900°C. Sample G2: T_{irr} = 350–390°C; T_{ann} = (*3*) 20, 100, 200, and 300°C; (*4*) 400, (*5*) 500, (*6*) 550, (*7*) 600, (*8*) 700, (*9*) 900, and (*10*) 1100°C. Sample G5: T_{irr} = 850°C; T_{ann} = (*11*) 20, 100, and 200°C; (*12*) 400, (*13*) 600, and (*14*) 900°C. The spectra were measured at T = 295 K.

The quality of transmutation-doped material was assessed from measurements of the spectral dependence $\alpha \propto \lambda^m$ in the region of the free-electron absorption as the postirradiation-annealing temperature was increased (Fig. 3). The exponent m varies in this case from 3.9 to 2.8 as the annealing temperature is changed from T_{ann} = 550°C (incomplete healing of radiation defects) to 1100°C. The final value of m for transmutation-doped and then annealed material is characteristic of GaAs doped with hydrogen-like impurities in the melt and is indicative (along with the data on Hall mobility) of the fairly high quality of the transmutation-doped material (see table).

We studied the influence of T_{irr} on the changes in the optical-absorption spectra of GaAs as a result of postirradiation isochronous annealing (Fig. 4). An increase in T_{irr} brings about the corresponding temperature shift of the onset of variation in the optical-absorption spectra of irradiated material (crystals G1 and G2) as a result annealing; however, for high annealing temperatures ($T_{ann} > T_{irr}$), the effect of T_{irr} on the optical-absorption spectra of studied materials was not observed. A characteristic feature of variation in the optical spectra as a result of heat treatment of material G5 (T_{irr} = 850°C) is the appearance of free electrons in the samples for $T_{ann} \approx$ 400°C (Fig. 4, curve *12*). As in the case of electrical measurements (Fig. 1), this is apparently caused by an annealing of the E and H point defects induced in this material by self-irradiation during storage; these defects act as the main compensating centers in such samples. The shift of the isochronous-annealing curve to higher temperatures compared to the curve of the electrical-conductivity recovery (Fig. 1) is caused by a small value of the cross section (~10^{-17} cm^2) for absorption by free electrons in GaAs. It should be expected that, in materials G1 and G2, such defects can also contribute to the low-temperature stage of the absorption-coefficient recovery; however, the presence of complex defects (clusters) in these materials pins the Fermi level in the vicinity of its ultimate position in irradiated GaAs (in the vicinity of the midgap) at the annealing temperatures of T_{ann} < 500°C.

3.3. Photoluminescence Properties

The PL measurements were mainly undertaken to analyze the quality of transmutation-doped material; the spectrum of the observed PL lines is not discussed here in detail because it has been considered in many publications, including those devoted to the transmuta-

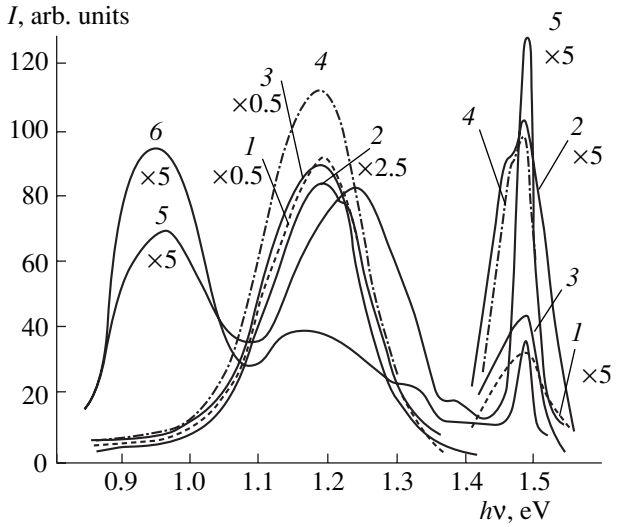

Fig. 5. Photoluminescence spectra of transmutation-doped samples (*1*, *2*) G1, (*3*, *4*) G2, and (*5*, *6*) G5 after annealing at temperatures T_{ann} = (*1*, *3*, *5*) 900 and (*2*, *4*, *6*) 1100°C. The spectra were measured at T = 78 K.

tion-doped GaAs (see, e.g., [9–11]). In this study, we measured for the first time the PL spectra of GaAs irradiated with pile neutrons with integrated fluxes of up to $D = 2 \times 10^{19}$ cm^{-2} at a temperature as high as $T_{irr} \approx$ 850°C which were subjected to subsequent isochronous annealing at T_{ann} = 1100°C.

The shape of the PL spectra $I(h\nu)$ and their variation at the annealing temperatures ranging from 900 to 1100°C in the studied samples are shown in Fig. 5. For the annealed samples, the most intense extrinsic PL bands peaked at $h\nu$ = 0.96 and 1.2 eV and a near-edge band peaked at $h\nu$ = 1.48 eV are observed. When the annealing temperature is raised to 1100°C, the shape of the PL spectra is generally retained; however, the relative intensities of the extrinsic and near-edge bands change. Thus, the ratio between the intensity of the band peaked at $h\nu$ = 1.2 eV and the edge-band intensity are 24.4 and 0.7 for T_{ann} = 900°C and 8, 2.3, and 1.1 for T_{ann} = 1100°C in samples G1, G2, and G5, respectively. For moderately (G2) and heavily (G1) irradiated samples, an increase in the annealing temperature from 900 to 1100°C results in an increase in the edge-band intensity, which is consistent with the data (obtained by measuring the optical-absorption spectra and electrical parameters) on the presence of appreciable concentration of radiation defects (the nonradiative-recombination centers) in irradiated GaAs even after an annealing at T_{ann} = 900°C. At the same time, for material G5 (low irradiation doses), an increase in T_{ann} from 900 to 1100°C results in quenching of the edge band and in transformation of the extrinsic bands peaked at $h\nu$ = 0.96 and 1.25 eV. We may note that the shape of extrinsic bands in the PL spectra of sample G5 (T_{irr} = 850°C) differs from the shape of corresponding bands in the spectra of samples G1 and G2. Thus, the band peaked at $h\nu$ = 0.96 eV is observed only in sample G5 (T_{irr} = 850°C); an increase in the annealing temperature from 900 to 1100°C transforms the emission band peaked at $h\nu \approx 1.25$ eV into the well-studied band at $h\nu \approx 1.2$ eV, which is attributed to the complexes that consist of a shallow-level donor and V_{Ga}. These data indicate that the origin of the residual defects in materials irradiated at temperatures of T_{irr} = 350–390°C differs from those irradiated at a temperature of about 850°C even if the irradiated samples are annealed at T_{ann} = 1100°C after irradiation.

4. DISCUSSION AND CONCLUSION

Both this study and the published data [2–4, 7–11] show that, in order to obtain transmutation-doped *n*-GaAs of high quality, the temperature of postirradiation annealing should not exceed 900°C. As a result of annealing at higher temperatures, the degree of compensation of transmutation-doped GaAs increases due to the thermal generation of acceptors, which leads to a decrease in the concentration of free electrons in the samples, especially for low integrated fluxes of reactor neutrons. For high levels of reactor-neutron irradiation, a short-term (10–30 min) heating to 1100°C does not bring about the complete elimination of radiation defects, which results in low transmutation-doping efficiency and in inferior electrical parameters of the material and necessitates a long heat treatment of such samples. However, even under such conditions of heat treatment of the heavily doped material, the efficiency of doping with shallow-level impurities (Ge and Se) remains much lower than unity, because, in addition to thermal generation of acceptors, self-compensation of GaAs occurs owing to redistribution of Ge over the Ga and As sublattices (this is due to the fact that Ge is an amphoteric impurity). An increase in the sample temperature to 850°C during irradiation with pile neutrons does not affect appreciably the electrical parameters of the material after an additional annealing.

ACKNOWLEDGMENTS

This study was supported in part by the Ministry of Education of the Russian Federation (the Program “Basic Research in the Fields of Nuclear Technology and the Physics of the Ionizing-Radiation Beams,” grant no. 97-12.9, 2-2) and the Ministry of Industry, Science, and Technologies (Program “Research and Development in the Main Lines of Progress in Science and Civil Technology,” grant no. 043).

REFERENCES

1. *Gallium Arsenide. Production and Properties*, Ed. by F. P. Kesamanl and D. N. Nasledov (Nauka, Moscow, 1973).

2. N. G. Kolin, L. V. Kulikova, V. B. Osvenskiĭ, *et al.*, Fiz. Tekh. Poluprovodn. (Leningrad) **18**, 2187 (1984) [Sov. Phys. Semicond. **18**, 1364 (1984)].

3. V. N. Brudnyĭ, N. G. Kolin, and A. I. Potapov, Fiz. Tekh. Poluprovodn. (St. Petersburg) **27**, 260 (1993) [Semiconductors **27**, 145 (1993)].

4. V. N. Brudnyĭ, N. G. Kolin, V. A. Novikov, *et al.*, Fiz. Tekh. Poluprovodn. (St. Petersburg) **31**, 811 (1997) [Semiconductors **31**, 686 (1997)].

5. V. N. Brudnyi, S. N. Grinyaev, and V. E. Stepanov, Physica B (Amsterdam) **202**, 429 (1995).

6. R. Coates and E. W. J. Mitchel, Adv. Phys. **24**, 594 (1975).

7. N. G. Kolin, L. V. Kulikova, and V. B. Osvenskiĭ, Fiz. Tekh. Poluprovodn. (Leningrad) **22**, 1025 (1988) [Sov. Phys. Semicond. **22**, 646 (1988)].

8. N. G. Kolin, V. B. Osvenskiĭ, V. V. Tokarevskiĭ, *et al.*, Fiz. Tekh. Poluprovodn. (Leningrad) **19**, 1558 (1985) [Sov. Phys. Semicond. **19**, 958 (1985)].

9. J. Carrido, J. L. Castano, and J. Piqueros, Phys. Status Solidi **65**, 103 (1981).

10. J. Carrido, J. L. Castano, and J. Piqueros, J. Appl. Phys. **57**, 2186 (1985).

11. V. A. Bykovskiĭ, V. A. Giriĭ, F. P. Korshunov, and V. I. Utenko, Fiz. Tekh. Poluprovodn. (Leningrad) **23**, 79 (1989) [Sov. Phys. Semicond. **23**, 48 (1989)].

Translated by A. Spitsyn

Semiconductors, Vol. 35, No. 6, 2001, pp. 714–717. Translated from Fizika i Tekhnika Poluprovodnikov, Vol. 35, No. 6, 2001, pp. 745–748.

SEMICONDUCTOR STRUCTURES, INTERFACES, AND SURFACES

CdTe Polycrystalline Surface Subjected to Pulsed Laser Irradiation

A. Baĭdullaeva*, A. I. Vlasenko, P. E. Mozol', and A. B. Smirnov

Institute of Semiconductor Physics, National Academy of Sciences of Ukraine, pr. Nauki 45, Kiev, 03028 Ukraine

** e-mail: baidulla@class.semicond.kiev.ua*

Submitted December 6, 2000; accepted for publication December 6, 2000

Abstract—Auger spectra, electron microscope images, the distribution of chemical elements over CdTe polycrystalline layers irradiated with Q-switched laser pulses with a duration of 2×10^{-8} s, and an energy density below the material melting or damage threshold are considered. The laser irradiation of the polycrystalline layers is shown to result in the removal of the insulator phase from the surface and in the surface modification accompanied by a change in stoichiometry within the ~3-μm-thick surface layer. The removal of this layer improves the homogeneity of the polycrystalline surface. The depth of carbon penetration into the polycrystalline layer is estimated. The correlation between the photoelectric properties of CdTe polycrystalline layers and the laser-induced changes in the surface stoichiometry is ascertained. © *2001 MAIK "Nauka/Interperiodica".*

CdTe polycrystalline layers are widely used as buffers for the epitaxial growth of CdHgTe solid solutions as well as for the production of solar cells and X-ray and gamma-ray detectors. For all of the devices mentioned, their long-term stability, which is affected by the state of the material surface, is of particular practical interest. In this context, the requirements on the quality of the surfaces become more stringent. Moreover, the study of CdTe polycrystalline layers can provide an insight into the physical and chemical effects that take place at the grain boundaries on the material surface during its technological processing [1, 2].

We report the results of Auger study of CdTe polycrystalline surfaces irradiated by laser pulses. Spectral dependences of photoconductivity are also studied for the samples with differently pretreated surfaces.

Cadmium telluride polycrystalline layers were grown by molecular beam epitaxy in a vacuum on sapphire substrates heated up to 670 K. The layer thickness was ~100 μm; the typical grain size was determined by electron microscopy at ~40–120 μm.

The samples were irradiated with Q-switched ruby laser pulses of 20-ns duration and energy density close to the damage or melting threshold of the material.

Unirradiated and irradiated samples were placed in a vacuum chamber ($p = 10^{-11}$ Torr) of a PHI-670 Nanoprobe Auger electron microscope (USA). The diameter of the probing electron beam was about 10 nm. A beam of 10-keV electrons with a current of 2×10^{-8} A was incident normally to the surface. The depth of Auger electron escape was about 20 Å. The surfaces to be studied were cleaned by argon ion etching up to a depth of ~0.1 μm, at 38 nm/min, with the vapor pressure in the vacuum chamber being $\sim 10^{-9}$ Torr. The chemical composition of the sample surface was measured both locally and by a surface scan (distributions of chemical elements over the surface were obtained with a resolution of ~2 μm).

Figure 1 shows the scanning electron microscope (SEM) images of (a) unirradiated CdTe polycrystalline sample surfaces and (b) the surfaces irradiated with ruby laser pulses. As can be seen, the grain surface of the irradiated sample is porous (Fig. 1b), and the grain boundaries are less clear-cut than those of a virgin sample (Fig. 1a). It is evident that the irradiation of polycrystalline layers with nanosecond ruby-laser pulses with an energy density close to the melting threshold changes the relief of the grain surface and boundaries due to the evaporation or tearing off of fragments (segments) from the grain surface and the dispersion of these fragments over the polycrystalline surface. After removing ~3 μm of the surface layer by ion etching, the grain boundaries become more pronounced, and the grain surfaces lose its porosity (Fig. 1c). It seems plausible that, after the removal of a surface layer to a certain depth in the irradiated sample, one can obtain a surface relief similar to that of an unirradiated sample (Fig. 1d).

We also studied the distribution of chemical elements over the virgin (Figs. 1a, 1c) and irradiated (Figs. 1b, 1d) CdTe polycrystalline surfaces. The high-contrast computer images of the Auger spectra present the distribution of chemical elements over the surface. The chemical elements existing at the surface have been indicated by different colors, which are substituted here by the figures: (*1*) for Te, (*2*) for Cd, (*3*) for the stoichiometric composition of the surface, (*4*) for the insulator phase, and (*5*) for carbon.

As can be seen from Fig. 1a, the regions close to the grain boundaries are rich in tellurium (*1*). Cadmium (*2*)

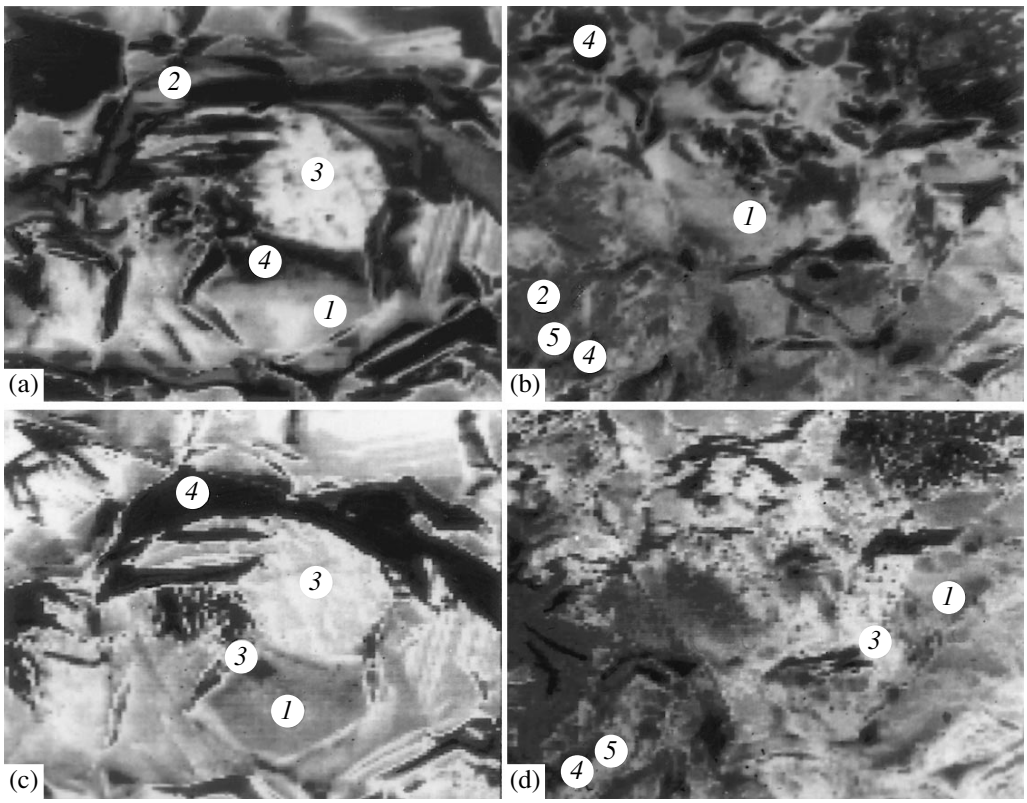

Fig. 1. Scanning electron microscope (SEM) images and maps of distribution of chemical elements over the surface of (a, c) unirradiated and (b, d) irradiated CdTe polycrystalline samples (c and d show the surface after the ion etching off of a ~3-μm-thick layer).

accumulates mainly at the grain boundaries and in the grain cavities. The regions with an enhanced concentration of defects can act as sinks for cadmium atoms. The regions indicated by (*4*) in Fig. 1 bear evidence of a considerable charge at the surface and can be associated with the insulator phase (oxide) formation, which is indicative of the initial inhomogeneity of the polycrystalline layer. Under the present experimental conditions, we failed to determine the chemical composition of the highly charged surface regions. The removal of about 3 μm of the surface layer of an irradiated sample results in a noticeable improvement in the stoichiometry of its composition (Fig. 1c). However, the tellurium-rich regions (*1*) and the small cadmium accumulations (*2*) are observed on the crystalline surface closer to the grain boundaries. The pronounced decrease in Cd concentration in the accumulations located near the grain boundaries can result from both the removal of the Cd layer by ion etching and the impossibility of determining it due to a highly charged surface. The area associated with the formation of the insulator phase (*4*) therewith decreases.

Laser irradiation of a CdTe polycrystalline surface also results in the formation of a well-pronounced tellurium film (*1*) (Fig. 1b). This indicates that, under the high-energy laser irradiation, evaporation or tearing of atoms from the polycrystalline surface is more intense for cadmium than for tellurium. Cadmium (*2*) is mostly concentrated at the grain boundaries. Further accumulation of Cd can occur in the laser-induced grain pores and in the macroregion (*2*). The irradiated surface also contains a considerable number of carbon atoms (*5*) mainly located in the vicinity of cadmium accumulations, which are regions of enhanced concentrations of defects. Carbon atoms may be "fired" by laser irradiation into the CdTe polycrystalline surface layer and then diffuse to sinks. A more stoichiometric pattern, similar to that of a virgin sample, is observed after the etching of an approximately 3-μm-thick layer from the irradiated surface (see Fig. 1d) where the background is indicated by (*3*). As a result of the laser irradiation, the fraction of surface area occupied by the insulator phase noticeably decreases (compared to that of a virgin sample), thus testifying to the laser-induced improvement in homogeneity of the CdTe layer.

Auger spectra of CdTe polycrystalline surfaces were measured in the grain before (Fig. 2a, curve *1*) and after (Fig. 2a, curve *2*) laser irradiation with an energy density close to the melting threshold of the material. The most pronounced peaks correspond to the tellurium and cadmium. The peak amplitudes relate as Cd/Te = 0.9, thus indicating that the original content of the sample surface slightly differs from the stoichiometric one. The surface also contains small amounts of

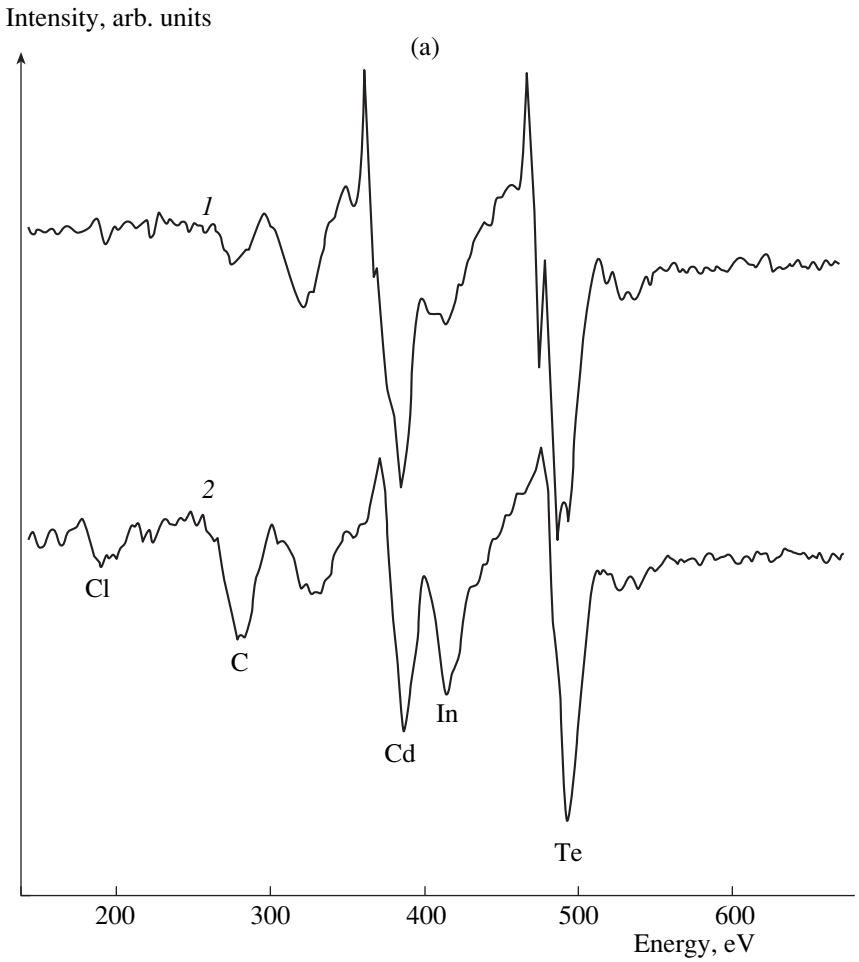

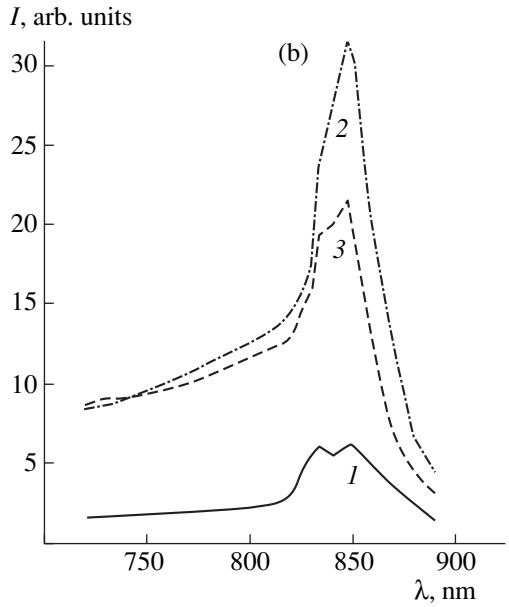

Fig. 2. (a) CdTe Auger spectra measured in the grain (*1*) before and (*2*) after irradiation with ruby laser pulses with an energy density below 0.16 J/cm^2; (b) photoconductivity spectra of CdTe polycrystalline layers (*1*) before and (*2*) after laser irradiation, and (*3*) after the ion etching off of a ~3-μm-thick layer.

carbon, chlorine, and indium. After irradiation, the ratio of the peak amplitudes becomes Cd/Te = 0.75, which means that the surface is enriched with tellurium. An increase in the concentration of carbon, chlorine, and indium at the surface is also observed.

Auger spectra measured at the grain boundaries of unirradiated CdTe polycrystalline samples exhibit main peaks similar to those obtained in the grain; whereas, in the spectra measured closer to the grain boundary, the main peak amplitudes show Cd/Te = 0.8 signifying that the grain boundary is enriched with tellurium. The concentrations of chlorine, indium, and carbon are not equal in the grain, at the grain boundaries, or close to the grain boundary. The impurity concentration at the grain boundaries slightly exceeds that in the grain and close to the grain boundary. Laser-induced changes in the Cd/Te peak ratio and in the content of impurities are similar to those observed for the spectra measured in the grain.

We have also studied the dependence of photoelectric properties of CdTe polycrystalline samples on the composition of the surface layer. Figure 2b shows the photoconductivity spectra obtained before (curve *1*) and after (curves *2*, *3*) the laser treatment. It is obvious that an increase in the photosensitivity of the samples results from laser treatment with an energy density close to the melting or damage threshold of the material (Fig. 2b, curve *2*). Alongside this, the resistance of samples decreases by a factor of 100. After the Te film has been rinsed in a 1% solution of KOH in methanol, the photosensitivity of the samples drops, whereas their "dark" and "light" resistances are still 10 times lower than those of the virgin layers. After the ion etching off of a layer ~3 μm thick, the photosensitivity of the sample decreases but still exceeds the initial value (Fig. 2b, curve *3*). The increase in photosensitivity stems from the fact that, under laser irradiation, the CdTe polycrystalline layer becomes covered with a Te film, which gives rise to recombination barriers that separate nonequilibrium charge carriers [1, 2]. According to our previous study [2], the growth of photosensitivity observed after the Te film etching may be connected with an increase in the concentration of both *r* centers and deep attachment levels. An increase in concentration of the deep attachment levels compensating the *r*-centers is possibly caused by Cd formation or by chlorine or indium release from accumulations, which give rise to shallow-level hydrogen-like donor centers in CdTe [3]. Laser-induced growth in chlorine and indium concentrations is confirmed by the results of Auger spectroscopy of the surface (Fig. 2a). The increase in photosensitivity resulting from etching off of the 3-μm layer may be associated with an increase in chlorine and indium concentrations, as well as with a laser-induced improvement in homogeneity of the polycrystalline surface.

To summarize the aforesaid, the analysis of the Auger spectra obtained in the experiment reveals that the laser irradiation of CdTe polycrystalline layers cleans their surfaces from the insulator phase and modifies the stoichiometry of a surface layer ~3 μm thick. The removal of this layer leads to an improvement in the homogeneity of the polycrystalline surface. Since etching off a 3-μm layer produces a drastic decrease in concentration and even disappearance of carbon from the irradiated surface, we managed to estimate the depth of carbon penetration into the polycrystalline layer to be several micrometers.

REFERENCES

1. A. Baĭdullaeva, A. I. Vlasenko, V. A. Gnatyuk, *et al.*, Fiz. Tekh. Poluprovodn. (St. Petersburg) **27**, 56 (1993) [Semiconductors **27**, 29 (1993)].
2. A. Baĭdullaeva, A. I. Vlasenko, A. V. Lyubchenko, *et al.*, Neorg. Mater. **36** (5), 545 (2000).
3. A. Baĭdullaeva, N. E. Korsunskaya, B. B. Dzhumaev, *et al.*, Ukr. Fiz. Zh. **34**, 1019 (1989).

Translated by A. Sidorova-Biryukova

Semiconductors, Vol. 35, No. 6, 2001, pp. 718–722. Translated from Fizika i Tekhnika Poluprovodnikov, Vol. 35, No. 6, 2001, pp. 749–753.

SEMICONDUCTOR STRUCTURES, INTERFACES, AND SURFACES

A Noncontact Electron-Probe Method for Measuring the Diffusion Length and the Lifetime of Minority Charge Carriers in Semiconductors

É. I. Rau* and Shiqiu Zhu

Moscow State University, Vorob'evy gory, Moscow, 119899 Russia

**e-mail: rau@pell157a.phys.msu.ru*

Submitted July 10, 2000; accepted for publication December 7, 2000

Abstract—A new method for measuring the diffusion length and the lifetime of minority charge carriers in semiconductor crystals was developed and implemented. The method is based on the detection of surface electron-induced potential in semiconductors and its phase shift in relation to the coordinate of probing in reference to the barriers. Experimental results of determining the electrical parameters of semiconductors by an example of silicon *p–n* junctions are reported. © *2001 MAIK "Nauka/Interperiodica".*

INTRODUCTION

The diffusion length L and the lifetime τ of nonequilibrium charge carriers are the most important characteristics of semiconducting materials. A method based on detecting the electron-beam-induced current (EBIC) in a scanning electron microscope (SEM) system is widely used for measurements of the above characteristics and for the direct observation of local crystallographic and other electrically active defects in semiconductors [1, 2]. The theory of the EBIC method is developed fairly well for semiconductor structures with *p–n* junctions and Schottky barriers; however, this method has a limited practical implementation. Its main drawbacks include the necessity for contacts to the sample, the presence of barriers separating the charge carriers, and the need to know *a priori* some of the semiconductor parameters. Detection of cathodoluminescence in a SEM is a noncontact method; however, silicon, widely used in microelectronics, does not possess cathodoluminescent properties.

We believe that it is topical and promising to use the method of the surface electron-induced potential (SEIP) for noncontact nondestructive local measurements of L and τ; this method has been previously developed for visualization of electrical inhomogeneities in crystals [3–5]. In this paper, we describe the basics of measuring L and τ by this method and report the first experimental results.

EXPERIMENTAL

The new method is based on the noncontact detection of variations in the surface (or barrier) potential that arise during the irradiation of a semiconductor object with the SEM electron beam. The experimental layout is schematically represented in Fig. 1. A semiconductor crystal (e.g., *p*-Si) is typically grounded from the bottom by table M2 of SEM, whereas the upper crystal surface remains free. When the semiconductor is irradiated with the SEM electron beam (e. b.), the nonequilibrium charge carriers generated in a microvolume (g. v.) are separated in the surface space-charge region (SCR) and affect the band bending at the crystal surface; as a result, the surface potential is changed by ΔV. Variations ΔV depend on the local electronic properties of the surface and on fundamental

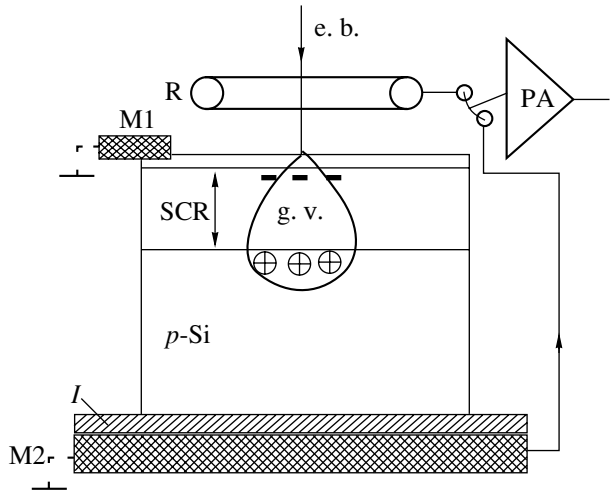

Fig. 1. Schematic representation of detection of the surface electron-induced potential in a SEM. The generation volume (g. v.) of the charge carriers is represented arbitrarily. The abbreviation e. b. stands for electron beam.

1063-7826/01/3506-0718$21.00 © 2001 MAIK "Nauka/Interperiodica"

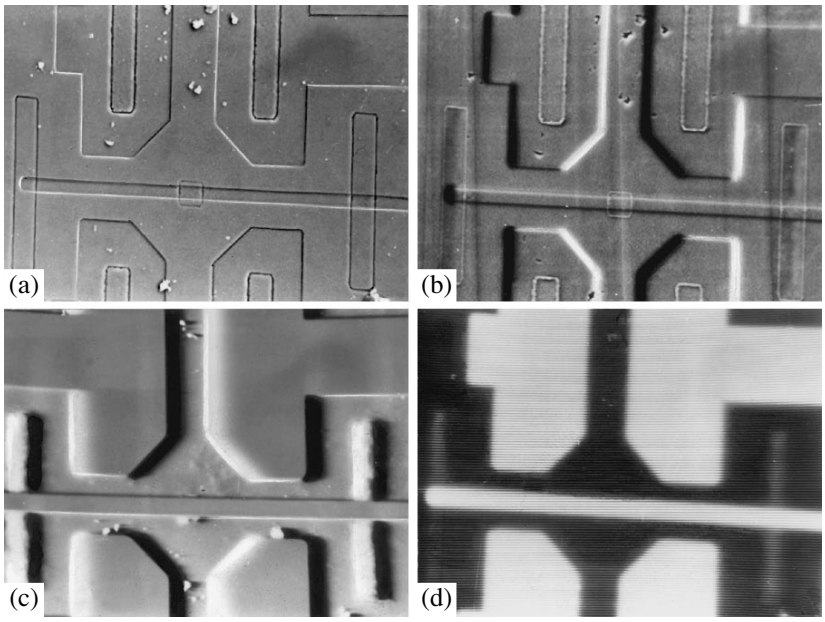

Fig. 2. Images of an *n*-Si wafer with local areas having the *p*-type conductivity. The images were obtained (a) using the secondary electrons; (b) in the differential SEIP mode, with the signal being detected from the top surface of the sample; (c) in the same mode as (b) but with the signal detected from the bottom surface; and (d) using the detection with a lock-in amplifier.

parameters of semiconducting material. A metal ring R playing the role of a detector is installed about 0.5 mm from the surface; the SEIP signal is derived from this ring. Transmission of the ΔV signal in such a configuration is accomplished via the capacitive coupling between the irradiated area of the crystal surface and the ring electrode. The induced signal from the detector is fed first to a charge-sensitive preamplifier (PA) and then to measuring devices or to the SEM display.

Basically, it is also possible to detect the SEIP signal from the rear (bottom) surface of the crystal. In that case, the upper crystal surface irradiated with the electron beam is grounded using a metal contact M1 (see Fig. 1), whereas the ac signal ΔV is detected by the metal plate M2, which is now not grounded, via the capacitance of insulating layer I. The signal polarity is inverted in this configuration, and its magnitude increases appreciably due to an increase in the coupling capacitance. Still another advantage of detecting the signal via the bottom unirradiated surface of the sample is related to a decrease in the contribution of the secondary and reflected electrons; this contribution is appreciable when the signal is detected with the upper ring electrode. This statement is illustrated by the microphotographs in Fig. 2 showing the images of the *n*-Si crystal surface with local *p*-type areas doped with boron. The photographs demonstrate the potentials of noncontact visualization of electrically active inhomogeneities in the crystal and the spatial distribution of an implanted impurity that forms planar *p–n* junctions in the silicon wafer. Photographs 2b and 2c were obtained without gating the electronic probe, whereas photograph 2d was obtained in the gating mode.

We now consider the potentialtities of the SEIP method for measuring the parameters L and τ. If the *p–n* junction or the Schottky barrier is located in the plane perpendicular to the irradiated crystal surface, the detected SEIP signal ΔV (scanning in the direction X starting from the *p–n*-junction boundary) is given to the first approximation by [6]

$$\pm\Delta V = C\beta\ln[1 + (G_{\text{eff}}I_0/I_s)\exp(-X/L)] \qquad (1a)$$

or

$$\pm\Delta V = C\beta\ln[1 + (\Delta n/N_0)\exp(-X/L)], \qquad (1b)$$

where C is the capacitive coupling coefficient for the detector [3, 5]; $\beta = kT/q$ is the thermal potential; $G_{\text{eff}} = G_0S/(1 + S)$ is the effective generation rate of excess charge carriers, with $G_0 = (E_0/E_{\text{eh}})(1 - k)$, S denoting the reduced surface-recombination rate for charge carriers, E_0 standing for the energy of primary electrons, E_{eh} denoting the energy needed for generation of an electron–hole pair, and k standing for the fraction of the reflected electron probing-beam energy; I_0 is the probe current; I_s is the saturation reverse current of the *p–n* junction; and Δn and N_0 are the concentrations of the nonequilibrium and majority charge carriers, respectively. The "+" sign corresponds to the surface depletion layer (or to the layer with a slight inversion) for the *n*-type, whereas the "–" sign corresponds to the same for the *p*-type. As can be seen from expression (1), the curve $\Delta V = f(L)$ is nonlinear; therefore, it is impossible to determine L from the exponential dependence as is accepted in the widely used classical EBIC method

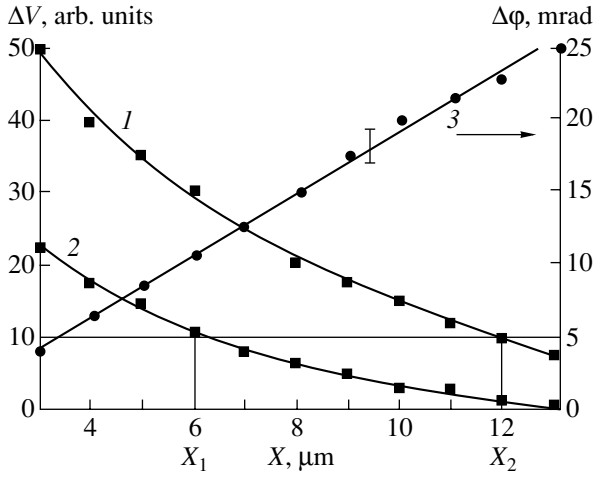

Fig. 3. Dependences of (*1*, *2*) the SEIP signal ΔV and (*3*) the phase shift $\Delta\varphi$ on the coordinate of probing for a silicon *p–n* junction.

(see, for example, [1, 7]). In addition, expression (1) includes a number of the *a priori* unknown parameters, such as G, I_s, C, and S, which also precludes the calculation of L directly from formula (1). In this situation, it is reasonable to use the approach in which the measured quantity remains constant when several other controlled experimental parameters change. For example, this approach is used in the method of the constant surface photovoltage which is recorded while the intensity and spectrum of the optical irradiation of semiconductor are varied [8].

In the situation we consider, this approach is applied in the following way. We detect the dependences $\Delta V(X)$ when the electron probe is scanned along the line X perpendicular to the *p–n* junctions with currents of I_{01} and I_{02}; in the obtained curves, we can always determine the points X_1 and X_2 such that

$$\Delta V_1(I_{01}X_1) = \Delta V(I_{02}X_2), \text{ for } X_{1,2} \geq L,$$

i.e.,

$$\begin{aligned}\Delta V_1 &= C\beta\ln[1 + (G_{\text{eff}}I_{01}/I_s)\exp(-X_1/L)] \\ &= \Delta V_2 = C\beta\ln[1 + (G_{\text{eff}}I_{02}/I_s)\exp(-X_2/L)].\end{aligned} \quad (2)$$

Using Eqs. (1) and (2), we obtain a simple and unique relationship for determining the quantity L, i.e.,

$$\ln(I_{01}/I_{02}) = (X_2 - X_1)/L. \quad (3)$$

We note that the initially unknown quantities S, I_s, C, and G_{eff} do not appear in Eq. (3), whereas determination of the quantity $\Delta X = (X_2 - X_1)$ does not require the knowledge of the true distance between the measurement point X and the *p–n* junction; rather, only the absolute difference in the coordinates ΔX is required to be known.

As for the measurements of the lifetime of the minority charge carriers τ, the known method for determining τ from the EBIC signal decay in the case of pulsed irradiation [9, 10] is inapplicable to the situation under consideration since, first, the decay $\Delta V(t)$ is not purely exponential and, second, the input impedance of the preamplifier is too high (the passband is 100 kHz), which prevents the lifetimes of $\tau < 10$ μs from being measured. An alternative to measuring the decay time of the signal is the measurement of the phase shift $\Delta\varphi$ between the irradiation pulse and the detected signal maximum. This elegant method [7, 11] is almost insensitive to the surface recombination rate and, more importantly, is applicable when the modulation frequencies of the electron probe f satisfy the condition $\omega\tau < 0.1$ ($\omega = 2\pi f$).

It has been shown previously [7, 11] that, if the probe is scanned along the coordinate X perpendicular to the *p–n*-junction plane, the phase-shift gradient $\Delta\varphi/\Delta X$ increases proportionally to τ in the region of $\omega\tau < 0.5$, and the product $Ld\varphi/dx$ is a function of $\omega\tau$ alone; i.e., we have

$$d\varphi/dX = \omega\tau/2L = \omega L/2D = \omega\sqrt{\tau}/2\sqrt{D} \quad (4a)$$

or, in a more accurate approximation,

$$Ld\varphi/dX = 0.62(\omega\tau)^{1/2}[1 + 2.8(\omega\tau)^{-3/2}]^{-1/3}. \quad (4b)$$

Thus, simultaneously measuring both the amplitude and phase of the detected signal using a lock-in amplifier with a phase output, we can determine L and τ from relationships (3) and (4). We note that expressions (1) and (4) may be used only in the small-signal mode (when $\Delta V < \beta$ or $\Delta n/N_0 \ll 1$).

RESULTS AND DISCUSSION

In Fig. 3, we show experimental curves of the SEIP-signal decay in relation to the coordinate X that indicates the distance between the measurement point and the *p–n*-junction boundary; the electron-probe currents were $I_{01} = 4$ nA (curve *1*) and $I_{02} = 2$ nA (curve *2*). We studied the emitter–base *p–n* junction of a silicon bipolar transistor. The accelerating voltage of SEM was 20 kV, and the probe modulation frequency was $f = 40$ kHz. The SEIP signal was measured from the emitter side; i.e., the values of τ_p and L_p were determined.

If we assume that $\Delta V_1 = \Delta V_2 = 10$ in Fig. 3, we have $\Delta X = X_2 - X_1 = 6.0$ μm; in this range, the gradient of the measured phase shift is equal to $d\varphi/dX = 2$ mrad/μm. Therefore, $L_p = \Delta X\ln(I_{01}/I_{02}) = 8.7$ μm and $\tau_p = 2L_p(d\varphi/dX)\omega^{-1} = 0.14$ μs. Here, the condition $\omega\tau < 1$ is satisfied; however, the value $D_p \approx 5.4$ cm^2/s calculated from the relation $L^2 = D\tau$ is indubitably underestimated. A similar discrepancy has been observed previously [11, 12]; in order to clarify the origin of this discrepancy, a further consideration and the method cor-

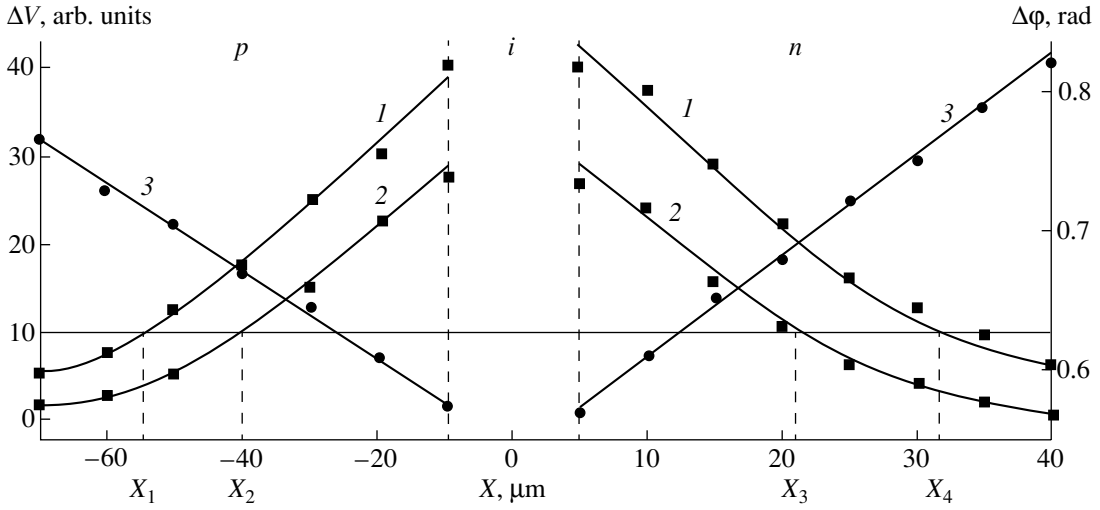

Fig. 4. Dependences of (*1*, *2*) the SEIP signal ΔV and (*3*) the phase shift $\Delta\varphi$ on the coordinate X for a silicon p–i–n diode.

rection are required. One of the drawbacks consists in the fact that, in the calculations in this study, we used relationship (3) derived for induced current rather than for potential described by formula (1a). A negative contribution of relaxation of capacitances in the measurement channel and the diffusion capacitance of the p–n junction is also possible. All these factors should be taken into account when developing the suggested method.

It is important for these measurements that the condition $\Delta n/N_0 \ll 1$ be satisfied. If this requirement is fulfilled, expression (1b) may be written as

$$\Delta V = C\beta[1 + (\Delta n/N_0)\exp(-X/L)]; \qquad (5)$$

it is for this case that formula (4a) was derived. Generally, the density of nonequilibrium charge carriers Δn is expressed in terms of the generation rate for electron–hole pairs G and the lifetime of the minority charge carriers τ [13] as

$$\Delta n = G\tau = (I_0E_0/E_{eh}qV_0)(1 - \eta\bar{E}/E_0), \qquad (6)$$

where q is the elementary charge, V_0 is the generation volume in the crystal, and η the coefficient of reflection of electrons with the mean energy $\bar{E}$. The volume V_0 in which the density of nonequilibrium charge carriers is estimated depends on the generation volume governed by the reduced penetration depth of primary electrons R_0 (thereby, by their energy E_0) and by the diffusion length L of the charge carriers. $V_0 = (4/3)\pi R_0^3$ for small L ($L \lesssim R_0$), whereas $V_0 = (4/3)\pi L^3$ for large L ($L > R_0$, as is the case, e.g., for Si). Assuming that, in our experiments (E_0 = 20 keV, $I_0 = 10^{-9}$ A, and η(Si) = 0.8), L = 15 μm and $\tau = 10^{-6}$ s, we obtain $\Delta n = 10^{16}$ cm^{-3}, whereas $N_0 \gtrsim 10^{18}$ cm^{-3} in the studied samples; i.e., the requirement $\Delta n/N_0 \ll 1$ was fulfilled.

The results of experiments with another object (a silicon p–i–n diode) are shown in Fig. 4. In this case, the measurements were performed for the Si surface areas with the p-type and n-type conductivity; the central i-type part of the junction (the region of ~10 μm in extent with intrinsic conductivity) was excluded from measurements. During the measurements, the SEM accelerating voltage was 20 keV, the modulation frequency of electron probe was f = 40 kHz, and the probe currents were I_{01} = 2 nA (curve *1*) and I_{02} = 1 nA (curve *2*). Curve *3* represents the measured phase shift $\Delta\varphi$ as a function of the coordinate X in the p and n regions of the p–i–n diode. The semiconductor parameters determined from the curves in Fig. 4 are L_p = 14.3 μm, L_n = 21.4 μm, τ_p = 0.75 μs, and τ_n = 0.4 μs.

Despite the fact that the method has a number of limitations, its merits are obvious. If the method is further improved, its flaws can be remedied to a large extent.

ACKNOWLEDGMENTS

We are indebted to Prof. E. Plies and M. Kienle (University of Tübingen, Germany) for their collaboration with us in conducting this study.

REFERENCES

1. H. J. Leamy, J. Appl. Phys. **53**, R51 (1982).
2. E. B. Yakimov, Izv. Akad. Nauk, Ser. Fiz. **56** (3), 31 (1992).
3. A. V. Gostev, Yu. S. Kleĭnfel'd, É. I. Rau, and G. V. Spivak, Mikroélektronika **16** (4), 311 (1987).

4. A. V. Gostev, Sh. Kh. Moll, É. I. Rau, and E. B. Yakimov, Izv. Akad. Nauk, Ser. Fiz. **62** (3), 599 (1998).
5. É. I. Rau, N. N. Sedov, Hu Wengou, and Zhu Shiqiu, Poverkhnost, No. 2, 4 (2000).
6. E. I. Rau, Shiqiu Zhu, and E. B. Yakimov, Inst. Phys. Conf. Ser. **164**, 22 (1999).
7. S. G. Konnikov, O. V. Salata, V. E. Umanskiĭ, and V. M. Chistyakov, Izv. Akad. Nauk SSSR, Ser. Fiz. **54** (2), 284 (1990).
8. L. P. Pavlov, *Methods for Determination of Key Parameters of Semiconducting Materials* (Vysshaya Shkola, Moscow, 1987), Chap. 4, p. 130.
9. D. E. Ioannou, J. Phys. D **13** (4), 611 (1980).
10. S. G. Konnikov, V. E. Umanskiĭ, V. M. Chistyakov, and I. I. Lodyzhenskiĭ, Fiz. Tekh. Poluprovodn. (Leningrad) **22** (10), 1803 (1988) [Sov. Phys. Semicond. **22**, 1140 (1988)].
11. T. Fuyuki and H. Matsunami, J. Appl. Phys. **52**, 3428 (1981).
12. M. Kittler and W. Seifert, Rev. Phys. Appl. **24**, C6 (1989).
13. *Semiconductor Material and Device Characterization*, Ed. by D. K. Schroder (Wiley, New York, 1998), p. 453.

Translated by A. Spitsyn

Semiconductors, Vol. 35, No. 6, 2001, pp. 723–726. Translated from Fizika i Tekhnika Poluprovodnikov, Vol. 35, No. 6, 2001, pp. 754–757.

LOW-DIMENSIONAL SYSTEMS

Manifestations of Quantum Confinement in Semiconductor Structures with Wide Doped Wells

A. A. Sherstobitov and G. M. Min'kov*

Institute of Physics and Applied Mathematics, Ural State University, pr. Lenina 51, Yekaterinburg, 620083 Russia

** e-mail: grigori.minkov@usu.ru*

Submitted November 23, 2000; accepted for publication November 27, 2000

Abstract—To clarify the importance of the quantum confinement effect in wide doped quantum wells, Shubnikov–de Haas oscillations in modulation-doped GaAs:Si structures are investigated in detail. It is demonstrated that quantum confinement manifests itself even in structures where the mean free path is only one-third of the well width. © *2001 MAIK "Nauka/Interperiodica".*

It is known that the quantum Hall effect (QHE) is characteristic of two-dimensional (2D) systems and originates from the special features in the energy spectrum and the localization phenomena specific to the 2D charge carrier system in a magnetic field [1]. However, recent publications [2, 3] report the observation of the QHE in the samples with wide (~100 nm) heavily doped quantum wells (QWs), where the well width d exceeds the mean free path l by as much as a factor of 3. These results were interpreted [2, 3] as a first observation of the QHE in a system with the three-dimensional (3D) spectrum. It is believed [2, 3] that a strong electron–electron interaction is the physical factor that causes the quantization of the Hall voltage in this case.

On the other hand, it is possible that the QHE in the structures of this type is due to the quantum confinement of the charge carriers, even though $l < d$.

In order to clarify the role of the quantum confinement in the wide doped QWs, in this study we investigated in detail the temperature, field, and angle dependences of Shubnikov–de Haas oscillations in the structures similar to those considered previously [2, 3].

The samples under study were grown by molecular-beam epitaxy on semi-insulating GaAs(100) substrates and contained the following layers: an undoped GaAs buffer (0.6 μm), a short-period GaAs/AlGaAs superlattice, an n^--GaAs layer (1 μm), a heavily Si-doped GaAs layer of thickness d = 100 nm, and an n^--GaAs layer (1 μm). Note that, in the temperature range $T < 10$ K (where the Shubnikov–de Haas oscillations were examined and the Hall concentration was determined), most of the carriers in the n^--layers are frozen out (captured by donors), and the conductance of these regions is negligibly low in comparison to the conductance of the heavily doped layer. The magnetoresistance and its field-strength derivative $d\rho/dB$ were measured in the fields up to 6 T in the temperature range of 1.5–20 K. A modulation technique was used to measure $d\rho/dB$.

Several samples with different carrier densities from 6×10^{11} to 2.5×10^{12} cm^{-2} were investigated. In this paper, we report the results obtained for one samples with the electron density $n_e = 1.6 \times 10^{12}$ cm^{-2} and mobility at $T = 1.5$ K, $\mu = 2400$ cm^2 V^{-1} s^{-1} (these values were determined from the field and temperature dependences of the resistance and the Hall coefficient). In the 3D case, the electron free path length $l = (\hbar\mu/e)(3n\pi^2)^{1/3} = 27$ nm, so that $d \approx 3.7l$. Thus, the electron density and mobility and the ratio $l/d \approx 0.3$ are all close to the values of these parameters in the structures where the QHE was observed [2, 3].

Figure 1 displays the magnetic-field dependences of the resistance and its derivative with respect to the magnetic field for different orientations of the field relative to the direction of the current j and the normal n to the plane of the structure. The negative magnetoresitance observed in the entire range of magnetic fields is related to the contribution from electron–electron interaction and, for $B \lesssim 0.5$–1 T, to the interference correction to the conductance [4]; this issue will not be discussed in this paper. We emphasize that the oscillation amplitude and the positions of peaks depend strongly on the orientation of the magnetic field relative to the plane of the structure and virtually do not depend on the field orientation relative to the direction of the current. Such a behavior of the Shubnikov–de Haas oscillations cannot be explained in the model of the 3D isotropic motion of the charge carriers (anisotropy of the GaAs conduction band is negligibly small); even this points to the importance of quantum confinement.

To quantitatively analyze the magnetoresistance oscillations, let us consider the corresponding Fourier spectra (Fig. 2). One can see that the spectrum of $\rho_\perp(\mathbf{B} \parallel \mathbf{n})$ features, along with the main peak at $k_1^2 = 3 \times 10^{12}$ cm^{-2}, several components with smaller k^2. It should be noted that, using the 3D model to calculate

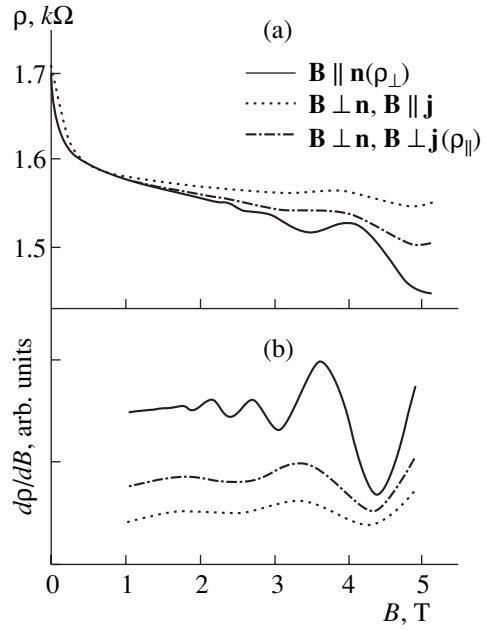

Fig. 1. (a) Magnetoresistance and (b) its derivative with respect to the magnetic field for different magnetic field orientations relative to the plane of the structure and the direction of the current; $T = 1.5$ K.

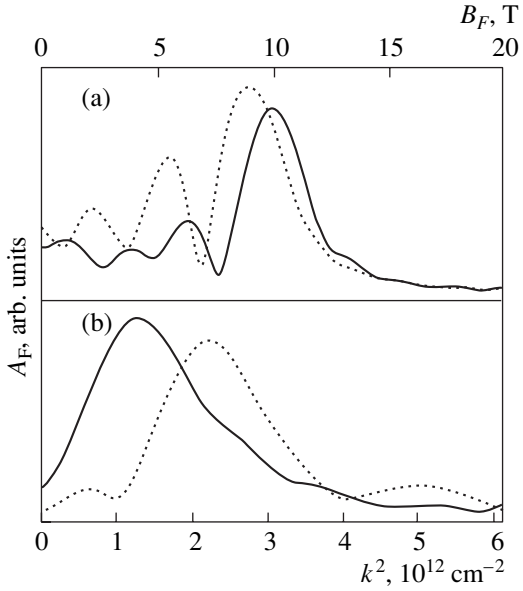

Fig. 2. Fourier spectra of the experimentally measured ρ(*B*) dependences (solid lines) and of the calculated dependences of the density of states at the Fermi level (dashed lines): (a) **B** ∥ **n** and (b) **B** ⊥ **n** and **B** ∥ **j** (**n** denotes the normal to the plane of the structure).

the carrier concentration corresponding to k_1^2, one obtains the value $n_{3D} = 1.8 \times 10^{17}$ cm^{-3}, which differs significantly from the value $n_e/d = 1.6 \times 10^{17}$ cm^{-3} determined from the Hall-effect data. In contrast to the Fourier spectrum of $\rho_\perp$, the spectrum of the $\rho_\parallel$ oscillations (**B** ⊥ **n**) features only one peak, whose position $k_2^2 = 1.3 \times 10^{12}$ cm^{-2} differs considerably from k_1^2. The discrepancy between n_{3D} and n_e—the difference in the positions of the main peaks in the Fourier spectra of oscillations $\rho_\perp$ and $\rho_\parallel$—and the appearance of additional components in the spectrum of $\rho_\perp$ cannot be explained in the context of the 3D model.

Let us analyze the results obtained taking the quantum confinement into account. We consider a simple model where the smooth part of the average donor potential is represented by a square potential well of width $d = 100$ nm, the Fermi level outside the well is fixed at 5 meV below the bottom of the conduction band (5 meV is the ionization energy of the shallow-level donors in GaAs), and the depth of the well is chosen in such a way that the total electron density in all subbands is equal to n_e. The calculation of the energy spectrum for the electron effective mass of $0.067m_0$ results in the well depth $U = 21$ meV; in such a well, five quantum-confinement subbands exist [5]. The subband energies E_i measured from the bottom of the well and the values of k_i^2 at the Fermi level are given in the table. The self-consistent solution of the Schrödinger and Poisson equations yields almost the same values for these parameters.

We assume that the magnetoresistance oscillations are proportional to the oscillations in the density of states at the Fermi level. The broadening of the density of states maxima is taken into account phenomenologically, assuming that the broadening of each state is described by a Gaussian. The broadening magnitude $\Delta = 3.5$ meV is chosen in such a way that the calculated oscillation amplitude is close to that determined experimentally.

Under a magnetic field perpendicular to the plane of the structure, each quantum-confinement subband is split into a series of zero-dimensional Landau levels and the density of states is the sum of the contributions from the Landau levels of different subbands. The Fourier spectrum of the oscillations in the density of states at the Fermi level calculated in the frame of this model is plotted by a broken line in Fig. 2a. It can be seen that the calculated curve is close to the experimental one: there is a main peak with $k^2 = 2.7 \times 10^{12}$ cm^{-2} and several peaks with a lower k^2. We believe that the difference in the spectral positions of the peaks in the two curves is related to the approximations made in the rough model adopted here: the square shape of the potential well and the equal magnitude of the Landau level broadening independent of the magnetic field strength as well as the number of the subband (we note that, according to [6], consideration of the magnetic-field dependence of the broadening magnitude Δ does not change significantly the Fourier spectrum of the oscillations).

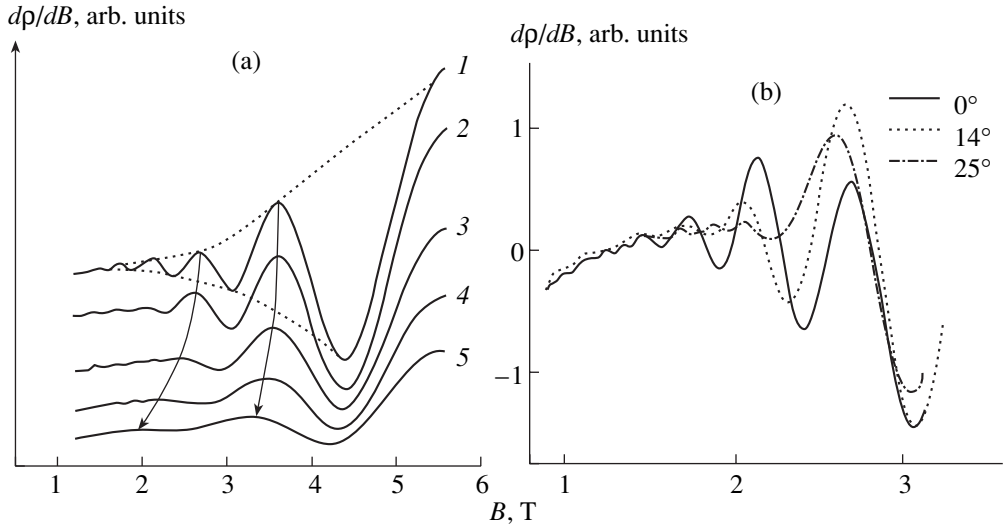

Fig. 3. (a) Derivative $d\rho/dB$ for different orientations of the magnetic field (the dashed lines show the oscillation envelope curves and the arrows show the angular shift of the oscillation maxima); the angle θ between the direction of the magnetic field **B** and the normal **n** to the plane of the structure equals (*1*) 0°, (*2*) 19°, (*3*) 39°, (*4*) 54°, and (*5*) 90°. (b) The same quantity in the range of field strengths and orientations where the most pronounced nonmonotone behavior of the angular dependence of the oscillation amplitude was observed.

We next consider, in the context of this model, oscillations in a longitudinal magnetic field (**B** ⊥ **n**). In this case, the calculation of the electron energy spectrum is reduced to the solution of the problem of the electron under a combined potential of the square well and the magnetic parabolic potential [5]. The energy of each state depends on the momentum k_H in the magnetic field direction and the position x_0 of the cyclotron-orbit center. This dependence was calculated numerically, and then, after the summation over all states, the density of states at the Fermi level $D(E_F, B)$ was determined. The Fourier spectrum for $D(E_F, B)$ is shown by a broken line in Fig. 2b. One can see that this spectrum exhibits a single broad peak characterized by the fundamental field $B_F = (c\hbar)/(2ek^2)$ significantly lower than that for the main peak in the case **B** || **n**, which is consistent with the experimental results (see Figs. 2a, 2b). A certain difference in the positions of the peaks in the calculated and experimentally measured spectra for the case **B** ⊥ **n** is, in our opinion, again related to the rough model approximations made.

In our view, the effect of the quantum confinement manifests itself most vividly in the angular dependence of the Shubnikov–de Haas oscillation amplitude $A(B, \vartheta)$. The oscillation amplitude for a given field was defined as the difference between the envelope curves drawn through the oscillation maxima and minima (in Fig. 3a, the envelope curves are plotted by broken lines). The angular dependences $A(B, \vartheta)$ derived in this way for different magnetic fields are shown in Fig. 4. One can see that in low fields the oscillation amplitude decreases very rapidly with the angular deviation of the field from the normal and oscillations vanish even for $\vartheta = 20°$. Under magnetic fields of intermediate strength (B = 2–3 T), the angular dependence of the oscillation amplitude is nonmonotonic. In high fields, the amplitude decreases steadily by a factor of nearly 3.5. Such behavior of $A(B, \vartheta)$ clearly indicates that the observed oscillations result from a superposition of several contributions with different periods and angular dependences. In the case under study, these contributions come from different quantum-confinement subbands.

Thus, the dependences of the amplitude of the oscillations and the shape of their Fourier spectra on the orientation of the magnetic field with respect to the plane of the structure are inconsistent with the 3D model but can be explained if the quantum confinement of the electron gas is taken into account.

At first glance, the shift of the oscillation maxima to the lower fields with the change of the magnetic field orientation from **B** || **n** to **B** ⊥ **n** (see Fig. 3a) contradicts the existence of the quantum confinement, since a high-field shift should occur in the purely 2D case. However, for a wide well, the observed oscillations result from the sum of the contributions from different subbands,

Table

i	E_i, meV	k_i^2, 10^{12} cm^{-2}
0	0.45	2.8
1	1.8	2.6
2	4	2.2
3	7	1.6
4	11	0.9

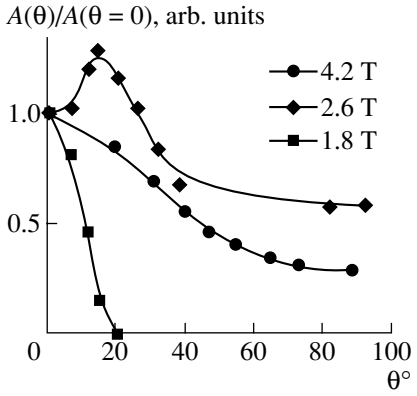

Fig. 4. Dependences of the Shubnikov–de Haas oscillation amplitude on the angle between the direction of the magnetic field **B** and the normal **n** to the plane of the structure for different magnetic field strengths.

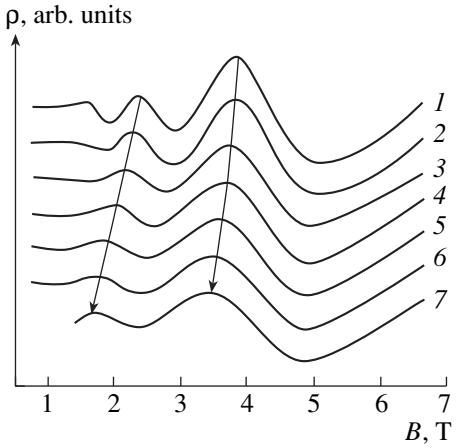

Fig. 5. Oscillations in the density of states at the Fermi level calculated for different magnetic field orientations in the parabolic-well approximation under the following assumptions: four quantum-confinement levels are occupied, the energy position spacing between them E_{01} = 3 meV, the Fermi level position measured from the bottom of the well E_F = 11 meV, and the level broadening Δ = 1.9 meV. The angle θ between the direction of the magnetic field **B** and the normal **n** to the plane of the structure equals (*1*) 0°, (*2*) 13°, (*3*) 26°, (*4*) 39°, (*5*) 52°, (*6*) 65°, and (*7*) 78°.

each with its own period and angular dependence. This can lead both to the nonmonotone angular dependence of the oscillation amplitude (mentioned above) and to the shift of the net oscillation peaks to lower fields. Unfortunately, to our knowledge, there are no studies where the electron spectrum in a wide square potential well under a magnetic field of arbitrary orientation is calculated. Thus, we consider the closely related problem of the spectrum of a parabolic QW for which the solution for an arbitrary field orientation exists [7]. The parameters of the parabolic well should be chosen in such a way that, at a zero field, the characteristics of the energy spectrum and the number of the occupied subbands are close to those in the structures under study. The oscillations of the density of states at the Fermi level calculated in terms of such a model are plotted in Fig. 5. One can see that, for the chosen parameters of the parabolic well, the maxima in the net density of states at the Fermi level shift to the lower, rather than to the higher fields.

Thus, the results presented in this paper demonstrate that, even though in the structures under study the well width exceeds the electron free path length by a factor of 3–4, the effect of quantum confinement is evident. Therefore, one more explanation for the appearance of the QHE in similar structures can be given. In the field range of $B > 6$–10 T, where the QHE was observed [2], only a few 2D Landau levels remain below the Fermi level. In contrast to the conventional 2D systems, they are not the Landau levels with different magnetic quantum numbers; rather, they are the lowest Landau levels from different quantum-confinement subbands. The states lying between these subbands can be localized similarly to the conventional 2D case.

ACKNOWLEDGMENTS

We are grateful to O.É. Rut and A.V. Germanenko for their useful participation in discussions.

This study was supported by the Russian Foundation for Basic Research (project no. 00-02-16215), the Programs "Physics of the Solid-State Nanostructures" (project no. 97-1091) and "Universities of Russia: Basic Research" (project nos. 990409 and 990425), and the US Civil Research and Development Foundation (project REC-005).

REFERENCES

1. É. I. Rashba and V. B. Timofeev, Fiz. Tekh. Poluprovodn. (Leningrad) **20** (6), 977 (1986) [Sov. Phys. Semicond. **20**, 617 (1986)].
2. S. S. Murzin, I. Claus, and A. G. M. Jansen, Pis'ma Zh. Éksp. Teor. Fiz. **68** (4), 305 (1998) [JETP Lett. **68**, 327 (1998)].
3. S. S. Murzin, I. Claus, A. G. M. Jansen, *et al.*, cond-mat/9810224.
4. B. L. Altshuler and A. G. Aronov, in *Electron–Electron Interaction in Disordered Systems*, Ed. by A. L. Efros and M. Pollak (North-Holland, Amsterdam, 1985), Part 1.
5. S. Flügge, *Practical Quantum Mechanics* (Springer-Verlag, Berlin, 1971; Mir, Moscow, 1974).
6. T. Ando, A. B. Fowler, and F. Stern, Rev. Mod. Phys. **54**, 437 (1982); *Electronic Properties of Two-Dimensional Systems* (Mir, Moscow, 1985).
7. R. Merlin, Solid State Commun. **64** (1), 99 (1987).

Translated by M. Skorikov

Semiconductors, Vol. 35, No. 6, 2001, pp. 727–733. Translated from Fizika i Tekhnika Poluprovodnikov, Vol. 35, No. 6, 2001, pp. 758–765.

LOW-DIMENSIONAL SYSTEMS

Momentum Alignment and Spin Orientation of Photoexcited Electrons in GaAs in the Transition from Two- to Three-Dimensional Structures

I. A. Akimov, D. N. Mirlin*, V. I. Perel', and V. F. Sapega

Ioffe Physicotechnical Institute, Russian Academy of Sciences, Politekhnicheskaya ul. 26, St. Petersburg, 194021 Russia

**e-mail: mirlin@dnm.ioffe.rssi.ru*

Submitted December 28, 2000; accepted for publication December 28, 2000

Abstract—The effect of miniband formation in superlattices on the selection rules for optical transitions has been analyzed by studying the polarized hot electron luminescence (HEL). Two regions can be distinguished in the range of variation of miniband parameters in superlattices, each characterized by its own selection rules. The specificity of the selection rules for each of the regions is manifested in the linear and circular polarization of the PL, the distribution of photoexcited electrons over quasi-momenta, and the behavior of photoelectrons in the magnetic field. © *2001 MAIK "Nauka/Interperiodica".*

1. INTRODUCTION

The light emitted in radiative recombination of hot electrons in III–V semiconductors is polarized if the exciting radiation is polarized. The absorption of linearly polarized light leads to the momentum alignment of photoexcited electrons and holes [1–4]. The recombination of momentum-aligned electrons gives rise to a linearly polarized hot electron luminescence (HEL). The degree of linear polarization of the luminescence for electrons with wave vector $\mathbf{K} = (k_x, k_y, k_z)$, recombining with heavy holes, can be written as [2]:

$$\rho_{l\mathbf{k}} = \frac{k_y^2 - k_x^2}{k_x^2 + k_y^2 + 2k_z^2}. \quad (1)$$

The degree of linear polarization of radiation propagating along the z direction is given by $\rho_l = (I_x - I_y)/(I_x + I_y)$, where I_x and I_y are the intensities of light with polarization vector $\mathbf{e}_{\text{lum}}$ directed along the x and y axes, respectively. Thus, electrons recombining with heavy holes emit light with preferential polarization perpendicular to the projection of the wave vector $\mathbf{K}$ onto the (x, y) plane.

Similar effects of the momentum alignment have been observed recently in GaAs/AlGaAs quantum wells (QWs) [5–10], and considered theoretically in [11]. The specificity of the momentum alignment of 2D electrons, in distinction to the 3D case, manifests itself in the strong dependence of the HEL polarization on the kinetic energy of photoexcited electrons in QWs. The degree of linear polarization in QW structures varies between $\rho_l = 0$ for electrons with zero kinetic energy and $\rho_l \approx 0.5$ for those with kinetic energies exceeding the electron energy of the first confined state. A qualitative dependence of the linear polarization on the kinetic energy of electrons generated in QWs can be obtained from relation (1) by replacing k_z^2 with $\langle k_z^2 \rangle \sim (\pi/L)^2 \sim 2m_c E_1/\hbar^2$, where L is the QW width, m_c is the electron effective mass, and E_1 is the first electron confinement energy.

The absorption of circularly polarized light leads to spin orientation of photoexcited electrons and circular polarization of the luminescence. It seems at first glance that, at the instant of excitation, the spin of an electron excited in the interband absorption of circularly polarized light must be aligned with the incident beam, i.e. with the angular momentum of the exciting photon. What actually happens is that the spin of photoexcited electrons in a bulk sample has a lateral component perpendicular to the beam [2]. This component $\mathbf{S}_\perp$ is described by the expression

$$\mathbf{S}_\perp = \beta \mathbf{K}_\perp k_z, \quad (2)$$

where $\mathbf{K}_\perp$ is the lateral component of the wave vector perpendicular to the exciting beam, and β is a coefficient. This effect, named spin–momentum correlation, stems from the complex structure of the valence band. For the same reasons, electrons with lateral spin contribute to the circular polarization of HEL. This contribution is proportional to $(\mathbf{S}_\perp \cdot \mathbf{K}_\perp)$. Here $\mathbf{K}_\perp$ refers to the instant of emission, and in relation (2), to the instant of excitation. The z-axis-aligned magnetic field caused rotation of the vector $\mathbf{K}_\perp$ and precession of the spin $\mathbf{S}_\perp$. Since the rotation and precession velocities differ (in GaAs, the angular velocity of $\mathbf{K}_\perp$ is higher), the scalar product $(\mathbf{S}_\perp \cdot \mathbf{K}_\perp)$ decreases with increasing field, and, correspondingly, the HEL circular polarization decreases. It is precisely this effect that has been observed in bulk GaAs samples [12], thereby furnish-

ing direct experimental evidence of the spin–momentum correlation. However, this effect is absent in QW structures during absorption of light directed perpendicular to the plane of the well [7]. This is due to the absence of $\hbar k_z$ in QWs.

The magnetic field affects the linear polarization of the HEL during linearly polarized excitation. In bulk GaAs, the momentum distribution function of electrons rotates around the axis coinciding with the direction of the field vector **B**. Consequently, the degree of linear polarization of HEL is modified, unless the **B** direction coincides with the symmetry axis of the electron momentum distribution [2, 4]. In a QW, the lateral electron motion (in the *xy*-plane) corresponds to free electron motion with isotropic effective mass. Therefore, the magnetic field $\mathbf{B} \parallel z$ (Faraday configuration) rotates the electron momentum distribution about the *z*-axis. In this case, the Stokes parameters for the linear polarization in a QW are described in the same way as those in a bulk semiconductor [6, 7]. However, in the Voigt configuration (**B** perpendicular to the direction of light propagation), the effect of the magnetic field on the linear polarization differs significantly for bulk samples and QWs. In bulk GaAs, the linear polarization is modified with increasing magnetic field, whereas in QWs the polarization is independent of the **B** magnitude if the electron magnetic length exceeds the QW width [7].

It can be concluded that the momentum alignment and spin orientation of hot electrons, and also their behavior in an external magnetic field differ substantially for the cases of bulk samples and samples with QWs. The most important qualitative distinctions are listed below (for QWs, normal orientation of the exciting beam with respect to the QW plane is assumed).

(i) In bulk samples under linearly polarized excitation, the linear polarization of luminescence depends only slightly on the kinetic energy of the photoexcited carriers. In QWs, the linear polarization vanishes when the kinetic energy approaches zero.

(ii) In bulk samples under linearly polarized excitation in the Faraday configuration, the circular polarization of HEL depends on the magnetic field because of the breakdown of the spin–momentum correlation. In QWs, there is no such dependence, the spin–momentum correlation being absent.

(iii) In bulk samples studied in the Voigt configuration, the magnetic field affects the linear polarization of HEL. In QWs in the same geometry, the magnetic field does not affect the linear polarization of HEL if the magnetic length exceeds the well width.

The results of previous studies [13–15] show that the polarization properties of HEL in superlattices (SLs) differ from the properties of both bulk samples and QWs. In this report, we generalize these results for the case of a smooth transition from 2D (isolated QWs) to 3D (bulk GaAs) systems.

In the second section of the paper, the samples studied and the experimental methods used are described. The results obtained in studying the dependence of the HEL polarization on the kinetic energy of photoexcited electrons and the restoration of the spin–momentum correlation in SLs are presented in Section 3. It is shown that the polarization characteristics of narrow-miniband SLs are well described in the tight-binding approximation, and the applicability limit of this approximation is determined experimentally. In Section 4, we discuss the behavior of the linear polarization of HEL in an external magnetic field in the Faraday and Voigt configurations.

2. EXPERIMENTAL

The samples were grown by MBE on (100) GaAs substrates. The GaAs QW width L was the same (~40 Å) in all the samples. The energy width of the electron minibands was determined by the varied width of the ($Al_xGa_{1-x}As$) barriers, b, and by the varied Al content x (i.e., by the barrier height). The central part of wells $L/2$ was doped with beryllium ($N_{Be} \le 10^{18}$ cm^{-3}), with the regions adjoining the interfaces remaining undoped. The number of periods in each sample was 60.

Hot carriers were excited by radiation of He–Ne and Kr-ion lasers, and also dye (R6G and DCM) and Ti–sapphire lasers pumped by an Ar^+-ion laser. The luminescence was detected with DFS-24 and SPEX 1404 spectrometers equipped with cooled FÉU-79 and GaAs-FÉU photomultipliers, respectively, and a conventional photon counting system. Studies of HEL in the back-reflection configuration were done with the exciting and reflected beams perpendicular to the (001) plane of the structure. The measurements in magnetic fields of up to $B \le 10$ T were performed in the Faraday and Voigt configurations.

All the experimental data were obtained under excitation by linearly or circularly polarized light. In the former case, the electric vector of the laser radiation $\mathbf{e}_{exc}$ was aligned with the [110] axis of the sample. The degree of linear polarization of the HEL was determined using the relation $\rho_l = (I_\parallel - I_\perp)/(I_\parallel + I_\perp)$, where $I_\parallel$ and $I_\perp$ are the intensities of luminescence polarized parallel ($\mathbf{e}_{lum} \parallel \mathbf{e}_{exc}$) or perpendicular ($\mathbf{e}_{lum} \perp \mathbf{e}_{exc}$) to the polarization of the exciting light, respectively. In the Voigt configuration, the linear polarization was also measured under circularly polarized excitation (see Section 4). In this case, $I_\parallel$ and $I_\perp$ were defined as intensities with polarization ($\mathbf{e}_{lum} \parallel \mathbf{B}$) and ($\mathbf{e}_{lum} \perp \mathbf{B}$), respectively. The degree of circular polarization of the HEL was determined using a similar expression $\rho_l = (I_+ - I_-)/(I_+ + I_-)$, where I_+ and I_- are, respectively, the intensities of likewise and oppositely (with respect to the polarization of the exciting light) circularly polarized luminescence.

The HEL polarization curves were taken at temperature $T = 4$ K and moderate pumping density $P =$

10–15 W/cm^2. Thus, the HEL spectrum was formed by the recombination of photoexcited electrons with holes bound at neutral acceptors (transitions of the type $1hh \longrightarrow 1c \longrightarrow A^0$). For all the samples, the HEL spectra consisted of a zero-phonon peak associated with recombination of electrons at the generation point, and its *LO*-phonon replicas. The kinetic energy of the photoexcited electrons was found using the relation $E = \hbar\omega_{\text{lum}} - (E_g - E_A)$, where $\hbar\omega_{\text{lum}}$ and $(E_g - E_A)$ are the experimental HEL and the edge luminescence quantum energies, respectively. Here E_g is the band gap of the superlattice, and E_A, the acceptor ionization energy.

3. POLARIZATION OF HOT ELECTRON PHOTOLUMINESCENCE

3.1. Dependence of the Linear Polarization of the HEL on the Kinetic Energy of Photoexcited Electrons

Figure 1 shows the linear polarization ρ_l at the maximum of the zero-phonon HEL peak versus the electron kinetic energy E for SLs with a varied Al content (x = 0.3–1) at a fixed barrier width of 6 Å (data set *1*, blank circles). For each case, calculated values of $\eta = \Delta_G/\Delta$ are given, where Δ is the energy width of the first electron miniband, and Δ_G is the energy gap between the first and second minibands, calculated in terms of the Kronig–Penney model. The electron miniband width Δ is shown by a vertical arrow for each SL. For clarity, the figure also presents the $\rho_l(E)$ dependences obtained in a GaAs/AlAs (40 Å/80 Å) structure with isolated QWs (Fig. 1a, data set *2*, black squares), and in bulk GaAs (Fig. 1f, data set *2*, black squares). The experimental data for bulk GaAs are approximated by a dashed straight line reproduced in all parts of Fig. 1. The $\rho_l(E)$ dependence for an SL with the highest barriers, x = 1, (Fig. 1a) is approximated by a solid line also shown in all the other parts (b–f) of Fig. 1.

Let us first consider the energy dependence of the linear polarization for an SL with high barriers, i.e., with x = 1 (Fig. 1a). In this case, the $\rho_l(E)$ dependence is similar to that observed in QWs, namely, the polarization strongly depends on the kinetic energy of electrons, and the slope of the dependence remains the same. However, in the QW structure, the polarization vanishes when the energy approaches zero (see data set *2* and its linear approximation in Fig. 1a), whereas in the SL ρ_l is extrapolated to zero at an energy of 115 meV, which is close to the calculated value of the electron miniband width Δ = 120 meV (see data set *1* and its linear approximation in Fig. 1a). This behavior is accounted for by the formation of an electron miniband in the SL, resulting in the quasi-3D motion of electrons.

In the discussed GaAs/AlAs SL (x = 1), the barriers are high enough to justify the application of the tight-binding approximation, which assumes that the overlapping of the electron and hole wave functions of neighboring QWs is negligible [14]. In this case, the matrix elements for intersubband optical transitions remain the same as those in an isolated QW, and the HEL polarization in the SL depends only on the lateral electron energy ε_k, similarly to what occurs in a QW. It also follows that, similarly to the case of QWs, the probability of the generation of electrons with the lowest energy ε_k is the highest [11]. Hence, the photoexcited electrons with a total kinetic energy $E < \Delta$ mainly move along the SL direction (z-axis), and their luminescence is unpolarized. With increasing E, the lateral energy ε_k becomes higher, while the energy of motion along the SL remains unchanged, equal to Δ. This results in the increase of the linear polarization of the HEL. Alternatively, if the electrons are generated with energy E substantially exceeding Δ, they move mainly in the QW (xy) plane, and the degree of linear polarization ρ_l is close to that observed in QWs. Such a feature of the energy dependence of the momentum distribution function for photoexcited electrons results in the linear polarization ρ_l tending to zero when the energy E decreases to a value coinciding with the first miniband width Δ (see data set *1* and the approximating line in Fig. 1a). This effect allows an experimental determination of the electron miniband width in an SL.

Evidently, with increasing overlap of the wave functions of electrons and holes localized in the neighboring QWs, the contribution from interwell optical transitions cannot be neglected. A significant contribution of these transitions affects the HEL polarization and may indicate a deviation from the tight-binding approximation. As seen in Fig. 1, pronounced changes in the $\rho_l(E)$ dependence are observed for SLs with $x \le 0.6$, where the reduction of the barrier height strongly modifies the $\rho_l(E)$ behavior. First, in the electron energy range $0 < E < \Delta$, the degree of linear polarization is definitely nonzero, and increases gradually. Second, the slope of the $\rho_l(E)$ dependence at $E > \Delta$ gradually decreases with the barrier height becoming lower. The strongest changes are observed for a SL with x = 0.3 (data set *1* in Fig. 1f), where the $\rho_l(E)$ dependence is quite similar to that in bulk GaAs (data set *2*).

It follows from the data presented in Fig. 1 that the contribution of interwell optical transitions cannot be neglected when the width of the first electron miniband Δ approaches the energy gap between the first and the second minibands Δ_G, that is, $\eta \approx 1$ ($x \approx 0.6$). Therefore, $\eta > 1$ is a necessary condition for the applicability of the tight-binding approximation for calculating the matrix elements of interband optical transitions in SLs. In what follows, we designate samples with $x > 0.6$ as "narrow-miniband" superlattices, and those with $x < 0.6$, as "wide-miniband" SLs.

3.2. Restoration of the Spin–Momentum Correlation in a SL

Another experimental result indicating a manifestation of the optical properties of bulk GaAs in superlat-

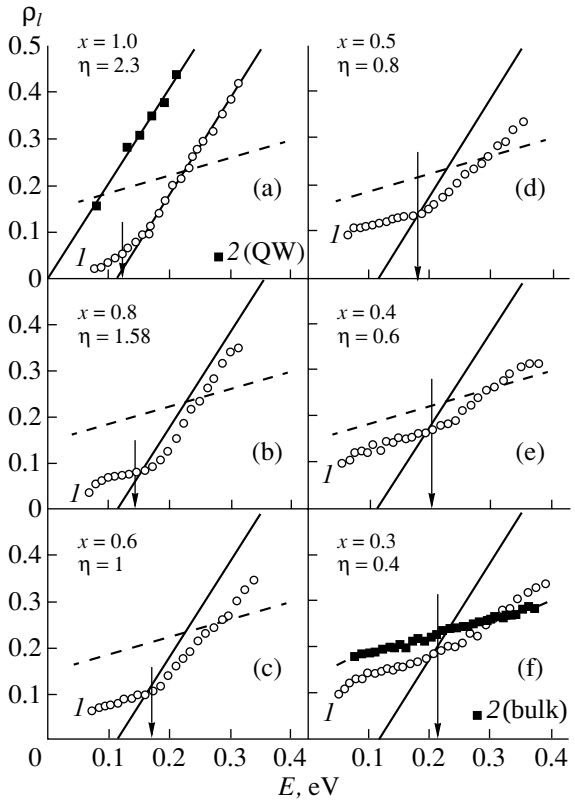

Fig. 1. Linear polarization ρ_l at the maximum of the zero-phonon HEL peak vs. kinetic energy of photoexcited electrons, E, under excitation of various structures by linearly polarized light. (*1*) GaAs/Al_xGa_{1-x}As (40 Å/ 6 Å) SLs with varied Al content in the barriers (x = 0.3–1). The width of the electron miniband Δ for each structure is denoted by a vertical arrow. (*2*) GaAs/AlAs (40 Å/80 Å) structure with isolated QWs (a) and bulk GaAs (f). Experimental data for bulk GaAs (f) and for the highest-barrier SL (x = 1) (a) are approximated by, respectively, dashed and solid lines reproduced in all the graphs.

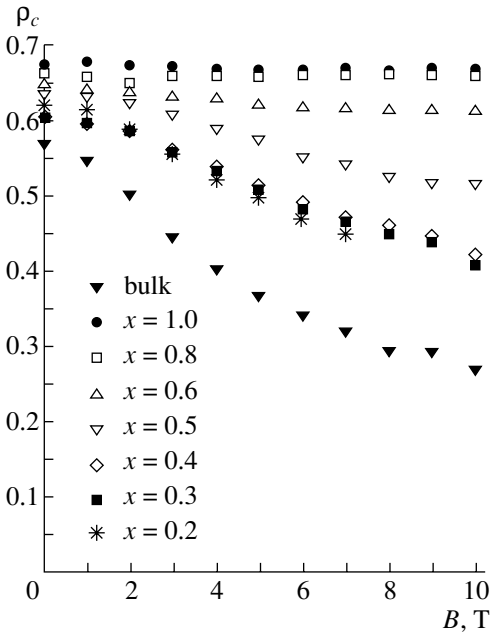

Fig. 2. Circular polarization ρ_c at the maximum of the zero-phonon HEL peak vs. magnetic field B, measured in the Faraday configuration under excitation of SLs with x = 0.2–1 and bulk GaAs by circularly polarized light. The kinetic energy of photoexcited electrons in the SL corresponds to $E \approx$ 80–100 meV.

tices, is that the spin–momentum correlation is restored with increasing miniband width. As discussed above (see the Introduction), the suppression of the circular polarization ρ_c (under circularly polarized excitation) in a longitudinal magnetic field indicates the existence of a correlation between the spin and momentum of photoexcited electrons.

Figure 2 presents the dependence of ρ_c on the magnetic induction B, taken in the Faraday configuration for electrons with the kinetic energy $E \approx$ 80–100 meV. For bulk GaAs, ρ_c decreases steeply with increasing B owing to the breakdown of the spin–momentum correlation. For "narrow-miniband" SLs, (x = 1, 0.8), ρ_c is field-independent, as occurs in QWs, where the spin–momentum correlation is absent because the $\hbar k_z$ momentum component is zero. This behavior of $\rho_c(B)$ is accounted for by the matrix elements of interband optical transitions in the narrow-miniband SLs remaining the same as those in the QW structures, since the contribution of interwell transitions is negligible. However, taking these transitions into account restores the spin–momentum correlation even in the tight-binding approximation.

In the tight-binding approximation, the electron wave functions in the conduction (Φ) and valence bands (Ψ) are written as

$$\Phi = e^{i\mathbf{k}\rho}\sum_n \varphi(z-na)e^{iQna},$$

$$\Psi = e^{i\mathbf{k}\rho}\sum_n \psi(z-na)e^{iQna},$$

where $\varphi(z)$ and $\psi(z)$ are the wave functions in an isolated QW, a is the superlattice period, Q is the miniband wave number, and $\mathbf{k}$ is the lateral wave vector in a QW. In the tight-binding approximation, the matrix element of the optical transition can be written as

$$\langle\Phi|\mathbf{D}\cdot\mathbf{e}|\Psi\rangle \propto f_0 + f_+\cos(Qa) + f_-\sin(Qa), \quad (3)$$

$$f_0 = \langle\varphi(z)|\mathbf{D}\cdot\mathbf{e}|\psi(z)\rangle,$$
$$f_\pm = \langle\varphi(z+a)|\mathbf{D}\cdot\mathbf{e}|\psi(z)\rangle \pm \langle\varphi(z-a)|\mathbf{D}\cdot\mathbf{e}|\psi(z)\rangle. \quad (4)$$

Here, $\mathbf{D}$ is the dipole moment operator, and $\mathbf{e}$ is the vector of the exciting light polarization (for circular polarization, $\mathbf{D}\cdot\mathbf{e} = D_x + iD_y$). Here we consider only the terms describing the transitions from the valence to conduction band inside a single well (f_0 term) and

between neighboring wells (terms including $f_{\pm}$). The last term in Eq. (3) is responsible for the spin–momentum correlation, its sign reversing on replacing Q by $-Q$. It is this term that gives the spin of a photoexcited electron a contribution similar to that described by relation (2), with the factor $\pm k_z$ replaced by $\pm Q$.

When transitions into the first electron subband are considered, $\varphi(z) = \varphi(-z)$, the value of f_- is nonzero only if the $\psi(z)$ function for holes contains an odd component. Such a component is absent at $k = 0$ in the first heavy-hole subband for a symmetric well. However, at $k \neq 0$ states with an angular momentum of +1/2 (–1/2) (i.e., light-hole states) are admixed with states +3/2 (–3/2), with the odd contribution coming from the light-hole subbands with even numbers.

A detailed calculation of the influence exerted by the magnetic field on the circular polarization of HEL in electron recombination via acceptor levels in the Faraday configuration would require a knowledge of the matrix elements of optical transitions, and, therefore, will not be performed here. Nevertheless, a general agreement of the above-described pattern with the experimental data follows from the fact that this influence becomes noticeable at the Al content $x = 0.4$ when the energy of the second light-hole subband exceeds the barrier height in the valence band, so that the overlapping integral due to the admixture of these states becomes significant. As follows from Fig. 2, the breakdown of the spin–momentum correlation in the magnetic field for SLs with $x \leq 0.4$ is already comparable with the same effect in bulk GaAs.

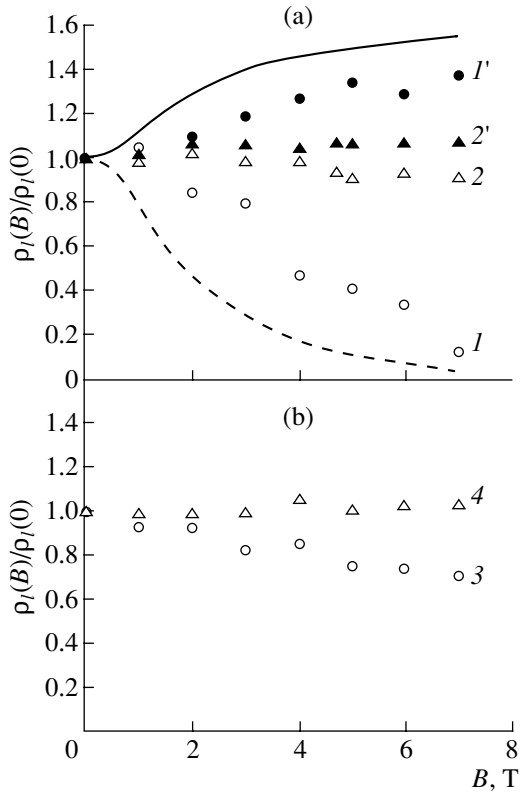

Fig. 3. Linear polarization ρ_l at the maximum of the zero-phonon HEL peak vs. magnetic field B, measured in the Voigt configuration under linearly polarized excitation: (a) GaAs/AlAs (40 Å/6 Å) SL: (*1*, *1*') $E \approx \Delta$, (*2*, *2*') $E \approx 2\Delta$, (*1*', *2*') $\mathbf{B} \parallel \mathbf{e}_{exc}$, and (*1*, *2*) $\mathbf{B} \perp \mathbf{e}_{exc}$; solid and dashed lines: calculated $\rho_l(B)$ for $\mathbf{B} \parallel \mathbf{e}_{exc}$ and $\mathbf{B} \perp \mathbf{e}_{exc}$, respectively. (b) bulk GaAs (*3*) and GaAs/AlAs (40 Å/80 Å) QW structures (*4*).

4. LINEAR POLARIZATION OF HOT ELECTRON PHOTOLUMINESCENCE IN A MAGNETIC FIELD

In this section, we analyze the behavior of photoexcited electrons in a magnetic field. In the Faraday configuration, the magnetic field is aligned with the SL axis and causes rotation of the lateral **k** vector, similarly to the QW case. The wave vector of the motion along the SL, **Q**, remains unchanged. This results in the depolarization of the HEL, and, by analogy with bulk GaAs [2, 4] and QWs [6, 7], the linear polarization depends on the magnetic field as

$$\rho_l(B) = \rho_l(0)/(1 + 4\omega_c^2\tau^2), \qquad (8)$$

where ω_c is the cyclotron frequency, and τ is the time in which an electron leaves the initial energy state, corresponding, in the case in question, to the time of scattering on an optical phonon. However, the effect of a magnetic field on the electron motion in QWs, narrow-miniband SLs, and bulk GaAs is different when **B** lies in the QW plane (Voigt configuration).

Figure 3a shows how the linear polarization ρ_l depends on the magnetic field B in the Voigt configuration for a GaAs/AlAs (40 Å/ 6 Å) SL with miniband width $\Delta = 120$ meV, for two excitation energies. If the energy of excited electrons exceeds the miniband width ($E \approx \Delta$) only slightly, electrons move mainly along the SL (z-axis). In a transverse magnetic field, the vector **Q** decreases, and the lateral component perpendicular to the magnetic field, $k_\perp$, increases, so that total kinetic energy of an electron E is conserved. This leads to a substantial variation of the linear polarization (see points *1*, *1*' in Fig. 3a), which depends on the anisotropy of the momentum distribution in the QW plane. If the magnetic field is aligned with the polarization of the exciting beam ($\mathbf{B} \parallel \mathbf{e}_{exc}$), then the y-component of the lateral momentum, perpendicular to the $\mathbf{e}_{exc}$ vector, increases; in accordance with relation (1), an increase in polarization would be expected, and is observed in the experiment (points *1*'). If the magnetic field is perpendicular to the polarization vector ($\mathbf{B} \perp \mathbf{e}_{exc}$), the k_x component increases, and the polarization decreases (points *1*). The solid and dashed lines in Fig. 3a represent calculations for the $\mathbf{B} \parallel \mathbf{e}_{exc}$ and $\mathbf{B} \perp \mathbf{e}_{exc}$ configurations, done in the tight-binding approximation with the overlapping of the electron and hole wave functions neglected [14]. As seen in Fig. 3b (points *3*), the polar-

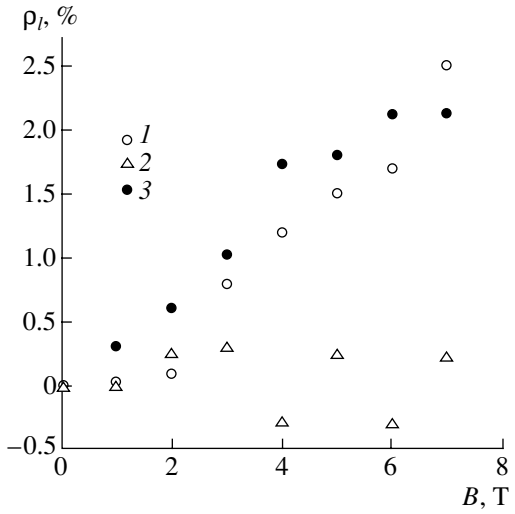

Fig. 4. Emergence of linear polarization ρ_l in magnetic field B (Voigt configuration) under excitation by circularly polarized light of (*1*) GaAs/AlAs (40 Å/6 Å) SL at $E \approx \Delta$, (*2*) GaAs/AlAs (40 Å/80 Å) structure with isolated QWs, and (*3*) bulk GaAs. The positive sign of ρ_l means that the HEP polarization vector $\mathbf{e}_{\text{lum}}$ is preferentially aligned with the magnetic field **B**; for a structure with isolated QWs this effect is absent.

ization in bulk GaAs also depends on the magnetic field because of the rotation of aligned momenta about the axis coinciding with the magnetic field direction; however, it can only decrease in this case. In QWs, the polarization is independent of the field intensity, since the magnetic length exceeds the QW width under the experimental conditions (points *4* in Fig. 3b).

It should be noted that the effects of the magnetic field on the linear polarization in SLs and in bulk GaAs are similar when the kinetic energy of electrons exceeds the energy width of the electron miniband only slightly ($E \approx \Delta$). The experimental data presented in Fig. 3a (points *2*, *2*') show that, with the electron kinetic energy in SL doubled, the polarization dependence becomes similar to that observed in QWs. This behavior is accounted for by the fact that the lateral kinetic energy ε_k grows when the total kinetic energy E of an electron increases. When ε_k substantially exceeds the energy width of the miniband, the change in the lateral momentum $\hbar k$ by $\sim\sqrt{2m_c\Delta}$ becomes insignificant.

A striking experimental illustration of the specificity of the quasi-3D electron motion in narrow-miniband SLs is the emergence of linear polarization under unpolarized pumping in a magnetic field. Figure 4 presents the $\rho_l(B)$ dependences for QWs (data set *2*), SLs with $x = 1$ (data set *1*), and bulk GaAs (data set *3*). To determine the degree of linear polarization, two components of the HEL intensity were measured: parallel ($I_\parallel$) and perpendicular ($I_\perp$) to the **B** vector. As for bulk GaAs, the linear polarization of the HEL in SLs emerges in a magnetic field, the effect being zero in QWs. In a bulk semiconductor subjected to unpolarized pumping, the momentum distribution function is axially symmetric about the direction of the light propagation [2], and $\rho_l = 0$ at $\mathbf{B} = 0$. The transverse magnetic field causes rotation of the momentum distribution, giving rise to an anisotropy in the plane perpendicular to the direction of light propagation. This yields a linearly polarized HEL. The positive sign of ρ_l means that the photoexcited electrons mainly move along the light beam. In QWs, the linear polarization remains unchanged, because the magnetic length exceeds the QW width [7] in the magnetic fields used in the experiment. In SLs, the transverse magnetic field modifies the electron motion along the SL (**Q** vector) and the in-plane motion (component of the lateral vector **k** perpendicular to **B**), if $E \leq \Delta$. Similarly to the bulk case, this effect manifests itself in the linear polarization of the HEL, and the positive sign of ρ_l means that the photoexcited electrons move mainly along the SL.

The results presented in this section confirm the conclusion that the momentum distribution function in "narrow-band" SLs is extended along the SL direction if $E \leq \Delta$.

5. CONCLUSION

The formation of an electron miniband in a $GaAs/Al_xGa_{1-x}As$ SL results in the momentum distribution function of photoexcited electrons strongly depending on the ratio between their kinetic energy E and the width of the electron miniband Δ. This is accounted for by the fact that the majority of electrons excited with $E \leq \Delta$ move along the SL, while the motion of electrons excited with $E > \Delta$ is preferentially in-plane. This is particularly clearly evidenced by the dependence of the linear polarization on magnetic field in the Voigt configuration. With increasing widths of the electron and hole minibands in the SL, the matrix elements of optical transitions are substantially modified. The dependence of polarization on the kinetic energy of photoexcited electrons becomes similar to that in the bulk semiconductor, i.e., it is weak. In a SL with wide minibands, the effect of spin–momentum correlation, typical of bulk GaAs but absent in QW structures, is restored. These results show that a transition from quasi-3D momentum alignment and spin orientation of photoexcited electrons to the limit of a bulk semiconductor occurs when the width of the first electron miniband becomes equal to the width of the first forbidden band of the SL. This condition determines the applicability limits of the tight-binding approximation in calculating matrix elements of intersubband optical transitions.

REFERENCES

1. D. N. Mirlin, I. Ya. Karlik, L. P. Nikitin, *et al.*, Solid State Commun. **37**, 757 (1981).

2. B. P. Zakharchenya, D. N. Mirlin, V. I. Perel', and I. I. Reshina, Usp. Fiz. Nauk **136** (3), 459 (1982) [Sov. Phys. Usp. **25**, 143 (1982)].
3. S. A. Lyon, J. Lumin. **35**, 121 (1986).
4. M. A. Alekseev, I. Ya. Karlik, D. N. Mirlin, and V. F. Sapega, Fiz. Tekh. Poluprovodn. (Leningrad) **23** (5), 761 (1989) [Sov. Phys. Semicond. **23**, 479 (1989)].
5. D. N. Mirlin and V. I. Perel', Semicond. Sci. Technol. **7**, 1221 (1992).
6. B. P. Zakharchenya, P. S. Kop'ev, D. N. Mirlin, *et al.*, Solid State Commun. **69** (3), 203 (1989).
7. P. S. Kop'ev, D. N. Mirlin, D. G. Polyakov, *et al.*, Fiz. Tekh. Poluprovodn. (Leningrad) **24** (7), 1200 (1990) [Sov. Phys. Semicond. **24**, 757 (1990)].
8. J. A. Kash, M. Zachau, M. A. Tischler, and U. Ekenberg, Phys. Rev. Lett. **69** (15), 2260 (1992).
9. M. Zachau, J. A. Kash, and W. T. Masselink, Phys. Rev. B **44** (8), 4048 (1991).
10. D. N. Mirlin, V. F. Sapega, A. A. Sirenko, *et al.*, Fiz. Tekh. Poluprovodn. (St. Petersburg) **27** (6), 990 (1993) [Semiconductors **27**, 537 (1993)].
11. I. A. Merkulov, V. I. Perel', and M. E. Portnoĭ, Zh. Éksp. Teor. Fiz. **99** (4), 1202 (1991) [Sov. Phys. JETP **72**, 669 (1991)].
12. I. Ya. Karlik, D. N. Mirlin, L. P. Nikitin, *et al.*, Pis'ma Zh. Éksp. Teor. Fiz. **36** (5), 155 (1982) [JETP Lett. **36**, 192 (1982)].
13. V. F. Sapega, V. I. Perel', A. Yu. Dobin, *et al.*, Pis'ma Zh. Éksp. Teor. Fiz. **63** (4), 285 (1996) [JETP Lett. **63**, 305 (1996)].
14. V. F. Sapega, V. I. Perel', A. Yu. Dobin, *et al.*, Phys. Rev. B **56** (11), 6871 (1997).
15. V. F. Sapega, V. I. Perel', D. N. Mirlin, *et al.*, Fiz. Tekh. Poluprovodn. (St. Petersburg) **33** (6), 738 (1999) [Semiconductors **33**, 681 (1999)].

Translated by D. Mashovets

Semiconductors, Vol. 35, No. 6, 2001, p. 734. Translated from Fizika i Tekhnika Poluprovodnikov, Vol. 35, No. 6, 2001, p. 766.

PERSONALIA

Vadim Valentinovich Emtsev (Dedicated to His 60th Birthday)

We whole-heartedly congratulate Vadim Valentinovich Emtsev, the deputy editor-in-chief of the journal *Fizika i Tekhnika Poluprovodnikov* (*Semiconductors*), on the occasion of his 60th birthday.

After having graduated from the Leningrad Polytechnical Institute in 1964 and having worked for several years at a defense enterprise in Kazan, V.V. Emtsev joined the Ioffe Physicotechnical Institute. For more than 30 years, he was affiliated with this prominent scientific center.

V.V. Emtsev has been and is engaged with success in studies of impurity centers and native defects in diamond-like semiconductors. His studies of the interaction of native point defects with various impurities in silicon and germanium are of great importance. In recent years, he has supervised intense studies of precipitation of oxygen in silicon, including precipitation under the effect of high hydrostatic pressure. A number of important results have been obtained; these results made it possible to determine the main patterns in the behavior of rare-earth impurities in silicon. The studies of structural defects in such topical materials as the gallium and indium nitrides have been stimulated and extended.

V.V. Emtsev is an author and coauthor of more than 140 scientific publications, including a monograph. Since 1997, he has been a member of consultative committees of International Conferences on the Defects in Semiconductors (ICDS-19, ICDS-20, and ICDS-21). As the deputy editor-in-chief of this journal, V.V. Emtsev contributed to the regular publication and the high scientific level of the journal *Fizika i Tekhnika Poluprovodnikov* (*Semiconductors*) in spite of the difficult economical situation.

Invariable benevolence and charm, in combination with the vitality of V.V. Emtsev, make working with him enjoyable and fruitful. We wish V.V. Emtsev many happy returns of the day, good health, and further creative endeavors.

Colleagues, friends,
and the members
of editorial staff
of this journal

Translated by A. Spitsyn

1063-7826/01/3506-0734$21.00